

The donor and acceptor side of photosystem II: Structural and functional investigations

vorgelegt von
Dipl.-Biophys.
Carina Glöckner
aus Rosenheim

von der Fakultät II – Mathematik und Naturwissenschaften
der Technischen Universität Berlin
zur Erlangung des akademischen Grades

Doktor der Naturwissenschaften
– Dr. rer. nat. –

genehmigte Dissertation

Promotionsausschuß:

Vorsitzender: Prof. Dr. T. Ressler
Gutachterin: Prof. Dr. A. Zouni
Gutachter: Prof. Dr. T. Friedrich
Gutachter: Prof. Dr. H. Dobbek

Tag der wissenschaftlichen Aussprache: 21. Juni 2013

Berlin 2013

D83

*Für meine Eltern
Monika und Hansjörg*

Zusammenfassung

Die oxygene Photosynthese ist ein einzigartiger und essentieller photochemischer Prozess in dem Sonnenenergie zur Oxidation von Wasser und Bildung von Kohlehydraten genutzt wird. Dem Multiproteinkomplex Photosystem II (PSII) kommt dabei eine Schlüsselfunktion zu, da es den Ort der Wasserspaltung beherbergt. Eine Grundvoraussetzung, den Mechanismus der lichtinduzierten Wasserspaltung vollständig zu enthüllen, ist die detaillierte Aufklärung der molekularen Struktur und der dynamische Prozesse von PSII.

In der vorliegenden Arbeit wurden PSII Kernkomplexe (PSIIcc) des thermophilen Cyanobakterium *Thermosynechococcus elongatus* benutzt, um die zwei Funktionsseiten des PSII, bekannt als Akzeptor und Donor Seite, mittels zwei verschiedener Ansätze zu untersuchen:

Die Akzeptor Seite des PSII ist Wirkungsziel vieler kommerziell genutzter Herbizide, die mit dem nativen Elektronenakzeptor Plastochinon um die Bindung an der Q_B Seite konkurrieren und so den Elektronentransfer von Q_A nach Q_B blockieren. In dieser Arbeit wird die erste Röntgenkristallstruktur von dimerem PSIIcc (dPSIIcc) mit gebundenem Herbizid bei einer Auflösung von 3.2 Å vorgestellt. Es wird gezeigt, dass das Herbizid Terbutryn durch mindestens zwei Wasserstoffbrücken in der Q_B Bindungstasche fixiert ist, ähnlich wie in photosynthetischen Reaktionszentren der anoxygenen Purpurbakterien. Die Herbizid Bindung in dPSIIcc wird auch im Hinblick auf ihren Einfluss auf das Redoxpotential von Q_A diskutiert, von dem bekannt ist, dass es sich auf die Photoinhibition auswirkt. Zudem wurde eine zweite und neue Chlorid-Bindungsstelle in der Kristallstruktur des dPSIIcc/Terbutryn-Komplexes identifiziert. Diese neue Chlorid-Bindungsstelle befindet sich in der Nähe des Mn_4Ca -Clusters auf der Donor Seite von dPSIIcc. Die neu entdeckte Chlorid-Bindungsstelle wird in folgenden Zusammenhängen diskutiert: (i) Chlorid-Positionen in den nativen dPSIIcc Strukturmodellen mit Auflösungen von 2.9 und 1.9 Å (Guskov, A. *et al.* (2009) *Nat. Struct. Mol. Biol.* 16, 334–342; Umena, Y. *et al.* (2011) *Nature* 473, 55–60), (ii) mögliche Wechselwirkung zwischen der Akzeptor und der Donor Seite von dPSIIcc, (iii) Protonentransfer zum Lumen.

Die Donor Seite des PSII beherbergt den katalytischen Ort der oxidativen Wasserspaltung, den anorganischen Mn_4Ca -Cluster. Während der Oxidation von Wasser durchläuft dieser Metallcluster eine Abfolge verschiedener Oxidationsstufen (S_0 bis S_4), die als S-Zyklus bezeichnet wird. In der vorliegenden Arbeit wurde Röntgenabsorptionsspektroskopie (XAS) an dPSIIcc Lösungsproben eingesetzt, um die strukturellen Veränderungen des Mn_4Ca -Clusters während der Übergänge der S Zustände zu untersuchen. Es wurde beobachtet, dass sich speziell die kurzen Mn-Mn Abstände während des katalytischen Zyklus ändern. Basierend auf der Mn_4Ca -Cluster Geometrie aus polarisierten XAS Modellen (Yano, J. *et al.* (2006) *Science* 314, 821-825) und aus der nativen dPSIIcc Kristallstruktur mit 1.9 Å Auflösung des Cyanobakteriums *T. vulcanus* (Umena, Y. *et al.* (2011) *Nature* 473, 55–60), wird in dieser Arbeit ein Model für die Strukturveränderungen des Mn_4CaO_5 -Cluster während des S-Zyklus vorgeschlagen. In diesem Model hat der Mn_4CaO_5 -Cluster im S_1 und S_2 Zustand eine Struktur, die einem offenen Würfel ähnelt. Beim Übergang in den S_3 Zustand ändert sich diese zu einer geschlossenen würfelartigen Struktur. Ebenfalls mittels XAS Untersuchungen an dPSIIcc Lösungsproben, wird außerdem die Auswirkung des Strahlenschadens auf den Mn_4Ca -Cluster während Röntgendiffraktionsmessungen dargestellt. dPSIIcc Lösungsproben, in denen die Mn Reduktion durch Röntgenstrahlen induziert wurde, zeigen deutliche Unterschiede in den XAS Spektren im Vergleich zu intakten dPSIIcc Lösungsproben. Genauere Informationen über die Veränderung der Mn Abstände während des S-Zyklus, sowie Informationen über deren Orientierung kann durch polarisierte XAS an PSIIcc Einkristallen gewonnen werden. Bei dieser Methode ist die Untersuchung von Einkristallen der monomeren PSIIcc Form (mPSIIcc) sehr vielversprechend, aufgrund der für orientierungsabhängige Spektroskopie vorteilhaften Anordnung der PSII Proteine im Kristall. In der vorliegenden Arbeit wird gezeigt, dass mPSIIcc Lösungsproben für XAS-Studien geeignet sind, jedoch wurde ein relativ hoher Gehalt an freiem Mn(II) in den mPSIIcc Kristallen entdeckt. Sauerstoffaktivitätsmessungen und Elektronenspinresonanz Studien zeigen, dass die hohe Menge an $CaCl_2$ in den Kristallisationsbedingungen von mPSIIcc der Grund für die Mn Reduktion ist. Diese Arbeit zeigt erste Versuche mPSIIcc unter anderen Bedingungen zu kristallisieren, beginnend mit Veränderungen an dessen Aufreinigungsprotokoll.

Abstract

Oxygenic photosynthesis is a unique and essential photochemical process in which solar energy is used to oxidize water and to form carbohydrates. The multi-subunit protein complex Photosystem II (PSII) plays a key role in the photosynthetic reactions as it harbors the site of water cleavage. A prerequisite for a complete understanding of the mechanism of light-induced water oxidation is the detailed elucidation of the molecular structure of PSII and its dynamic processes.

In the present work, PSII core complexes (PSIIcc) from the thermophilic cyanobacterium *Thermosynechococcus elongatus* are used to investigate the two functional sides of PSII, known as acceptor and donor side, by applying two different approaches:

The acceptor side of PSII is the target of various commercially used herbicides. They compete with the native electron acceptor plastoquinone for binding at the Q_B site in the D1 subunit and, thus, block the electron transfer from Q_A to Q_B . In this work, the first X-ray diffraction crystal structure of dimeric PSIIcc (dPSIIcc) with a bound herbicide at a resolution of 3.2 Å is presented. In the dPSIIcc/terbutryn co-crystals, the herbicide terbutryn is found to bind via at least two hydrogen bonds to the Q_B site similar to photosynthetic reaction centers in anoxygenic purple bacteria. Herbicide binding to dPSIIcc is also discussed in respect to their influence on the redox potential of Q_A , which is known to affect photoinhibition. Furthermore, a second and novel chloride position could be identified in the dPSIIcc/terbutryn crystal structure at 3.2 Å resolution. This novel chloride binding site is located close to the Mn_4Ca cluster at the donor side of dPSIIcc. The new discovered chloride site is discussed in the context of (i) chloride positions found in the structural models of native dPSIIcc at 2.9 Å and 1.9 Å resolution, respectively (Guskov, A. *et al.* (2009) *Nat. Struct. Mol. Biol.* 16, 334–342; Umena, Y. *et al.* (2011) *Nature* 473, 55–60), (ii) a possible interplay between the acceptor and donor side of dPSIIcc, and (iii) proton transfer to the lumen.

The donor side of PSII harbors the catalytic site of water cleavage, which is the inorganic Mn_4Ca cluster. During water oxidation, this metal cluster undergoes a series of oxidation state transitions (S_0 to S_4), a process called S state cycle. In this work, X-ray absorption spectroscopy (XAS) on dPSIIcc solution samples was used to study the structural changes of the Mn_4Ca cluster during each S state transition. It was found, that especially the short Mn-Mn interactions alter during the catalytic cycle. Based on the geometry of the Mn_4Ca cluster as obtained from polarized XAS models (Yano, J. *et al.* (2006) *Science* 314, 821-825) and the 1.9 Å resolution crystal structure of native dPSIIcc from the cyanobacterium *T. vulcanus* (Umena, Y. *et al.* (2011) *Nature* 473, 55–60), the present study proposes a model for the structural changes of the Mn_4CaO_5 cluster during the S state cycle. In this model, the Mn_4CaO_5 cluster in the S_1 and S_2 states has an open-cubane like structure that changes to a closed-cubane like structure upon the S_2 to S_3 state transition. Additionally, the effect of radiation damage to the Mn_4Ca cluster during X-ray diffraction measurements is demonstrated by XAS studies on dPSIIcc solution samples, in which Mn reduction was induced by exposure to X-rays. The XAS spectra of these samples are significantly different from XAS spectra of intact dPSIIcc solution samples. More detailed information on Mn distance variations during the S state transitions as well as orientational information can be gained from polarized XAS studies on single PSIIcc crystals. In this method, the use of single crystals of the monomeric form of PSIIcc (mPSIIcc) is highly promising due to the spectroscopic advantageous orientation of the mPSIIcc units within the crystal. In the present study, mPSIIcc solution samples are shown to be suitable for XAS measurements, but a relatively high amount of free Mn(II) is discovered in single crystals of mPSIIcc. Using oxygen evolution measurements and electron paramagnetic resonance studies, the high amount of $CaCl_2$ necessary to crystallize mPSIIcc was found as reason for the Mn reduction. Initial experiments toward different crystallization conditions for mPSIIcc, starting with alternations of the purification protocol of mPSIIcc, are reported in this work.

Publications

Parts of the present work have been published in:

Glöckner C.*, Broser M.*, Gabdulkhakov A., Guskov A., Buchta J., Kern J., Müh F., Dau H., Saenger W., Zouni A. (2011) „Structural basis of cyanobacterial photosystem II inhibition by the herbicide terbutryn.” *J. Biol. Chem.* **286**:15964-15972.

* contributed equally

Glöckner C., Kern J., Broser M., Zouni A., Yachandra V., Yano J. (2013) „Structural Changes of the Oxygen Evolving Complex in Photosystem II during the Catalytic Cycle.” *J. Biol. Chem.* DOI:10.1074/jbc.M113.476622.

Further publications:

Burkhardt A., Warmer M., Panneerselvam S., Wagner A., Zouni A., Glöckner C., Reimer R., Hohenberg H., Meents A. (2012) “Fast high-pressure freezing of protein crystals in their mother liquor.” *Acta Cryst. F Struct. Biol. Cryst. Commu.* **68**(4):495-500.

Kern J., Alonso-Mori R., Hellmich J., Tran R., Hattne J., Laksmono H., Glöckner C., Echols N., Sierra R.G., Sellberg J., Lassalle-Kaiser B., Gildea R.J., Glatzel P., Grosse-Kunstleve R.W., Latimer M.J., McQueen T.A., Di Fiore D., Fry A.R., Messerschmidt M., Miahnahri A., Schafer D.W., Seibert M.M., Sokaras D., Weng T.-C., Zwart P.H., White W.E., Adams P.D., Bogan M.J., Boutet S., Williams G.J., Messinger J., Sauter N.K., Zouni A., Bergmann U., Yano J., Yachandra V.K. (2012) “Room temperature femtosecond X-ray diffraction of photosystem II microcrystals.” *Proc. Natl. Acad. Sci. U.S.A.* **109**(25):9721-9726.

Sierra R.G., Laksmono H., Kern J., Tran R., Hattne J., Alonso-Mori R., Lassalle-Kaiser B., Glöckner C., Hellmich J., Schafer D.W., Echols N., Gildea R.J., Grosse-Kunstleve R.W., Sellberg J., McQueen T.A., Fry A.R., Messerschmidt M.M., Miahnahri A., Seibert M.M., Hampton C.Y., Starodub D., Loh N.D., Sokaras D., Weng T.-C., Zwart P.H., Glatzel P., Milathianaki D., White W.E., Adams P.D., Williams G.J., Boutet S., Zouni A., Messinger J., Sauter N.K., Bergmann U., Yano J., Yachandra V.K., Bogan M.J. (2012) “Nanoflow electrospinning serial femtosecond crystallography.” *Acta. Cryst. D Biol. Cryst.* **68**(11):1584-1587.

Alonso-Mori R., Kern J., Gildea R.J., Sokaras D., Weng T.-C., Lassalle-Kaiser B., Tran R., Hattne J., Laksmono H., Hellmich J., Glöckner C., Echols N., Sierra R.G., Schafer D.W., Sellberg J., Kenney C., Herbst R., Pines J., Hart P., Herrmann S., Grosse-Kunstleve R.W., Latimer M.J., Fry A.R., Messerschmidt M.M., Miahnahri A., Seibert M.M., Zwart P.H., White W.E., Adams P.D., Bogan M.J., Boutet S., Williams G.J., Zouni A., Messinger J., Glatzel P., Sauter N.K., Yachandra V.K., Yano J., Bergmann U. (2012) "Energy-dispersive X-ray emission spectroscopy using an X-ray free-electron laser in a shot-by-shot mode." *Proc. Natl. Acad. Sci. U.S.A.* **109**(47):19103-19107.

Kern J., Alonso-Mori R., Tran R., Hattne J., Gildea R.J., Echols N., Glöckner C., Hellmich J., Laksmono H., Sierra R.G., Lassalle-Kaiser B., Koroidov S., Lampe A., Han G., Gul S., Di Fiore D., Milathianaki D., Fry A.R., Miahnahri A., Schafer D.W., Messerschmidt M., Seibert M.M., Koglin J.E., Sokaras D., Weng T.-C., Sellberg J., Latimer M.J., Grosse-Kunstleve R.W., Zwart P.H., White W.E., Glatzel P., Adams P.D., Bogan M.J., Williams G.J., Boutet S., Messinger J., Zouni A., Sauter N.K., Yachandra V.K., Bergmann U., Yano J. (2013) "Simultaneous Femtosecond X-ray Spectroscopy and Diffraction of Photosystem II at Room Temperature." *Science*. DOI:10.1126/science.1234273

Brecht M., Skandary S., Hellmich J., Glöckner C., Konrad A., Hussels M., Meixner A.J., Zouni A., Schlodder E. (2013) "Spectroscopic properties of Photosystem II Core Complexes from *Thermosynechococcus elongatus*." *J. Am. Chem. Soc.* **submitted**.

Reviews:

Guskov A., Gabdulkhakov A., Broser M., Glöckner C., Hellmich J., Kern J., Frank J., Müh F., Saenger W., Zouni A. (2010) "Recent progress in the crystallographic studies of photosystem II." *ChemPhysChem*. **11**(6):1160-71.

Müh F., Glöckner C., Hellmich J., Zouni A. (2012) "Light-induced quinone reduction in photosystem II." *Biochim. Biophys. Acta* **1817**(1):44-65.

Talks:

"Strukturaufklärung Photosystem II", Biochemistry and plant physiology seminar for students, 2010, Interdisciplinary Center of Photonics, University of Potsdam, Germany.

“Focus on the Acceptor Side: Structural Basis of Photosystem II Inhibition by the Herbicide Terbutryn” International Conference on Photosynthesis Research for Sustainability, 2011, Baku, Azerbaijan.

Poster presentations:

Glöckner C., Broser M., Gabdulkhakov A., Kern J., Guskov A., Müh F., Saenger W., Zouni A. (2010) “Crystal Structure of Monomeric Photosystem II at 3.6 Å Resolution.” in: *15th International Congress on Photosynthesis*, Beijing, China.

Zouni A., Glöckner C., Broser M., Gabdulkhakov A., Guskov A., Kern J., Müh F., Buchta J., Dau H., Saenger W. (2011) „First Crystal Structure of Cyanobacterial Photosystem II with Terbutryn at 3.2 Å Resolution.” in: *International Conference on Photosynthesis Research for Sustainability*, Baku, Azerbaijan.

Abbreviations

ATP	adenosine-5'-triphosphate
β DM	n-dodecyl- β -D-maltoside
BN-PAGE	blue native polyacrylamide gel electrophoresis
<i>B. viridis</i>	<i>Blastochloris viridis</i>
Car	carotenoid
Chla	chlorophyll <i>a</i>
CMC	critical micelle concentration
CSC	critical solubilization concentration
CV	column volume
cyt	cytochrome
DCBQ	2,6-dichloro-1,4-benzoquinone
DEAE	diethylaminoethyl
DFT	density functional theory
DGDG	digalactosyldiacylglycerol
DMSO	dimethyl sulfoxide
dPSIIcc	dimeric photosystem II core complex
EDTA	ethylenediaminetetraacetic acid
EET	excitation energy transfer
E_m	redox midpoint potential
ENDOR	electron nuclear double-resonance
EPR	electron paramagnetic resonance
EXAFS	extended X-ray absorption fine structure
Fd	ferredoxin
FNR	ferredoxin:NADP:oxidoreductase
FTIR	Fourier-transform infrared spectroscopy
HTG	n-Heptyl- β -D-thiogluconide
LCLS	Linac Coherent Light Source
LMW	low molecular weight
MALDI-TOF	matrix assisted laser desorption ionization time of flight
MD	molecular dynamics
MES	2-(N-morpholino)ethanesulfonic acid
MGDG	monogalactosyldiacylglycerol
mPSIIcc	monomeric photosystem II core complex
MS	mass spectrometry
NADPH	nicotinamide adenine dinucleotide phosphate (reduced form)

OEC	oxygen evolving complex
PBQ	p-benzoquinone
pbRC	purple bacterial reaction center
PC	plastocyanin
PDB	protein data bank
PEG	polyethylene glycol, poly(oxyethylene)
PF	prompt fluorescence
PG	phosphatidylglycerol
Pheo	pheophytin <i>a</i>
PIPES	piperazine-N,N'-bis[2-ethanesulfonic acid]
P _i	orthophosphate
PSIcc	photosystem I core complex
PSIIcc	photosystem II core complex
PsbA-Z	protein encoded by the corresponding PSII gene <i>psbA-Z</i>
PQ	plastoquinone
PQH ₂	plastoquinol
Q _A	primary quinone electron acceptor
Q _B	secondary quinone electron acceptor
Q _C	third quinone molecule
RC	reaction center
ROS	reactive oxygen species
S _i	oxidation state of the OEC (with <i>i</i> = number of oxidizing equivalents)
SQDG	sulfoquinoldiacylglycerol
<i>T. elongatus</i>	<i>Thermosynechococcus elongatus</i>
<i>T. vulcanus</i>	<i>Thermosynechococcus vulcanus</i>
TMH	transmembrane α -helix
Tyr _D or Y _D	Tyrosine D (D2-Tyr160) of PSII
Tyr _Z or Y _Z	Tyrosine Z (D1-Tyr161) of PSII
XANES	X-ray absorption near edge spectroscopy
XAS	X-ray absorption spectroscopy
XFEL	X-ray Free-Electron Laser
XRD	X-ray diffraction

Contents

Zusammenfassung	v
Abstract	vii
Publications	ix
Abbreviations	xiii
Contents	xv
1. Introduction	1
1.1 Overview of photosynthesis	2
1.2 Oxygenic photosynthesis	5
1.3 Photosystem II	9
1.3.1 Overall structure	10
1.3.2 Subunits	14
1.3.3 Functions of PSIIcc cofactors	17
1.3.4 Donor side	21
1.3.5 Acceptor side	33
1.3.6 The monomeric form of PSIIcc	39
1.3.7 Comparison of <i>T. elongatus</i> and <i>T. vulcanus</i> native dPSIIcc XRD structures ..	41
1.4 Project aims	43
2. Materials and Methods	45
2.1 Chemicals and Materials	45
2.2 Methods	46
2.2.1 Cell cultivation and protein extraction	46
2.2.2 Protein purification	46
2.2.3 Crystallization of mPSIIcc	48
2.2.4 Co-crystallization of dPSIIcc and terbutryn	48
2.2.5 Oxygen evolution measurements	49
2.2.6 Gel permeation chromatography	49
2.2.7 Mass spectrometry	49
2.2.8 Blue native polyacrylamide gel electrophoresis	49

2.2.9 Single flash induced Chla fluorescence measurements.....	50
2.2.10 X-ray diffraction data collection.....	51
2.2.11 X-ray absorption spectroscopy on PSIIcc	51
2.2.11.1 Theoretical basics of X-ray absorption spectroscopy	51
2.2.11.2 Experimental procedures.....	56
3. Herbicide binding to dPSIIcc.....	61
3.1 Introduction	61
3.2 Single flash-induced Chla fluorescence in the presence of terbutryn.....	62
3.3 Crystal structure of terbutryn-bound dPSIIcc.....	64
3.3.1 Crystallographic analysis.....	65
3.3.2 Terbutryn binding at the acceptor side.....	66
3.3.3 Interplay between the acceptor and donor side	73
3.4 Summary	79
4. X-ray absorption spectroscopy on PSIIcc.....	81
4.1 Previous X-ray absorption spectroscopy on PSII.....	82
4.2 Structural changes of the Mn ₄ CaO ₅ cluster during the catalytic S state cycle	84
4.3 Effect of radiation damage to the Mn ₄ CaO ₅ cluster in the S ₁ state.....	95
4.4 X-ray absorption spectroscopy on mPSIIcc solution samples in the S ₁ state.....	98
4.5 X-ray absorption spectroscopy on single crystals of mPSIIcc.....	100
4.6 Initial experiments toward new crystallization conditions for mPSIIcc.....	105
4.6.1 Purification	105
4.6.2 Characterization	107
4.6.3 Crystallization screens	113
4.7 Summary	113
5. Outlook	117
Appendix.....	119
List of Figures and Tables.....	123
Danksagung	127
References	129

1. Introduction

"Breath is life. We should pay as much attention to it as any other aspect of beingness."

(Swami Nostradamus Virato)

The average adult at rest inhales and exhales about eight liters of air per minute. The air that is inhaled consists of 20.95% molecular oxygen (1), a molecule vital for the proper function of our whole metabolism and therefore, for complex life. With every breath, we consume about one quarter of the inhaled molecular oxygen. This is equivalent to 400 ml oxygen per minute (2, 3). At the 2012 world population of about seven billion people (estimated by the United States Census Bureau), a volume of at least 2.8 billion liters molecular oxygen is consumed every single minute just by us human beings. But how is the constant oxygen supply on Earth ensured? And what is the origin of molecular oxygen?

The source of almost all oxygen in Earth's atmosphere is water. However, water is a very stable molecule and the formation of molecular oxygen by oxidation of water requires a very strong oxidizing agent. The photosynthetic oxygen evolving complex (OEC) in cyanobacteria, algae and plants is the only known biochemical system that performs this reaction and thus, constantly produces molecular oxygen for us to inhale. For example, a beech tree with about one million leaves produces around 4600 kg oxygen per year. This amount is equal to a molecular oxygen volume of six liter per minute. Therefore, one beech tree is able to supply 15 human beings with molecular oxygen¹ (4). In oxygenic photosynthesis $2 - 4 \times 10^{18}$ kJ/year of light energy (corresponds to 0.1% of the total light energy arriving on the earth's surface) is used to oxidize water and to fix more than 10% of the total aerial carbon dioxide per year. As a consequence, molecular oxygen is released and carbohydrates are formed, which serve as food for all living organisms (5).

Oxygenic photosynthesis is a unique and essential process of very high interest in science. The complete elucidation and understanding of its mechanism is one of the greatest challenges for scientists. A long term aim is the technical use of solar energy and artificial photosynthesis as regenerative energy sources. Likewise, hydrogen production from water splitting is considered as a great fuel for the future ((6) and references therein).

¹Note, the consume of molecular oxygen by human beings as well as the oxygen production of a tree depends on several factors (e.g. height, weight, age, climate conditions) and can therefore only be calculated hypotheticalal.

1.1 Overview of photosynthesis

All photosynthetic organisms convert light energy into a form suitable for storage and use in metabolism, thereby consuming per year up to 2.5×10^{18} kJ solar energy (7). For the efficient absorption of sunlight, photosynthetic pigments with appropriate absorption properties are needed (8). These pigments form light harvesting systems which mainly consist of three classes of chromophores: (bacterio-) chlorophylls with a cyclic π -electron system of tetrapyrroles; phycobilins with an open chain tetrapyrrole; and carotenoids with a linear chain of conjugated isoprene units and varying modifications at the cyclized ionone end group. In cyanobacteria, the cyclic tetrapyrrole chlorophyll *a* (Chl*a*) and its demetallation product pheophytin *a* (Pheo) are found (Fig. 1.1). Chl*a* and Pheo ensure the light absorption in the region around 430 nm and 670 nm. Other organisms harbor chemically related tetrapyrroles such as Chl*b*, and bacteriochlorophyll *a* and *b* (BChl*a*, BChl*b* in purple bacteria). The pigment class of phycobilins can also be found in cyanobacteria and in red algae. The two major forms in cyanobacteria are phycocyanobilin and phycoerythrobilin (Fig. 1.1), which are incorporated into phycobiliproteins via a covalent thioether linkage. Phycobiliproteins are assembled to so-called phycobilisomes and function as extrinsic antennae, with absorption maxima between 500 nm and 650 nm (9). The carotenoids β -carotene (Fig. 1.1), lutein and zeaxanthin are very common in cyanobacteria and absorb strongly between 430 nm and 480 nm. Together, the three different pigment classes cover almost the complete spectrum of visible light (Fig. 1.2), enabling a very efficient light absorption and energy transfer to the reaction center.

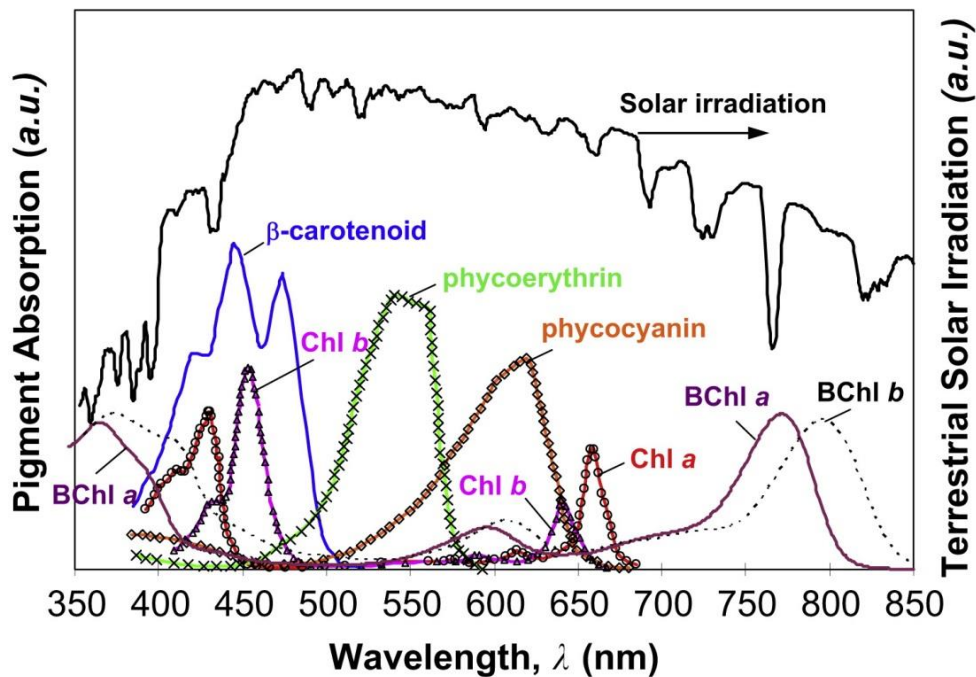


Figure 1.2 Absorption spectra of photosynthetic pigments.

Absorption spectra of chlorophyll a (red), chlorophyll b (pink), bacteriochlorophyll a (purple), bacteriochlorophyll b (black dots), β -carotene (blue), phycoerythrin (green) and phycocyanin (orange) are shown in relation to the terrestrial solar irradiation spectrum (linear scale). Figure taken from (10).

A photosynthetic reaction center (RC) is the smallest unit able to perform the primary energy conversion reactions of photosynthesis. It is a complex of several proteins, pigments and other cofactors which are anisotropically incorporated into a membrane. The RC of a photosystem is capable of generating light induced charge separation and its subsequent stabilization. Although separated by billions of years of evolution, the functional arrangement and architecture of the RCs are homologous for all photosynthetic species. RCs can be subdivided into a donor side and an acceptor side, referring to the electron transfer reactions. Light excitation of the primary electron donor (a homo-, di- or multimer of chlorophylls) and consequent electron transfer to the primary electron acceptor lead to charge separation. This charge separated state is further stabilized by the following electron transfer to a terminal electron acceptor. The formed electron “hole” of the primary electron donor is satisfied by the oxidation of an appropriate electron source.

The first photosynthetic organisms evolved about 3.5 billion years ago and used hydrogen or hydrogen sulfide as an electron source. In this process no oxygen is produced and, therefore, it is called anoxygenic photosynthesis. About half billion years later, cyanobacteria evolved, which were able to use water as reducing agent. In this process,

called oxygenic photosynthesis, molecular oxygen is released as waste product and started to oxygenate the atmosphere, allowing the evolution of complex life (11).

Photosynthetic organisms can also be divided into two types of photochemical RCs, classified by the chemical nature of their terminal electron acceptor: type I RCs (RCI) use ferredoxin-like iron-sulfur clusters as terminal electron acceptors (heliobacteria, green-sulphur bacteria and photosystem I of oxygenic photosynthesis), whereas type II RCs (RCII) utilize a quinone molecule as terminal electron acceptor (purple bacteria, green filamentous bacteria and photosystem II of oxygenic photosynthesis). Cyanobacteria, algae and plants contain both RC types (RCI and RCII) and, therefore, are able to perform oxygenic photosynthesis.

The present work is focused on oxygenic photosynthesis in cyanobacteria. For our studies, the thermophilic cyanobacterium *Thermosynechococcus elongatus* BP1 was used, an organism isolated from a hot spring in Beppu, Japan (12). The main advantage of using a thermophilic organism for protein studies is its high stability, facilitating its handling and biophysical investigation.

1.2 Oxygenic photosynthesis

In cyanobacteria, the protein complexes participating in oxygenic photosynthesis are accumulated mostly in an inner membrane network. These membranes are called thylakoid membranes and develop from plasma membrane infoldings. The space enclosed by these thylakoids is called lumen, and the exterior space is called cytoplasm. In higher plants, oxygenic photosynthesis takes place in the chloroplasts, which are mostly accumulated in the mesophyll cells of leaves. The involved protein complexes are likewise embedded in the thylakoids, the internal membranes of the chloroplast. The thylakoid membranes of chloroplasts form a large interconnected membrane system and separate the inner region, also called lumen, from the exterior, called stroma.

The thylakoids are the site of the light reactions, whereas the carbon fixation reactions take place in the cytoplasm or stroma, catalysed by water-soluble enzymes (13). The lipid composition of thylakoid membranes is highly conserved among oxygenic organisms and is composed of four main lipids (Fig. 1.3): monogalactosyldiacylglycerol (MGDG; ~ 50%), digalactosyldiacylglycerol (DGDG; ~ 30%), sulfoquinovosyldiacylglycerol (SQDG; ~ 5 - 12%), phosphatidylglycerol (PG; ~ 5 - 12%) (14). The thylakoid membrane harbors all four main protein complexes of the oxygenic photosynthetic machinery: photosystem I (PSI), photosystem II (PSII), cytochrome *b₆f* complex (cyt *b₆f*), and ATP synthase. The overall

arrangement of the photosynthetic protein complexes in the thylakoid membrane is shown in Figure 1.4.

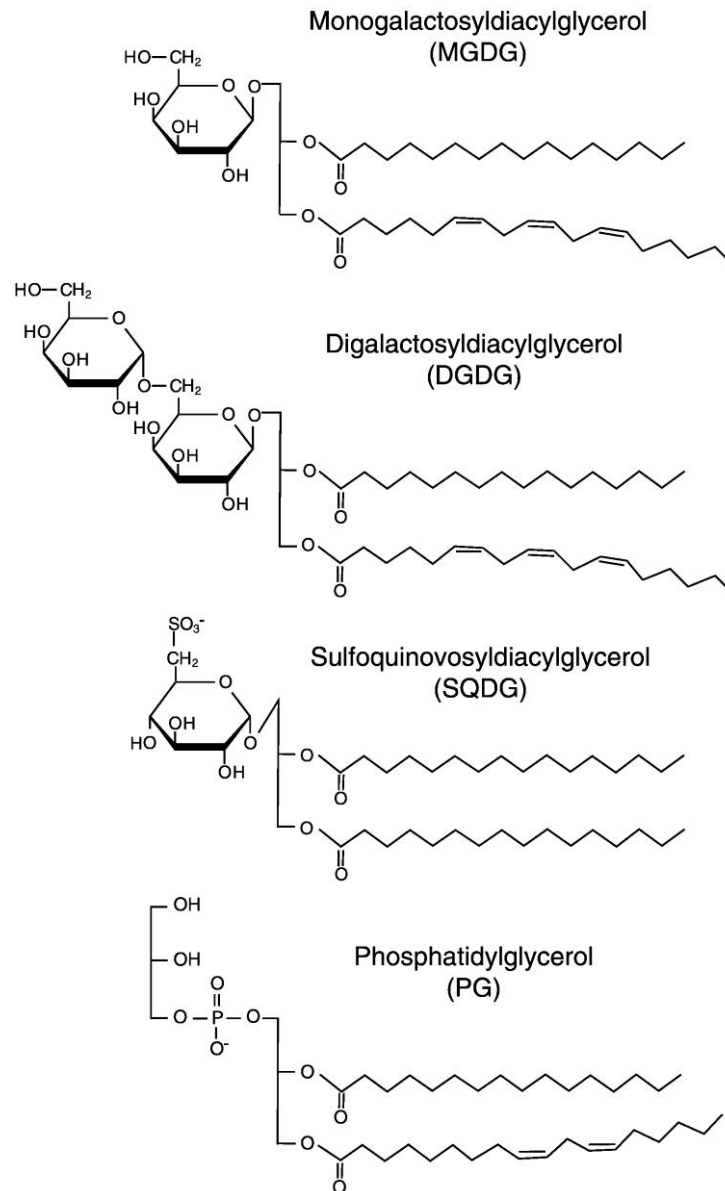


Figure 1.3 Structure of lipids in thylakoid membranes.

Chemical structures of monogalactosyldiacylglycerol (MGDG), digalactosyldiacylglycerol (DGDG), sulfoquinovosyldiacylglycerol (SQDG) and phosphatidylglycerol (PG) are shown. This figure depicts the typical fatty acids bound to each class of lipid in *Synechocystis* sp. PCC 6803. Figure taken from (15).

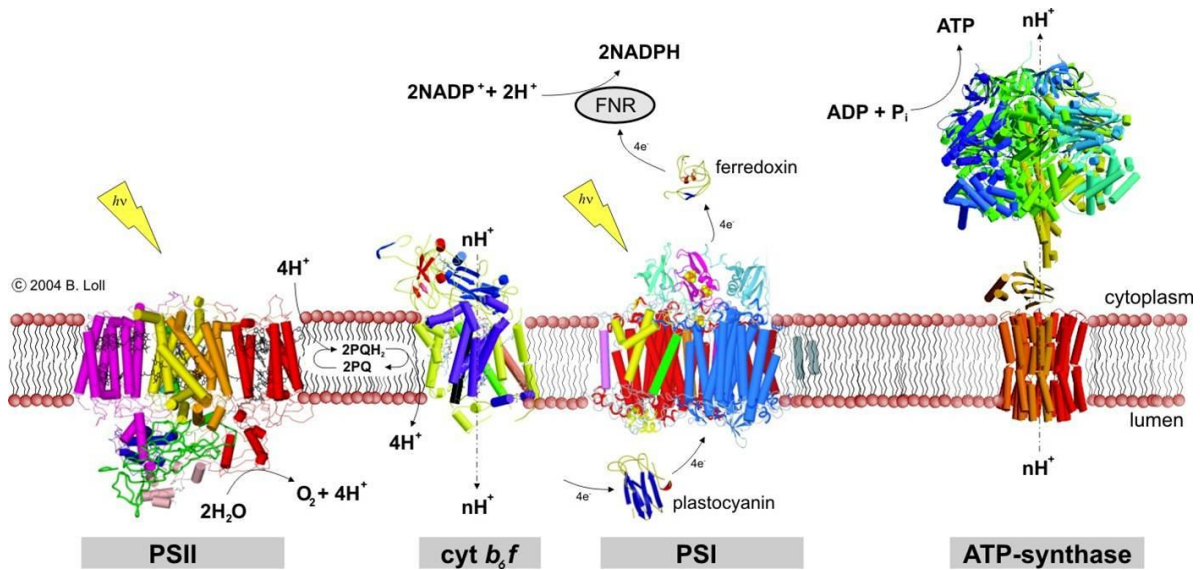


Figure 1.4 Schematic view of the thylakoid membrane with protein complexes involved in oxygenic photosynthesis.

The crystal structures of the protein complexes of PSI, PSII, *cyt b₆f* and ATP-synthase are shown (only one monomer of each complex). The protein complex PSII oxidizes water, thereby releasing protons into the lumen. Reduced plastoquinone transfers electrons to *cyt b₆f*, which in turn reduces plastocyanin that transports the electrons to PSI. PSI reduces NADP^+ to NADPH. The ATP-synthase forms ATP using the electrochemical H^+ gradient across the membrane (Picture © B. Loll).

The basic equation of oxygenic photosynthesis can be written as equation (1) in Table 1.1. Note, that only the RCs of PSI and PSII are able to convert light energy into a biochemically accessible form. The process of oxygenic photosynthesis starts with the light excitation and consequent charge separation in the RC of PSII. PSII acts as a light driven water:plastoquinone:oxidoreductase. The primary electron donor oxidizes, via a redox active tyrosine residue, the close located Mn cluster at the luminal side (donor side) of the complex. The Mn cluster catalyzes the oxidation of two water molecules to four protons and molecular oxygen. Dioxygen is released into the atmosphere, whereas the protons are released into the lumen. At the cytosolic side (acceptor side) of PSII, the final electron acceptor plastoquinone (PQ) is doubly reduced and leaves, after the uptake of two protons from the cytoplasm, the complex as plastoquinol (PQH_2) (equation (2), Table 1.1). PQH_2 is a mobile electron carrier and moves within the membrane to *cyt b₆f*. There, it is reoxidized to PQ and two protons are released into the lumen. The electrons are further transferred to plastocyanin (PC), a copper containing soluble one electron carrier at the luminal side (equation (3), Table 1.1). The reduced PC passes the electron on to PSI. PSI can be described as light-driven plastocyanin:ferredoxin:oxidoreductase. After light excitation of the RC chlorophyll in PSI, the electron is transferred to a primary electron acceptor and, via a series of protein bound iron-sulphur clusters, to the soluble

electron carrier ferredoxin (Fd). Fd is located at the cytoplasmic side and passes the electron on to the membrane-associated flavoprotein ferredoxin:NADP:oxidoreductase (FNR), which in turn catalyzes the reduction of NADP^+ to NADPH (summarized in equations (4) and (5), Table 1.1).

The reactions described so far are called light-dependent or light reactions of photosynthesis. The three protein complexes PSII, *cyt b₆f* and PSI are linked in series and the linear electron transfer process between them is usually depicted in the so called Z-scheme (Fig. 1.5). Under certain conditions, a cyclic electron flow can also occur between *cyt b₆f* and PSI. The cyclic electron flow contributes to the generation of the proton gradient across the membrane, which is needed to ensure the energy supply of the cell. In this cyclic reaction neither water is oxidized nor NADPH is created (16, 17).

The electrochemical gradient caused by the charge separation across the thylakoid membrane is used by the ATP synthase to produce ATP from ADP and P_i . The overall reaction for the light-dependent processes of non-cyclic electron flow can be written as equation (6) in Table 1.1. The stored energy in form of NADPH and ATP is used in the carbon fixation reactions of photosynthesis (summarized in equation (7), Table 1.1), which take place in the cytosol or the stroma (in chloroplasts). In this light-independent reactions, the enzyme Rubisco (ribulose-1,5-bisphosphate carboxylase oxygenase) captures carbon dioxide from the atmosphere and in a chain of reactions, known as the Calvin cycle, carbon dioxide is reduced to carbohydrates (16, 17).

Table 1.1 Equations of oxygenic photosynthesis.

Nr.	Educts	Products
(1)	$\text{CO}_2 + \text{H}_2\text{O}$	$\longrightarrow [\text{CH}_2\text{O}] + \text{O}_2$
(2)	$2\text{H}_2\text{O} + 2\text{PQ} + 4\text{H}^+_{\text{cytoplasm}}$	$\xrightarrow{4 \text{ photons}} \text{O}_2 + 2\text{PQH}_2 + 4\text{H}^+_{\text{lumen}}$
(3)	$\text{PQH}_2 + 2\text{PC}_{\text{ox}} + 2\text{H}^+_{\text{cytoplasm}}$	$\longrightarrow \text{PQ} + 2\text{PC}_{\text{red}} + 4\text{H}^+_{\text{lumen}}$
(4)	$\text{PC}_{\text{red}} + \text{Fd}_{\text{ox}}$	$\xrightarrow{1 \text{ photon}} \text{PC}_{\text{ox}} + \text{Fd}_{\text{red}}$
(5)	$2\text{Fd}_{\text{red}} + \text{NADP}^+ + 2\text{H}^+$	$\xrightarrow{\text{FNR}} 2\text{Fd}_{\text{ox}} + \text{NADPH} + \text{H}^+$
(6)	$2\text{H}_2\text{O} + 2\text{NADP}^+ + 3\text{ADP} + 3\text{P}_i$	$\xrightarrow{8 \text{ photons}} 2\text{NADPH} + 2\text{H}^+ + 3\text{ATP} + \text{O}_2$
(7)	$\text{CO}_2 + 2\text{NADPH} + 2\text{H}^+ + 3\text{ATP}$	$\longrightarrow [\text{CH}_2\text{O}] + 2\text{NADP}^+ + 3\text{ADP} + 3\text{P}_i + \text{H}_2\text{O}$

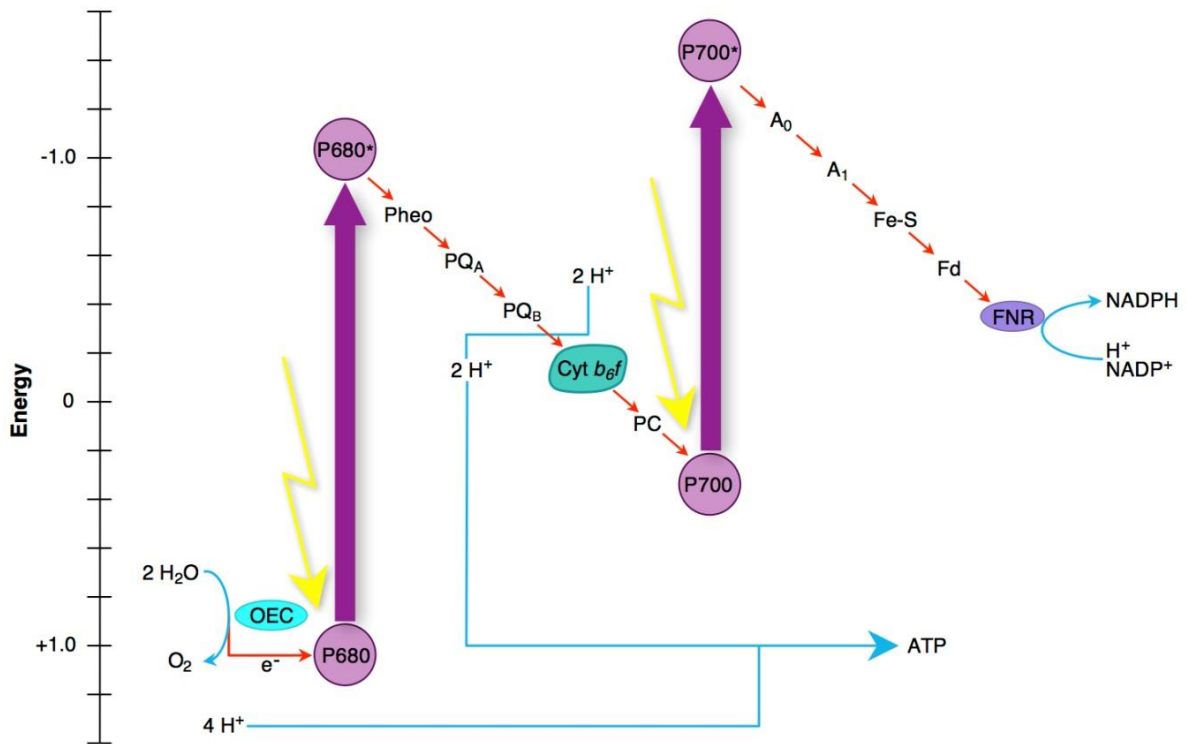


Figure 1.5 Z-scheme of photosynthesis.

The Z-scheme shows the midpoint redox potentials and the electron flow between the protein complexes involved in the light-reactions of photosynthesis. RC chlorophylls of PSII and PSI are shown as purple spheres named P680 and P700, respectively, and *cyt b₆f* as indicated. Photon absorption is indicated by the vertical arrows. Electron transport is indicated by red arrows and proton transport by blue arrows. Water is oxidised by the oxygen-evolving complex (OEC) thereby passing electrons via *Y_Z* (a tyrosine residue, not shown) to P680. The electron transport chain starts at the excited P680 (P680*) and goes via pheophytin (Pheo), the plastoquinones *Q_A* and *Q_B*, *cyt b₆f* complex and plastocyanin (PC) to the oxidised P700*. The electron transport chain of P700* goes via *A₀* (a chlorophyll), *A₁* (a quinone), a series of membrane bound iron-sulphur proteins (Fe-S) and ferredoxin (Fd) to the ferredoxin-NADP reductase (FNR), that finally reduces NADP*.

1.3 Photosystem II

One important aspect to reveal molecular details of the photosynthetic reactions is the resolution of the structure of the involved protein complexes. The structure of the water-splitting protein complex PSII has been investigated in the last two decades by several methods such as electron microscopy, electron paramagnetic resonance (EPR), cryo-electron crystallography on 2D crystals and X-ray spectroscopic measurements, using PSII from different organisms. X-ray diffraction (XRD) crystallography is likewise a method for structural research, and enormous progress has been achieved in this field. The crystal structure of the RC of purple bacteria (pbRC) of *Blastochloris viridis*, reported in 1984 by Deisenhofer *et al.* (18), was the first crystal structure of a membrane protein. It

showed that membrane protein structures can be solved by X-ray crystallography. The functional core of pbRC is a heterodimer of the subunits L and M, which bind all active cofactors: four bacteriochlorophylls, two bacteriopheophytins, two quinones and a non-heme iron center.

In the case of PSII, a milestone in 2001 was the first X-ray diffraction crystal structure of PSII capable of light-induced oxygen production at a resolution of 3.8 Å reported by Zouni *et al.* (19). PSII was isolated as core complexes (PSIIcc) from the thermophilic cyanobacterium *T. elongatus*. These core complexes are functional entities in which the photosynthetic RC is surrounded only by the intrinsic antenna systems and the extrinsic antenna complexes are split off. PSIIcc from *T. elongatus* can be isolated as monomeric (mPSIIcc) and dimeric (dPSIIcc) forms, both active in light-induced water oxidation. The structure of dPSIIcc could be improved to resolutions of 3.5 Å (20) and 3.0 Å (21) and was refined to 2.9 Å in 2009 (22). The crystallization of the mPSIIcc was achieved lately and led to the first crystal structure at 3.6 Å resolution (23). dPSIIcc were also isolated from the cyanobacterium *T. vulcanus* and a first structural model was obtained at 3.7 Å resolution (24). Recently, the crystal structure of this complex was published at a resolution of 1.9 Å (25). The latter crystal structure of *T. vulcanus* dPSIIcc provides so far the most detailed structural information about the PSII protein complex. The 3D-crystallization of dPSIIcc from the red alga *Cyanidium caldarium* has also been reported (26), but the structure elucidation is still at an early stage. In 2010, the first crystal structure of dPSIIcc derived from a higher plant (*Nicotiana tabacum*) became available with a resolution of 7.0 Å (27).

The following introduction on PSII is restricted to PSIIcc isolated from cyanobacteria (if not stated otherwise) and is based mainly on the 2.9 Å resolution crystal structure of dPSIIcc from *T. elongatus* (PDB codes 3BZ1, 3BZ2) (22) with additional information from the 1.9 Å resolution crystal structure of dPSIIcc from *T. vulcanus* (PDB code 3ARC) (25). For explanation and comparison of these two structural models see Section 1.3.7.

1.3.1 Overall structure

The existence of PSIIcc as a monomeric and dimeric form provides a basis for controversial discussions, concerning their respective contribution to the functionality of the photosynthetic apparatus (28, 29). The dimeric form of PSII is mostly understood as the full assembled and functional relevant form, whereas the monomeric form is seen as an intermediate during the assembly process of dPSII (30). A detailed description of mPSIIcc and comparison with the dimeric form is given in Section 1.3.6.

The two identical monomers of dPSIIcc are related by a local-C₂ rotation axis orientated perpendicular to the membrane plane. Each monomer consists of at least 20 protein

subunits, of which 17 are membrane-intrinsic and three are membrane-extrinsic. Each monomer binds the following cofactors: 35 Chl_a molecules, 12 carotenoid molecules, two Pheo molecules, 25 integral lipids, two heme groups (cyt *b559* and cyt *c550*), three PQ molecules, a non-heme iron, four manganese ions (in the OEC), calcium and chloride ions (13, 22, 25).

The core of the RC is formed by the proteins D1 (systematic name: PsbA) and D2 (PsbD), the antenna proteins CP43 (PsbC) and CP47 (PsbB), and cyt *b559* (Fig. 1.6). The core antenna proteins CP43 and CP47 surround the D1/D2 heterodimer and bind 13 and 16 Chl_a, respectively. These pigments serve for light harvesting and transfer the excitation energy to the RC. The PSII RC is structurally homologous to pbRC (31-33) and harbors most of the redox-active cofactors, that are arranged in two symmetry-related branches with respect to the vertical axis crossing the non-heme iron center (Fig. 1.7): At the luminal side the four Chl_a molecules P_{D1}, P_{D2}, Chl_{D1} and Chl_{D2}, in the middle the two Pheo molecules Pheo_{D1} and Pheo_{D2} and at the cytosolic side the two PQ molecules Q_A and Q_B. A non-heme iron is located between these two PQ molecules, coordinated by a bicarbonate anion and conserved histidine residues of subunits D1 and D2. The two Chl_a molecules Chl_{zD1} and Chl_{zD2} are situated in the periphery of the RC. The two redox active tyrosine residues Y_Z (in D1) and Y_D (in D2) are in bridging positions between the four RC chlorophylls and the manganese-containing catalytic site of the OEC. The Mn₄CaO₅ cluster is located at the luminal side of subunit D1.

Further details on the roles of the cofactors, charge separation and electron transfer are given in the following sections.

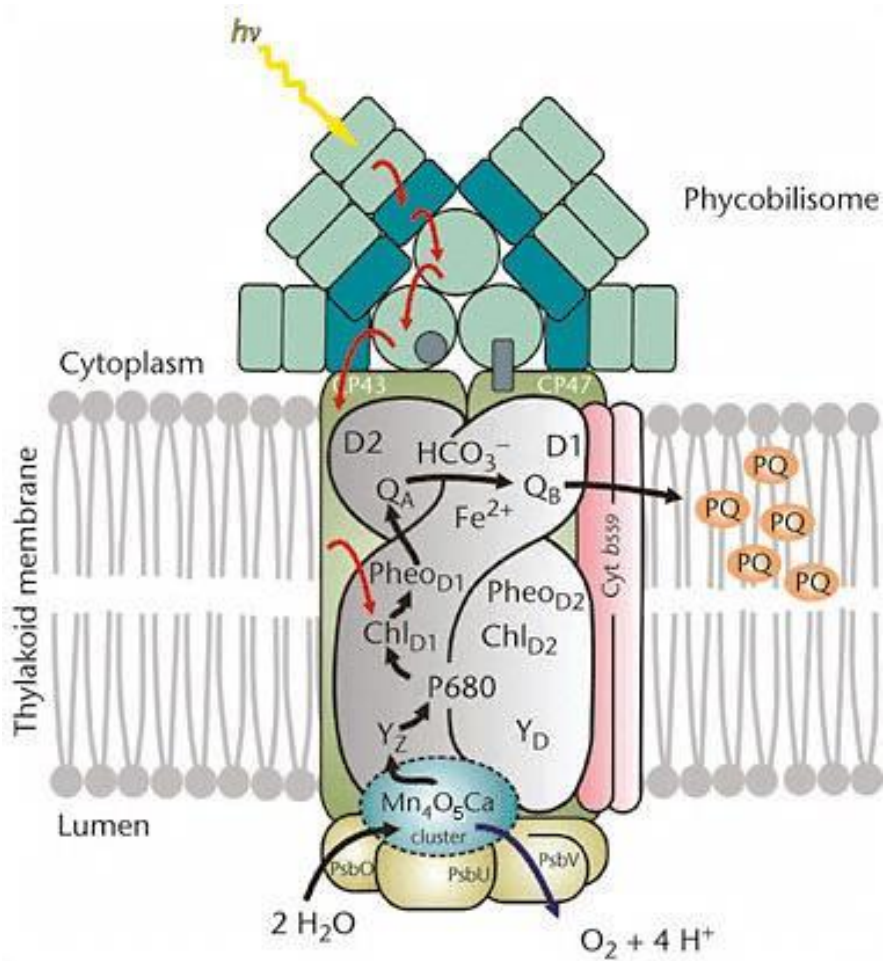


Figure 1.6 Schematic representation of components of PSIIcc in cyanobacteria.

Only the major subunits are shown: D1 and D2 (gray), CP43 and CP47 (green), cyt b559 (light red), PsbO, PsbU and PsbV (light green). The manganese cluster is shown in blue. The electron transfer pathway from the water splitting site (donor side) to plastoquinone Q_B (acceptor side) is depicted by black arrows. Light energy transfer from the extrinsic phycobilisome to the RC chlorophylls is shown by red arrows. Figure adapted from (34).

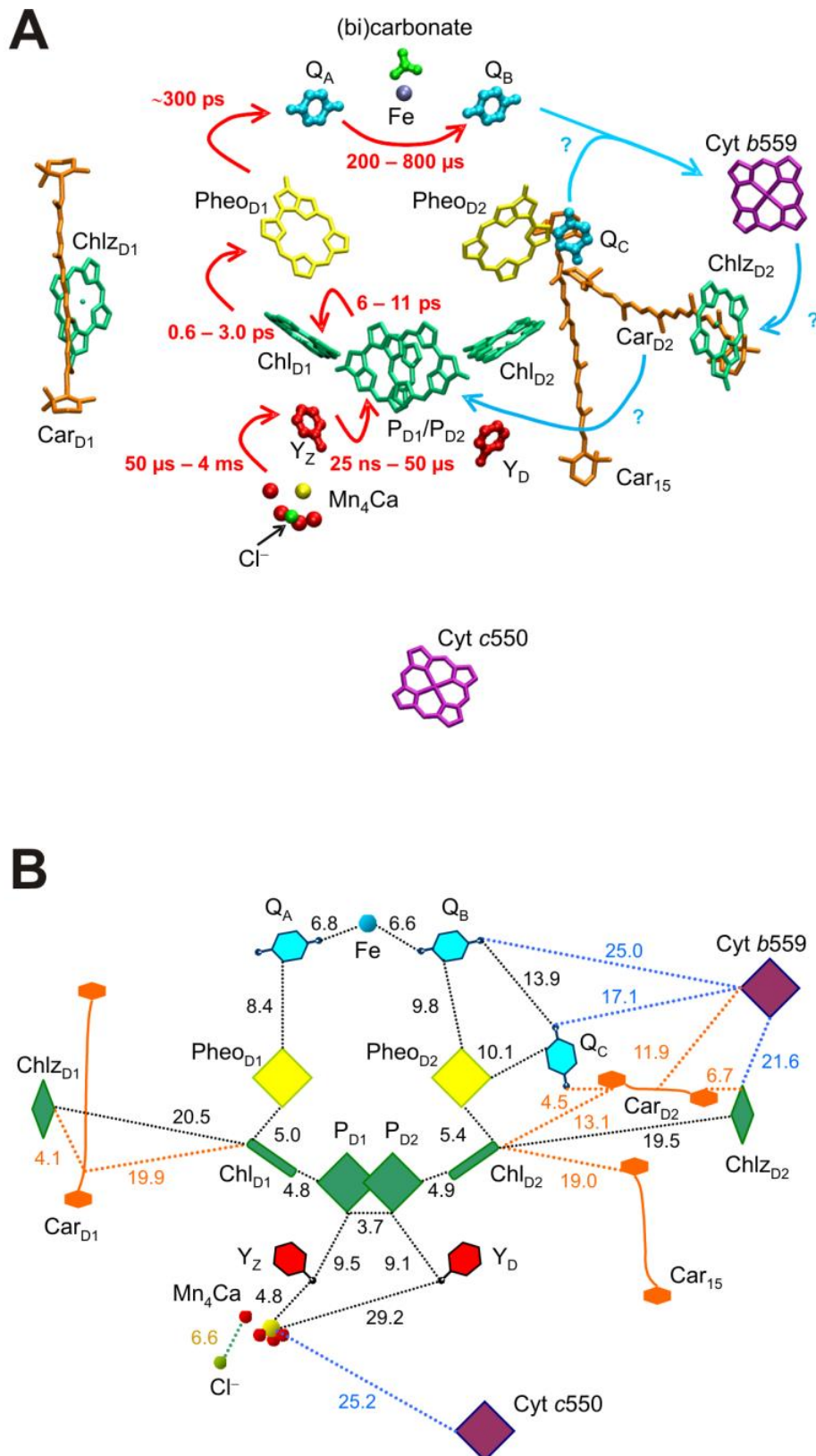


Figure 1.7 Cofactor arrangements in dPSIIcc.

Arrangement of cofactors (as labeled) in and around the RC of dPSIIcc, according to the crystal structure at 2.9 Å resolution (22). **(A)** Electron transfer steps are indicated by red arrows along with their transfer time. Blue arrows denote possible side-path electron transfer processes, probably including Y_D , $ChlZ_{D2}$, Car_{D2} , Car_{15} , heme group of cyt b559 and Q_C . **(B)** Schematic representation of the cofactor arrangement including edge-to-edge distances given in Å. Figure taken from (35).

The reaction pattern of the light-induced charge separation in PSII partially resembles that of pbRC (36) due to their structural similarity. Subunit D1 of PSII_{cc} corresponds to subunit L in pbRC, and subunit D2 to subunit M, which was already proposed by (31). With the first three-dimensional crystal structure of cyanobacterial dPSII_{cc} it was shown, that the redox active cofactors of both RCs (PSII_{cc} and pbRC) are coordinated in a similar manner (19). Despite high similarities, differences between both systems regarding the electron acceptor site were observed. In pbRC, several types of quinones are used as electron acceptors and also Q_A and Q_B are not chemically identical in many species, whereas the formation of the respective quinol (Q_BH₂) proceeds in an analog way to PQH₂ formation in PSII (37-39).

1.3.2 Subunits

As mentioned earlier, one monomer of dPSII_{cc} is composed of at least 17 membrane-intrinsic and three membrane-extrinsic protein subunits (Fig. 1.8).

The membrane-intrinsic subunits include the four large ones D1, D2, CP43, CP47 and the 13 small subunits PsbE, PsbF, PsbH, PsbI, PsbJ, PsbK, PsbL, PsbM, PsbT, PsbX, PsbY, PsbZ and Ycf12 (also called Psb30). The small subunits are also referred to as low molecular weight (LMW) or low molecular mass (LMM) subunits. The proteins D1 and D2 feature five transmembrane- α -helices (TMH) each, and are flanked by the two antenna proteins CP43 and CP47, each with six TMH and additional larger luminal loops. Out of the four larger subunits, D1 plays a special role. As this subunit harbors the highly reactive OEC and chlorophyll cofactors, it suffers from damage by reactive radicals formed in side reactions. To circumvent the functional loss of the protein complex, the D1 subunit is replaced constantly in a process called D1-turnover (turnover half-time constant: 30min) (40, 41). It is known, that under different growth conditions three isoforms of D1 are expressed in *T. elongatus* named PsbA1, PsbA2 and PsbA3 (42, 43). These D1 proteins show mainly variations in the amino acid sequence close to redox-active cofactors. This led to the suggestion, that the redox properties of the RC are adapted to the environmental conditions (44-47).

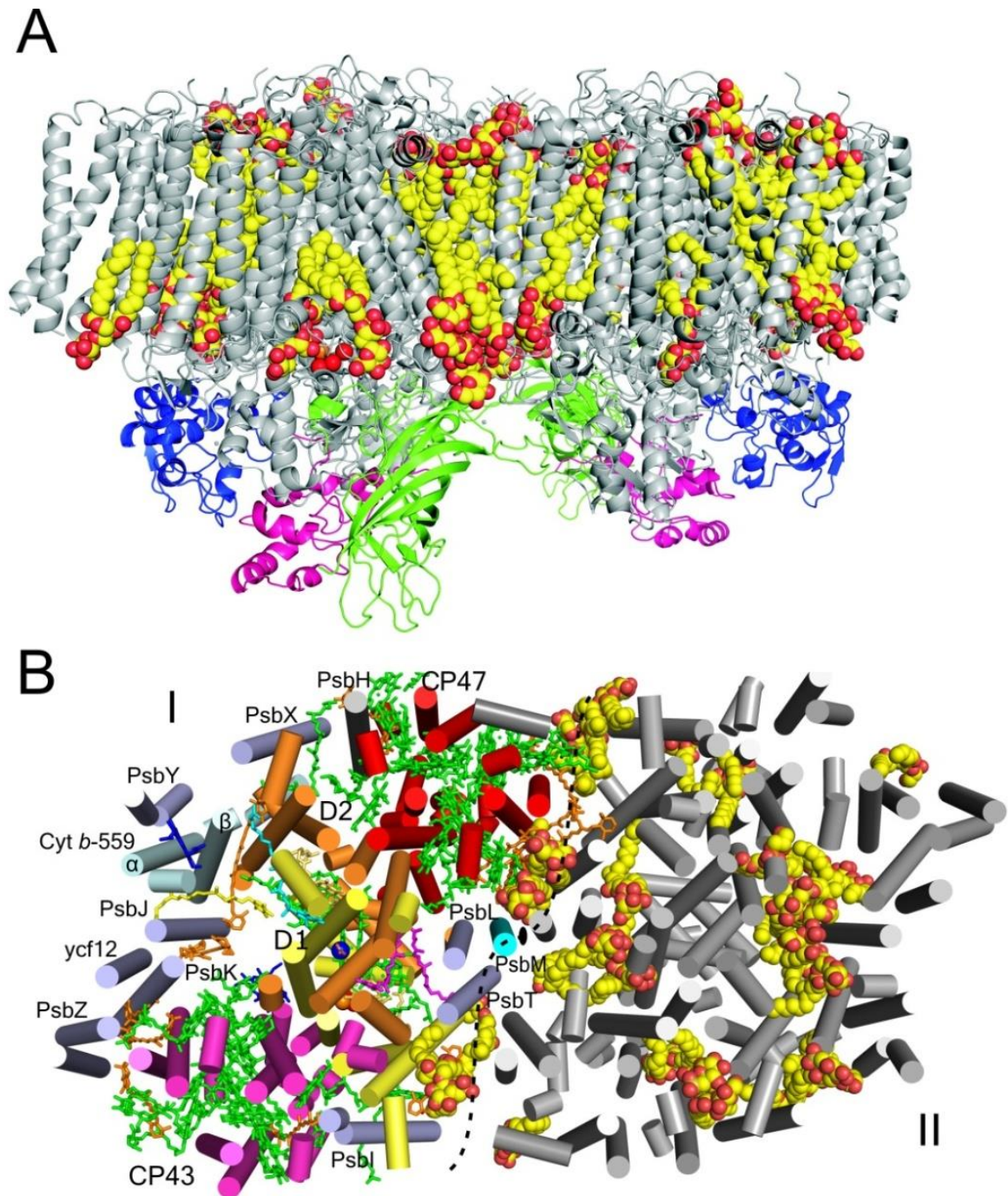


Figure 1.8 General architecture of dPSIIcc according to the structural model at 2.9 Å resolution.

(A) Side view of the PSIIcc homodimer along the membrane plane with the cytoplasm at top and the lumen at bottom. The 25 lipid and 7 detergent molecules per monomer are shown in space-filling mode (carbon, yellow; oxygen, red), the protein subunits in gray, and the three membrane-extrinsic subunits in green (PsbO), violet (PsbU) and blue (PsbV). (B) View of PSIIcc from the cytoplasmic side (membrane-extrinsic subunits omitted). The monomer-monomer interface is indicated by a black dashed line. Helical parts are shown as cylinders. In monomer I, subunits D1 (PsbA, yellow), D2 (PsbD, orange), CP43 (PsbC, magenta), CP47 (PsbB, red), cyt b559 (cyan, subunits PsbE, α , and PsbF, β), PsbM (blue) and the remaining eleven small subunits (light blue) are labeled. Cofactors are shown in stick mode: Chl (green), Car (orange), heme (blue). In monomer II, all protein subunits in gray, lipids and detergents are shown as spheres (carbon, yellow; oxygen, red). Figure taken from (48).

The role of the 13 LMW subunits and their contribution to the functional pattern of PSII is not yet understood (for review see (49)). All LMW subunits contain one TMH, besides subunit PsbZ, which shows two TMH. They are all post-translational modified at their N termini, except subunit PsbL (22). The subunits PsbE and PsbF build cyt *b559* in the RC core, each binding a heme group. The PsbY subunit is only present in the 2.9 Å crystal structure (22) and not in the high resolution crystal structure (25). Due to its poor electron density, PsbY was suggested to be only loosely attached to the complex. In the just recently obtained 2.1 Å resolution crystal structure of Sr-substituted dPSII_{cc} isolated from *T. vulcanus*, subunit PsbY could be assigned in one of the dPSII_{cc} monomers (50). Subunit PsbJ was found to play an important role for the electron transport from single reduced Q_A to the PQ pool (51). This is consistent with its contribution to a putative PQ/PQH₂ exchange channel suggested in (22). Subunit PsbH was found to influence the stability and assembly of PSII, the protection from photoinhibition, and the Q_A to Q_B electron transfer (52-55). At the monomer-monomer interface the subunits PsbM, PsbT and PsbL are located and form a three-helix bundle (Fig.1.8 (B)). Most likely, they play a role in the dimerization process of the protein complex (56, 57). The two symmetry-related subunits PsbM and PsbM' represent the main protein-protein contacts between the two monomers as they interact by virtue of a heptad motif of aliphatic side chains as in a leucine zipper (22). However, the deletion of PsbM as in a mutant of the mesophilic cyanobacterium *Synechocystis* sp. PCC 6803 was shown not to be sufficient to prevent dimer formation. Only the additional deletion of subunit PsbT prevented dimerization (57). The three extrinsic subunits found in the crystal structure of dPSII_{cc} from *T. elongatus* are located at the luminal side and are named PsbO, PsbU and PsbV. Subunit PsbO forms an extended β-barrel structure and harbors a calcium ion binding site (22, 58-60). PsbO was found to be important for maintaining a high oxygen evolving rate in cyanobacteria, as PsbO lacking mutants of green algae and higher plants are not capable of oxygen evolution (61, 62). PsbO is assumed to stabilize the functional conformation of the manganese cluster and is therefore as well named manganese-stabilizing protein (63). PsbO is also suggested to trigger the monomerization of photodamaged PSII by its detachment or structural reorganization (30). Subunit PsbV is a heme protein (cyt *c550*), but until now there is no evidence for its involvement in the enzymatic function of the complex. A PsbV deletion mutant possesses besides a decreased oxygen evolving capacity, a reduced thermostability arguing for a role in stabilizing the OEC (64, 65). In contrast, subunit PsbU binds no cofactors, but is also believed to stabilize the structure of the donor side. The absence of PsbU leads as well to reduced oxygen evolving rates and an increased dissociation of the phycobilisomes. Hence, it is proposed, that the binding of

subunit PsbU facilitates the binding of the phycobilisomes by mediating long range structural changes (66).

Besides PsbO, PsbU and PsbV, the subunits PsbQ and PsbP were also found in cyanobacteria, but their functions are still unclear. Possibly, more extrinsic subunits do exist and are lost during the purification procedure or might only bind in an intermediate state of PSII during assembly (e.g. Psb27, see Section 1.3.6). Green algae and plants feature no PsbV or PsbU, but bind PsbQ, PsbP and PsbR instead (for reviews on extrinsic proteins in PSII see (63, 67)).

1.3.3 Functions of PSIIcc cofactors

This section deals only with the Chla, β -carotene and lipid cofactors. Details about the location and function of metals bound to PSIIcc and the PQ cofactors are given in the following two sections.

Chlorophyll a

The crystal structures of PSIIcc revealed 35 Chla molecules (22, 25). The majority of the Chla molecules is assigned to the integral antenna proteins CP43 and CP47 which bind 13 and 16 Chla, respectively. Four of the remaining six Chla represent the RC chlorophylls P_{D1} , P_{D2} , Chl_{D1} and Chl_{D2} . The other two chlorophylls are Chl_{ZD1} and Chl_{ZD2} , which can be found in the periphery of the RC (Fig. 1.7). These pigments have several functions: In the intrinsic antenna proteins CP43 and CP47, they absorb light and transfer the excitation energy with minimum losses (close to 0%, (68)) to the RC. In the RC, they act as primary electron acceptors/donors in light-induced charge separation across the photosynthetic membrane. In addition, all Chla molecules contribute to the stabilization of the protein complex.

The excitation energy transfer (EET) from the antenna Chls to the RC takes about 40 - 50 ps. This process is rather slow due to the relatively large distance between antenna Chls and RC (49, 69, 70). Charge separation in the RC, however, represents a fast process (< 1ps) and therefore the EET to the RC is most likely the rate-limiting step in this process (71, 72). Since the first excited state of the RC is strongly localized on Chl_{D1} , it is assumed that charge separation starts from this pigment by transfer of an electron to $Pheo_{D1}$ (0.6 – 3.0 ps) (Fig. 1.7 (A)). The second radical pair, $P_{D1}^{++}Pheo_{D1}^{*-}$, is formed in 6 – 11 ps, where P_{D1}^{++} is a cation radical with an exceptionally strong oxidizing power (1.25 eV, (73)), which is needed for water oxidation. It is able to extract electrons via the redox active tyrosine Y_Z from the OEC (see Sec. 1.3.4 for further details). The charge separation is further stabilized by formation of $P_{D1}^{++}Q_A^{*-}$ in about 300 ps. For reviews on charge separation in PSII RC see (70, 73, 74).

β-carotenes

Per monomer, twelve β-carotene (Car) molecules could be assigned in the crystal structure of dPSIIcc from *T. elongatus* (22) and eleven in the high resolution crystal structure derived from *T. vulcanus* dPSIIcc (25). Eight Car molecules (with Car₁₅ only being present in the 2.9 Å resolution crystal structure) are associated with the internal antenna proteins (CP43 and CP47) and the other five are located at the monomer-monomer interface. The Car pigments fulfill several functions in photosynthetic proteins (75-80). Most of them serve for light harvesting, energy transfer to Chl_a, quenching of Chl triplet states, scavenging of singlet oxygen and structure stabilization. They might also play an important role in the assembly of functional dPSII. Most of the eight carotenes harbored by CP43 and CP47 are located close to Chl_a molecules (distance less than 4 Å), which is necessary for efficient quenching of Chl_a triplet states. Car_{D1} and Car_{D2} are associated with the RC subunits D1 and D2, respectively. Car_{D1} is oriented perpendicular to the membrane plane, whereas Car_{D2} is nearly parallel. The latter is believed to play a role in a possible side path electron transfer process together with the nearby cofactors Q_C, cyt *b559*, Chl_{ZD2} and Chl_{D2} (Fig. 1.7). Car_{D2} might also be involved in the quenching of singlet oxygen (78). Car_{D1} is located in close contact to Chl_{ZD1} (4.1 Å edge-to-edge distance of the π-systems) and it may act as a quencher of Chl_{ZD1} triplet states.

Integral lipids

A large number of lipid cofactors was found in the dPSIIcc crystal structures, whereas the amount and lipid composition per monomer varies slightly between the 2.9 Å and 1.9 Å resolution crystal structures (22, 25). The crystal structure at 2.9 Å resolution revealed 25 lipids and in the high resolution structure 23 lipids were assigned of which three are of unknown species. Additionally to the 23 lipids, 15 single alkyl chains with unknown identities were modelled and some of these may belong to lipids. The variations between the two structural models most likely arise from the different organisms and the different applied purification protocols regarding the detergent concentrations and compositions. The application of a detergent is necessary to isolate PSIIcc from the membrane and to keep it soluble in aqueous solutions. For a successful isolation of membrane proteins, the applied detergent concentration needs to be higher than its critical micelle concentration (CMC). To ensure a proper solubilisation, the concentration of the detergent has to be above the critical solubilization concentration (CSC). The CSC of a detergent is always higher than its CMC and depends linearly on the concentration of the membrane protein according to the equation $CSC = CMC + n \times C_{\text{protein}}$ (81-84). The mild and non-ionic detergent n-dodecyl-β-D-maltoside (βDM) is used for PSIIcc isolation. The CMC of βDM is around 0.16 mM. Note that the CMC of detergents vary depending on the present

conditions such as pH, ionic strength, temperature as well as the presence of proteins, lipids and other detergent molecules (85). PSIIcc from *T. elongatus* were isolated with 0.6% β DM (equal to 11.7 mM) (86), whereas PSIIcc from *T. vulcanus* were isolated with twice the concentration of β DM (1.2%) and additionally treated with an unknown amount of a second detergent named HTG (n-Heptyl- β -D-thiogluco-side, see structural model, PDB code: 3ARC) (25) (see also Section 1.3.7). As detergents are able to extract and substitute native lipids (due to the similarity of the sugar head groups), the employed detergent concentration in protein extraction and purification is a very critical point. The high amounts of detergents as used for the high resolution structure may have influenced and altered the lipid composition and could explain the high amount of unassigned lipid molecules. The lipid and detergent compositions revealed in both structural models are opposed in Table 1.2.

Table 1.2 Comparison of lipid and detergent content (per monomer) in dPSIIcc crystal structures from *T. elongatus* at 2.9 Å resolution (22) and *T. vulcanus* at 1.9 Å resolution (25).

Lipids	2.9 Å	1.9 Å
MGDG	11	6
DGDG	7	5
SQDG	5	4
PG	2	5
Unknown alkyl chains	-	15
Unknown diglycerides	-	3
Detergents		
β DM	7	6/5
HTG	-	9/10

Among the photosynthetic membrane proteins, PSII possesses the highest lipid content and reflects the lipid composition of the thylakoid membrane. The asymmetrical lipid distribution in the protein complex reflects the one in the membrane (14): The head groups of negatively charged SQDG and PG are located only at the cytoplasmic side, those of uncharged DGDG solely at the luminal side and those of MGDG on both sides. The fatty acid chains of the lipids are placed within the membrane spanning part of PSIIcc. Each lipid head group forms polar contacts (i.e., hydrogen bonds or salt bridges) with at least two different protein subunits. This finding indicates that integral lipids, inter alia,

support the stability of PSIIcc by connecting nearby protein subunits. Lipids may also play an important role in dimer formation and dissociation (e.g. during D1 turnover) as seven pairs of lipids (MGDG, DGDG, SQDG) and four pairs of β DM molecules were found at the monomer-monomer interface in the 2.9 Å crystal structure (22). In the 1.9 Å resolution crystal structure, the monomer-monomer interface is occupied by pairs of two SQDG, one MGDG, three PG, three β DM, three HTG and three unknown alkyl chains (25). Within each monomer, lipids are arranged in a belt-like structure surrounding subunits D1 and D2, thus partly separating the RC from other membrane-intrinsic subunits. A cluster of at least eight lipid molecules (containing all four types of lipids) forms an isolated bilayer at the Q_B site and may provide a hydrophobic interior needed for the exchange of PQ and PQH₂. This lipid cluster is slightly different in the 2.9 Å and 1.9 Å resolution crystal structures (Fig. 1.9). One MGDG molecule (MGDG18) in the 2.9 Å structure was assigned as a PG molecule in the high resolution structure. At the position of PG22 in the model at 2.9 Å resolution (Fig. 1.9 (A)), an unknown lipid molecule was assigned in the 1.9 Å structure (Fig. 1.9 (B)). Additional two unknown lipids were revealed in the high resolution structure, which are associated with this lipid cluster.

The number of PG molecules increased to five in the high resolution structure, which is in accordance with biochemical assays (87). In recent studies on mutant cells of cyanobacterium *Synechocystis* sp. PCC 6803, it was found that two PG molecules regulate the function of Q_B . These two PG molecules most likely correspond to the two PG sites assigned in the lipid cluster close to Q_B (see Fig. 1.9) and were identified as a high and a low affinity PG site (88). The high affinity site was found to be essential for the binding of CP43 and Q_B , and its loss leads to the release of Q_B . These findings are in accordance with earlier studies by Gombos *et al.*, which showed that the deprivation of PG leads to the inactivation of Q_B (89). In the structural model at 2.9 Å resolution (22), however, PG molecules are not in direct contact with Q_B and are located more than 8 Å away. The Q_B isoprenoid tail was found to interact considerably with the lipid MGDG18 (90) (see Section 1.3.5). Exactly this MGDG molecule is replaced with a PG molecule in the PSIIcc crystal structure at 1.9 Å resolution (25) (Fig. 1.9). Accordingly, in *Synechocystis* the position equally to MGDG18 might be occupied as well with a PG molecule and the PG molecule that was shown to influence the Q_B binding (88, 89) is the lipid located in the position of MGDG18. This would point toward a key role for the direct interaction of Q_B with a lipid molecule in controlling the photoreaction of PSII.

The other three – newly assigned - PG molecules, which are located around Q_A , are assumed to be essential for the assembly of D2 and the whole PSII protein (88). This is also in accordance with former studies by Sakurai *et al.* in which PG lipids were found to be important for the stabilization and formation of dPSIIcc (91).

Furthermore, a functional role of lipids as possible dioxygen diffusion pathways within PSIIcc was proposed due to noble gas derivatization experiments (92-94). Such pathways could serve to guide dioxygen from the lumen into the membrane, shielding the redox active cofactors of the RC from direct contact with dioxygen. Lipids are also involved in the formation of pathways (channel I and II) for fast PQ/PQH₂ exchange (48, 95) (see Section 1.3.5).

For the latest reviews on lipid-PSII interactions, see (15, 96).

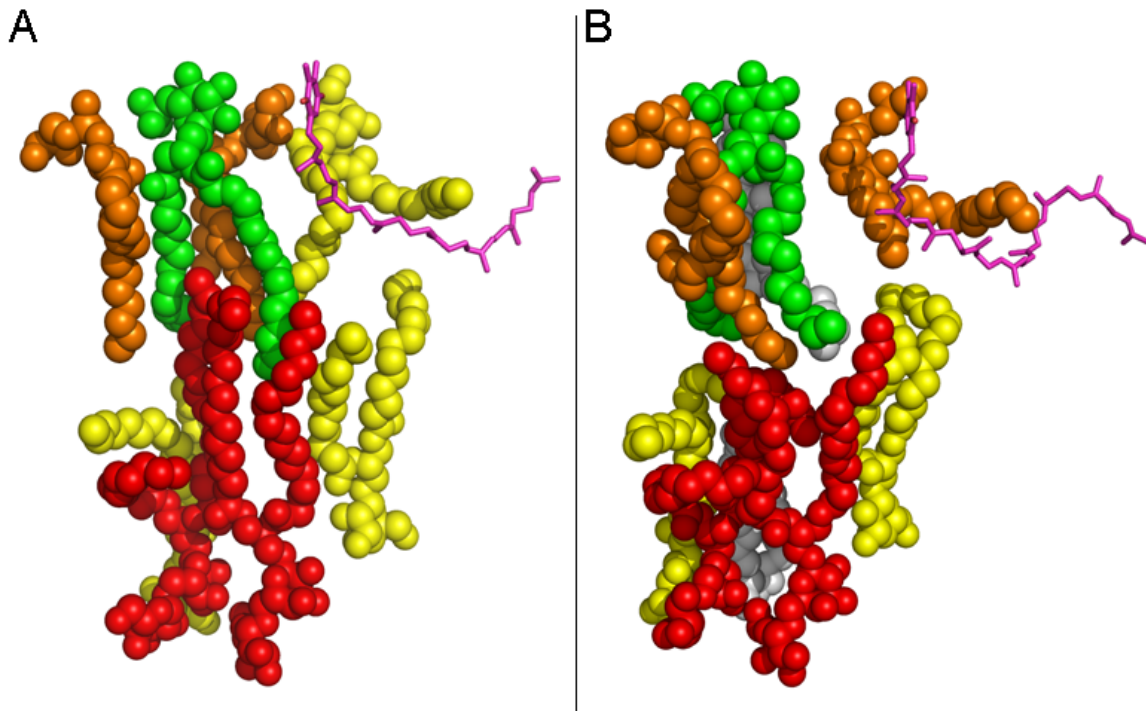


Figure 1.9 Cluster of lipids forming a bilayer structure within dPSIIcc.

View along the membrane plane of the lipid cluster of at least eight lipids forming a bilayer structure in the PQ/PQH₂ exchange cavity of dPSIIcc as revealed in (A) the 2.9 Å resolution crystal structure (22) and (B) the 1.9 Å resolution crystal structure (25). Q_B molecules are shown in pink and lipids are color-coded as follows: PG orange, SQDG green, MGDG yellow, DGDG red and unknown lipids in gray. (A) The charged PG3, PG22 and SQDG4 and neutral MGDG18 are on the cytoplasmic side (top) and the neutral MGDG19, DGDG5, DGDG6 and MGDG7 are on the luminal side (bottom). (B) MGDG18 was assigned as a PG molecule in the high resolution structure and the position of PG22 was assigned as an unknown lipid molecule. Additional two unknown lipids were revealed on the luminal side.

1.3.4 Donor side

The donor side of PSII, at the luminal side of the complex, is defined as the site of water cleavage and dioxygen formation. The catalytic center of this reaction is an inorganic

Mn₄Ca cluster (connected by μ -oxo bridges) that, together with its coordinating amino acids, is named OEC. The electron transfer between the OEC and the RC of PSII is mediated by Y_Z (Tyr161A). This tyrosine residue is located in between them. The, through light induced charge separation, formed cation radical P_{D1}⁺⁺ in the RC core is reduced by Y_Z, thereby forming a tyrosine radical. This oxidized Y_Z is in turn reduced by electrons extracted from the Mn₄Ca cluster (see Fig. 1.7).

Mechanism of water oxidation

Until now, the mechanism of natural water oxidation is still an unsolved mystery in bioinorganic chemistry. In 1969, Pierre Joliot and coworkers found that oxygen evolution in algae and chloroplasts, induced by single flashes, shows a maximum on every fourth flash, with the first maximum on the third flash (97). Based on these findings, Kok *et al.* proposed a stepwise cycle of water oxidation in a model named Kok-cycle (98) (Fig. 1.10). In this model, each photochemical reaction leads to the abstraction of one electron from the OEC, thereby shifting its oxidation state. After the accumulation of four oxidizing equivalents, oxygen is spontaneously evolved and the system returns to its initial state to run the next cycle. The OEC cycles through five oxidation states, termed S states (S₀, S₁, S₂, S₃ and S₄), whereas S₀ represents the most reduced state and S₄ the most oxidized one. Kok *et al.* also proposed that most OECs are in the S₁ state in dark-adapted PSII RCs, explaining the first maximum of oxygen production after the third flash. Consequently, the formation of molecular oxygen happens during the S₄ to S₀ transition in a spontaneous and light independent reaction (74, 99). Up to the S₃ state no stable O-O intermediate is formed, making the elucidation of the chemical steps leading to the oxidation of water a challenging problem (100). Additionally, there is presently no experimental evidence for the existence of the - formally needed - S₄ state in terms of a resolvable redox intermediate (see (101)).

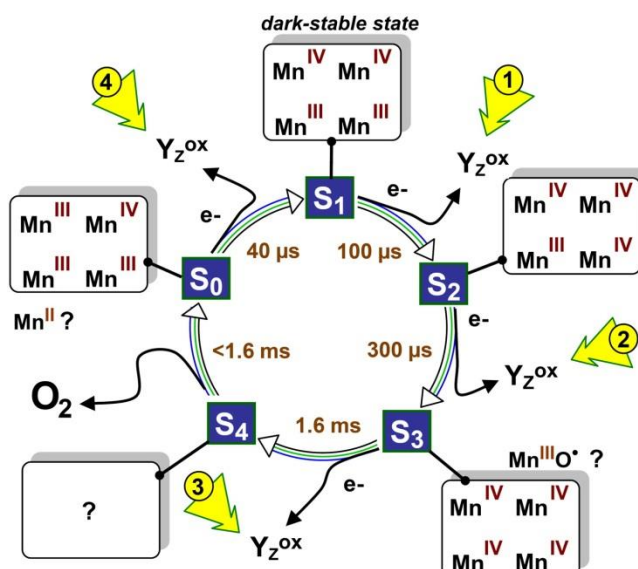


Figure 1.10 Kok-cycle of water oxidation.

The classical S state cycle of photosynthetic water oxidation based on the Kok-cycle is illustrated. Starting in the dark-stable S₁ state, absorption of a photon leads to the formation of Y_Z⁺⁺ within less than one μs. Reduction of Y_Z⁺⁺ via electron transfer from the manganese complex results in the transition to the next S state. Typical time constants of the electron transfer step and a plausible set of oxidation-state combinations of the four Mn ions in the different S states are indicated. Figure taken from (102).

The S state cycle as shown in Figure 1.10 was extended by the removal of four protons from the Mn₄Ca complex and their relocation toward the aqueous phase (103) (Fig. 1.11). The in Figure 1.11 shown proton-release pattern of 1:0:1:2 (S₀ to S₁, S₁ to S₂, S₂ to S₃, and S₃ to S₀) is proposed and supported by several studies including the most recent work using IR spectroscopy (104). However, the proposed alternation of electron and proton removal from the Mn₄Ca cluster is so far (partially) still hypothetical (105).

The mechanism of O-O bond formation is still unresolved, but it is assumed that the key step of O-O bond formation occurs at the S₄ oxidation state level. It probably consists of a sequence of events: deprotonation, O-O bond formation, evolution of molecular oxygen, rearrangement of the Mn₄Ca cluster, and binding of the substrate water molecule (106-109). A large number of detailed mechanisms for the oxidation of water were proposed in the past (99) and mentioning them all would go beyond the scope of this work. Also, several hypothetical mechanisms got ruled out by the structural model of the Mn₄Ca cluster obtained in the 1.9 Å resolution crystal structure (25, 102) (see next paragraph). The presently most developed DFT-based mechanistic model of water oxidation in PSII by Siegbahn (108, 110) is in good agreement with the 1.9 Å resolution dPSIIcc crystal structure data (25). It proposes that a hydroxide, bound to a Mn atom during the S₂ to S₃ state transition, is deprotonated and oxidized in the S₃ to S₄ state transition forming an oxygen radical. Thus, the O-O bond formation is supposed to take place in the S₄ state

between this oxygen radical and an oxygen that bridges two Mn atoms and the Ca atom in the Mn_4Ca cluster (108, 110). Another possibility for the O-O bond formation based on the 1.9 Å resolution crystal structure of dPSIIcc (25) was discussed by Grundmeier and Dau (102): the nucleophilic attack of the W3 water molecule, coordinated to the calcium ion, on a second water group (W2) coordinated to Mn4 (see next paragraph and Fig. 1.12). However, to really understand the water-oxidation mechanism it is very important to capture the S_4 state intermediates by following the $S_3 \rightarrow (S_4) \rightarrow S_0$ transition in a time resolved manner. A first step toward that direction was reported very recently with the innovative simultaneous XRD/XES (X-ray emission spectroscopy) study on dPSIIcc microcrystals at room temperature using intense femtosecond X-ray pulses (111). XRD data were presented from the dark state (S_1) and the first illuminated state (S_2) of dPSIIcc (see Chapter 5).

A various number of proposed mechanisms for the oxidation of water by the OEC are reviewed in (102). For several working hypotheses of possible water splitting mechanisms based on the structural data from the 1.9 Å resolution crystal structure see (112).

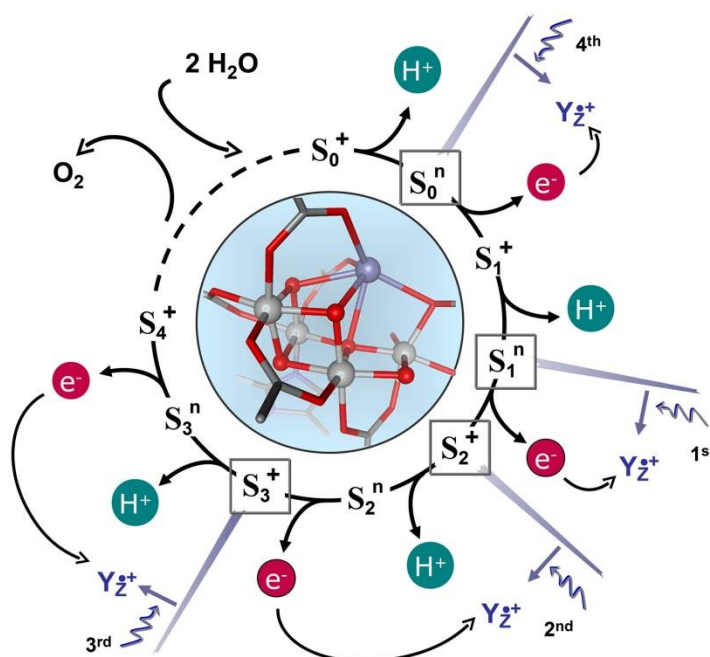


Figure 1.11 Extended S state cycle.

The classical S state cycle model is extended by including not only four oxidation but also four deprotonation steps. Four of the nine states of the Mn complex are stable for tens of seconds or fully dark-stable (S_1^n , S_2^n , S_3^n , and S_0^n). They correspond to the states S_1 , S_2 , S_3 , and S_0 of Kok's reaction cycle and are marked by a rectangular frame. Electrons and protons are removed alternately from the Mn complex by electron transfer to Y_z^{++} and proton relocation towards the aqueous phase, respectively. Figure taken from (102).

Structure of the Mn_4Ca cluster

The elucidation of the structural composition of the Mn_4Ca cluster is essential for the understanding of the water splitting mechanism. Various methods have been used for investigating the structure of the OEC, among others EPR and electron nuclear double-resonance (ENDOR) spectroscopy, Fourier-transform infrared (FTIR) spectroscopy, X-ray absorption spectroscopy (XAS) and XRD on PSIIcc crystals (see Introduction of Sec. 1.3). With the XRD crystal structure of dPSIIcc from *T. vulcanus* at an atomic resolution of 1.9 Å, the first reliable structure of the OEC became available including the detection of water molecules (25). The five metal atoms of the Mn_4Ca cluster turned out to be linked by five oxo bridges, forming a Mn_4CaO_5 cluster (Fig. 1.12).

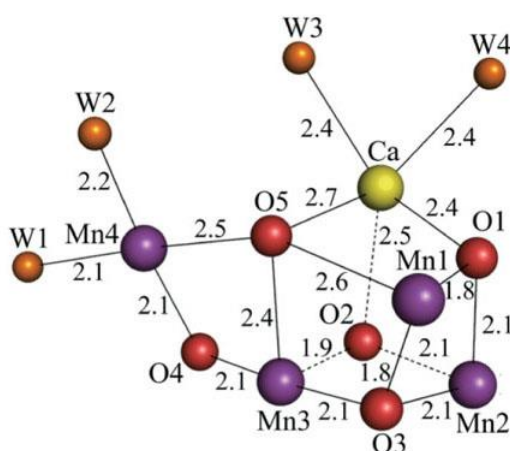


Figure 1.12 Structure of the Mn_4CaO_5 cluster.

The structure of the Mn_4CaO_5 cluster as revealed in the 1.9 Å resolution dPSIIcc crystal structure (25) is shown. Manganese ions (Mn1-Mn4) are depicted in purple, calcium ion (Ca) in yellow, oxygen atoms (O1-O5) in red and water molecules (W1-W4) in orange. Distances are given in Å. Figure taken from (25).

In the structural model of Umena *et al.* (25), three manganese, the calcium and four oxygen atoms form a cubane-like structure, in which each corner is occupied by one of these atoms. The cubane-like structure is not an ideal and symmetric one, as the bond lengths between the atoms are not equal. The cluster arrangement and bond lengths are depicted in Figure 1.12. The fourth manganese ion (Mn4) is located outside the cubane and is linked to two manganese ions within the cubane (Mn1, Mn3) by one oxygen atom of the cubane (O5) and the fifth oxygen (O4) via a di- μ -oxo bridge. The overall structure of the Mn_4CaO_5 cluster resembles a distorted chair, with the asymmetric cubane forming the seat base and the aside located Mn4 and O4 serving as the back of the chair. Every two adjacent manganese ions are linked by di- μ -oxo bridges: Mn1 and Mn2 are linked via O1 and O3, Mn2 and Mn3 are linked via O2 and O3, and Mn3 and Mn4 are linked via O4 and

O5. The calcium ion is linked to all four manganese ions: to Mn1 via the di- μ -oxo bridge formed by O1 and O5, to Mn2 via O1 and O2, to Mn3 via O2 and O5, and to Mn4 via the mono- μ -oxo bridge formed by O5. Additionally, four water molecules could be assigned in the Mn_4CaO_5 cluster. Two water molecules (W1 and W2) are coordinated to Mn4 outside the cubane, whereas the other two water molecules (W3 and W4) are coordinated to the calcium ion. Some of these water molecules were proposed to function as substrates for water oxidation (113). The amino acids coordinated to the cluster were assigned as carboxylate and imidazole groups (Fig. 1.13). Only one monodentate mode of carboxylate is observed (Glu189A to Mn1) and other carboxylate groups serve as bidentate modes. Together with the oxo bridges and waters, each of the manganese atoms possesses six ligands and the calcium has seven ligands (25, 60) (see Table 1.3). The high resolution crystal structure of dPSIIcc from *T. vulcanus* (25) largely confirmed the ligand assignment of Loll *et al.* (21), with two exceptions: In the recent structural model Asp170A is bridging between Mn4 and the calcium ion, whereas Glu189A is not in a bridging position between metal ions but serves as monodentate ligand to Mn1. A comparison of these two XRD models is given in (102).

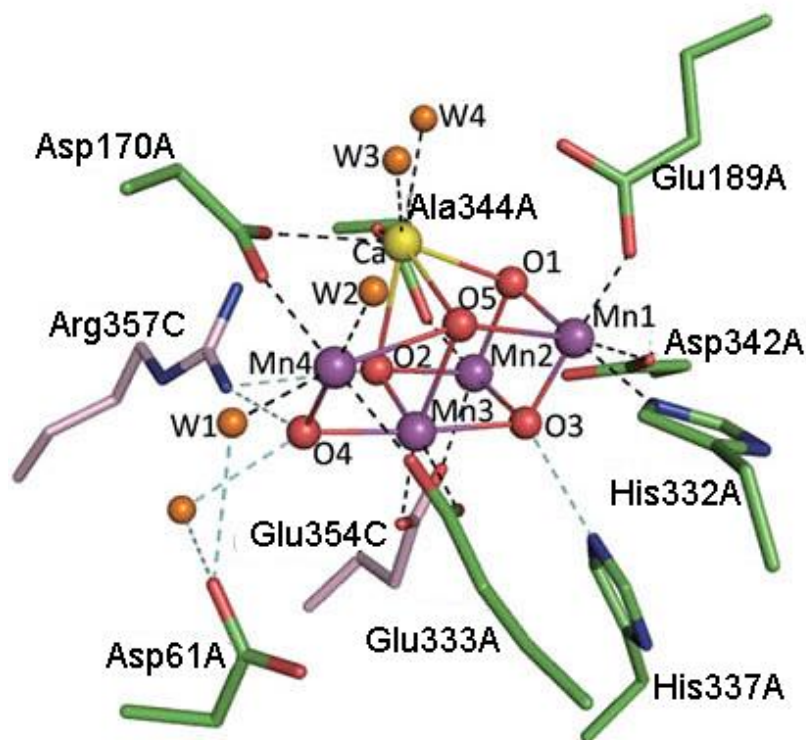


Figure 1.13 Ligands of the Mn_4CaO_5 cluster.

The structure of the Mn_4CaO_5 cluster and its ligand environment is shown according to the 1.9 Å resolution dPSIIcc crystal structure (25). Manganese ions (Mn1-Mn4) are depicted in purple, calcium ion (Ca) in yellow, oxygen (O1-O5) atoms in red, water molecules (W1-W4) in orange, subunit D1 in green and subunit CP43 in pink. Figure taken from (25).

Table 1.3 Ligands of the manganese and calcium ions of the Mn_4CaO_5 cluster.

Ligands of the manganese and calcium ions of the Mn_4CaO_5 cluster are listed as revealed in the dPSIIcc crystal structure at 1.9 Å resolution (25).

Mn1	Mn2	Mn3	Mn4	Ca
O1	O1	O2	O4	O1
O3	O2	O3	O5	O2
O5	O3	O4	W1	O5
Glu189A	Asp342A	O5	W2	W3
His332A	Ala344A	Glu333A	Asp170A	W4
Asp342A	Glu354C	Glu354C	Glu333A	Asp170A
				Ala344A

Radiation Damage

The XRD structure of dPSIIcc at a resolution of 1.9 Å led to a great progress in unravel the microenvironment of the manganese cluster (25). However, a critical problem of using the technique of XRD for PSIIcc studies is the inherent sensitivity of the redox-active high-valent Mn_4CaO_5 cluster to X-ray radiation.

X-rays belong to the class of ionizing radiation that is able to generate free radicals when interacting with a macromolecular sample. In biological samples, free radicals can be generated directly, as a result of the solvent atoms absorbing the ionizing radiation, or indirectly, through reaction with products arising from the radiolysis of water (e.g. hydrated electrons). In protein crystals, free radicals and hydrated electrons diffuse through the crystal, causing damage by further chemical reactions with amino acid residues or protein cofactors (e.g. metal atoms). The radiation damage depends predominantly on the amount of absorbed energy and photons, but varies likewise with the nature of the solvent and factors such as temperature (at low temperatures diffusion processes are minimized) (114, 115).

It was found by XAS studies that Mn(III) and Mn(IV), as present in the intact OEC, are rapidly reduced to Mn(II) when exposed to X-ray doses as used in protein crystallography (116, 117). Hence, in all current XRD structures of PSIIcc the Mn_4CaO_5 cluster is reduced at levels ranging from about 80% (for structures described in (19-22, 24)) to 25% (for the high resolution structure (25)) despite the low measuring temperature of 100 - 150 K. This X-ray photoreduction not only reduces the Mn atoms, but modifies the arrangement of the manganese ions in the OEC, suggesting the disruption of μ -oxo bridges and alternations in the coordination pattern of the ligated amino acids (116). Several research groups have addressed the issue of radiation damage by applying a combination of XRD and non-destructive XAS (explained in Sec. 2.2.11.1). A number of models for the structure of the

Mn_4CaO_5 cluster have been proposed so far and are reviewed and evaluated in (102). In the present work, also the combination of XRD and XAS was used to investigate the structural and electronic changes of the Mn_4CaO_5 cluster during the S state transitions (see Sec. 4.2). The effect of radiation damage to the Mn_4CaO_5 cluster even with the lower Mn(II) content of 25% is evaluated in more detail (see Sec. 4.3). Very recently, however, a new promising method for protein crystallography was established at the X-ray Free-Electron Laser (XFEL) of the Linac Coherent Light Source (LCLS), in which ultra-short X-ray pulses of high intensity were used and made it possible to collect diffraction data at room temperature before the onset of radiation damage (118-122). This “probe before destroy” approach was shown to be applicable even for the highly sensitive Mn_4CaO_5 cluster in PSII using dPSIIcc microcrystals (123). This method is at an early stage, but has the potential to lead to a great progress in unraveling the native structure of the catalytic Mn_4CaO_5 cluster (see also Chapter 5).

Channels

To ensure the water-oxidation cycle of the OEC, the fast and efficient delivery of educts (water molecules) and removal of products (protons, electrons and potentially harmful oxygen) is essential.

Complex networks of putative water, oxygen and proton channels leading from the OEC to the luminal side have been proposed based on computational studies using the dPSIIcc crystal structures at 3.5 Å (20, 124), 3.0 Å (21, 125) and 2.9 Å (22, 92) resolution (Fig. 1.14 (A)). In these studies applied cavity search algorithm identifies possible trajectories for a sphere of specified radius (126). In the PSII protein, these trajectories start at the OEC and lead to the bulk solvent. As the cavity search algorithm was operated on static pictures of dPSIIcc, dynamic motions within the protein are not considered. Therefore, the by this method obtained results represent initial identifications of possible channels within dPSIIcc. In the latest study of that field, by Gabdulkhakov *et al.*, nine pathways emerging from the OEC and leading to the lumen were calculated (92) (Fig. 1.14 (B)). Due to the channel width or hydrophobicity (depending on the amino acid residue composition), the identified wider channels were putatively assigned to water (A1 and A2) and oxygen (B1 and B2), and the narrower channels to protons (C-G). Note, at that stage water molecules were not visible in the existing dPSIIcc XRD crystal structures, and protons cannot be detected in XRD experiments as the X-rays are diffracted by the electrons. For simplification, the channels revealed by the cavity search algorithm method are called “static” channels in the following.

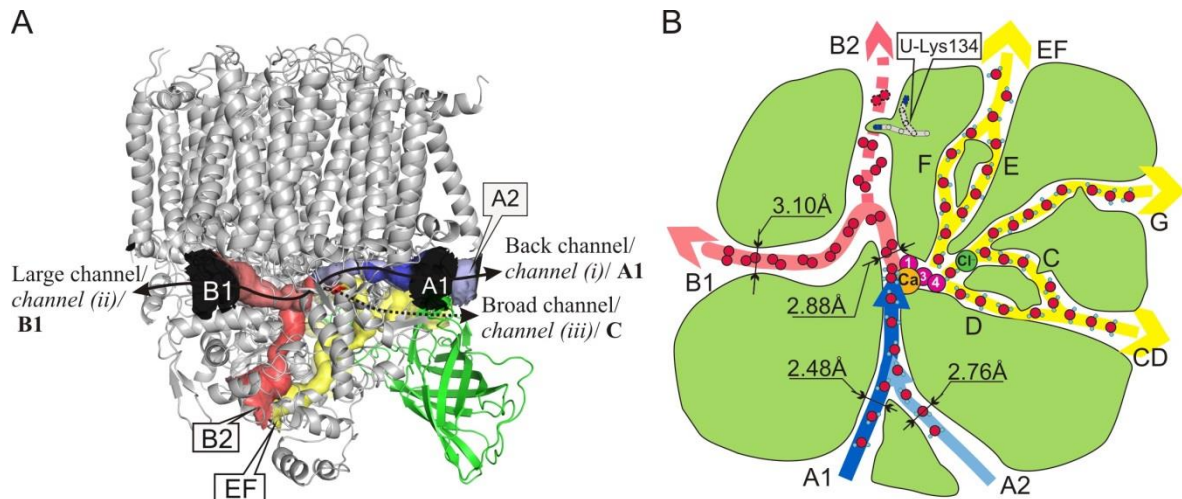


Figure 1.14 Possible trajectories of substrate and product channels leading to and away from the OEC as obtained by the cavity search algorithm method.

(A) Overlay of relative orientations of channels in *dPSIIcc* based on XRD crystal structures. View is along the membrane plane of one monomer (cytoplasm, top; lumen, bottom). Channels A1, B1 and C (**bold**) by Gabdulkhakov *et al.* (92) are compared with those proposed by Ho and Styring (125) and Murray and Barber (*italic*) (124). **(B)** Schematic illustration of the nine possible substrate and product channels (A1, A2, B1, B2, C-G) in *dPSIIcc* as calculated in (92). View is from the stromal side onto the membrane plane. Minimum diameters of the water/oxygen channels are indicated by black arrows. Thick colored arrows illustrate the suggested pathways for water supply (blue), oxygen (red) and proton (yellow) removal. The exit of channel B2 is blocked by the amino acid residue Lys134U, but opens after a conformational change of this residue. Figure adapted from (48).

However, channels are dynamic at physiological temperatures and in order to fully understand their function within the PSII protein, a dynamic point of view is essential. This is not possible by only considering one particular static conformation of *dPSIIcc*.

Vassiliev *et al.* performed molecular dynamics (MD) simulations of PSIIcc in the presence of distinct solvent water molecules (127, 128). These studies provide a dynamic and, therefore, a physically more realistic picture of possible channels within PSII. The water molecules moved between the OEC and the bulk water within 10 ns. A large network of branching pathways of water diffusion in PSII leading to the OEC and connecting to several openings on the lumenal side was revealed. Temporarily changes in the connections between the channels and entrance points could also be observed, mediating the flow of water near the OEC as well as the exchange of water inside and outside of the protein. The most recent MD study by Vassiliev *et al.* (128) used the new structural information about the OEC gained from the 1.9 Å resolution crystal structure (25). It is focused on the identification and energetic characterization of water channels leading to the Mn_4CaO_5 cluster. The work showed, that water molecules injected near Ca^{2+} or Mn^{4+} (where binding sites for substrate water molecules have been suggested (113); see Fig.

1.12) permeate through eight channels which are partially identical or overlap with the previously identified “static” channels (Fig. 1.15). Table 1.4 gives an overview of the channel nomenclature in the various studies.

Table 1.4 Overview the channel nomenclature.

Study	Channel names					
Vassiliev <i>et al.</i> (128)	1	2	3	4A	4B	5
Gabdulkhakov <i>et al.</i> (92)	D, (C)	E, F	G	B1	B2	A1, A2
Ho and Styring (125)	-	“narrow”	“broad” (partial overlap)	“large channel system”	“large channel system”	“back”
Murray and Barber (124)	iii	-	-	ii	ii	i

Vassiliev *et al.* (128) studied the energetics of water permeation through all “static” channels and could confirm water movement through three of the water channels found in earlier studies: channels B1 and B2, channels E and F and channel G (see Table 1.4). Additionally, water movement through a channel (named channel 1 in (128)) previously suggested as a proton exit pathway (channel (iii), see Table 1.4) was observed. In contrast, the previously identified channels A1 and A2 (see Table 1.4) were found to be impermeable for water molecules, but might serve as oxygen channel. Furthermore, a new channel, named channel X, for water movement was identified (128) (Fig. 1.15). All identified channels possess activation energies of at least 9 - 10 kcal/mol and, thus, regulatory mechanisms might control the flow of water molecules to the catalytic site. The permeability of channels in PSII for oxygen, protons and other compounds like calcium, manganese and chloride is still an open question.

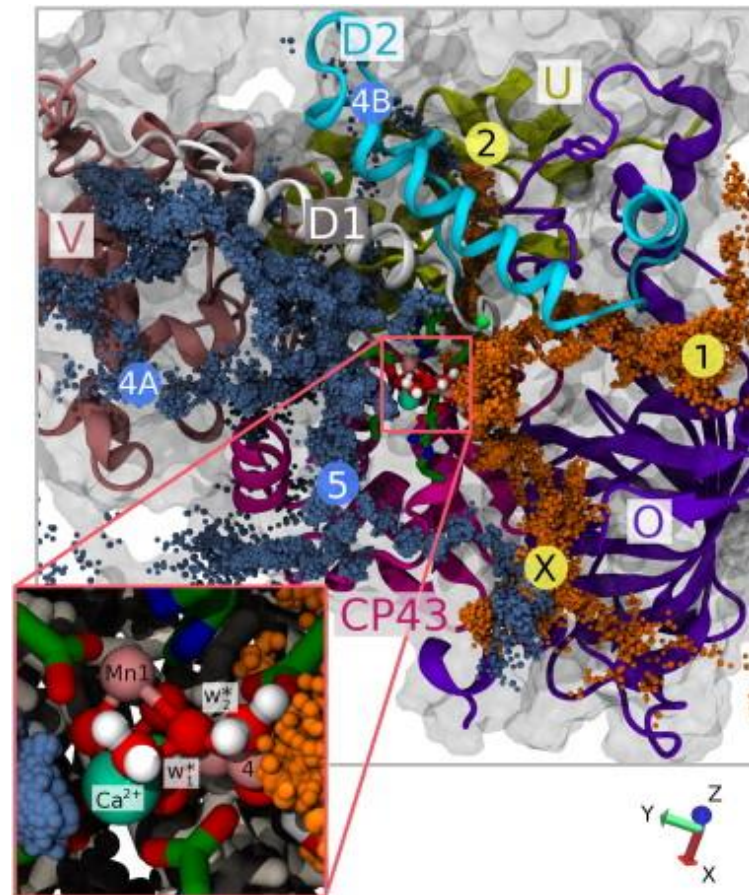


Figure 1.15 Possible trajectories of water molecules leading to and away from the Mn_4CaO_5 cluster.

Pathways of injected water molecules within dPSIIcc obtained by MD simulations (128) are shown. Water molecules injected in dPSIIcc at one side of the OEC (near water binding site w_1^*) are depicted as blue spheres and water molecules injected at another side of the OEC (near water binding site w_2^*) are depicted as orange spheres. View is from the stromal side approximately along the normal to the membrane (Z-axis), with the membrane in the XY plane. For clarity, the protein above the OEC is omitted. The zoomed panel shows the locations of the binding sites w_1^* and w_2^* as well as the OEC atoms, Mn1, Mn4, and Ca^{2+} . Segments of PSIIcc polypeptides O, U, V, D1, D2 and CP43 are shown in colored cartoon mode and are labeled. The locations of water channels 1, 2, 4A, 4B, 5 and X are shown. Figure taken from (128).

Chloride ions

It is well known that chloride binding is essential for water oxidation as the depletion of chloride suppresses the evolution of oxygen (129-131). The crystal structure of dPSIIcc at 1.9 Å resolution revealed in total three chloride binding sites named Cl-1, Cl-2 and Cl-3. Whereas Cl-3 is located between subunits PsbU and PsbV, the other two chlorides are found in the second coordination sphere of the Mn_4CaO_5 cluster (25). The finding of the latter ones confirms former crystallographic studies on bromide-substituted PSIIcc, in which bromide ions are located at the same positions (132, 133). Based on earlier

experiments, the existence of more than one chloride binding site was already proposed, whereas each position possesses different binding affinities. The activity of PSII was supposed to be controlled by chloride binding to the high affinity site and to be further modulated by the occupancy of a low affinity site (134, 135). Still, it has to be identified which of the two chloride binding sites found in the crystal structure at 1.9 Å resolution (25) represents the high affinity site and which one the low affinity site. The crystal structure of dPSIIcc at a resolution of 2.9 Å revealed only one chloride binding site, which is identical to the position Cl-1 in the high resolution structure (22). This finding points to position Cl-1 taking on the role of the high affinity site. The binding site Cl-1 is located in a 6.7 Å distance to Mn4 and Cl-2 in a 7.4 Å distance to Mn2 (Fig. 1.16).

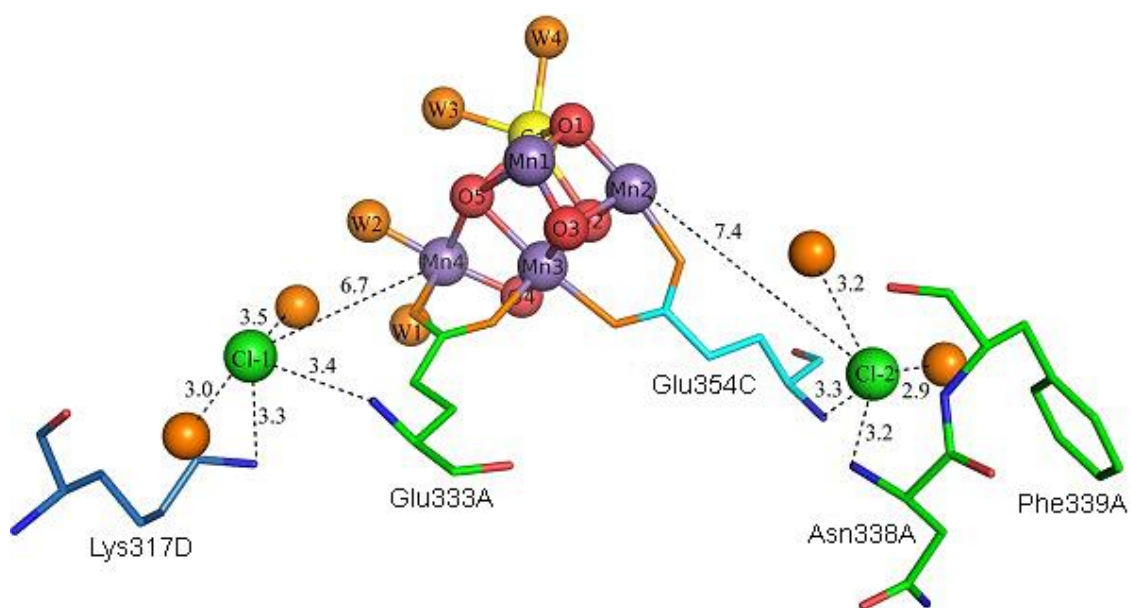


Figure 1.16 Two chloride binding sites in the vicinity of the Mn_4CaO_5 cluster.

Structural arrangement of the two chloride binding sites (Cl-1, Cl-2) in the vicinity of the Mn_4CaO_5 cluster is shown according to the dPSIIcc structural model at 1.9 Å resolution (25). Color code: chloride ions in green, manganese ions in purple, calcium ion in yellow, oxygen atoms in red, water molecules in orange, subunit D1 in green, CP43 in light blue and D2 in blue. Hydrogen bond distances are given in Å. Figure taken from (60).

Both chloride ions are surrounded by four ligands, respectively. Besides two water molecules, the chloride at the Cl-1 site interacts with the amino group of Lys317D and the backbone nitrogen of Glu333A. The chloride at position Cl-2 interacts, in addition to two water molecules, with the backbone nitrogens of Asn338A and Glu354C (25, 60). Among these, the only charged amino acid residue is Lys317D in a distance of 3.3 Å to Cl-1. All other groups are either hydrophilic or water molecules with rather long distances to the two chloride binding sites, suggesting that the chloride ions are predominately bound by hydrogen-bonds. However, the Lys/Glu combination is likely to provide a stronger binding

strength to the chloride in position Cl-1 than the Asn/Glu combination to the chloride in position Cl-2. This is another indication for the Cl-1 site to function as the high affinity site, and the Cl-2 site could correspond to the low affinity site.

Chloride is proposed to be involved in proton transfer from the OEC to the lumen (136). This is supported by the location of the chloride ions in the entrance of possible proton pathways (see Chapter 3) (22, 25, 92, 124, 125, 127). Moreover, electrostatic calculations combined with molecular dynamic studies showed that the depletion of chloride induces the formation of a salt-bridge between the residues Lys317D and Asp61A (137). This salt bridge would modify the pK_a of Asp61A and could lead to the suppression of proton transfer to the lumen (as proposed elsewhere (138)). The Cl-1 site would, thus, set the conformation appropriate for the efficient transfer of protons. A recent study on iodide-substituted dPSII from *T. elongatus* (139) showed that the chloride/iodide exchange considerably slows down the $S_3\text{Tyr}_2^{\cdot} \rightarrow S_0$ reactions. A model was proposed in which the calcium binding site and the chloride binding site interact, most likely mediated by the hydrogen-bond and/or water molecules network connecting the two distant sites.

1.3.5 Acceptor side

The acceptor side of PSII, at the cytoplasmic side of the complex, defines the site of electron uptake as a consequence of light-induced charge separation (for review see (35)). The primary electron acceptor is the PQ molecule Q_A , which acts as fixed one-electron transmitter. Q_A ultimately delivers electrons to the substrate PQ molecule Q_B . Q_B functions as mobile two-electron carrier and diffuses, in the form of PQH_2 , into the membrane toward cyt *b₆f*. PQH_2 is replaced by fresh PQ from the so called PQ pool in the thylakoid membrane (140) (see Fig. 1.4). Although both, Q_A and Q_B , consist of a PQ-9 molecule (a 2,3-dimethyl-1,4-benzoquinone head group with a hydrophobic tail of nine isoprenoid units) and their head groups are aligned in a pseudo C_2 symmetry in the RC (see Section 1.3.1), their physiological roles are completely different as well as their physicochemical properties. E.g. the redox potential of Q_B is by about 80 mV higher than that of Q_A (141, 142) making the electron flow from Q_A to Q_B possible. Also, in contrast to Q_A , which is strongly bound to the protein, Q_B can leave its binding site as a substrate and can even be replaced by other artificial quinone molecules or various herbicides (143, 144) (see Chapter 3).

The role of the third identified PQ molecule, Q_C , is not yet understood. It has been proposed to have functions as (i) a waiting PQ to enter the Q_B site for a fast PQ exchange after double reduction (22, 35, 145), (ii) an electron donor to the low potential form of cyt *b₅₅₉* in a secondary electron transfer pathway (146), and (iii) a regulator of the reactivity of cyt *b₅₅₉* by modulating its redox potential (147, 148).

The different functions and properties of Q_A , Q_B , and Q_C most likely derive from differences within their molecular interactions at the individual binding sites.

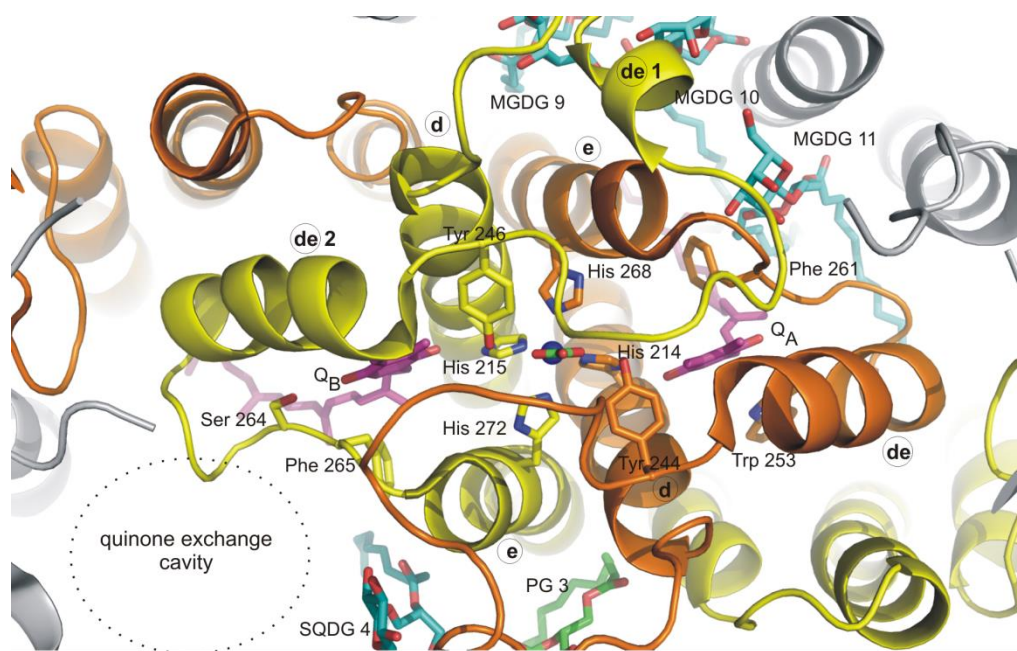


Figure 1.17 Structure of the acceptor side of dPSIIcc.

The binding sites of the two plastoquinone molecules Q_A and Q_B and of the non-heme iron are shown in a view direction from the cytoplasm onto the membrane plane, according to the 2.9 Å resolution crystal structure of dPSIIcc (22). Color code: Protein subunit D1 in yellow, D2 in orange, and segments of other subunits in gray. The non-heme iron is shown as blue sphere (located in the center of the figure), plastoquinone molecules in magenta, lipids in light blue (SQDG), light green (PG) and cyan (MGDG) and the bicarbonate in green. Helical segments of D1/D2 are indicated by small letters in circles. The dotted ellipse indicates the location of the large cavity proposed to function as quinone diffusion pathway (see (21) and (22)). Figure taken from (149).

Binding sites of PQ cofactors

The binding sites of the Q_A and Q_B cofactors are harbored in subunits D2 and D1, respectively, with a non-heme iron situated in between (Fig. 1.17). Their binding pockets are similar in the 2.9 and 1.9 Å resolution dPSIIcc crystal structures and were found to be essentially devoid of water molecules (22, 25).

Q_A is located between Phe_{D1} and the non-heme iron. The position of the Q_A head group is fixed by two hydrogen bonds and a kind of π -stacking interaction with residue Trp253D (Fig. 1.18 (A)). Hydrogen bonds are formed between the keto-oxygens of the quinone head group and the δ -nitrogen of residue His214D (which is ligand to the non-heme iron) and to a backbone amide group of residue Phe261D (dotted lines in Fig. 1.18 (A)). The π -stacking of Q_A with Trp253D is in an offset-stacked geometry (150) with a slight tilt of the π -planes against each other. The surface helix **de**(1) of D2 and the loop region connecting

de(1) and TMH **e** form a shield toward the cytoplasmic side, therefore protecting the redox active Q_A head group from wasteful electron flow to exterior redox components (Fig. 1.17). The non-heme iron is located at a distance of 7.8 Å from the head group of Q_A , bridged by residue His214D (22). The non-heme iron is a hexa-coordinated Fe(II) with a distorted octahedral geometry. Four vertices of the octahedron are occupied by the ϵ -nitrogens of the following histidyl ligands: His214D, His268D, His215A and His272A (illustrated in Fig. 3.9 (A) in Chapter 3). One of the histidines on each side is engaged in hydrogen bonding with the respective PQ. The remaining two ligand positions are taken over by the oxygen atoms of bicarbonate. The Q_B binding pocket in subunit D1 is formed by the C-terminal part of TMH **d**, the cytosolic surface helix **de**, the following loop region and the N-terminal part of TMH **e** (Fig. 1.17). The head group of Q_B is placed between the residues Phe255A and Leu271A. The keto-oxygens of the Q_B head group form hydrogen bonds between the δ -nitrogen of His215A, the amide hydrogen of Phe265A and to the γ -oxygen of Ser264A (Fig. 1.18 (B)). The distance of the Q_B head group to the non-heme iron is 7.5 Å, bridged by His215A (22).

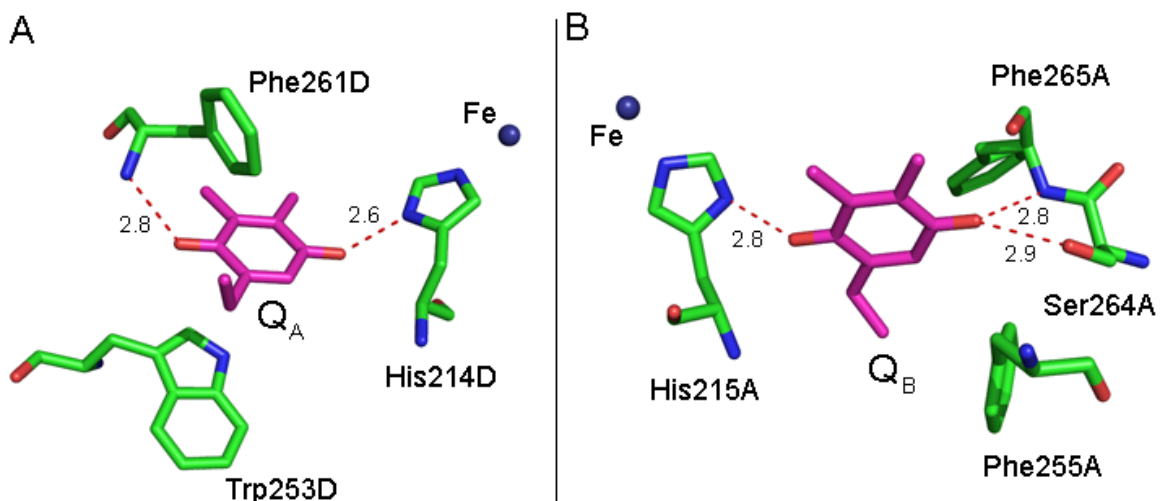


Figure 1.18 Positions of the head groups of the Q_A and Q_B cofactors.

Positions of (A) Q_A and (B) Q_B head groups and the respective protein environments are shown according to the structural model of *dPSIIcc* at 2.9 Å resolution (22). The red dotted lines indicate possible hydrogen bonds with distances given in Å.

The third PQ molecule Q_C could be modelled exclusively in the crystal structure of *dPSIIcc* at 2.9 Å resolution (22). The head group of Q_C is located at a distance of ~ 14 Å from the head group of Q_B (see Fig. 1.7 (B)). In the crystal structure of *mPSIIcc* at 3.6 Å resolution (23), an electron density was found at exactly the same position but a precise assignment to a quinone head group was not possible due to a low definition. The whole Q_C molecule

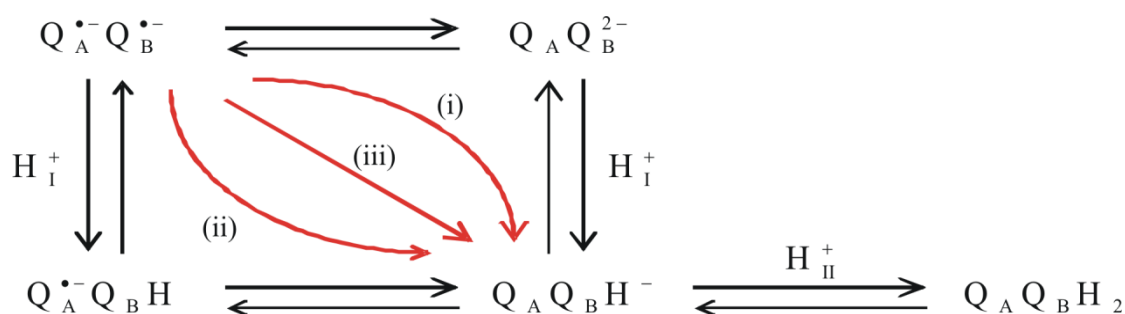
sits in a rather hydrophobic environment without any obvious polar contact or π -stacking that could stabilize the orientation of the head group.

The binding energies of Q_A , Q_B and Q_C in *T. elongatus* were calculated very recently to -56.1, -37.9 and -30.1 kcal/mol, respectively. These calculations were conducted by Hasegawa and Noguchi (90) using the fragment molecular orbital method and the 2.9 Å resolution structure model of dPSIIcc (22). The mobility of a PQ molecule will increase when it is stabilized mainly by mobile lipids and cofactors. The contributions of lipids and cofactors to the total binding energies were estimated to be 0, 24, and 45% for Q_A , Q_B and Q_C , respectively (90). This finding is in line with the order of the mobility of the PQ cofactors, as Q_A possesses the lowest and Q_C the highest mobility. Moreover, it was reported in (90) that in all three PQ molecules the isoprenoid tail is more responsible for the binding than the head group. The amino acid residues Phe261D and Trp253D were shown to bind most the head group of Q_A through strong π - π or CH- π interactions (Fig. 1.18 (A)). The head group of Q_B was found to be stabilized by π - π or CH- π interactions with Phe255A and Phe265A (Fig. 1.18 (B)). The isoprenoid tail of Q_B showed high interaction energies with the cyt *b559*, MGDG18 (see Section 1.3.3 and Fig 1.9) and the phytol chain of Chl_{D2}. The head group of Q_C , which is surrounded mostly by lipids and cofactors, was shown to interact mainly with MGDG18 and the Chl_{D2} chain, whereas the Q_C tail interacts mostly with the LMW subunits PsbJ, PsbE and PsbF (90) (Fig 1.19). Conclusively, hydrogen bonds of the keto-oxygens of the PQ head groups rather serve to fix the orientation of the head group in the binding pocket and may have important roles in controlling the PQ redox potentials (151, 152), than contributing to the binding of PQ. As Q_C has neither hydrogen bond nor π - π interactions in its binding site, its lower stability and affinity compared to Q_A and Q_B becomes more reasonable.

Electron transfer steps

Two turnovers of the RC are necessary to form PQH₂ from PQ in a two-step one-electron transfer reaction, coupled with the uptake of two protons. In the first electron transfer step, a semiplastoquinone anion radical Q_B^- is formed, which is likely stabilized by protonation of the adjacent amino acid side chains. The electron transfer from Q_A to Q_B was found to be heterogeneous and has to be described with at least two time constants of 0.2-0.3 ms and 2-3 ms (153). Additionally, this first electron transfer step is influenced by several factors e.g. pH, dehydration and temperature. See review (35) and references therein for a more detailed description. The second electron transfer step to Q_B is coupled to the first proton transfer. However, at the present stage it is not completely clear in which sequence the second electron and the two protons are transferred. Possible options are illustrated in Scheme 1. Based on studies on pbRC (154-156), it is assumed that in PSII RCs the

second electron transfer follows the first proton transfer (37, 157, 158) (pathway (ii) in Scheme 1).



Scheme 1 Possible reaction sequences for the transport of the second electron and two protons to Q_B^- . (i) Proton transfer follows electron transfer via $Q_A Q_B^{2-}$, (ii) electron transfer follows proton transfer via $Q_A^{\bullet-} Q_B H$, or (iii) electron transfer and proton transfer occur in a concerted manner. Scheme taken from (35).

PQ/PQH₂ exchange pathways

After the second protonation step, the mobile PQH₂ leaves the Q_B site and has to be replaced by fresh PQ from the PQ pool in the membrane. As the Q_B site is buried inside PSIIcc, pathways connecting the Q_B site with the membrane phase are needed for fast exchange of these hydrophobic molecules. Two possible pathways for PQ/PQH₂ exchange were discovered in the 2.9 Å resolution crystal structure of dPSIIcc (22). These pathways were named channel I and II and are located in subunit D1 (Fig. 1.19). They converge in the Q_B cavity and end directly in the fatty acid environment of the membrane interior. Both channels are formed by amino acid residues, phytol chains of chlorins and fatty acid chains of lipids, building a flexible and hydrophobic environment necessary for PQ/PQH₂ exchange. Channel I is occupied by the third PQ molecule Q_C , whereas the hydrophobic isoprenoid tail of Q_B is situated in channel II (depicted in Fig. 1.19). For the PQ/PQH₂ exchange, three possible mechanisms were suggested (see (22, 48)) involving the revealed channels I and II. A key question in this respect is, whether Q_C is a PQ in a “waiting position” to enter the Q_B site or is involved in other redox reactions. The heme iron of cyt *b559* is located about 20 Å away from the head group of Q_C , between the channels I and II. The redox state of cyt *b559* was demonstrated to be affected by PQ molecules in a way that suggests the presence of a PQ binding site distinct from Q_B and close to cyt *b559* (146). The observation that certain herbicides not only block the electron transfer at the Q_B site, but seem to influence the cyt *b559* redox potential by binding at a position different from Q_B , led to a similar conclusion (147). These findings point toward a role of Q_C in redox reactions coupled with cyt *b559*.

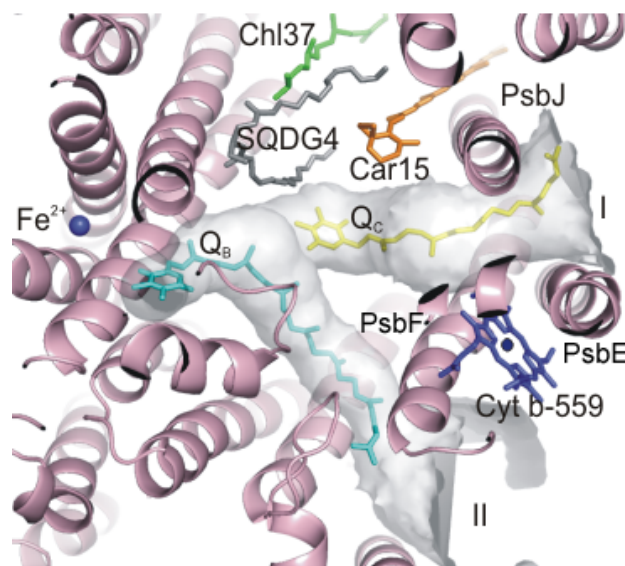


Figure 1.19 Calculated channels for PQ/PQH₂ exchange.

Calculated channels I and II (in gray) for PQ/PQH₂ exchange between the PQ pool and the Q_B and Q_C sites are shown according to the 2.9 Å resolution crystal structure of dPSIIcc (22). Q_B is situated in channel II and Q_C in channel I. View is from the cytoplasmic side. Color code: Q_B in light blue, Q_C in yellow, non-heme iron as blue sphere, Car15 in orange, Chl37 in green, SQDG4 in gray, cyt b-559 heme in dark blue and the surrounding proteins in pink. Figure taken from (22).

Role of Q_A in photoinhibition

In the case of an insufficient supply of PQ to the Q_B site, acceptor side induced photoinhibition occurs (for reviews on photoinhibition see (41, 159)). When the electron transfer from Q_A⁻ to Q_B or Q_B⁻ is slowed down or interrupted due to an unoccupied Q_B site, charge separated states can be formed such as S₂Q_A⁻, S₂Q_B⁻ or S₃Q_B⁻ (101). These states can recombine to P_{D1}⁺⁺Q_A⁻. From that state on, highly toxic reactive oxygen species (ROS) such as singlet oxygen can be generated through further charge recombination processes, thereby causing oxidative damage (160-164). The charge recombination of P_{D1}⁺⁺Q_A⁻ can occur in several possible ways and, depending on the chosen route, ROS are formed (see (35) for details). In PSII the path of charge recombination is influenced by the redox properties of Q_A. Depending on the redox midpoint potential (E_m) of Q_A, a harmless or potentially harmful recombination pathway is favored (see Fig. 1.20). The E_m of Q_A in PSIIcc of *T. elongatus* active in oxygen evolution was found to be -110 mV (165). However, the E_m value can vary strongly as a consequence of (i) changes at the donor side (165, 166), (ii) herbicide binding at the Q_B site (167) or (iii) mutations at the Q_A binding site (168). Further details on herbicide binding to the Q_B pocket and their influence on the redox potential of Q_A are given in Chapter 3. The possibility of modulating the redox potential of Q_A provides a protective way against photoinhibition, which is for example relevant during the assembly of the RC (166, 169, 170).

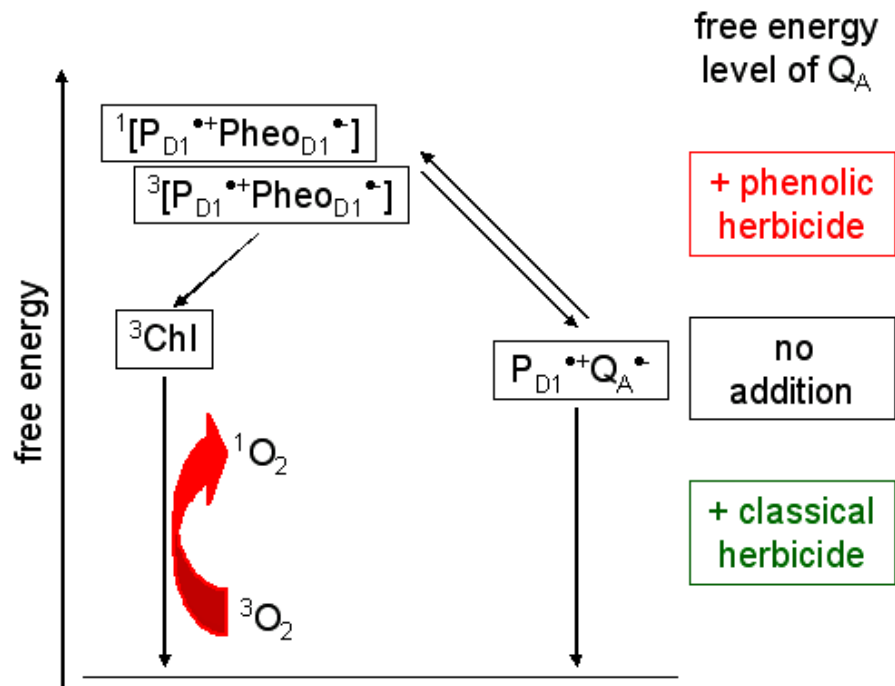


Figure 1.20 Simplified scheme for possible charge recombination pathways of $P_{D1}^{++}Q_A^{-}$.

A very simplified scheme for possible charge recombination pathways of the $P_{D1}^{++}Q_A^{-}$ state under the influence of the free energy level of Q_A upon herbicide binding to PSII is shown. Harmless direct non-radiative recombination of $P_{D1}^{++}Q_A^{-}$ to the ground state (right pathway) is favored when the redox potential of Q_A increases as in the case of classical herbicide binding. Indirect non-radiative recombination of $P_{D1}^{++}Q_A^{-}$ can occur via the singlet or triplet state of $P_{D1}^{++}Pheo_{D1}^{•-}$. The triplet radical pair decays non-radiatively to the ground state via triplet Chl, thereby likely producing singlet oxygen upon contact with triplet oxygen (red arrow). The latter recombination way represents the potentially harmful pathway and is favored when the energy level of Q_A decreases as in the case of phenolic herbicide binding.

1.3.6 The monomeric form of PSIIcc

The monomeric form of PSII appears during the assembly of all known 20 subunits and the repair cycle of photodamaged subunit D1 (30). The assembly of PSII is a stepwise and highly regulated process (171), that includes many auxiliary proteins which are absent in the crystallized complexes. In cyanobacteria, an intermediate Psb27-PSII complex, which has no functional manganese cluster, regulates the assembly of the Mn_4CaO_5 cluster and the binding of the extrinsic subunits PsbO, PsbU and PsbV prior to the dimerization of the PSII complex (172, 173). Monomerization of photodamaged PSII was suggested to be triggered by the detachment or structural reorganization of PsbO on the lumenal side (30).

Broser *et al.* (23) reported the first crystal structure of mPSIIcc at a resolution of 3.6 Å. The mPSIIcc were also isolated from *T. elongatus* and possess a high oxygen evolution

activity. It was shown, that in mPSIIcc 19 of the 20 subunits are arranged identically to the corresponding subunits in the dimer (22). Similar to the 1.9 Å resolution crystal structure of dPSIIcc (25), no electron density was obtained for subunit PsbY. However, subunit PsbY was found to be present in most of the redissolved mPSIIcc crystals examined by MALDI-TOF mass spectrometry. This finding supports the suggestion of a loose association of PsbY with PSIIcc. The structures of mPSIIcc and dPSIIcc were found to be almost identical, reflected by the location of the Chl_a and Pheo cofactors and the non-heme iron. Also, the assignment of 11 carotenes at positions expected from dPSIIcc could be confirmed. One of the five carotene molecules located at the monomer-monomer interface in the dPSIIcc (22) is missing in the mPSIIcc structure. This carotene is found in a bridging position across the monomer-monomer interface and may detach due to its exposed position in the monomer. The PQ cofactor at the Q_A site could be assigned, but at the Q_B position a buffer molecule was detected instead. An electron density was found at the Q_C site, but could not be interpreted. The majority of the lipids and detergent molecules harbored in the dPSIIcc structure at 2.9 Å resolution (22) were also found in the monomeric structure. Concerning the dimerization surface, only five lipids and four βDM molecules were found. These molecules are located next to the D1 protein (surrounding the RC), to PsbT and PsbM, but not at the surface provided by CP47. Therefore, these lipids were interpreted to play a functional or structural role in the RC or in the repair cycle of D1 rather than being only involved in the dimerization of PSIIcc.

No indications were found, that the mPSIIcc as used for crystallization in (23) represents a precursor complex or a photodamaged product of dPSIIcc. The mPSIIcc samples possess essentially the same oxygen evolution activity as dPSIIcc and the crystal structure of mPSIIcc at the resolution of 3.6 Å showed neither indications of a destabilized subunit D1 nor a structural reorganization of subunit PsbO (23).

The arrangement of the mPSIIcc proteins in the crystal unit cells (space group C222₁) is different to the one of dPSIIcc proteins in the unit cell (space group P2₁2₁2₁) (22, 23). These differences are of great significance for investigations of the Mn₄CaO₅ cluster with orientation-dependent spectroscopy (e.g. XAS). In each unit cell of dPSIIcc crystals four dimers of PSIIcc (equally to eight PSIIcc monomers) are arranged in different orientations and each dPSIIcc protein contains two Mn₄CaO₅ clusters that are related by a non-crystallographic C₂ symmetry (see Sec. 1.3.1). In contrast, the unit cell of mPSIIcc crystals contains only four mPSIIcc units in different orientations and for all of these orientations the membrane normal is oriented perpendicular to the crystallographic *b*-axis (Fig. 1.21). Additionally, the non-crystallographic C₂ symmetry of the Mn₄CaO₅ clusters does not exist in the crystal form of mPSIIcc. These features of the mPSIIcc crystals are of high advantage in polarized EXAFS studies as (i) the lack of the non-crystallographic

C_2 symmetry (as present in the dimeric form) reduces the number of possible orientations for the manganese cluster in the unit cell and (ii) the orientation of the membrane normal perpendicular to the crystallographic b -axis (Fig. 1.21) could facilitate a better distinction between absorber-backscatter vectors oriented parallel and perpendicular to the membrane plane (see Sec. 4.5).

The present work reports XAS measurements using mPSIIcc solution samples and polarized EXAFS measurements using mPSIIcc single crystals in Chapter 4.

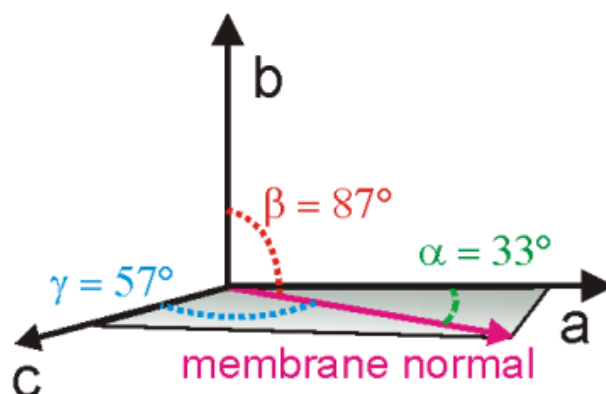


Figure 1.21 Orientation of the membrane normal vector in mPSIIcc crystals.

The orientation of the membrane normal vector (pink arrow) in mPSIIcc crystals is shown, relative to the crystal axes. The membrane normal vector corresponds to the local C_2 -axis of the dimer. For clarity, only one of the four possible orientations is shown. For other orientations, the membrane normal vector has to be rotated by 180° around the a , b , and c axes. In any orientation, the angle between the membrane normal and the b -axis is nearly 90° . Figure adapted from (23).

1.3.7 Comparison of *T. elongatus* and *T. vulcanus* native dPSIIcc XRD structures

As already mentioned above, the two latest crystal structures of native dPSIIcc derived from two different thermophilic cyanobacteria (*T. elongatus* and *T. vulcanus*) and were obtained with different resolutions (22, 25). Even though the structural resolution is different by 1.0 \AA , this work refers mainly to the structural model at 2.9 \AA resolution (22). The reason is significant distinctions between the two dPSIIcc crystal structures concerning the cofactors, which are found despite the high analogy of the protein sequences of both PSII complexes (97.17% sequence identity of the four large subunits D1, D2, CP43, CP47; calculated with UniProt). Differences between the structural models of dPSIIcc at 2.9 \AA and 1.9 \AA resolution were already explained in the respective sections and are summarized in Table 1.5. Besides the assignment of water molecules, the biggest variation between the two dPSIIcc structures is the amount and the type of detected

detergent molecules. In the 1.9 Å resolution dPSIIcc crystal structure an additional type of detergent was used, namely HTG. Nine and eight HTG molecules are located in each monomer, which is a relatively high amount. As pointed out in Section 1.3.3, PSIIcc from *T. elongatus* are isolated solely with β DM and PSIIcc from *T. vulcanus* are isolated with β DM and additionally treated with the non-ionic detergent HTG. It was not reported in (25) which amount or in which step of the dPSIIcc isolation, purification and crystallization the detergent HTG was introduced. However, the use of two detergents leads to the formation of mixed micelles and the CMC becomes usually an intermediate between the CMC values of the pure components (174). Consequently, the detergent belt that is formed around the hydrophobic parts of the dPSIIcc protein contains both, β DM and HTG. As HTG molecules possess shorter alkyl chains than β DM and also a different head group shape, this detergent belt will vary from the detergent belt formed only by β DM molecules (as in (22)). This variation can influence possible intramolecular protein and detergent contacts during the crystallization of dPSIIcc and, thus, might change the packing of the crystal and its diffraction quality (85, 175). Most likely the combination of this detergent belt modification and the dehydration procedure that was performed prior to XRD data collection, as described in (25), led to the improvement of the crystal structure resolution of dPSIIcc from *T. vulcanus*.

The outlined variations of the used detergent concentrations and compositions in the different laboratories are probably as well a reason for the distinctions in the carotenoid, lipid and detergent content in the two structures. Likewise, the absence of Q_C in the high resolution structure and the different amounts of assigned calcium and chloride ions may result from differences in the applied protein preparation protocols (for example Umena *et al.* (25) used 330 mM NaCl for the PSIIcc elution, whereas $MgSO_4$ is used in our protocols for protein elution, see Sec. 2.2.2) and crystallization procedures, rather than misassignments due to the lower resolution. The loss of subunit PsbY in the high resolution structure can be ascribed to the use of the strong anion exchange matrix Mono Q for chromatographic protein purification (25). Also, in the 2.1 Å resolution crystal structure of Sr-substituted *T. vulcanus* dPSIIcc, which was purified in the same way as the native *T. vulcanus* dPSIIcc, the PsbY subunit is present only in one monomer (50). In contrast, dPSIIcc of *T. elongatus* were purified with a weak anion exchange matrix (DEAE-Sepharose) and subunit PsbY could be assigned in both monomers of dPSIIcc despite its lower crystal structure resolution of 2.9 Å (22).

Table 1.5 Differences in the subunit and cofactor compositions (per monomer) between the structural models of dPSIIcc crystals at 2.9 Å (22) and 1.9 Å (25) resolution.

	2.9 Å	1.9 Å
protein subunits	20	19
chlorophyll <i>a</i>	35	35
pheophytins	2	2
carotenoids	12	11
integral lipids	25	20 (+3)
calcium ions	3	5/4
chloride ions	1	3
plastoquinones	3	2
βDM	7	6
HTG	-	9/8
water molecules	(1)	1438/1357

1.4 Project aims

In this work two main goals were pursued, whereas the first one is related to the acceptor side of PSII and the second one to the donor side of PSII.

(1) The binding of herbicides to the Q_B site in both PSII and pbRC is studied since several decades using a wide variety of methods. The studies on herbicide binding to pbRC profited from structural information derived from XRD crystallography. The first crystal structure of pbRC with a bound herbicide exists since 1986 (176), and in the case of the herbicide terbutryn the crystal structure was improved in 2000 to a resolution of 2.0 Å (177). Therefore, the pbRC/herbicide structures served so far as models for PSII inhibition by herbicides as no direct structural information was available (38). The information obtained from pbRC/herbicide structures were also used as starting points for theoretical studies on herbicide binding to PSII (178). When this work was started, the first crystal structure of a pbRC/herbicide complex existed almost 25 years. Hence, one major aim of this project was the successful co-crystallization of dPSIIcc and the herbicide terbutryn to obtain a first actual XRD crystal structure of a dPSIIcc/herbicide complex. The structural information would not only experimentally verify the theoretical models of herbicide binding to PSII, but also provide a structural basis for understanding the observed redox potential shift of Q_A as a consequence of herbicide treatment.

Furthermore, at this time the resolution of the native dPSIIcc crystal structure was limited to 2.9 Å and, in order to improve the resolution, ideas to overcome heterogeneities in the crystals (which have a negative influence on the diffraction quality) were discussed. The binding sites of the mobile PQ molecules (Q_B and Q_C) are potential positions that give rise to heterogeneity in the crystals, as the binding pockets are not fully occupied or the PQ molecules occupy different positions in a crystal due to their mobility. The binding of an immobile herbicide to the Q_B site might help to overcome these micro-heterogeneities and could lead to an improvement of the crystal structure resolution.

(2) XRD crystallography provides a static picture of the donor side of PSII. However, the Mn_4CaO_5 cluster in the OEC is known to undergo structural and electronic changes while cycling through the S states. Therefore, it is important to extend the static picture obtained from XRD crystallography and gain information on the actions occurring during oxygen evolution. Additionally, information from XRD on PSIIcc crystals suffers from radiation damage and, therefore, cannot give reliable data about the structure of the intact Mn_4CaO_5 cluster (116). The technique of XAS has the main advantage of avoiding radiation damage, by applying low X-ray doses. Additionally, the Mn oxidation state can be controlled constantly. Hence, a second major aim of this study was to reveal changes in the local geometry and electronic structure of the Mn_4CaO_5 cluster that are expected to occur during the S state transitions. The detailed knowledge about structural changes of the Mn_4CaO_5 cluster during the catalytic S state cycle is crucial for understanding the mechanism of O-O bond formation. XAS studies of the S state transition were so far only performed with spinach thylakoid membrane fragments (179). XRD measurement, however, were performed on crystals of PSIIcc. The present work aimed at eliminating this discrepancy, by using dPSIIcc solution samples for XAS measurements, the same samples which have been used for crystallography. Furthermore, the detailed geometry of the Mn_4CaO_5 cluster obtained in the recent 1.9 Å resolution crystal structure (25), can be used for the first time as the basis to build a model for structural changes happening at the Mn_4CaO_5 cluster.

Polarized EXAFS measurements on single crystals can increase the information about structural changes, especially when using the crystals of mPSIIcc. Therefore, a further aim of the present project was to prove mPSIIcc suitable for XAS measurements and to perform polarized EXAFS on mPSIIcc single crystals.

2. Materials and Methods

2.1 Chemicals and Materials

Chemicals

All used chemicals were of analytical grade and supplied either by VWR/Merck or by AppliChem if not indicated otherwise. The chemicals betaine monohydrate and PEG 2,000 were supplied by Fluka/Sigma, the detergent β DM by Glycon, Luckenwalde, and the herbicide terbutryn by Sigma-Aldrich. For all aqueous solutions and buffers exclusively filtered and autoclaved Millipore MilliQ water was employed.

Buffers

A	25 mM MES (pH 6.3), 1 M betaine, 15 mM NaCl, 5 mM MgCl ₂ , 5 mM CaCl ₂ , 0.03% (w/w) β DM
A ⁻	100 mM PIPES-NaOH (pH 7.0), 10 mM CaCl ₂
A ⁺	A ⁻ + 0.03% (w/w) β DM
ABC ⁻	100 mM PIPES-NaOH (pH 7.0), 10 mM CaCl ₂ , 0.5 M betaine monohydrate
ABC ⁺	ABC ⁻ + 0.03% (w/w) β DM
Anode buffer	25 mM imidazole/HCl (pH 7.0)
Cathode buffer B	50 mM tricine (Roth), 7.5 mM imidazole, 0.02% Coomassie G-250
Cathode buffer B/10	50 mM tricine (Roth), 7.5 mM imidazole, 0.002% Coomassie G-250
Cb ₀	20 mM MES-NaOH (pH 6.0), 20 mM CaCl ₂ , 0.02% (w/w) β DM, 0.5 M betaine monohydrate
Cb ₁₀₀	Cb ₀ + 100 mM MgSO ₄
Cg ₀	20 mM MES-NaOH (pH 6.0), 20 mM CaCl ₂ , 0.02% (w/w) β DM, 5% (w/v) glycerine
Cg ₅₀	Cg ₀ + 50 mM MgSO ₄
Cg ₁₀₀	Cg ₀ + 100 mM MgSO ₄
MCM	20mM MES-NaOH (pH 6.0), 20 mM CaCl ₂ , 10 mM MgCl ₂
MC*M*	MCM + 0.15 M MgCl ₂ , 0.3 M CaCl ₂
MCMB	MCM + 0.5 M betaine monohydrate
MCMG	MCM + 25% (w/v) glycerine
MMCM	MCM + 500 mM mannitol, 0.2 μ g DNase/ml
M10 ⁵⁵	10 mM MES-NaOH (pH 6.0), 5 mM CaCl ₂ , 5 mM MgCl ₂ , 0.02% (w/w) β DM

Chromatography material and system

For anion-exchange chromatography various columns (Kronlab ECO^{Plus}, Kronlab GmbH) of different sizes were used and packed either with ToyoPearl DEAE 650 S (Toso Haas), HR-Sepharose Q (Amersham Pharmacia Biotech) or DEAE-Sepharose Fast Flow (GE Healthcare). For gel permeation chromatography a pre-packed Superose 6 column (10 mm diameter, 300mm length, GE Healthcare) was used. All chromatographic separation steps were performed on an ÄKTA™ Explorer FPLC System (Amersham Pharmacia Biotech).

2.2 Methods

2.2.1 Cell cultivation and protein extraction

Cells from the cyanobacteria *T. elongatus* were grown, as described in (86), at 56°C in a PBR25 photobioreactor (IGV Potsdam, Germany and Sartorius-BBI Systems, Melsungen, Germany) with a volume capacity of 32 l.

For the preparation of thylakoid fragments the cells were washed with ~ 3 l of MCM buffer, sedimented by centrifugation at 4,500 rpm for 5 min (JLA rotor, Beckman) and resuspended in ~ 300 ml of MMCM buffer, containing 0.2% (w/v) lysozyme (Sigma). After an incubation period of 30 min at 48 °C, cell disruption was performed via a Yeda-Press at 30 atm nitrogen pressure. Broken cells were diluted with 3 l of MCM buffer and sedimented at 8,000 rpm for 5 min (JLA rotor). The following wash steps were each performed twice (JLA rotor, 8,000 rpm, 5 min): with ~ 6 l of buffer MC*M* to reduce the amount of phycobilisomes, with ~ 3 l of buffer MCM and in the end with either MCMB or MCMG buffer. The final Chl_a concentration was brought to 1.8 mM in MCMB or MCMG buffer.

The protein extraction was carried out at room temperature by incubation of the membranes with 0.55% (w/v) β DM, 0.25 mM PEFA in buffer MCMB or MCMG for 5 min under continuous gentle agitation. After adding a similar volume of Cb₀ or Cg₀ buffer, the solubilized extract was centrifuged at 4°C for 20 min at 48,000 rpm (70Ti rotor, Beckman). The yielded supernatant was directly used in column chromatography for protein purification.

2.2.2 Protein purification

All following steps were performed under dim green light at 6°C.

The purification procedure of crude PSII extract followed the protocols published by Kern *et al.* (86) and Broser *et al.* (23). The main modification of the latest protocol is the

replacement of 5% glycerol by 0.5 M betaine monohydrate in all buffers and an additional chromatographic purification step for mPSIIcc. In the following, the purification procedure is described for the case of betaine monohydrate usage, whereas differences for the use of glycerine are mentioned in parentheses and are indicated by a * sign.

The first chromatographic column is 50 mm in diameter and 400 mm in length, packed with Toyo Pearl DEAE 650 S (Toso Haas) and was equilibrated by a mixture of buffer Cb₀ and Cb₁₀₀ (Cg₀ and Cg₅₀)* providing a conductivity of ~ 5.0 mS/cm (~ 4.0 mS/cm)*. After sample loading, the column was washed at constant salt concentration for five to eight column volumes (CV) at a constant flow rate of 20 ml/min. An isocratic step to ~ 8.7 mS/cm (~ 7.2 mS/cm)* was applied to elute the protein. The PSIIcc-containing fractions were pooled and diluted with buffer Cb₀ to reduce the conductivity to ~ 5.0 – 5.4 mS/cm (~ 4.3 – 4.5 mS/cm)*.

The second chromatographic column is 25 mm in diameter and 350 mm in length, also packed with Toyo Pearl DEAE 650 S and was preequilibrated to a conductivity of ~ 5.0 – 5.4 mS/cm (~ 4.3 – 4.5 mS/cm)*. After loading the sample obtained from the first column, the second column was washed at a flow rate of 8 ml/min for about 10 CV at a constant or very slowly increasing salt concentration. A linear salt gradient (~ 20 mM MgSO₄ in 8 CV) at a flow rate of only 6 ml/min was applied to elute two fractions containing either mPSIIcc or dPSIIcc. Both fractions were concentrated using consecutively Amicon stirring cells with a Millipore Biomax 100 membrane (Millipore, MA, USA) and Sartorius Ultra Free 100 concentrators.

The dPSIIcc was adjusted to a Chla concentration of 0.74 mM in buffer ABC⁺ (A⁺)*. Recrystallization of the protein was conducted by slowly adding a similar volume of buffer ABC⁻ (A⁻)* containing 12 – 13% (w/w) PEG 2,000 and incubation overnight at 6°C. Microcrystalline dPSIIcc was harbored by centrifugation, redissolved and concentrated in buffer ACB⁺ (A⁺)* to a concentration of 4 mM Chla and stored in liquid nitrogen.

MPSIIcc containing samples were concentrated to a Chla concentration of about 5 mM in buffer Cb₀ and further purified in a third chromatographic step. For this third purification step a column with a diameter of 15 mm and a length of 410 mm was used, and two different approaches were performed. The first approach was developed in (180). The column was packed with HR-Sepharose Q (Amersham Bioscience) and equilibrated with buffer Cb₀. After sample loading, the column was washed with a flow rate of 3 ml/min for 6 CV at a constant salt concentration. mPSIIcc was eluted in a linear salt gradient (0 – 50 mM MgSO₄ in 8 CV). The fraction of mPSIIcc was concentrated to 3 mM Chla in buffer M10⁵⁵ and stored in liquid nitrogen. In the second approach, the column was packed with DEAE-Sepharose Fast Flow (GE Healthcare) and preequilibrated to a conductivity of ~ 4.9 mS/cm by a mixture of buffer Cg₀ and Cg₁₀₀ with pH 5.5. About 4 μmol of mPSIIcc

containing sample in buffer Cg₀ were loaded onto the column. The column was washed with a flow rate of 1.5 ml/min for 3 CV at a constant salt concentration. The mPSIIcc was eluted in a linear salt gradient (20 – 80 mM MgSO₄ in 9 CV). The fractions of mPSIIcc were pooled and concentrated to 3 mM ChIa in buffer M10⁵⁵ and stored in liquid nitrogen.

2.2.3 Crystallization of mPSIIcc

The crystallization of mPSIIcc was carried out as described in Broser *et al.* (23). Microbatch crystallization was performed by mixing the protein solution (3 mM ChIa corresponding to ~ 25 mg/ml protein) with the same volume of precipitant solution. The finally obtained solution contains ~ 19% (w/v) PEG 400, 0.1 M PIPES (pH 7.0), 0.2 M CaCl₂, 0.01% (w/w) βDM. Between 4 and 10 μl of this solution was placed in either a 96 well plate (IMP@CT, Greiner-Bio-one) or the middle of a Teflon tube (60 mm length, 1 mm inner diameter; YCM Europe) and closed with sealing tape or sealing plaster. The crystals grew at 18°C in the dark within three to six days.

Crystallization screens were performed with mPSIIcc extracted from the third purification step using DEAE-Sepharose Fast Flow as column material. Crystallization screens were set up using a robot (in the group of Prof. Dr. H. Dobbek, Humboldt Universität zu Berlin) and the sitting drop vapor diffusion method with a drop volume of 0.4 μl. For each condition, two different protein concentrations were tested: 4.3 and 8.5 mg/ml (equal to ChIa concentrations of 0.5 and 1.0 mM, respectively). The following screens were tested: Structure Screen 1 and 2, PACT premier, JCSG-plus, MIDAS, ProPlex (all from Molecular Dimensions), PEG/Ion Screen, Natrix, MembFac (all from Hampton Research) and Wizard 1 and 2 (Emerald).

2.2.4 Co-crystallization of dPSIIcc and terbutryn

For the co-crystallization of dPSIIcc and terbutryn, dPSIIcc (4 mM ChIa in buffer A⁺) were illuminated for 10 s using a two-armed Halolux 250 cold light source (Streppel, Wermelskirchen-Tente, Germany). After the addition of 2 mM terbutryn dissolved in DMSO (yielding 2% DMSO in the sample, stock solution: 100 mM terbutryn in DMSO), samples were dark-adapted for 120 min. For batch crystallization, dPSIIcc/terbutryn samples were mixed with the same volume of precipitant solution, containing 6.4 – 8.2% PEG 2,000 in buffer A⁻. The final terbutryn concentration in each crystal setup was 1 mM. A volume of about 5 μl of the obtained solution was placed in either a glass capillary (75 mm length, 1.15 mm inner diameter) or a polytetra-fluoroethylene tube (about 60 mm length, 1 mm inner diameter). Crystals grew in the dark at 20°C within three to five days

and were cryo-protected by stepwise addition of glycerol to a concentration of 30 - 35% (w/v).

2.2.5 Oxygen evolution measurements

A home built Clark type electrode (181) was used to measure the oxygen evolution per flash of PSIIcc samples at room temperature. The sample was excited via repetitive 1 Hz flashes from a xenon flash lamp. The electrode was calibrated using air-saturated and nitrogen-saturated water at atmospheric pressure. Before light excitation, samples were diluted to 20 – 50 μ M Chl*a* in buffer MCM. As artificial electron acceptors, $K_3[Fe(CN)_6]$ and phenyl-p-benzoquinone were added with final concentrations of 2 mM and 0.4 mM, respectively.

2.2.6 Gel permeation chromatography

For gel permeation chromatography, a Superose 6 column with a diameter of 10 mm and a length of 300 mm (GE healthcare) was used. The column was equilibrated with buffer Cg₀ containing 25 mM MgSO₄. A volume of 200 μ l protein solution (0.5 – 2 mg/ml) was loaded onto the column. The protein was eluted with an isocratic flow at 0.3 ml/min and detection was performed at a wavelength of 280 nm. For comparison, purified mPSIIcc and dPSIIcc were used as standards.

2.2.7 Mass spectrometry

Matrix-assisted laser desorption/ionization time-of-flight mass spectrometry (MALDI-TOF-MS) analysis was conducted using an Ultraflex II Spectrometer (Bruker Daltonics) in the linear mode using sinapinic acid as matrix. PSIIcc samples (2- 4 mM Chl*a*) were diluted 1:30 with 40% (v/v) acetonitrile, 0.1% trifluoroacetic acid. An aliquot of the obtained solution was mixed in a 1:1 ratio with a saturated solution of sinapinic acid in 40% (v/v) acetonitrile. 0.7 μ l of this sample (equivalent to ~ 140 pmol Chl*a*) were placed on a target (stainless steel) and air dried. The sample was either directly measured or a layer of sinapinic acid (0.5 μ l) was placed on top of the sample and dried.

The MALDI-TOF MS measurements were performed by Dr. C. Weise (Freie Universität Berlin).

2.2.8 Blue native polyacrylamide gel electrophoresis

Blue-native polyacrylamide gel electrophoresis (BN-PAGE) was performed in a water cooled electrophoresis chamber (LKB, Bromma; 4°C). Gradient gels, with a dimension of 14 x 14 cm, were made following the protocol of (182) using 30% acrylamide solution

(Rotiphorese Gel A, Roth) and 2% bisacrylamide solution (Rotiphorese Gel B, Roth). Samples were mixed in a 1:3 ratio with solubilization buffer (containing 50 mM NaCl, 50 mM imidazole, 1 mM EDTA (Roth) and 2 mM ϵ -aminocaproic acid (pH 7)) resulting in a Chla concentration of 0.05 mM. 2.5 μ l β DM (20% (w/w) stock solution in water) were added to a sample volume of 50 μ l and incubated for 20 min on ice and in the dark. After centrifugation of the samples (16 000 g, 4 °C, 10 min), the supernatant was mixed with 5 μ l glycerin (50% (w/w) stock solution in water) and 1.25 μ l Coomassie G-250 (Roth, 5% (v/v) in 750 mM ϵ -aminocaproic acid). The samples were applied on the gel and the run started at a voltage of 100 V. After the samples passed the stacking gel, the current was adjusted to 15 mA and the voltage was limited to 500 V. The cathode buffer B was exchanged to cathode buffer B/10 when the dye front passed one third of the running distance. The gels were destained in 10% acetic acid.

2.2.9 Single flash induced Chla fluorescence measurements

The influence of terbutryn on the electron transfer to Q_B was studied by applying a concentration series of the herbicide. Samples of dPSIIcc were diluted to 10 μ M Chla (equal to 0.143 μ M dPSIIcc) in buffer A and terbutryn, dissolved in DMSO, was added. The final herbicide concentrations ranged from 10^{-11} to 10^{-3} mol/l. Control samples contained no herbicide but 2% DMSO instead. The DMSO concentrations used in all experiments had no influence on the PSIIcc oxygen evolution activity (92). Sample preparation and fluorescence measurements were performed under dim green light.

Single flash-induced Chla fluorescence was measured using a laboratory-built apparatus with a commercial double-modulation fluorometer (Photo Systems Instruments FL3000) as described in (183-185). Saturating flash excitation of the dPSIIcc samples was provided by a frequency-doubled Q-switched Nd:YAG laser (Continuum Minilite II, wavelength = 532 nm, full width at half-maximum = 5 ns). A series of 32 flashes with a flash interval of 0.7 s was applied. Laser pulse intensities were adjusted to 13 mJ/cm using the internal attenuator of the laser and determined using a Nova-Laser-Power/Energy-Monitor equipped with a measuring head PE10 (Ophir Optronics). The fluorescence was excited by discrete weak light pulses from a diode array (wavelength of about 620 nm, duration of 8 μ s), which were linearly spaced on a logarithmic time scale. The first data point was recorded 76 s after the excitation flash. The amplitude of the fast decay phase (explained in Sec. 3.2) of the prompt fluorescence (PF; see Fig. 3.2) was defined as the difference between the maximum fluorescence yield reached after flash excitation (F_M) and the amplitude after 7.2 ms ($F_{7.2}$), according to the following equation

$$PF = \frac{FM - F_{7.2}}{FM - F_{700}}$$

F_{700} represents the fluorescence level reached about 700 ms after flash excitation, as in control samples about 80% of the total Q_A reoxidation happens within this time range. The obtained PF values were plotted over the herbicide concentrations and fitted by a standard binding function.

The fluorescence measurements were performed in cooperation with J. Buchta in the group of Prof. Dr. H. Dau (Freie Universität Berlin).

2.2.10 X-ray diffraction data collection

X-ray diffraction data from several dPSIIcc/terbutryn crystals were collected using monochromatic synchrotron radiation at a wavelength of 0.93 Å at beamline ID 14-4 of ESRF (Grenoble, France). The beamline was equipped with a nitrogen gas stream thermostat (Oxford Cryosystems) and a Q315r ADSC detector. Diffraction data were collected at 100 K in oscillation mode with an oscillation range between 0.2° and 1°/frame depending on the resolution and mosaicity of each crystal. After collecting a partial dataset with about 50 frames, the crystal had to be shifted by at least 100 μm along the spindle axis before the next part of the dataset could be recorded. The data with the highest resolution were processed with the XDS program package (186) to 3.2 Å resolution (see Table 3). The structure was solved by the method of molecular replacement with the program PHASER (187) using one monomeric part of the 2.9 Å resolution structure of dPSIIcc as a search model (PDB code 3BZ1 (22)). Model rebuilding and refinement were done with COOT (188) and the CNS 1.2 package (189), respectively, employing non-crystallographic symmetry. The rigid-body procedure was used for refining the protein part of the complex, whereas the annealing procedure was applied for refining the cofactors and side chains of the protein subunits. The final model shows R/R_{free} factors of 0.269/0.299, with root mean square deviations from an ideal geometry of 0.013 Å for bond lengths and 2.2° for bond angles. Terbutryn molecules were placed in the appropriate difference electron density in $F_o - F_c$ maps.

All data processing and model building of the 3.2 Å structure of the dPSIIcc/terbutryn complex was performed by A. Gabdulkhakov and A. Guskov in the group of Prof. Dr. W. Saenger (Freie Universität Berlin).

2.2.11 X-ray absorption spectroscopy on PSIIcc

2.2.11.1 Theoretical basics of X-ray absorption spectroscopy

X-ray absorption spectroscopy (XAS) is based on the following physical events: The energy of an X-ray photon is able to eject a core electron of an atom into the lowest unoccupied molecular orbital (see Fig. 2.2) or into the continuum, thereby producing a

photoelectron (Fig. 2.1, left panel). The ejected electron originates either from the K or the L electron shell. The caused electron “hole” can be filled by an electron from a higher level under the emission of fluorescence. Depending on whether this electron comes from the L or the M electron shell, the X-ray fluorescence is referred to as K_α or K_β transition, respectively (Fig. 2.1, right panel).

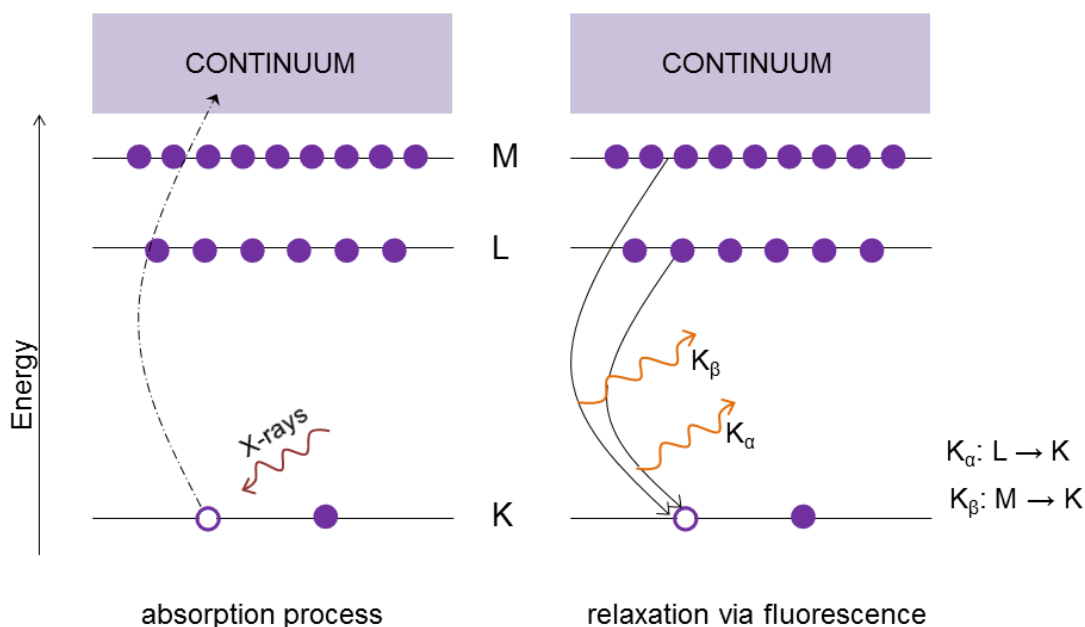


Figure 2.1 Schematic illustration of X-ray photon absorption.

A simplified schematic illustration of the absorption of an X-ray photon by an electron from the K shell, which is ejected into the continuum, is shown on the left. The right panel depicts the X-ray fluorescence that is emitted when the electron hole at the K shell is filled by electron transfer from the higher L or M shell. These events are named K_α or K_β transition, respectively.

XAS experiments are usually performed at synchrotron radiation sources, which provide intense and tunable X-ray beams. The absorption spectrum is recorded while scanning through the required energy range, which depends on the investigated element. The ejection of a core electron of the absorbing element becomes visible in the X-ray absorption spectra as a sharp absorption increase at a specific energy (see Fig. 2.3, green arrow). The energy at which this absorption increase takes place is characteristic for the absorbing element and is called absorption edge. The name of the edge depends on the shell of the excited core electron: when the ionization is from a 1s electron it is named K-edge (as illustrated in Fig. 2.1), and when the ionization is from a 2s or 2p electron it is named L-edge (Fig. 2.2). The most intense features of a K-edge spectrum are due to 1s to np electron transitions, whereas the most intense features of an L-edge spectrum are due to 2p to nd electron transitions (with $n = 1, 2, 3, \dots$).

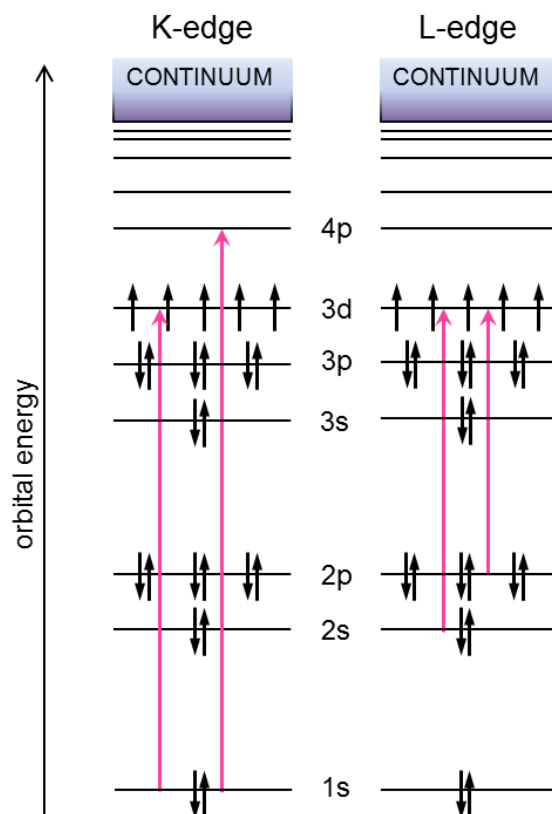


Figure 2.2 Schematic illustration of K-edge and L-edge transitions for Mn(II).

An orbital energy scheme for the K-edge (left panel) and L-edge (right panel) transitions for Mn(II) are illustrated. Electron transitions are indicated by the pink arrows. Transitions of 1s to 3d and 4p are possible at the K-edge and 2s and 2p to 3d at the L-edge. The dominant contribution to the K-edge spectrum comes from the 1s to 4p transitions, with 4p being the lowest unoccupied p orbital. The energy levels are not drawn to scale. The energy level of the 4s orbital is omitted for clarity.

An XAS spectrum can be measured in two different ways: the transmission mode or the fluorescence mode. In the first case, the intensity of the X-ray beam is measured before (I_0) and after passing through the sample (I_1) using ion chamber gas detectors. Thus, the number of X-ray photons absorbed by core electrons to create a photoelectron (and an electron “hole”) is counted. The XAS spectrum shows the variation of $(\log I_0/I_1)$ against the energy (in eV). The fluorescence mode takes advantage of a secondary process, the radiative decay of photoexcited states (Fig. 2.1, right panel). The fluorescence radiation (F) from the sample is measured, using a photo diode (e.g. Lytle detector) or a Germanium detector. The number of fluorescence photons emitted from the sample, when an electron from a higher level fills the “hole” in the core level, is counted. The XAS spectrum then shows the variation of (F/I_0) against the energy (in eV). The fluorescence mode is used, when the concentration of the element of interest is very low in the sample and the variation of $(\log I_0/I_1)$ is too small. In PSIIcc the amount of Mn is in the range of 1

mM or even less. Therefore, the experimental set up applied in this work, used the more sensitive fluorescence mode for the detection of the absorption spectra.

A typical XAS spectrum can be divided into three regions: the pre-edge region, the X-ray absorption near-edge structure (XANES) region, and the extended X-ray absorption fine structure (EXAFS) region (Fig. 2.3). This division is related to the electron transitions from the 1s level to either nd (pre-edge), or to $(n+1)p$ (XANES), or even to the continuum (EXAFS) at higher energies.

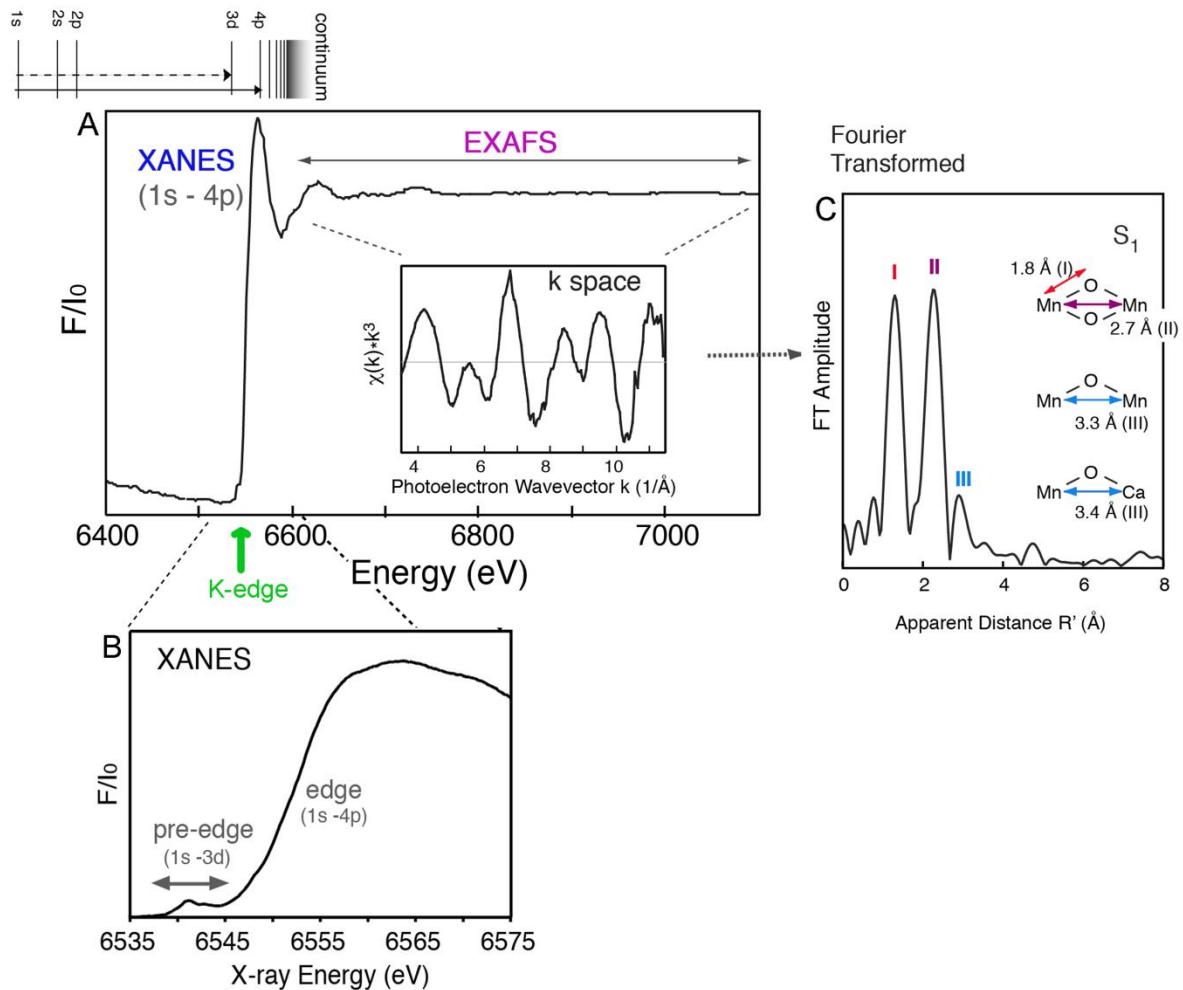


Figure 2.3 XANES and EXAFS spectra of Mn XAS of dPSIIcc samples.

Mn XAS spectra of a dPSIIcc sample from *T. elongatus* are used to illustrate the different regions in a XAS spectrum. **(A)** The XANES and EXAFS regions of the spectrum are shown. The energy levels of the Mn electrons are indicated on top of the panel and visualize the correlation between the electron transitions and the regions of the XAS spectra. The enlargement shows the k-space EXAFS spectrum. **(B)** The Mn K-edge XANES with the pre-edge (1s to 3d transitions) and the rising edge (1s to 4p transitions) region is depicted. **(C)** The FT of the k-space EXAFS data is shown. The three major FT amplitude peaks were attributed to the distances of Mn-O/N (peak I), Mn-Mn (peak II) and Mn-Mn/Ca (peak III) interactions which distribute in the range of 1.8 – 2.2 Å, 2.7 – 2.8 Å and 3.3 – 3.4 Å, respectively. Figure adapted from (190).

The XANES region provides information about the symmetry and the electronic structure (oxidation state) of the investigated site. The oxidation state of an atom can be determined by the K-edge shift of the corresponding XANES spectra as the K-edge absorption energy increases with increasing oxidation states. The EXAFS region gives information about the numbers, types and distances to ligands and neighboring atoms of the investigated atom (191). As described above, when the energy of the X-ray photon exceeds the ionization energy (above the K-edge energy) and an electron is ejected into the continuum, a photoelectron is produced which harbors the excess energy as translational kinetic energy. Due to its wave nature, the released photoelectron can be back-scattered by nearby atoms, leading to interference between the outgoing and back-scattered electron wave. The occurring constructive and destructive interference result in a modulation of the absorption coefficient and this oscillation is the basic phenomenon of EXAFS (Fig. 2.4). The EXAFS oscillation starts immediately after the absorption edge and continues to about 1 keV above the edge. The EXAFS signal is expressed as function of the photoelectron wave vector k ($k = 2\pi/\lambda$). The modulation of the absorption coefficient is depicted in the so called k -space (Fig. 2.3 (A), enlargement) in which the x-axis is converted from eV to wave vector k with the unit \AA^{-1} (inverse of wavelength). It can still be considered as an energy axis. The EXAFS oscillation (y-axis) can be weighted with the k -value to see the EXAFS oscillation in the higher k -space (region between 8 - 12 \AA^{-1}) more pronounced. Usually k^3 -weighted data is used for Fourier transformation (FT) (Fig. 2.3 (C)) and further analysis of the data. From the FT of the absorption coefficient modulation pattern a FT-amplitude spectrum with peaks at the apparent absorber-backscatterer distances is obtained (Fig. 2.3 (C)) and information about the distances between absorber and back-scatterer can be extracted with a high accuracy of $\sim 0.02 \text{ \AA}$ and a distance resolution of $\sim 0.1 \text{ \AA}$. In addition, information about the disorder of the ligand shell and about the number of backscatterers in each shell can be gained from the data.

For the analysis of the EXAFS data, curve fitting is usually performed. Curve fitting denotes the construction of a curve that approximates best (best fit) the experimental measured spectrum. This curve is constructed by computing the theoretical values for backscattering for each of the assumed atom-backscatterer paths and adding them all up. By varying the nature, number and distance of the backscatterers as well as the disorder for each of the paths, different theoretical solutions can be obtained and are compared with the experimental spectrum until an optimum solution is found.

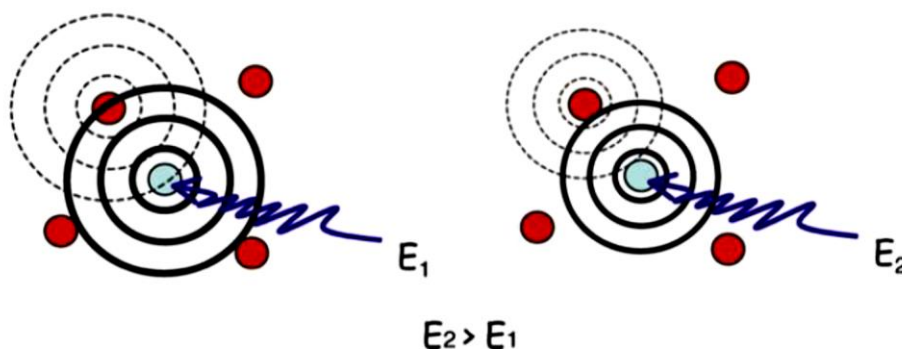


Figure 2.4 Schematic illustration of the outgoing and backscattered photoelectron wave.

This schematic picture of the outgoing and backscattered photoelectron wave illustrates the concept of interference in the EXAFS region. The central blue sphere represents the absorbing atom and the photoelectron is backscattered from the surrounding atoms (shown as red spheres). E_1 and E_2 are the energies of the incident X-ray photon with E_2 being higher than E_1 . On the left, the backscattered wave from the surrounding atoms (dashed black circular lines) is in phase with the outgoing wave (solid circular lines). This leads to an increase in the absorption coefficient. On the right, due to the shorter wavelength of the photoelectron, the backscattered wave can destructively interfere with the outgoing wave and decrease the absorption coefficient. This modulation of the absorption coefficient by the backscattered wave from neighboring atoms is the basic phenomenon of EXAFS. Figure taken from (190).

The XAS method has many advantages, but also some limitations. In XAS, radiation damage to biological samples is avoided by applying a low X-ray dose (two to three orders of magnitude lower than in XRD crystallography). Furthermore, XAS is element specific and allows focusing on one element without disturbance from other elements present in the investigated sample. XAS can be applied to powder samples, solutions, frozen samples and does not require single crystals of the sample to examine the local structure of a specific element. XAS is limited by the inability to distinguish between scattering atoms which have a small difference in the atomic number (e.g. C, N, O and Mn, Fe). Another problem of XAS is the attribution of a FT peak to one or to two distances. It is also difficult to determine the coordination number or number of backscatterers of the examined atom. Therefore, it is useful to include known structural information of model complexes in the interpretation of the spectra to narrow the range of possibilities.

2.2.11.2 Experimental procedures

Sample preparation

The preparation of mPSIIcc and dPSIIcc solutions from *T. elongatus* were performed as described in Section 2.2.2. Note, that the here used mPSIIcc was not further purified in a third chromatography step. mPSIIcc and dPSIIcc solutions were dissolved in a buffer

containing 100 mM MES (pH 6.5), 5 mM CaCl₂, and 0.015% βDM. After concentrating to about 15 mM Chla, mPSIIcc and dPSIIcc samples were slowly and stepwise mixed with 100% glycerol to a final concentration of 40% glycerol and 10 mM Chla. Lexan sample holders (inner dimensions: 22 × 3.2 × 0.8 mm³) were evenly filled with 40 μl aliquots of PSIIcc solution.

Sample illumination

In order to maintain a maximal synchronization of the PSII RCs upon flash illumination, the fast recombination reaction of the S₂ and S₃ states with the reduced form of the redox-active tyrosine residue Y_D has to be suppressed. This was achieved through one pre-flash and a following dark-adaptation period of 60 min at room temperature. This procedure synchronizes the PSII RCs into predominantly the S₁Y_D^{ox} state. The electron acceptor PBQ (50 mM in methanol) was added to each sample in a 1:40 ratio right before illumination. Each PSIIcc solution sample was illuminated with zero, one, two, three, four, five, or six flashes at room temperature, with a flash interval of 1.0 s. Cylindrical lenses were used to focus the frequency-doubled Nd:YAG laser (532 nm, 8 nsec pulse-width, 750 mJ/pulse) on a PSIIcc solution sample. After the last flash, samples were frozen immediately (within 1 s) in liquid nitrogen. EPR spectra of the flashed samples were collected to calculate their turnover as described in (179) (detailed results are given in (192)). The samples were then stored at 77 K for further use in the XAS experiments.

Data collection on PSIIcc solution samples

X-ray absorption spectra were collected at beamline BL7-3 of SSRL (Stanford, U.S.A.) using an electron energy of 3.0 GeV and an average current of 300 mA. The intensity of the incident X-rays was monitored by a N₂-filled ion chamber (I₀), which is located in front of the sample. The radiation was monochromatized by a Si(220) double-crystal monochromator. The total photon flux on the sample was limited to 1 × 10⁷ photons per μm². This amount was determined to be non-damaging on the basis of detailed radiation-damage studies of PSIIcc solution samples (116). A shutter, synchronized with the scan program, protected the measured sample from the beam during spectrometer movements between different energy positions. The samples were kept at 8 K in a He atmosphere at ambient pressure by using an Oxford CF-1208 continuous-flow liquid He cryostat. Data were recorded as fluorescence excitation spectra with a germanium 30-element energy-resolving detector (Canberra Electronics). For Mn XAS, the energy was calibrated by the pre-edge peak of KMnO₄ (6,543.3 eV), which was placed between two N₂-filled ionization chambers (I₁ and I₂) after the sample.

The recording of XAS spectra from X-ray damaged dPSIIcc solution samples followed the protocol described in (116). The intactness of each sample was proved prior to data collection by measuring XANES at a low dose (1×10^7 photons/ μm^2) at 10 K. The samples were then exposed at 100 K to X-rays at 13.3 keV. This energy corresponds to the wavelength of 0.933 Å used for diffraction measurements. The X-ray dose and the time required for depositing the dose were varied. After X-ray exposure, the sample was instantly returned to 8 K and the XANES and/or EXAFS spectra were collected at a low dose of 1×10^7 photons/ μm^2 . The XANES spectrum from successive scans was invariant during these measurements. A new sample was used for each exposure at a particular X-ray dose.

Data collection on single mPSIIcc crystals

For polarized XAS measurements on single mPSIIcc crystals, crystals with dimensions of about $0.8 \times 0.6 \times 0.2$ Å were mounted under dim green light on a myla loop (LithoLoops, Molecular Dimensions Limited). After soaking in 28% (w/v) PEG 400 for cryo-protection, crystals were frozen in liquid nitrogen. The experiment was conducted at beamline BL9-3 of SSRL (Stanford, U.S.A.) at a temperature of ~ 10 K. The experimental setup consist of a kappa goniometer (Huber Diffraktionstechnik), a liquid helium cryostream, a 30 element Ge-detector (Canberra Electronics) for collecting XAS-data and a MAR 345 imaging plate detector (Marresearch) for collecting X-ray diffraction data. After pre-orientating one crystal axis parallel to the e-vector of the X-ray beam (by following the morphology of the crystal) one X-ray diffraction image was measured. Based on the obtained diffraction pattern, the orientation of the crystal was judged and corrected if necessary. The XAS spectrum of the well oriented crystal was measured using the 30 element Ge-detector. X-ray diffraction data were collected afterwards with an oscillation of $1^\circ/\text{frame}$ covering ~ 20° (about 20 frames). The crystal was rotated by 90° and a similar set of around 20 frames was collected. The polarized XAS spectra of several mPSIIcc crystals (~ 45 crystals) with either the *a*, *b* or *c*-axis of the crystal lattice oriented parallel to the e-vector of the X-ray beam were measured.

Electron paramagnetic resonance

For the detection of Mn(II), low-temperature X-band EPR spectra were recorded using a Varian E109 EPR spectrometer equipped with a model 102 microwave bridge. The sample temperature was maintained at 20 K by using an Air Products LTR liquid helium cryostat. Spectrometer conditions were as follows: microwave frequency, 9.21 GHz; field modulation amplitude, 32 G at 100 kHz; microwave power, 1 mW; scan range 2000G centered around 3300 G; 2 min/scan, 1 scan/spectrum. Samples of mPSIIcc were

incubated for 45 min in three different conditions: (i) 30% glycerol, (ii) 30% glycerol and 20% PEG 400 and (iii) 30% glycerol and 0.2 M CaCl₂. Lexan sample holders (inner dimensions: 22 × 3.2 × 1.6 mm³) were evenly filled with 80 µl aliquots of mPSIIcc solution with a Chla concentration of 8 – 10 mM.

The XAS experiments were performed in cooperation with the group of V. Yachandra at the Lawrence Berkeley Lab (Berkeley, U.S.A.). The Mn EXAFS curve fits for the k^3 -weighted EXAFS spectra of dPSIIcc solutions in the S₀ to S₃ states (as depicted in Fig. 4.3 (a)) were performed by Junko Yano. The accordant fit data are shown in the Appendix and more detailed fit data are contained in (192). The EPR spectra for the Mn(II) detection were recorded by Jan Kern and Junko Yano.

3. Herbicide binding to dPSIIcc

3.1 Introduction

A wide variety of compounds compete with the native quinone molecules for binding at the Q_B site and, therefore, are able to block the electron transfer from Q_A to Q_B (143, 144). As a consequence, oxygen evolution is slowed down or abolished completely. Binding of these inhibitors with high affinity is a common feature of the Q_B site in both, PSII and pbRC. A very large number of compounds inhibit electron transport in PSII, but only very few substances bind to pbRC. Some of the PSII inhibitors are commercially used as herbicides in agriculture (for review, see (193)) and were divided into two classes: classical and phenolic herbicides. The group of classical herbicides can be subdivided into triazine and urea derivatives. The classification is based on the orientation of the respective herbicide molecule toward different amino acid residues in the Q_B pocket and was introduced by A. Trebst in 1987 (194): Classical urea- and triazine-types orient themselves toward Ser264A and phenolic derivatives orient themselves toward His215A. Frequently used and studied examples for urea, triazine and phenolic derivatives are DCMU (3-(3,4-dichlorophenyl)-1,1-dimethylurea), terbutryn (2-tert-butylamino-4-ethylamino-6-methylthio-1,3,5-triazine) and ioxynil (4-hydroxy-3,5-diiodobenzonitrile), respectively (Fig. 3.1). The electron transfer in pbRC can be inhibited by herbicides of the triazine group.

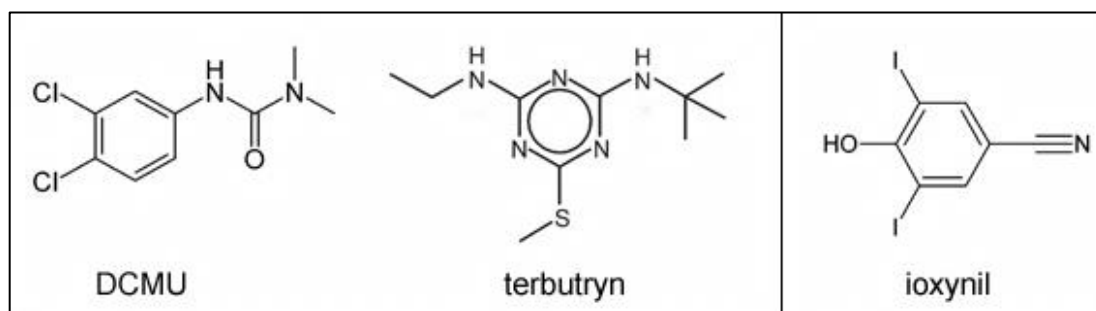


Figure 3.1 Structural formulas of the triazine herbicides DCMU and terbutryn, and the phenolic herbicide ioxynil.

Herbicide binding to PSII is studied for several decades using many different methods. Due to extensive mutational studies at the acceptor side of PSII from various species, it was possible to identify amino acid residues involved in the binding of herbicides (for review, see (143)). These studies show a role of Ser264A in herbicide binding, especially for triazines. Naturally occurring herbicide resistance in higher plants and cyanobacteria, which was first found in atrazine resistant *Amaranthus hybridus* (195), could as well be

attributed to the substitution of the amino acid Ser264A (196). Differential scanning and isothermal titration calorimetry, circular dichroism spectroscopy and oxygen evolution measurements were applied to investigate interactions of herbicides with isolated PSIIcc from *T. elongatus* (197). Zimmermann *et al.* observed differences in the binding parameters for the herbicide classes (197). Phenolic herbicides were found to bind endothermically and destabilize PSIIcc, whereas triazines and urea-type herbicides showed a negative binding enthalpy and tend to stabilize the protein complex. Other studies detected an influence of herbicides on the redox potential of the far located Q_A molecule and, hence, its free energy level (167, 198) (see Sec. 1.3.5). Depending on the type of the applied herbicide, the redox potential of Q_A is shifted to lower or higher potentials. Phenolic herbicides were found to lower the redox potential of Q_A by ~ 45 mV, whereas DCMU (urea-type) increases the potential by ~ 50 mV (167) (see Fig. 1.20). The upshift of the Q_A redox potential observed for DCMU binding seems to be representative for all urea- and also for triazine-type herbicides (167, 199). As pointed out in Section 1.3.5, changes in the redox potential of Q_A correlate with the suppression or stimulation of photoinhibition (35, 200).

Studying herbicide binding to pbRC benefited from structural information obtained through X-ray crystallography. The first structural information of pbRC with bound herbicides was attained in 1986 by Michel *et al.* at a resolution of 2.9 Å (176). For the triazine herbicides atrazine and terbutryn, more detailed descriptions of their interaction with the Q_B site in pbRC became possible at higher resolutions. These structures showed a similar hydrogen bonding pattern for atrazine (2.35 Å resolution, PDB code 5PRC (201)) and terbutryn (2.00 Å resolution, PDB code 1DXR (177)) in the Q_B pocket. The binding of terbutryn to the Q_B site of pbRC is described in detail in Section 3.3.2.

3.2 Single flash-induced Chl a fluorescence in the presence of terbutryn

The herbicide terbutryn has a low solubility in aqueous solution and, therefore, its maximal concentration useable for co-crystallization with dPSIIcc was limited to 1 mM. For the co-crystallization with dPSIIcc, however, it is essential to assure a full saturation of the Q_B binding sites with the herbicide. Thus, the minimal terbutryn concentration necessary for complete inhibition of the electron transfer from Q_A^- to Q_B had to be determined.

In former studies, a Clark-type electrode (181) was used to investigate the inhibition of oxygen evolution in isolated dPSIIcc due to the addition of herbicides (197). As Zimmermann *et al.* observed a high residual activity of dPSIIcc under the applied conditions, the extent of inhibition was suggested to be maximally about 50%

($I_{\max} = (45 \pm 2)\%$) (197). This residual activity was already observed in other studies, but so far its origin remains unclear. It has been discussed whether the high amount of detergent necessary for solubilisation of dPSIIcc leads to a damage of the Q_B binding site, resulting in a reduced possibility for herbicide binding (202). However, this stands in contrast to the similar dissociation constants found for the binding of herbicide to detergent solubilized dPSIIcc and to spinach thylakoid membrane fragments (203). Besides the possible influence of detergent molecules, it was also suggested that the oxygen evolution is maintained due to the artificial electron acceptor 2,6-dichloro-1,4-benzoquinone (DCBQ) (used in (197)). It might be possible that DCBQ is able to capture electrons directly from Q_A and not only at the Q_B binding site (87).

The method of single-flash induced Chl a fluorescence does not require the presence of an artificial electron acceptor and artifacts due to DCBQ do not emerge. In this approach, the variable Chl a fluorescence of dPSIIcc, after excitation with a single laser flash, was detected in the presence of terbutryn. This observable fluorescence derives from the excited state $P680^*$. $P680^*$ can decay by emitting a fluorescence photon on the pico- to nanosecond time scale, a process named prompt fluorescence (PF). The relaxation can also occur radiationless or through fast electron transfer (≤ 1 ps) to the primary electron acceptor $Pheo_{D1}$. The electron transfer reaction to $Pheo_{D1}$ is the predominant decay route of $P680^*$ and leads to the charge-separated state $P680^+ Pheo_{D1}^-$. Within some hundreds of picoseconds, an electron is transferred to the secondary electron acceptor Q_A , leading to the state $P680^+ Q_A^-$. The reduction of $P680^+$ by the redox-active tyrosine Y_Z finally leads to the state $Y_Z^+ Q_A^-$ (nano- to microsecond time scale). Q_A in its reduced form is not able to accept yet another electron. Thus, a RC with Q_A^- remains in the state $P680^+ Pheo_{D1}^-$ when excited by a light pulse. The accumulation of $P680^+ Pheo_{D1}^-$ allows for the recombination of this charge-separated state and the population of $P680^*$ increases. The resultant increase of the fluorescence yield can be related to the part of RC with Q_A^- .

The reoxidation of Q_A^- (formed due to the first single excitation flash) can therefore be observed by following the decay of the fluorescence yield, after excitation by weak probe flashes (183). The reoxidation of Q_A^- is composed of at least three kinetic components ((183) and references therein): (i) within hundreds of microseconds, Q_A^- is oxidized by electron transfer to Q_B or Q_B^- ; (ii) within milliseconds, PQ binds prior to process (i), in RC where no Q_B is initially bound; (iii) within hundreds of milliseconds to seconds, in RC without a terminal electron acceptor, a charge recombination between Q_A^- and the Mn_4CaO_5 cluster takes place. The two faster processes (i) and (ii) are referred to as fast phase.

In the presence of terbutryn, the oxidation of Q_A^- by electron transfer to Q_B is inhibited because of the competitive binding to the Q_B site. Therefore, the time decay of the Chl a

fluorescence is drastically slowed down with increasing terbutryn concentration and is represented by the changes of the amplitude of the fast phase. Figure 3.2 shows the change of the amplitude of the fast phase as a function of the terbutryn concentration. At a terbutryn concentration of 2×10^{-7} M, half inhibition of the electron transfer to Q_B is achieved which is consistent with the oxygen evolution measurements using a Clark-type electrode (197). Above $10 \mu\text{M}$ terbutryn, the fast fluorescence decay drops down to almost zero, indicating a completely blocked electron transfer from Q_A^- to Q_B .

In the crystallization setups 2 mM Chl a concentration, which is equal to 28.6 μM dPSIIcc, is used. Therefore, a terbutryn concentration of 1 mM is sufficient to ensure full saturation of herbicide binding to the Q_B site during crystal growth.

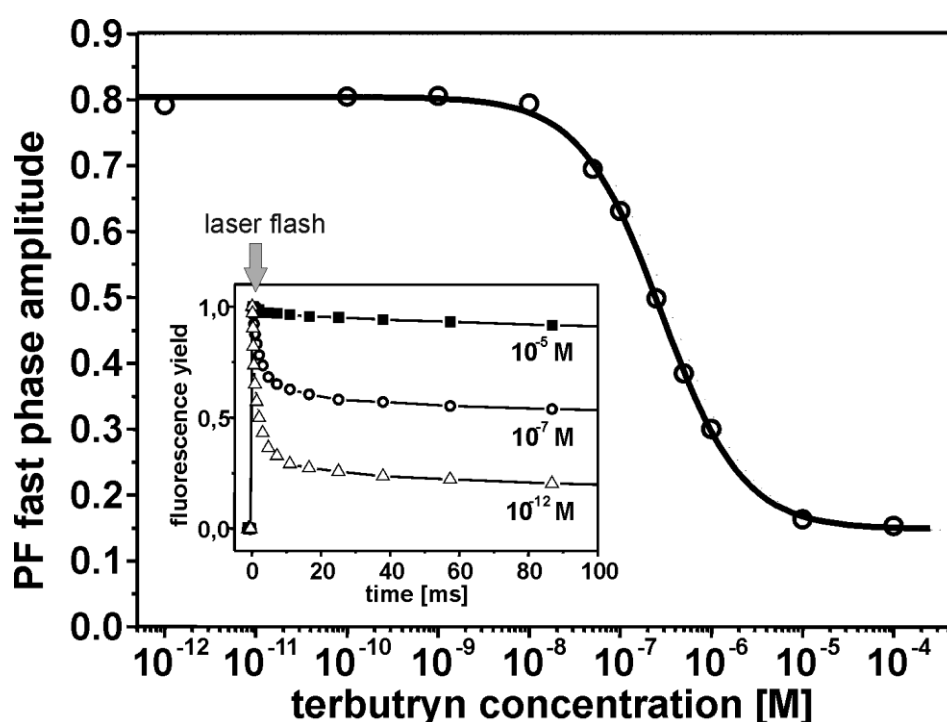


Figure 3.2 Terbutryn titration by flash-induced fluorescence measurements.

The fast phase amplitude of the PF is plotted over the terbutryn concentration (open circles). The solid line represents the fit of the data by a single-site binding function, which shows half-inhibition at a terbutryn concentration of $\sim 2 \times 10^{-7}$ M. The inset illustrates the disappearance of the fast decay phase with increasing terbutryn concentrations.

3.3 Crystal structure of terbutryn-bound dPSIIcc

In order to achieve full occupancy of terbutryn in the Q_B pocket, native dPSIIcc had to be illuminated prior to incubation with herbicide and crystallization. Although the fluorescence measurements (Fig. 3.2) showed that binding of terbutryn to the Q_B site occurs without pre-illumination, we observed that the occupancy in the Q_B site is not sufficient for a reliable crystallographic analysis unless an illumination period was applied (unpublished

data). Exposing native PSIIcc samples to light leads to turnovers of the RC and, therefore, PQ is reduced to PQH₂. PQH₂ is known to possess a lower affinity to the Q_B pocket and may be required to prevent a slow exchange of bound terbutryn against oxidized PQ during the crystallization period. Thus, a full binding of the herbicide becomes feasible. An implication of this result is that PQ competes with terbutryn for binding to the Q_B site or at least disturbs terbutryn binding during the growth phase of the crystals.

3.3.1 Crystallographic analysis

dPSIIcc/terbutryn co-crystals feature the orthorhombic space group P2₁2₁2₁ and the cell constants $a = 126.9 \text{ \AA}$, $b = 225.0 \text{ \AA}$ and $c = 304.9 \text{ \AA}$, which are similar to the native dPSIIcc crystals (22). A full data set was collected and processed to a resolution of 3.2 Å (Table 3). The structure could be solved by the method of molecular replacement (187), using the 2.9 Å resolution model of native dPSIIcc (PDB code 3BZ1, (22)) as search model. The position of one terbutryn molecule in the Q_B site of each monomer was revealed by the difference peaks present in the F_o-F_c map. The positions of these terbutryn molecules in the dPSIIcc could be successfully refined with full occupancy. The atomic coordinates and structure factors have been deposited in the Protein Data Bank (PDB codes 3PRQ and 3PRR).

In the final obtained structure model, it was possible to assign per monomer 20 protein subunits, 35 Chl_a molecules, 25 lipids, 12 β-carotenes, two pheophytins, two heme-groups, the non-heme iron, plastoquinone Q_A and the Mn₄Ca cluster. All of these proteins and cofactors are almost identical to the crystal structure of native dPSIIcc at 2.9 Å resolution (22). In the obtained electron density, additional four DMSO molecules could be assigned: Two are located within a putative oxygen channel (see (92)) and two DMSO molecules reside at the periphery. Note, that terbutryn is dissolved in DMSO and, thus, DMSO molecules are present in the crystallization set-up and can penetrate into the dPSIIcc protein. Besides the seven βDM molecules in the native structure, one extra βDM molecule was found at the periphery of the complex. In the dPSIIcc/terbutryn crystal structure no electron density was observed at the position of the third PQ molecule Q_C (see Sec. 1.3.5). Therefore, it was not possible to model either PQ or terbutryn at this position. Also in contrast to the native dPSIIcc at 2.9 Å resolution, two sites for chloride ions with different occupancies were found close to the Mn₄Ca cluster (described in Sec. 3.3.3).

Table 3 Data collection and refinement statistics.

Data collection for dPSIIcc/terbutryn co-crystals	
Space group	P2 ₁ 2 ₁ 2 ₁
Unit cell parameters	
<i>a</i> [Å]	126.9
<i>b</i> [Å]	225.0
<i>c</i> [Å]	304.9
$\alpha = \beta = \gamma$ [°]	90
Resolution [Å]	50 - 3.2 (3.3 - 3.2) ^a
Measured reflections	711,691
Unique reflections	137,557
$\langle I / \sigma(I) \rangle$	7.76 (2.34) ^a
Redundancy	4.93 (5.07)
<i>R</i> _{sym}	0.129 (0.588) ^a
Completeness [%]	94.1 (90.9) ^a
Refinement	
Resolution [Å]	20 - 3.2 (3.83 - 3.2) ^a
No. of reflections	136,912
<i>R</i> _{work} / <i>R</i> _{free}	26.9/29.9 (46.2/48.6)
Root mean square deviations	
Bond lengths [Å]	0.013
Bond angles [°]	2.2

^aData in the highest resolution shell

3.3.2 Terbutryn binding at the acceptor side

The binding pocket of the mobile cofactor Q_B and the position of Q_B in native dPSIIcc are described in detail in Section 1.3.5. Figure 3.3 illustrates the binding of native Q_B from another view.

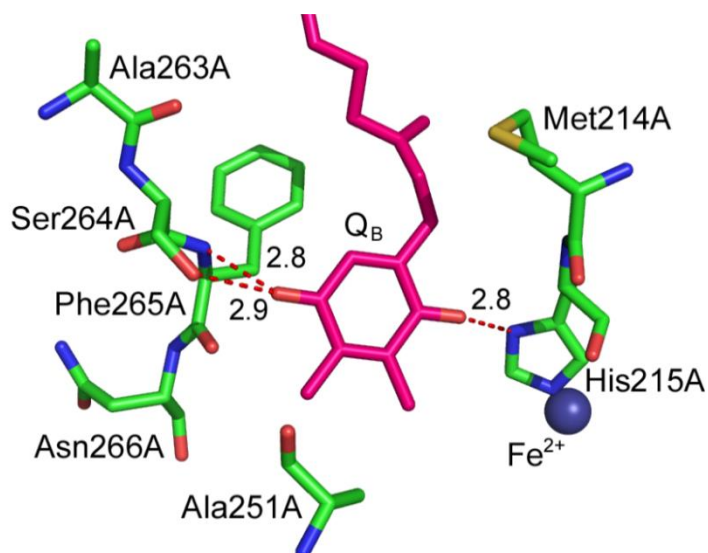


Figure 3.3 Plastoquinone bound to the Q_B site of native dPSIIcc.

Binding of PQ to the Q_B pocket in the crystal structure of native dPSIIcc at a resolution of 2.9 Å (22). PQ molecule is shown in pink, amino acid residues of subunit D1 in green and the non-heme iron as blue sphere. Possible hydrogen bonds between the head group of Q_B and surrounding residues are indicated as red dotted lines; distances are given in Å.

In the dPSIIcc/terbutryn crystal structure, the Q_B pocket is occupied by the inhibitor terbutryn instead of PQ and its binding position partially overlaps with that of the Q_B molecule in native dPSIIcc (Fig. 3.4). The 3.2 Å resolution crystal structure revealed that terbutryn is bound via four potential hydrogen bonds. These bonds could be formed by the three nitrogens of terbutryn at the side pointing away from the non-heme iron (Fig. 3.5 (A)). N5 of the terbutryn ring could form a hydrogen bond with the backbone amide of Phe265A (hydrogen bond distance 3.1 Å), the ethylamino nitrogen with the γ -oxygen of Ser264A (hydrogen bond distance 3.3 Å) as well as with the backbone carbonyl oxygen of Phe265A (hydrogen bond distance 3.2 Å). A fourth hydrogen bond seems to be possible between the *t*-butylamino nitrogen and the carbonyl oxygen of residue Ala263A with a hydrogen bond distance of 4.3 Å. Note here, that the maximum coordinate error of the model is 0.3 Å (as calculated by SFCHECK). The amino acid residues Ser264A and Phe265A are involved in both, PQ and terbutryn binding, whereas His215A does not contribute to the binding of terbutryn (Fig. 3.3 and 3.5).

Moreover, terbutryn binding is also stabilized through non-polar interactions. The aromatic ring of Phe255A is found in close contact to the triazine ring of terbutryn, but no reliable information about the orientation of its ring plane could be obtained due to the limited resolution (Fig. 3.5 (B)). Other non-polar interactions are provided by the residues Met214A and Leu271A, which are in van der Waals distance with the methylthio group of terbutryn.

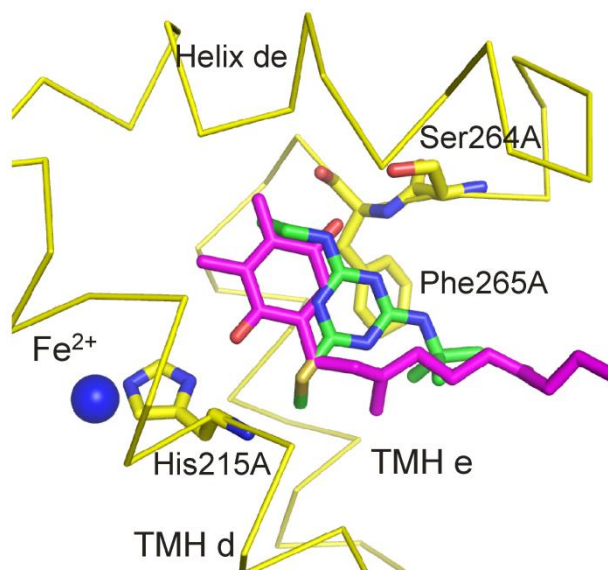


Figure 3.4 Superposition of plastoquinone and terbutryn binding in dPSIIcc.

Superposition of plastoquinone (position according to the structural model of dPSIIcc at 2.9 Å resolution (22)) and terbutryn in the Q_B site of the dPSIIcc/terbutryn crystal structure. PSIIcc subunit D1 is shown as a yellow ribbon with selected amino acids participating in hydrogen bonding. PQ (in pink) and terbutryn (in green) molecules are drawn as sticks and the non-heme iron is shown as blue sphere.

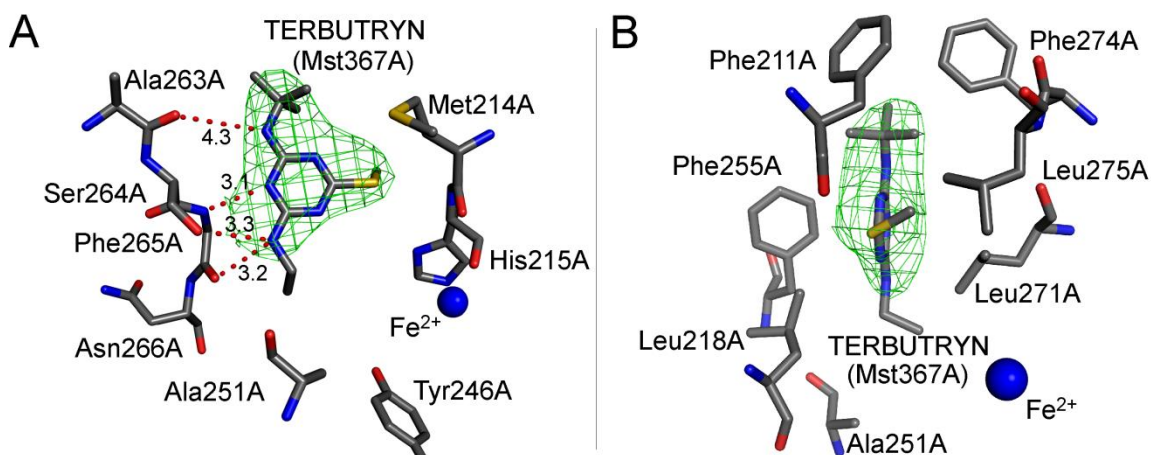


Figure 3.5 Terbutryn binding in the dPSIIcc/terbutryn crystal structure.

Terbutryn bound to the Q_B site of dPSIIcc as derived from the crystal structure at 3.2 Å resolution (PDB codes 3PRQ and 3PRR). Two orientations are shown, viewing either onto (A) or along (B) the ring plane of terbutryn. Terbutryn and the surrounding amino acid residues of subunit D1 are indicated and possible hydrogen bonds between the herbicide and the protein are shown as red dashed lines (distances are given in Å). The electron density of terbutryn is shown as green mesh at a contour level of 1.2 σ . The non-heme iron cofactor is depicted as blue sphere.

Crystal structures of terbutryn bound to pbRC have been published at resolutions of 2.5 Å for *Rhodobacter sphaeroides* (204) and 2.0 Å *B. viridis* (177). In both structures, the terbutryn molecule is bound to the Q_B site via three hydrogen bonds to subunit L (sequence homologous with D1 of PSII, see Sec. 1.3.1). These hydrogen bonds are as well formed by the three nitrogen atoms of terbutryn: N5 of the terbutryn ring, the *t*-butylamino nitrogen and the ethylamino nitrogen (Fig. 3.6 (A)). And the involved amino acid residues of subunit L are: Ile224L (backbone amide, hydrogen bond distance 3.1 Å), Ser223L (γ -oxygen, hydrogen bond distance 3.0 Å) and Tyr222L (backbone carbonyl oxygen, hydrogen bond distance 3.3 Å). Between terbutryn and the non-heme iron, two tightly bound water molecules were assigned, which are also involved in the hydrogen bond pattern that stabilizes the terbutryn binding. One water molecule (W1, see Fig. 3.6 (A)) forms a hydrogen bond with the nitrogen atom N1 of the terbutryn ring and with the δ -nitrogen of the amino acid residue His190L. The other water molecule (W2) is located between W1 and the ϵ -oxygen of the amino acid residue Glu212L, thereby completing the hydrogen bond network. The pbRC-terbutryn complex is probably further stabilized by nonpolar and π - π interactions with the surrounding protein matrix. The aromatic ring of the Phe216L is found to be oriented nearly parallel (14°) to the ring plane of terbutryn (Fig. 3.6 (B)), thereby contributing to the stability of the complex through π - π interaction (177).

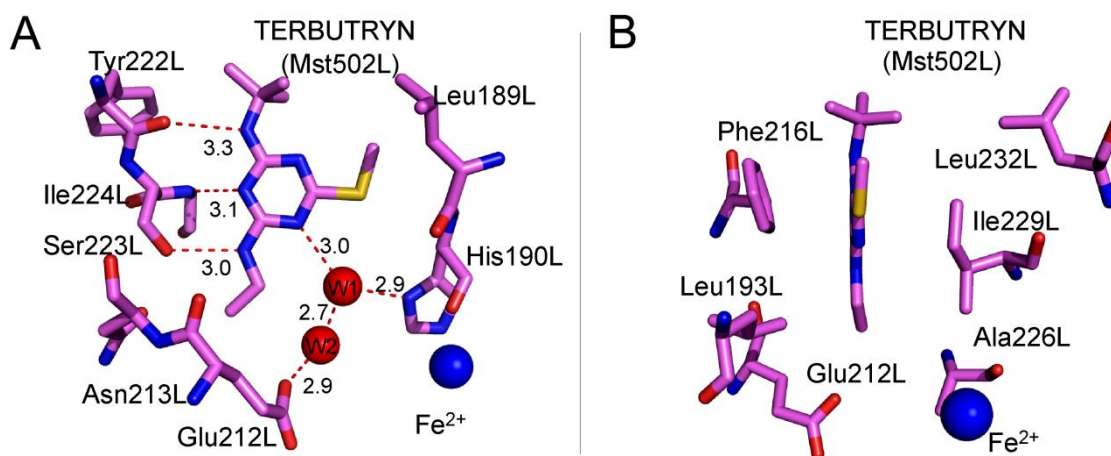


Figure 3.6 Terbutryn binding in the pbRC/terbutryn crystal structure.

Terbutryn bound to the Q_B site of the pbRC from *B. viridis* as derived from the crystal structure at 2.0 Å resolution (PDB code 1DXR (177)). Two orientations are shown, viewing either onto (A) or along (B) the ring plane of terbutryn. Terbutryn and the surrounding amino acid residues of subunit L are indicated, and possible hydrogen bonds between the herbicide and the protein are shown as red dashed lines (distances are given in Å). The non-heme iron and two water molecules (W1 and W2) are depicted as blue and red spheres, respectively.

The Q_B binding pocket of dPSIIcc and pbRC are arranged in a similar manner and therefore show analogies, but also distinct differences concerning the hydrogen bonding

pattern of the herbicide terbutryn. It was already proposed by several groups that Ser264A and Phe265A, which are homologous to Ser223L and Ile224L of pbRC, form hydrogen bonds to the ethylamino nitrogen and the aromatic ring nitrogen, respectively (37, 194, 205). Indeed, the hydrogen bonds to the side chain of the conserved serines (Ser264A and Ser223L) and to the following backbone amide are present in both complexes. The length of the hydrogen bond of the *t*-butylamino nitrogen to the respective backbone carbonyl oxygen (of Ala263A or Tyr222L) is significantly enlarged in dPSIIcc (Fig. 3.5 (A)). This hydrogen bond was already considered by Egner *et al.* (205) by analogy with Tyr222L in pbRC (Fig. 3.6 (A)), but was abandoned after energy minimization. The rather long distance between the backbone carbonyl oxygen of Ala263A and the *t*-butylamino nitrogen (Fig. 3.5 (A)) in our crystal structure suggests indeed no or weak binding at this site. A new result from the dPSIIcc/terbutryn crystal structure is the second possible hydrogen bond partner for the ethylamino nitrogen of terbutryn, provided by the backbone carbonyl oxygen of Phe265A, albeit at suboptimal geometry. This additional binding interaction could compensate for the weaker binding at the *t*-butylamino nitrogen. The changed backbone conformation of Phe265A with respect to its counterpart Ile224L in pbRC could be due to different steric constraints resulting from a variation in the sequence of the amino acid: In PSIIcc, Phe265A is followed by Asn266A, whose side chain provides a hydrogen bond to the phospholipid PG22, while in pbRC, the corresponding Ile224L is followed by Gly225L (not shown in Fig. 3.6 for clarity).

In contrast to pbRC, the *t*-butylamino moiety of terbutryn in dPSIIcc is surrounded by phenylalanine residues (Phe211A, Phe255A, Phe265A and Phe274A, all within a distance of less than 4.2 Å, see Fig. 3.4 and 3.5 (B)). Van der Waals interactions with these groups could contribute to the stabilization of inhibitor binding, also compensating for the rather long and weak hydrogen bond to Ala263A. This idea is supported by mutagenesis studies of *Synechococcus* sp. PCC 7002 as well as *Synechocystis* PCC 6714, where the replacement of Phe211A to the amino acid serine leads to an increased resistance to the herbicide atrazine (143).

Comparing the hydrophobic environment of terbutryn in both RCs revealed that the residues Met214A and Leu271A in PSIIcc replace the pbRC-residues Leu189L and Ile229L. These non-polar groups are of similar size, indicating a comparable steric surrounding.

At a resolution of 3.2 Å it is not possible to detect water molecules and, therefore, no statement can be made about a further stabilization of the dPSIIcc/terbutryn complex by water molecules contributing to the hydrogen bond network. However, there is sufficient space between terbutryn and the side chains of His215A and Tyr246A as well as the backbone of Ala251A to accommodate water molecules in an analogous way to the

pbRC. Since Ala251A is found at a homologous position to Glu212L, Tyr246A is the only amino acid residue that could form a possible hydrogen bond to a putative W2 position in dPSIIcc. According to the Fourier transform infrared (FTIR) studies of Takahashi *et al.* (206), Tyr246A is hydrogen bonded to bicarbonate and is believed to participate in a hydrogen bond network around the non-heme iron.

The 1.9 Å resolution crystal structure of native dPSIIcc (25) allowed the assignment of water molecules, but interestingly the Q_B site is essentially devoid of water molecules and none were found at positions similar to the ones found in the pbRC/terbutryn crystal structure (W1 and W2, Fig. 3.6 (A)) (177). However, there is one water molecule (W1138A) that forms hydrogen bonds, *inter alia*, with Tyr246A (bond length 3.2 Å) and with one oxygen of bicarbonate (bond length 3.2 Å) (207) (Fig. 3.7). The positions of water molecules (for example the position of W1138A), however, might change with the binding of an herbicide molecule as more space could be available or water molecules might be necessary for stabilizing the binding of an herbicide.

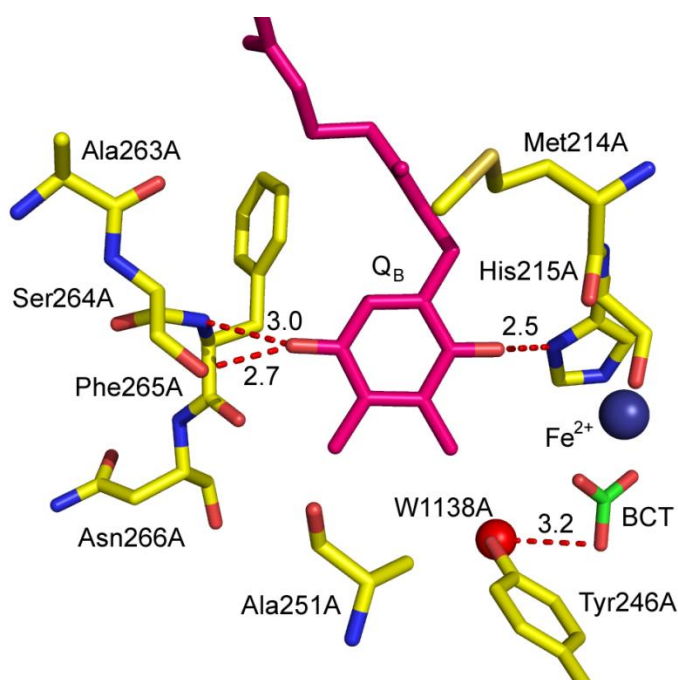


Figure 3.7 Plastoquinone binding in the crystal structure of native dPSIIcc at 1.9 Å resolution.

Binding of PQ to the Q_B pocket in the crystal structure of native dPSIIcc at a resolution of 1.9 Å (25) is illustrated. PQ molecule is shown in pink, amino acid residues of subunit D1 in yellow, bicarbonate (BCT) in green, the non-heme iron as blue sphere and the water molecule W1138A as red spheres. Possible hydrogen bonds are indicated as red dotted line, distances are given in Å. The hydrogen bond between Tyr246A and W1138A is hidden in this view.

The role of bicarbonate at its location, as a bidentate ligand to the non-heme iron and bridging Q_A and Q_B, is not yet clarified. It is assumed, that bicarbonate is involved or

regulates the electron and proton transfer to Q_B . It might also play a role in the release of PQH_2 . For a historical review on the role of bicarbonate see (207). A change in the position of bicarbonate upon herbicide binding would have been an interesting observation. However, at the obtained crystal structure resolution of 3.2 Å, no alternations could be found for the bicarbonate position. As shown in Figure 3.8, the bicarbonate position revealed in the native 2.9 Å dPSIIcc crystal structure (22) is almost identical to the one in the dPSIIcc/terbutryn complex.

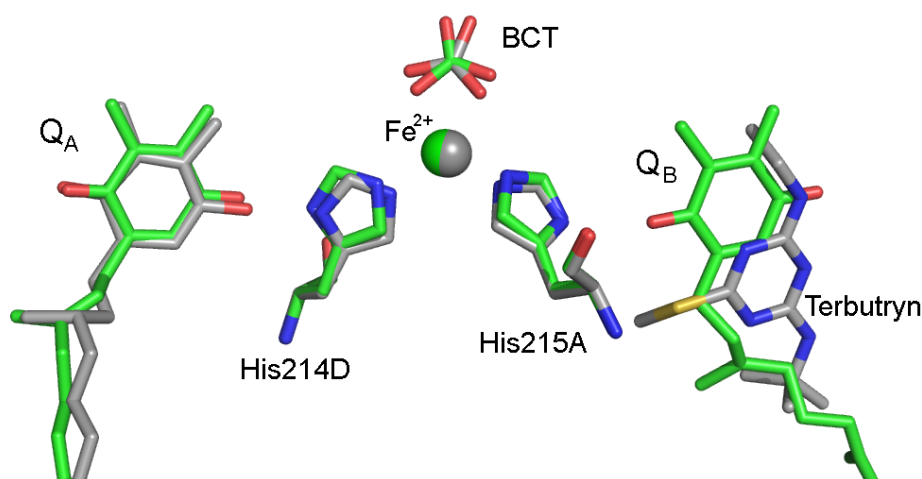


Figure 3.8 Superposition of bicarbonate in the native and terbutryn-bound dPSIIcc crystal structures.

The superposition of the bicarbonate in the native 2.9 Å dPSIIcc crystal structure (in green) (22) and in the 3.2 Å dPSIIcc/terbutryn crystal structure (in gray) is shown. The positions of the two PQ molecules Q_A and Q_B , terbutryn, the non-heme iron (as sphere), the amino acid residues His215A and His214D, and bicarbonate are overlapped.

As herbicide binding to the Q_B site also influences the redox potential of Q_A (see Sec. 1.3.5 and 3.1), the question remains how the different effects of phenolic and classical herbicides are transmitted to Q_A . It was suggested that phenolic herbicides (e.g. bromoxynil and ioxynil) interact directly with His215A instead of Ser264A due to their hydroxyl group (143, 194). Recent results of FTIR studies in combination with density functional theory and docking calculations by Takahashi *et al.* (208) indicate that phenolic herbicides in their deprotonated state are bound to His215A. This strong hydrogen bond between a phenolic herbicide and His215A was proposed to weaken the hydrogen bond between His214D and the carbonyl group of $Q_A^{\cdot-}$ mediated by the non-heme iron (199, 208) (Fig. 3.9 (A)). The decreased hydrogen bond strength between His214D and $Q_A^{\cdot-}$ most likely causes the downshift of the Q_A redox potential. As a consequence, the opposite observed potential shift induced by DCMU and other urea-type herbicides as well as by triazines was ascribed to the lack of a direct hydrogen bond to His215A. For DCMU,

such a binding mode was postulated based on docking calculations using the 2.9 Å resolution structure of dPSIIcc (208). The present crystallographic data of terbutryn binding to dPSIIcc confirms this proposal and, as illustrated in Fig. 3.9 (B), no direct hydrogen bond can be formed between His215A and terbutryn.

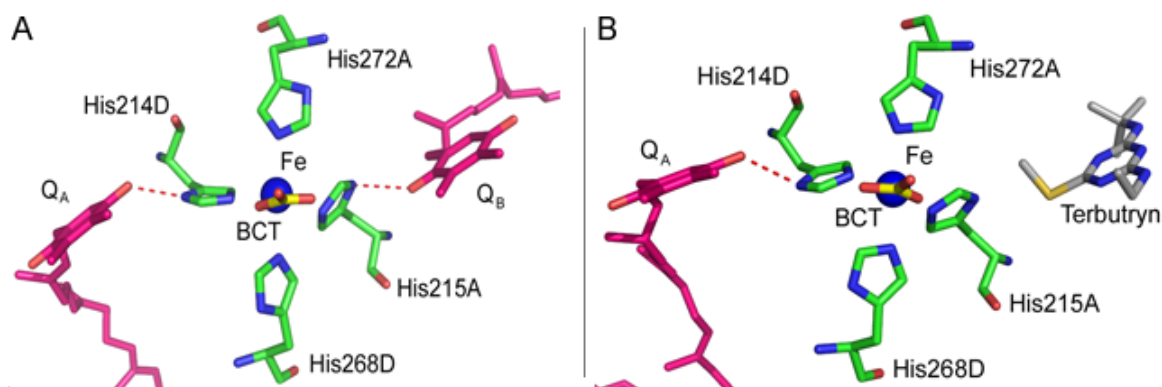


Figure 3.9 The Q_A -His214D-Fe-His215A- Q_B bridge in the native and terbutryn bound dPSIIcc crystal structures.

Top view on the Q_A -His214D-Fe-His215A- Q_B bridge in (A) the native dPSIIcc 2.9 Å resolution structure (22) and (B) the crystal structure of the dPSIIcc/terbutryn complex. PQ molecules are shown in pink, terbutryn in grey, subunits of D1 and D2 in green, bicarbonate in yellow and the non-heme iron as blue sphere. Possible hydrogen bonds are indicated as red dotted lines.

As already mentioned, no terbutryn molecule could be found at the third PQ binding site Q_C , which was also not expected due to its environment. The Q_C site offers no polar contacts for the binding of a quinone head group or terbutryn, contrary to the Q_B pocket (see Sec. 1.3.5). PQ is held in the Q_C site most probably by van der Waals contacts mainly between its isoprenoid chain and surrounding cofactors (Car_{D2} , fatty acids of SQDG4, MGDG7, the isoprenoid chain of Q_B and the phytol chain of Chl_{D2}). Since terbutryn would probably form less van der Waals contacts with this environment, it is unlikely to have a particular affinity to the Q_C binding pocket. The illumination of the samples prior to crystallization could be a reason for the lack of the PQ molecule at the Q_C site. Still, the role of Q_C remains unclear.

3.3.3 Interplay between the acceptor and donor side

The crystal structure of the dPSIIcc/terbutryn complex also revealed new results in respect of the donor side of PSII. Similar to native dPSIIcc at 2.9 Å resolution (22), the metal ions of the Mn_4Ca cluster produce a pattern of high electron density of extended shape in the dPSIIcc/terbutryn structure. However, differences to the native dPSIIcc structures (22, 25) exist with regard to the position of the chloride ion, which is associated with the Mn_4Ca cluster.

3. Herbicide binding to dPSIIcc

As described in Section 1.3.4, the crystal structure of native dPSIIcc at a resolution of 1.9 Å revealed two chloride positions, Cl-1 and Cl-2 (Fig. 3.10 (A)), associated with the Mn_4CaO_5 cluster (25). Cl-1 is located at a distance of 6.7 Å to Mn4 and Cl-2 at a distance of 7.4 Å to Mn2. From these two chloride ions only Cl-1 is consistent with the single chloride position (Cl-1A) found in the native dPSIIcc crystal structure at 2.9 Å resolution (Fig. 3.10 (B)) (22).

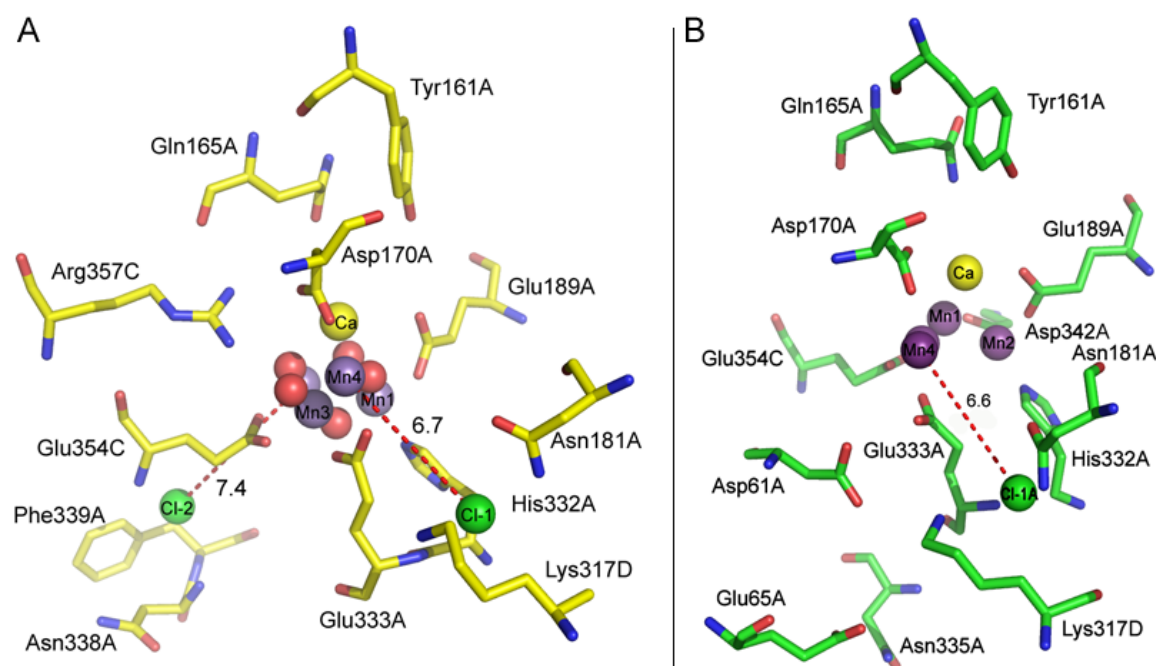


Figure 3.10 Opposition of chloride binding sites in both native dPSIIcc crystal structures.

Chloride positions found according to the (A) native dPSIIcc crystal structure at 1.9 Å resolution (25) and (B) native dPSIIcc crystal structure at 2.9 Å resolution (22). Chloride ions are depicted as green spheres, and positions are labeled Cl-1 and Cl-2 in (A) and Cl-1A in (B), all with occupancy of 100%. Manganese and calcium ions are drawn as purple and yellow spheres, respectively, oxygens as red spheres. Surrounding amino acid residues are shown in yellow (A) and green (B) and are labeled. Distances to Mn2 and Mn4 (red dashed lines) are given in Å.

In the crystal structure of the dPSIIcc/terbutryn complex a patch of electron density is visible at the same location as Cl-1 and Cl-1A and was assigned to a chloride ion, but with an occupancy of only ~ 30% (Cl-1A in Fig. 3.11). Instead, an additional electron density is present in the vicinity (~ 6.7 Å) of this chloride position and is assigned to a chloride ion with an occupancy of ~ 70% (Cl-1B in Fig. 3.11). Other small molecules and ions present in the crystallization buffer were tested as well, but only the assignment to chloride gave reliable results. The minimum distance from Cl-1B to one of the metal ions of the Mn_4Ca cluster was found for Mn4 with ~ 8.7 Å (Fig. 3.11). At this position, the chloride ion is surrounded by the positively charged side chains of Lys317D (3.5 Å, distance to the ϵ -amino-group), Arg334A (3.6 Å, distance to the guanidinium group) and the side chain

amide group of Asn335A (3.9 Å) with the carboxylate groups of Asp61A and Glu65A in close vicinity as well (3.2 Å and 2.8 Å, respectively). The exact orientations of all amino acid side chains cannot be defined within the error limit (0.3 Å) of our structural data and, therefore, it is possible that the amide group of Lys317D occurs in different orientations depending on the respective chloride positions. Taking these uncertainties into account, no indication was found for a changed protein environment at this second putative chloride position (Cl-1B).

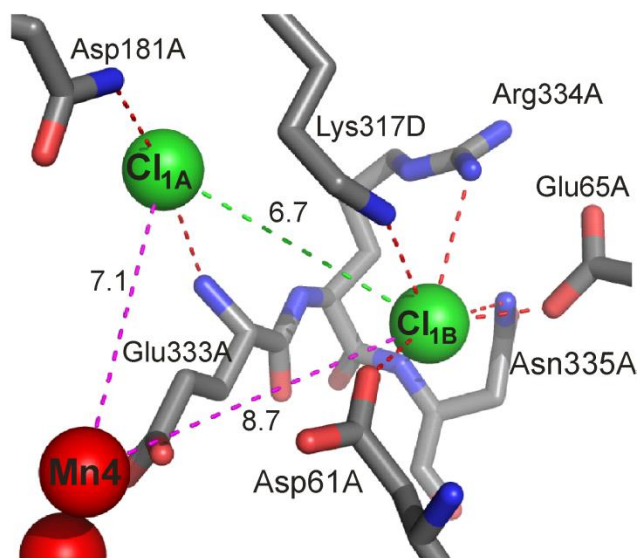


Figure 3.11 Positions of chloride ions in the crystal structure of the dPSIIcc/terbutryn complex at 3.2 Å resolution.

Chloride positions found according to the structural model at 3.2 Å resolution derived from dPSIIcc/terbutryn co-crystals. Chloride ions are depicted as green spheres, and positions are labeled either Cl-1A (occupancy of ~ 30%, corresponding to the chloride position in native dPSIIcc) or Cl-1B (occupancy of ~ 70%). Manganese ions are drawn as red spheres, surrounding amino acid residues are shown in grey and are labeled. Distances between the chloride positions (green dashed line) and to Mn4 (pink dashed lines) are given in Å. The dashed red lines indicate possible interaction of the anions with the surrounding amino acids (distances are given in the text).

This pronounced patch of electron density at Cl-1B is absent in the electron density map of native dPSIIcc at 2.9 Å resolution. Figure 3.12 shows a comparison of the chloride binding sites revealed in the dPSIIcc/terbutryn complex and the native dPSIIcc crystal structure at 2.9 Å resolution (22).

Also, the second chloride Cl-1B is different from the second site found in the 1.9 Å structure and is located closer to Mn4 (distance of 8.7 Å). In contrast, we found no electron density at the Cl-2 site, which could be a result from variations in the preparation procedures (as outlined in Section 1.3.7). Figure 3.13 shows a comparison of the chloride binding sites in the dPSIIcc/terbutryn complex and the native dPSIIcc crystal structure at

3. Herbicide binding to dPSIIcc

1.9 Å resolution (25). So overall, we found a third possible chloride binding site in the vicinity of the Mn_4Ca cluster.

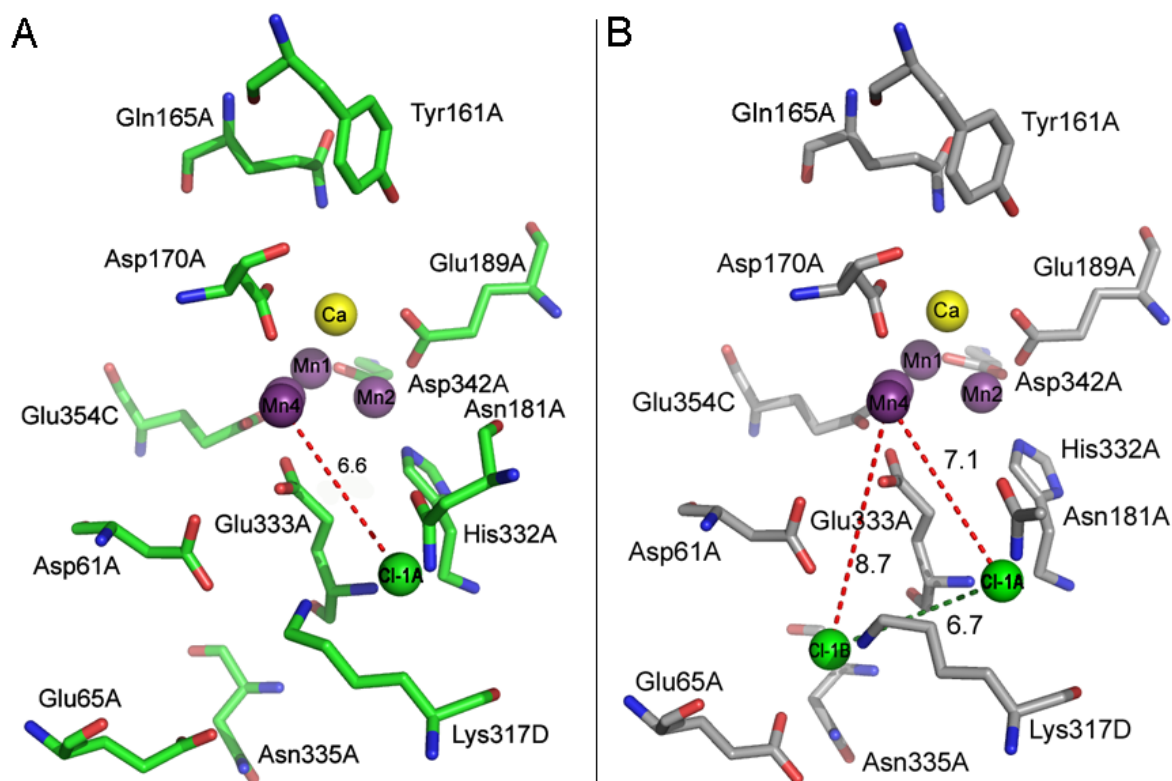


Figure 3.12 Opposition of chloride binding sites in the native dPSIIcc (2.9 Å resolution) and in the dPSIIcc/terbutryn crystal structure.

Chloride positions found according to the (A) native dPSIIcc crystal structure at 2.9 Å resolution (22) and (B) dPSIIcc/terbutryn crystal structure at 3.2 Å resolution. Chloride ions are depicted as green spheres, and positions are labeled either Cl-1A (occupancy of 100% in native structure and of ~ 30% in the terbutryn-bound structure) or Cl1-B (occupancy of ~ 70%). Manganese and calcium ions are drawn as purple and yellow spheres, respectively. Surrounding amino acid residues are shown in green (A) and grey (B) and are labeled. Distances to Mn4 (red dashed lines) and between the chloride positions (green dashed line) are given in Å.

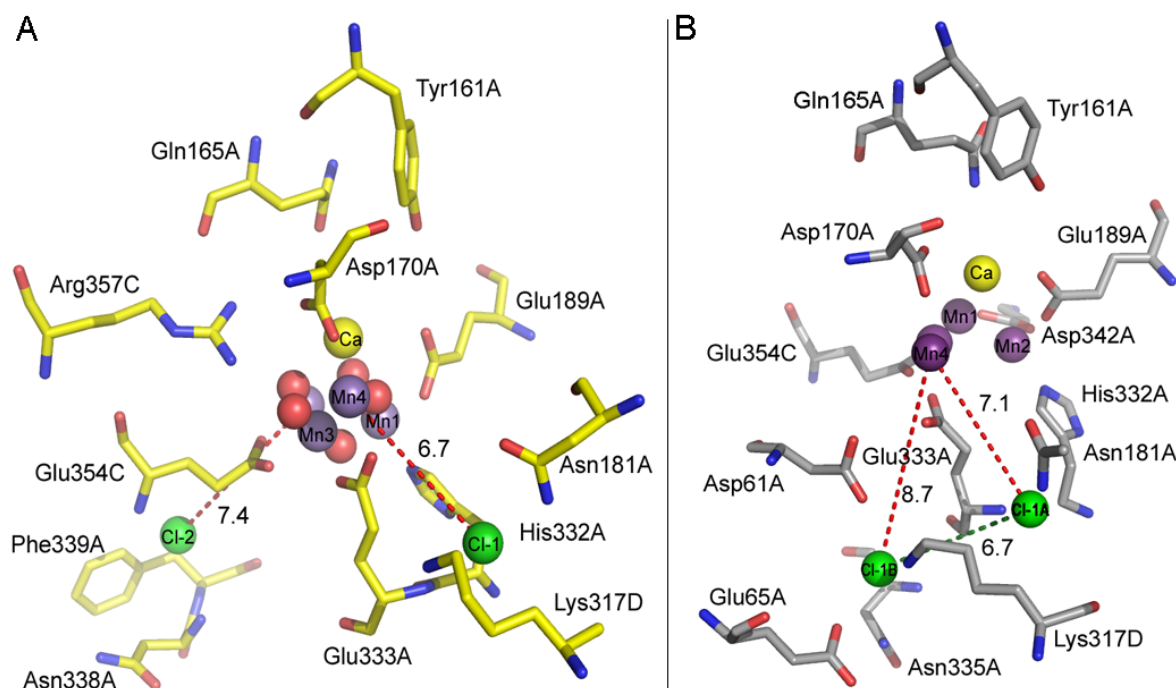


Figure 3.13 Opposition of chloride binding sites in the native dPSIIcc (1.9 Å resolution) and in the dPSIIcc/terbutryn crystal structure.

Chloride positions found according to the (A) native dPSIIcc crystal structure at 1.9 Å resolution (25) and (B) dPSIIcc/terbutryn crystal structure at 3.2 Å resolution. Chloride ions are depicted as green spheres, and positions are labeled Cl-1 and Cl-2 in the native structure (occupancies of 100%), and Cl-1A (occupancy of ~ 30%) and Cl-1B (occupancy of ~ 70%) in the terbutryn-bound structure. Manganese and calcium ions are drawn as purple and yellow spheres, respectively, oxygens as red spheres. Surrounding amino acid residues are shown in yellow (A) and grey (B) and are labeled. Distances to Mn2 and Mn4 (red dashed lines) and between the chloride positions (green dashed line) are given in Å.

The finding of one fully occupied chloride binding site (Cl-1A) in the native *T. elongatus* dPSIIcc crystal structure at 2.9 Å resolution (22) and two binding sites (Cl-1A, Cl-1B) with occupancies of ~ 30% and ~ 70% in the *T. elongatus* dPSIIcc/terbutryn structure leads to the following interpretation: Cl-1A and Cl-1B represent two different positions of one chloride ion.

Regarding the different experimental treatments of the native and the terbutryn-bound dPSIIcc, there are two possible reasons for this position change of the chloride: (i) The illumination of the dPSIIcc sample prior to addition of terbutryn or (ii) the incubation with terbutryn in the dark. Our fluorescence measurements showed that most of the RCs contain a reducible Q_B and thus, exposure to light will cause at least one turnover of the Mn_4Ca cluster. Nevertheless, the subsequent dark adaptation period of 120 min likely allows for a relaxation in the S_1 state (about 40 min), even in the presence of terbutryn (209). This makes it very unlikely, that the observed shift of the chloride positions is

caused by redox state changes of the Mn_4Ca cluster (note, changes in structure of the Mn_4Ca cluster cannot be seen at this resolution). Hence, it seems that binding of terbutryn to the Q_B pocket at the acceptor side, affects the chloride position at the donor side. A structural linkage of these two functional areas in PSII was already proposed by Krieger-Liszkay *et al.* (200) as a result of the observed shift of the redox potential of the primary plastoquinone Q_A after depletion of Ca^{2+} from the Mn_4CaO_5 cluster.

The idea of chloride movement is also supported by former studies on PSII from spinach. Chloride binding was investigated by the use of radioactive $^{36}Cl^-$ and the presence of one chloride ion per Mn_4CaO_5 cluster was suggested (210), whereas this chloride was found to bind in two different modes. One mode represents high-affinity binding with a slow exchange rate and the other mode represents low-affinity binding with a high exchange rate. Interconversion between these two modes was found to be faster than exchange at the high-affinity site. This result was interpreted with two alternative models: a “one-site two-state” model (210) or a “two-site” model (135). The present structural data supports the “two-site” model with the suggestion of two binding sites for one chloride ion, between which this anion can move.

The role of a moving chloride ion is presently unknown, but looking at the location of Cl-1B gives a possible idea. The newly assigned chloride position Cl-1B is found to be shifted closer to the side chains of Asp61A and Glu65A (shortest distances are 3.2 Å and 5.63 Å, respectively) (Fig. 3.11). These two residues are discussed to be involved in the transfer of protons (211-213) and are located in the possible water permeation channels 1 and 3 (128), and in the putative “static” proton channel C (92) (see Fig. 3.14, and Sec. 1.3.4). The side chain of Asp61A is located in a critical position between the Mn_4CaO_5 cluster and the chloride binding sites, as it is the first residue which leads from the OEC to the luminal side of the membrane. The protonation state of Asp61A can be changed by hydrogen bonding and electrostatic interactions with the nearby amino acid residues Lys317D and Glu333A. It was proposed by Pohkrel *et al.* (138) that in the absence of chloride, salt bridges are formed between protonated Lys317D and the nearby carboxylate residue of Asp61A, and additionally or alternatively to Glu333A. An electrostatic interaction of Lys317D and Asp61A can cause a conformational change of Asp61A, thereby lowering its pK_a and making it an inefficient proton transferer during the catalytic cycle. Additionally, a conformational change of residue Asp61A was found to block the water permeability through a channel leading from the OEC to the lumen (128). Thus, it was suggested, that the breaking of the salt bridges between Lys317D and Asp61A and/or Glu333A is the role of chloride (137, 138). The in our study revealed two binding positions for one moving chloride can be brought into good agreement with the alternative existence of these two salt bridges. The chloride binding site Cl-1A would thus be

responsible to hinder the salt bridge between Lys317D and Glu333A, whereas Cl-1B can break the salt bridge between Lys317D and Asp61A (see Fig. 3.11 and 3.14). In that way, chloride movement during the S state cycle could control the conformation and protonation states of Asp61A and Glu333A and thereby regulate the proton transfer.

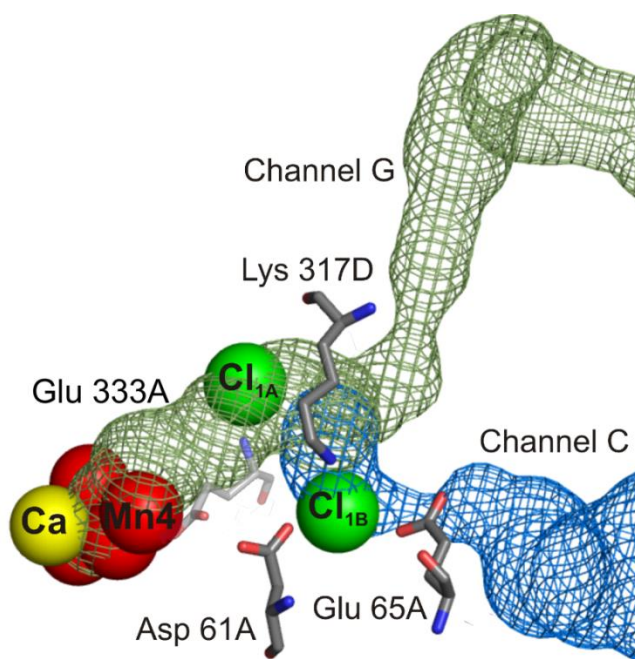


Figure 3.14 Chloride positions found according to the dPSIIcc/terbutryn crystal structure relative to calculated channels leading from the Mn_4Ca cluster to the lumen.

Arrangement of metal and chloride ions as well as the amino acids residues Asp61A, Glu65A, Glu333A and Lys317D according to the dPSIIcc/terbutryn structural model at 3.2 Å resolution, relative to the “static” channels C and G (92) calculated on the basis of the 2.9 Å resolution model of native dPSIIcc (22). Chloride, manganese and calcium ions are depicted as green, red and yellow spheres, respectively. The calculated trajectories of the channels are drawn as meshes (channel C colored blue, channel G colored green). Note, that the exact orientations of all amino acid side chains cannot be defined within the error limit (0.3 Å) of the structural data and, depending on the chloride position, different orientations of the side chains are possible.

3.4 Summary

In this work, the first X-ray crystal structure of a complex of dPSIIcc and the triazine-type herbicide terbutryn could be obtained with a resolution of 3.2 Å. A full occupancy of the Q_B pocket with the herbicide is necessary to get reliable data. This could be achieved through pre-illumination of the dPSIIcc samples. The consequential reduction of the native PQ substrate facilitated full binding of terbutryn to the Q_B site. The co-crystallization of dPSIIcc with terbutryn revealed information of great interest concerning the acceptor and also the donor side, even though no improvement in the crystal structure resolution was achieved.

The crystals of the dPSIIcc/terbutryn complex possess the same space group and cell parameters as the native dPSIIcc crystals (22). Only little differences concerning the proteins and cofactors of the dPSIIcc/terbutryn crystal structure were observed: four additional DMSO molecules, one additional β DM molecule, no electron density at the position of Q_C and two positions for chloride ions with different occupancies.

In earlier structural studies on PSIIcc inhibition by herbicides, homology modeling based on a comparison with the pbRC had to be used (176). Theoretical models employing energy-minimization techniques predicted the interaction between triazine derivatives and the Q_B site in PSIIcc at considerable detail (178, 205, 214, 215). In accordance with these theoretical models and in analogy to pbRC, our new structural information revealed that terbutryn forms at least two hydrogen bonds to the protein: N5 of the terbutryn ring with the backbone amide of Phe265A (hydrogen bond distance 3.1 Å) and the ethylamino nitrogen with the γ -oxygen of Ser264A (hydrogen bond distance 3.3 Å). Terbutryn was found not to interact directly with the amino acid residue His215A, which is a ligand to the non-heme iron. This result supports proposed models to explain the effect of herbicide binding to the Q_B site on the redox potential of Q_A .

Another important result of the present work is the identification of an additional and new chloride binding position close to the Mn_4Ca cluster suggesting mobility of the Cl^- cofactor. The different chloride positions might function as an alternating barrier to prevent or allow the formation of salt bridges between either Lys317D and Asp61A, or Lys317D and Glu333A. Therefore, a role of chloride in the regulation of proton transfer becomes very likely.

The finding of changes at the donor side as a consequence of a modification at the acceptor side supports the assumption of an interplay between the two functional sites of PSIIcc. How changes at one site are transmitted to the other side is a challenging task for future investigations (see Chapter 5).

4. X-ray absorption spectroscopy on PSIIcc

XRD crystallography on membrane proteins at high resolutions provides first essential insights into the protein structure on a molecular level. However, XRD crystal structures present a static picture of the investigated protein complex. In the case of PSII, it is important to additionally perform dynamic studies in order to unravel and understand the complete mechanism of the water splitting reactions. These studies should investigate the five-step catalytic cycle (S state transitions, see Fig. 1.10) that couples the one-electron photochemistry at the PSII RC with the four-electron redox process at the OEC (see Sec. 1.3.4). The formation of oxygen is a highly studied topic and it is believed that the key step of O-O bond formation occurs at the S_4 oxidation state level. But in contrast to the S_0 to S_3 states, the S_4 state is highly reactive and instable. Thus, the elusive S_4 state and has not yet been experimentally verified or characterized in a conclusive manner (see Sec. 1.3.4) (73, 101, 105, 216-218).

To understand the mechanism of water oxidation, it is essential to gain information about the distances between the atoms of the Mn_4CaO_5 cluster within a resolution of 0.1 Å. With this information, the Mn oxidation states, the type of the Mn-Mn and Mn-Ca bridging ligands and also the protonation state of these bridges as present in the Mn_4CaO_5 cluster can be identified. Also, structural changes of the Mn_4CaO_5 cluster during the S state transitions can be revealed. Distance changes within the Mn_4CaO_5 cluster can reflect several chemical parameters: Mn oxidation state changes, protonation state changes of bridging oxygens, ligation mode changes (e.g. bidentate/monodentate), as well as fundamental changes in the cluster geometry (i.e. dimeric, trimeric, or cubane-like structure).

XAS is a technique which allows the determination of the local geometric and electronic structure of the investigated sample with a high accuracy (~ 0.02 Å), without interference from absorption by a protein matrix, water or air (190). The clear advantage of using the technique of XAS for the investigation of the structure of the multi-nuclear metal cluster Mn_4CaO_5 in the OEC of PSII is the avoidance of radiation damage to the metal cluster (described in Sec. 1.3.4). This is due to the two to three orders of magnitude lower required X-ray dose compared to the dose used in XRD crystallography. Additionally, the reduction to Mn(II) can be monitored and controlled constantly by the observation of the K-edge position. Another important advantage of XAS is the obtainment of structural information around the Mn_4CaO_5 cluster even from solution samples. Polarized XAS studies on ordered samples like membranes and single crystals, however, can increase the obtainable information due to a distinct observable dichroism (see Sec. 4.5). Dichroism describes the dependence of the light absorption intensity on the polarization of

the light rays and provides information on the relative orientation of interatomic vector directions. Limitations of the XAS method are described in Section 2.2.11.1.

4.1 Previous X-ray absorption spectroscopy on PSII

Several approaches have been used to study the structure of the Mn_4Ca cluster using XAS. Mn XAS was performed on spinach thylakoid membranes and structural changes associated with transitions between the S states of the catalytic cycle of the water splitting reaction could be observed (179, 219). In both studies, it was shown that Mn oxidation occurs during the S_0 to S_1 and S_1 to S_2 state transitions based on K-edge shifts of 1 – 2 eV in the XANES spectra. In the study by Messinger *et al.* (179), a much smaller edge shift was observed during the S_2 to S_3 state transition, accompanied by a change in the edge shape. These findings were interpreted as an oxidation event occurring at an atom different to Mn (see next section). In contrast, Haumann *et al.* (219) proposed a Mn-centered oxidation during the S_2 to S_3 state transition. The differences of these studies most likely arise from variations in the applied deconvolution procedure and the method used to determine the edge positions. XAS spectra of spinach thylakoid membranes were also collected at the Ca K-edges (220) and the Mn and Sr K-edge of samples in which Ca was substituted by Sr (221-223). The presence of two to three Mn-Ca interactions at 3.4 Å was reported. Ca XAS on each S state is important to obtain detailed information about changes of Mn-Ca interactions in the Mn_4Ca cluster. However, it is quite ambitious to collect Ca XAS data on PSII as it is difficult to avoid contamination with Ca during the sample preparation and the data collection, and the higher absorption coefficient of Ca at its absorption energy (4,050 eV) leads to faster radiation damage. Therefore, Sr XAS measurements (Sr K-edge energy is 16,200 eV) on Sr-substituted PSII samples is a very useful method to obtain an idea of the distances and number of Ca-Mn interactions. Spinach thylakoid membranes in which chloride was substituted by bromide were investigated at the Br K-edge by (224) and it was found, that in the S_1 state the halide cofactor is neither a ligand to Mn nor to Ca and consequently the Mn-complex is not a manganese–calcium–chloride complex. The Mn EXAFS data of isotropic PSII samples can be brought into agreement with a large number of topological models of the Mn_4Ca cluster (for review see (225, 226)). The use of oriented samples such as oriented spinach thylakoid membranes and single PSIIcc crystals, however, are of high advantage to reduce the ambiguity: Namely, the EXAFS amplitude is orientation dependent and proportional to $\sim \cos^2\theta$, with θ being the angle between the electric field vector of the polarized X-ray beam and the absorber-backscatterer vector. A first refinement of the structure and geometry of the Mn_4Ca cluster was achieved by polarized EXAFS studies

on single crystals of dPSIIcc from *T. elongatus* in the S_1 state (227) in combination with the structural data from the dPSIIcc XRD model at 3.0 Å (21). The study by Yano *et al.* (227) proposed three alternative but similar models (I, II (IIa) and III) for the Mn_4Ca cluster in the S_1 state (Fig. 4.1). The models were placed into the 3.0 Å resolution crystal structure (21) by using information concerning the relative position of Ca and Mn ions from anomalous X-ray diffraction and the overall shape of the electron density.

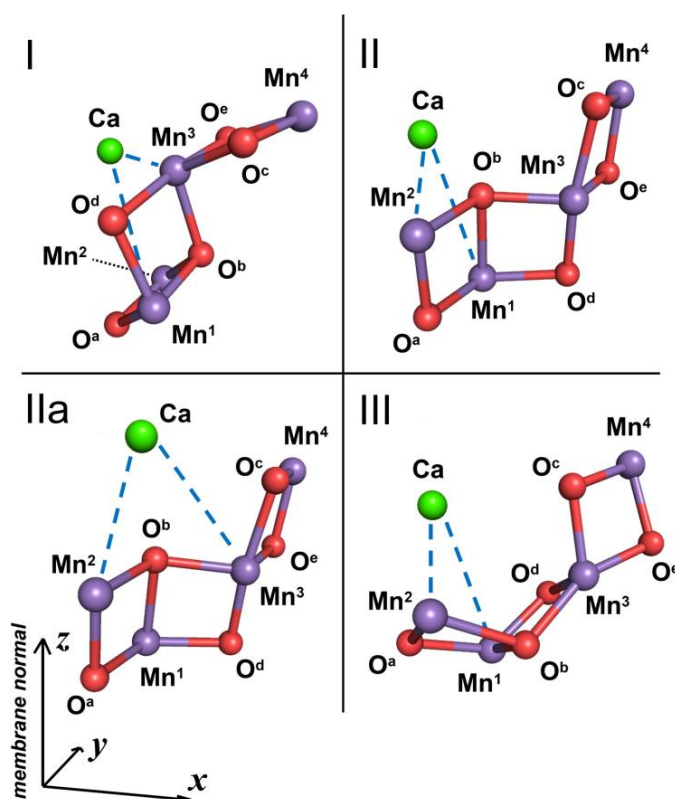


Figure 4.1 Proposed models of the Mn_4Ca cluster in the S_1 state.

Three alternative models for the Mn_4Ca cluster in the S_1 state were proposed in 2006 by Yano *et al.* based on polarized EXAFS measurements on single dPSIIcc crystals from *T. elongatus* (227). A modified version of the three models I, II (IIa) and III in the S_1 state is shown. Manganese, oxygen and calcium atoms are depicted as purple, red and green spheres, respectively. Figure adapted from (102).

The various EXAFS studies have commonly suggested that in the S_1 state there are three short Mn-Mn interactions around 2.7 Å, one long Mn-Mn interaction at around 3.3 Å, and two to three Mn-Ca interactions (based on the Sr XAS study (223, 228)) at around 3.4 Å. However, as pointed out in Section 2.2.11.1, for the interpretation of EXAFS data known structural information of the Mn_4Ca complex are important to reduce the range of possibilities. The limited knowledge about the accurate geometry of the Mn_4Ca cluster makes it difficult to correlate the spectroscopic EXAFS data to the structural changes of the cluster. So far, spinach thylakoid membranes were used for the EXAFS studies on the

catalytic S state cycle, whereas most of the XRD studies were performed with crystals of PSIIcc purified from the thermophilic cyanobacteria *T. elongatus* and *T. vulcanus* (22, 25, 48, 179). A structural model of spinach PSII crystals has not been reported, yet. Incorporating structural data of XRD on cyanobacterial PSIIcc crystals into EXAFS data obtained from spinach thylakoid membrane fragments, however, is not ideal due to possible variations in the inorganic catalytic cluster between these organisms (see Sec. 4.4).

4.2 Structural changes of the Mn_4CaO_5 cluster during the catalytic S state cycle

In the present XAS study, *T. elongatus* dPSIIcc preparations, the same solution samples which have been used for crystallography, are used for the first time to study the structural changes that occur during the S state transitions. A further innovation became possible through the high-resolved geometry of the OEC structure (with a limited effect of radiation damage; see Sec. 1.3.4) revealed by the recent XRD crystal structure of dPSIIcc at 1.9 Å resolution (25). In the here presented study, this more detailed OEC geometry (25) is used for the first time as the basis to interpret the obtained S_1 state EXAFS data of dPSIIcc solution samples. The EXAFS parameters obtained from the S_1 state are utilized in turn for the analysis of the other S states (S_0 , S_2 and S_3).

Changes in the XANES and EXAFS spectra

The XANES spectra of dPSIIcc solutions from S_0 to S_3 states show, that the K-edge position shifts to higher energies during the S_0 to S_3 state transitions (Fig. 4.2, top panel). Differences in the absorption edge energy are attributed to the oxidation of Mn. In the field of XAS, the inflection point of the rising Mn K-edge (electron transitions from 1s to 4p, Fig. 2.3 (B)) is used as an indicator of the oxidation state. The zero-crossing of the second derivative of the XANES spectra provides the inflection point energy (IPE), which quantifies the K-edge position of each S state. The second derivative spectra of the S_0 to S_3 state XANES spectra are depicted in Figure 4.2 (bottom panel) and the IPEs are 6,550.94 eV for S_0 , 6,553.45 eV for S_1 , 6,554.12 eV for S_2 , and 6,554.40 eV for S_3 . It was shown in detailed model compound studies, that a Mn oxidation through one electron in a set of Mn model compounds with similar ligands shifts the IPE by 1 - 2 eV toward higher energies (229). The XANES K-edge energy shift occurring during the S_0 to S_1 and S_1 to S_2 state transitions is 2.51 and 0.67 eV, respectively. Thus, these K-edge shifts are ascribed to the oxidation of Mn atoms during the S_0 to S_1 and S_1 to S_2 state transitions. A much smaller shift is observed during the S_2 to S_3 state transition (0.28 eV) and is accompanied

by a change in the edge shape. The observed K-edge energy shifts during the S_0 to S_3 transitions are similar to that observed in spinach thylakoid membrane fragments (179). In the study by Messinger *et al.* (179), the interpretation of these observations was that the chemical changes happening during the S_2 to S_3 state transition are different from that of the S_0 to S_1 and S_1 to S_2 state transitions. This could be explained with the oxidation of oxygen ligands instead of Mn atoms during the S_2 to S_3 state transition. However, changes in the XANES K-edge position and shape could be more complex when structural changes within the Mn_4CaO_5 cluster occur during this transition as well. For example, it was shown by Haumann *et al.* that a small variation in the edge position and shape could appear when the coordination state of one Mn atom increases from five to six (219). A similar observation has been proposed in a model by Siegbahn in which oxygen binds to the five-coordinated Mn atom at the S_2 to S_3 state transition, leading to a six-coordinated Mn (108). In any case, the structural changes observed in the S_2 to S_3 state transition are more substantial compared with other S state transitions (see discussion part below).

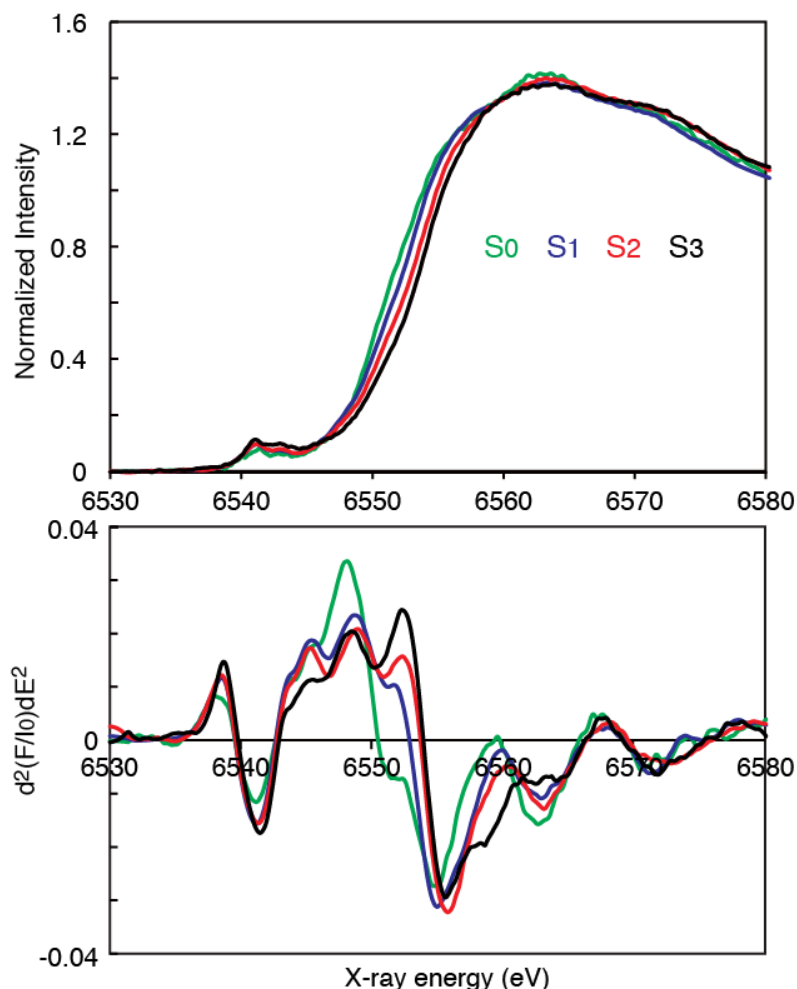


Figure 4.2 XANES spectra of dPSIicc solution samples in the S₀, S₁, S₂, and S₃ states.

Mn XANES (top) spectra and their second derivative (bottom) of dPSIicc solution samples in the S₀ (green line), S₁ (blue line), S₂ (red line) and S₃ (black line) states are shown. The XANES inflection point energies, provided by the zero-crossing of the second derivative spectra, are 6,550.94 eV for S₀, 6,553.45 eV for S₁, 6,554.12 eV for S₂ and 6,554.40 eV for S₃.

Figure 4.3 depicts the k^3 -weighted EXAFS spectra and its FT spectra of dPSIicc solution samples in the S₀ to S₃ states. During the S state transitions, the phases as well as the amplitudes of the k^3 -weighted spectra undergo changes (Fig. 4.3 (a)). An increase in the EXAFS oscillation frequency is visible in the S₂ to S₃ state transition in the higher k -space (region between 8 - 12 Å⁻¹). Due to the interference phenomena of the outgoing and backscattered photoelectron wave (Fig. 2.4), the EXAFS oscillations are related to the interatomic distances (191). An increase in the oscillation frequency means longer distances between the scatterer and backscatterer atoms. Hence, the observation of an increased EXAFS oscillation frequency in the S₃ state suggests the increase in some of the predominant scatterer-backscatterer distances during the S₂ to S₃ state transition. This finding was also reported in an earlier EXAFS study using spinach thylakoid membrane fragments (230). The positions of the three peaks (labeled I, II and III) in the FT spectra

(Fig. 4.3 (b)) correspond to the coordination shells of the backscatterers which are located at different distances from the absorbing Mn atom. Peak I derives from Mn-ligand interactions (Mn-O, Mn-N) at a distance of about 1.9 Å, peak II is mainly from di- μ -oxo-bridged Mn-Mn interactions with about 2.7 Å distance, and peak III comes from mono- μ -oxo-bridged Mn-Mn as well as from Mn-Ca interactions at distances of about 3.3 Å and 3.4 Å, respectively (see also Fig. 2.3 (C)). Several changes in the FT peak positions and intensities can be seen during the S state transitions (Fig. 4.3 (b)). Upon S_0 to S_1 state transition, the positions of peak I and II are shifted toward shorter distances (blue line, Fig. 4.3 (b)). This peak position shifts indicate a shortening of the Mn-ligand and the Mn-Mn distances during the S_0 to S_1 state transition. In the S_1 to S_2 state transition no peak shift is visible, whereas the peak intensity increases in peak I and II (red line, Fig. 4.3 (b)). In the S_2 to S_3 state transition, peak II shifts toward a longer distance and, additionally, the peak III region splits into two peaks (black line, Fig. 4.3 (b)). In the peak III region, the Mn-Ca EXAFS peak at about 3.4 Å is concealed by the presence of Mn-Mn interactions in the same region. Therefore, it would be ideal to additionally collect Ca XAS data on each S state to obtain detailed information about the Mn-Ca interactions. As described earlier (Sec. 4.1), however, Ca XAS on PSII samples is a challenging task. Hence, the information from a previous Sr EXAFS study (223) was used in this study to estimate the distances and the number of Ca-Mn interactions that contribute to Mn EXAFS at the peak III region. Note, that the more or less pronounced shoulder of peak I in all S state FT-amplitude spectra is a measurement artifact (Fig. 4.3 (b)).

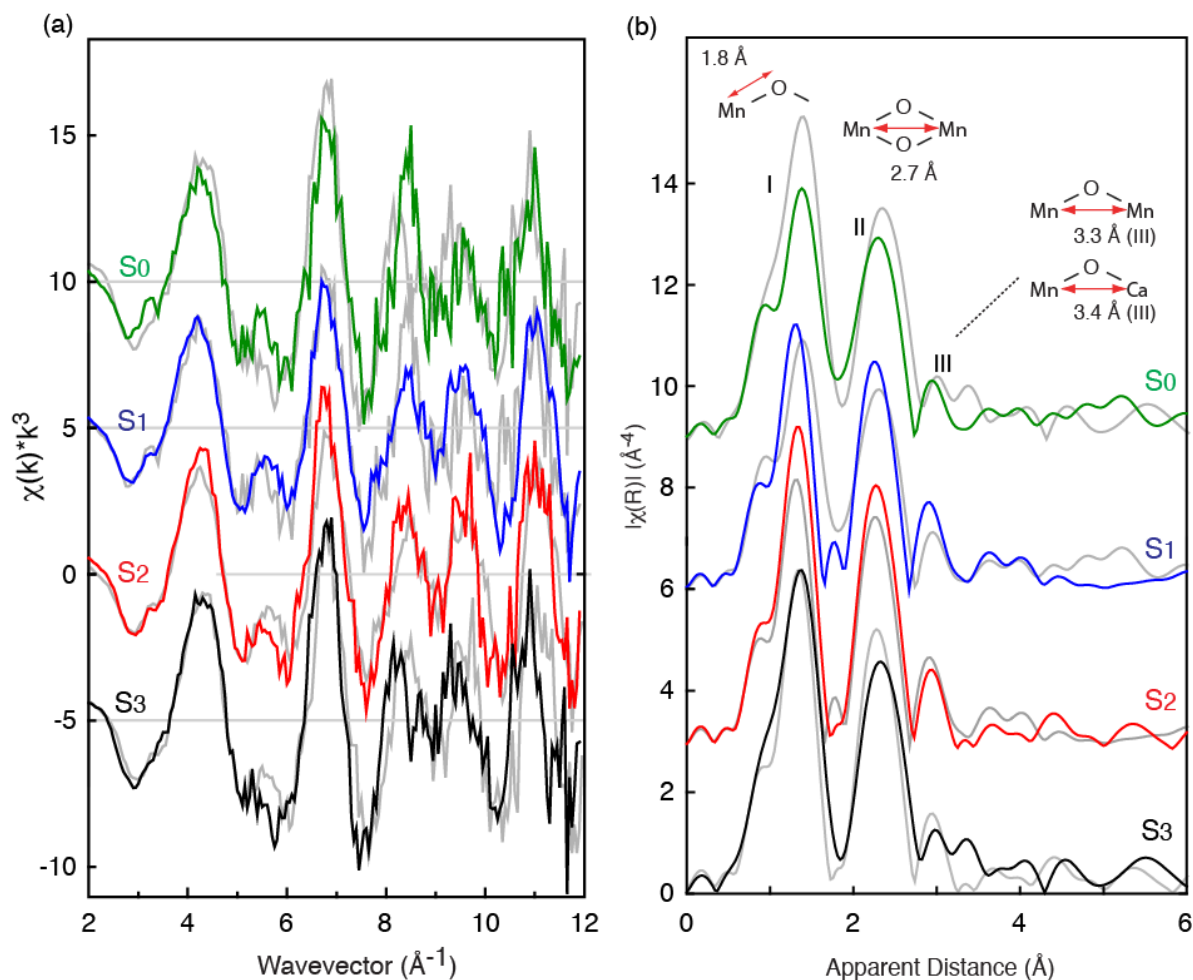


Figure 4.3 EXAFS and FT spectra of dPSIIcc solutions in the S_0 , S_1 , S_2 and S_3 states.

(a) The k^3 -weighted EXAFS spectra and (b) their FT of dPSIIcc solution samples in the S_0 (green line), S_1 (blue line), S_2 (red line) and S_3 (black line) states are shown. For comparison, the spectrum of the S_{n-1} state (in grey) is overlaid in the S_1 , S_2 , and S_3 spectra.

Results of EXAFS curve fitting

For the interpretation of the EXAFS data, Mn EXAFS curve fits (see Sec. 2.2.11.1) for the k^2 -weighted EXAFS spectra (Fig. 4.3 (a)) of the dPSIIcc solutions in the S_0 to S_3 states were performed. The corresponding FT spectra of the fits which approximate best the experimental data are shown in Figure 4.4. The respective fit table is given in the Appendix (Table A.1 and A.2) and the detailed fit data are reported in (192).

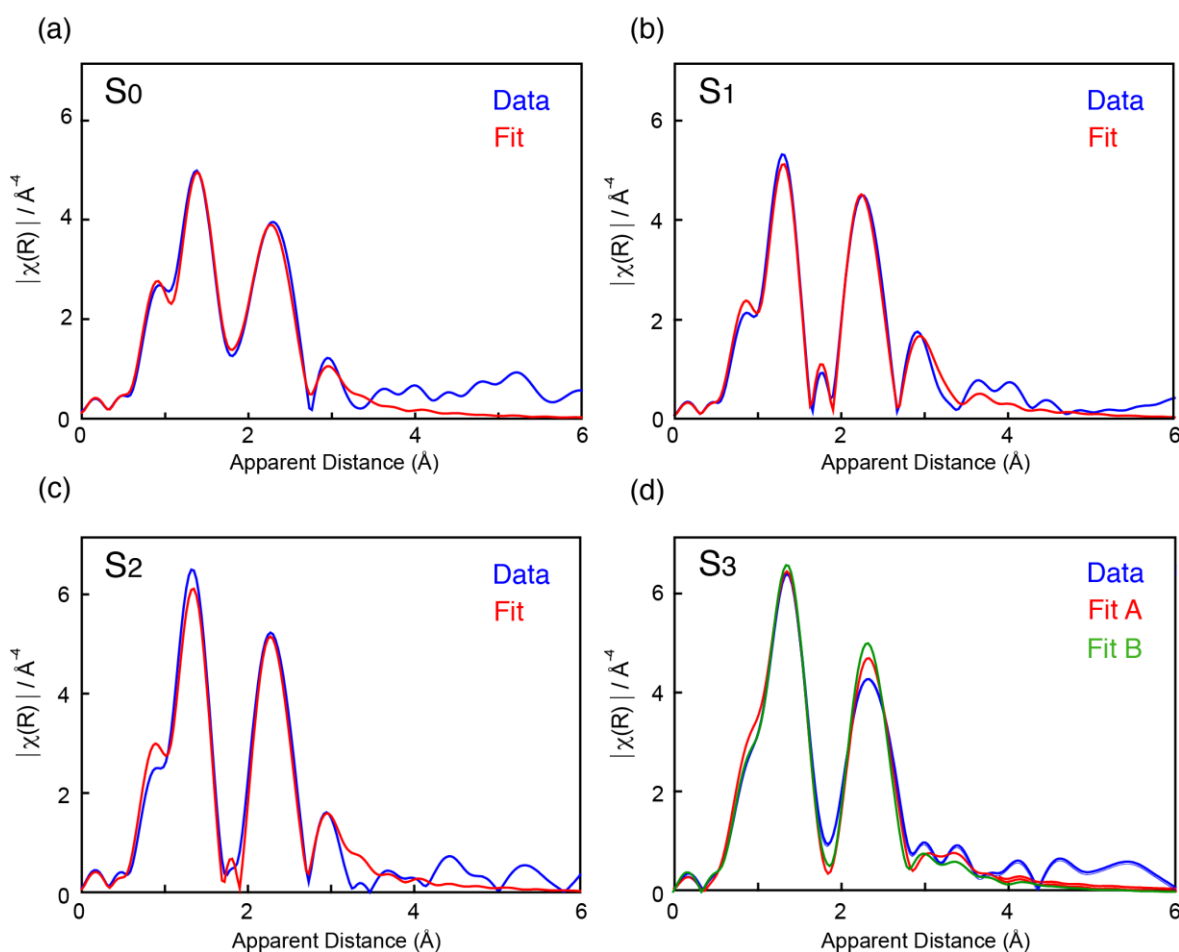


Figure 4.4 FT from Mn EXAFS curve fitting result of dPSIIcc solution in S_0 to S_3 states.

Mn EXAFS curve fitting result of dPSIIcc solution samples in (a) S_0 , (b) S_1 , (c) S_2 and (d) S_3 states. Only the best fitting results are shown. The experimental data are depicted in blue and the fits in red (and green). For details on the fitting parameters see Appendix (Table A.1 and A.2) and (192).

The discussion of the curve fit results is focused on the peak II region which contains the information about the Mn-Mn interactions (around 2.7 Å), which build the basic geometry of the Mn_4CaO_5 cluster. Additionally, the peak II region includes the most reliable data considering the higher uncertainties at the peak III region due to the superposed Mn-Mn and Mn-Ca distance information.

For the S_1 state, previous EXAFS studies on spinach thylakoid membrane fragments revealed about six Mn-ligand interactions at an average distance of 1.87 Å, three di- μ -oxo bridged Mn-Mn interactions at around 2.7 Å, and one longer Mn-Mn interaction at around 3.3 Å (231). These findings were confirmed in the present dPSIIcc solution study with about six Mn-ligand distances at an average of 1.9 Å, Mn-Mn interactions in the range of 2.7 - 2.8 Å and at 3.3 Å (Fig. 4.4 (b)). The peak II region was fitted using two different models with either one or two atom-backscatter distances (one or two shell fit). The fit with one atom-backscatter distance shows an average Mn-Mn distance of 2.73 Å (three distances), while the other fit shows two atom-backscatter distances at 2.71 Å and one at

2.79 Å. The latter model possesses a better fit quality and approximates the experimental peak II region slightly better (192). In the previous Sr XAS study on Sr-substituted dPSIIcc in the S_1 state (223), the data suggested that there are two distances for Sr-Mn interactions, one around 3.5 Å the other around 3.8 Å. The ratio of these interactions, however, was inconclusive as both a 2:2 or at 3:1 ratio for the short to the long Sr-Mn interaction did explain the experimental data. Just recently, a XRD crystal structure of Sr-substituted dPSIIcc from *T. vulcanus* at a resolution of 2.1 Å was obtained and reported a structural model of a Mn_4SrO_5 cluster (50). The revealed four Sr-Mn distances are the following: two at 3.5 Å, one at 3.6 Å and one at 4.0 Å. Taking the estimated standard uncertainty of 0.21 Å into account (50), these results support a 3:1 ratio for short to long Sr-Mn interactions. It has to be mentioned at this point, that the XRD model of the Mn_4SrO_5 cluster likewise suffers from radiation damage and the revealed Sr-Mn distances might be subject to error. The effect of radiation damage on the structure integrity of the Mn_4CaO_5 cluster in the S_1 state is addressed in the next section (Sec. 4.3). In the present XAS study, both possible ratios (2:2 and 3:1) for short to long Ca-Mn interaction were tested to approximate the data, but only slight differences were observed in the quality of the fits (see Appendix and (192)).

In the S_1 to S_2 state transition, a shortening of the Mn-Mn distances was observed. In the S_2 state (Fig. 4.4 (c)), the three Mn-Mn interactions at distances around 2.7 Å (peak II region) become more homogeneous, which is noticeable by the increased peak II intensity. Applying the two shell fit for peak II results in two closer distances of 2.72 Å and 2.75 Å, which are within the resolution limit of the conventional Mn EXAFS (~ 0.02 Å). The one shell fit for the peak II region shows the average Mn-Mn distances to be 2.74 Å. The two shell fit showed a better fit quality (192). Both cases lead to the suggestion that one longer Mn-Mn bond (2.79 Å) in the S_1 state gets shortened in the S_2 state (2.72 or 2.75 Å) as a consequence of the change of one Mn oxidation state from Mn(III) to Mn(IV).

In the S_2 to S_3 state transition essential spectral changes were observed especially in the peak III region (Fig. 4.3 (b)). The intensities of the peak II and III are weaker than in the S_2 state and peak III seems to split into two peaks. Therefore, two possible structural models were tested to approximate the experimental data (Fig. 4.4 (d)): Model (A) has a geometry similar to the S_1 and the S_2 states with three di- μ -oxo bridged Mn atoms (~ 2.7 Å) and a longer mono- μ -oxo bridge (~ 3.2 Å), and model (B) has four di- μ -oxo bridges (~ 2.7 Å) and no mono- μ -oxo bridge. The fit quality was slightly better in the case of model (A) (Table A.2 and (192)). In case of a simple Mn oxidation reaction during a S state transition, a shortening of the Mn-Mn interactions due to the elimination of the Jahn-Teller distortion in Mn(III) would be expected. The Jahn-Teller distortion describes the elongation (and sometimes shortening) of two from six metal-ligand distances in certain transition metal

complexes (with six ligands) in order to achieve a lower energetic ground state. They do not have an octahedral (six similar ligand-metal distances) coordination anymore. However, the increase of the Mn-Mn distances observed in the S_2 to S_3 state transition (for model (A) and (B), Fig. 4.4 (d)) implies that the structural changes which can be seen during this transition are not simply distance changes. This observation points toward the occurrence of fundamental geometrical changes of the Mn_4CaO_5 cluster during the S_2 to S_3 state transition.

During the S_3 to S_0 state transition, the OEC exchanges from the most oxidized state into the most reduced state of the catalytic cycle (see Fig. 1.10). In the here presented results, a decrease of the intensities of peak I and II and also a shortening of the averaged peak II distances can be seen (Fig. 4.4 (a)). When the two shell fit was applied to peak II, two distances around 2.8 Å and one shorter with about 2.7 Å are obtained. This 2:1 ratio is in conflict with former results reported by Robblee *et al.* using flash-illuminated S_0 state spinach thylakoid membrane fragments (232). In the latter study, two Mn-Mn distances with about 2.7 Å and one with 2.9 Å were observed. This difference might result from the improved fitting protocol which was applied in the current study.

Possible structural changes of the Mn_4CaO_5 cluster

The in this study presented EXAFS spectra and the corresponding curve fitting results of dPSIIcc solution samples clearly demonstrated that the structure of the Mn_4CaO_5 cluster changes during the catalytic S state cycle. By using the arrangement of the Mn atoms and the ligand environment of the Mn_4CaO_5 cluster as assigned in the 1.9 Å resolution dPSIIcc S_1 state crystal structure (25), models of the S_0 , S_1 , S_2 and S_3 states were built. These models are constructed on the basis of EXAFS distances, FITR and EPR results (233-239) and the in this work observed distance changes during the catalytic cycle obtained from the EXAFS spectra. Figure 4.5 illustrates the S state models and possible structural changes of the Mn_4CaO_5 cluster during the S state transitions.

The overall structure of the Mn_4CaO_5 cluster was reported as a closed cubane-like one in the 1.9 Å resolution crystal structure (25) (see Sec. 1.3.4). However, as shown in the next section (Sec. 4.3) due to the effect of radiation damage to the Mn_4CaO_5 cluster structure the closed cubane-like arrangement of the atoms might not be correct for the S_1 state. In the here proposed model (Fig. 4.5), an open-cubane like structure of the Mn_4CaO_5 cluster in the S_1 and S_2 state is assumed. This structure is supported by the proposed models obtained through polarized EXAFS studies on dPSIIcc single crystals (shown in Fig. 4.1) (227). The open cubane-like structure was also suggested by Siegbahn for the S_1 and S_2 states (108) and by the group of Neese for the S_2 state (240).

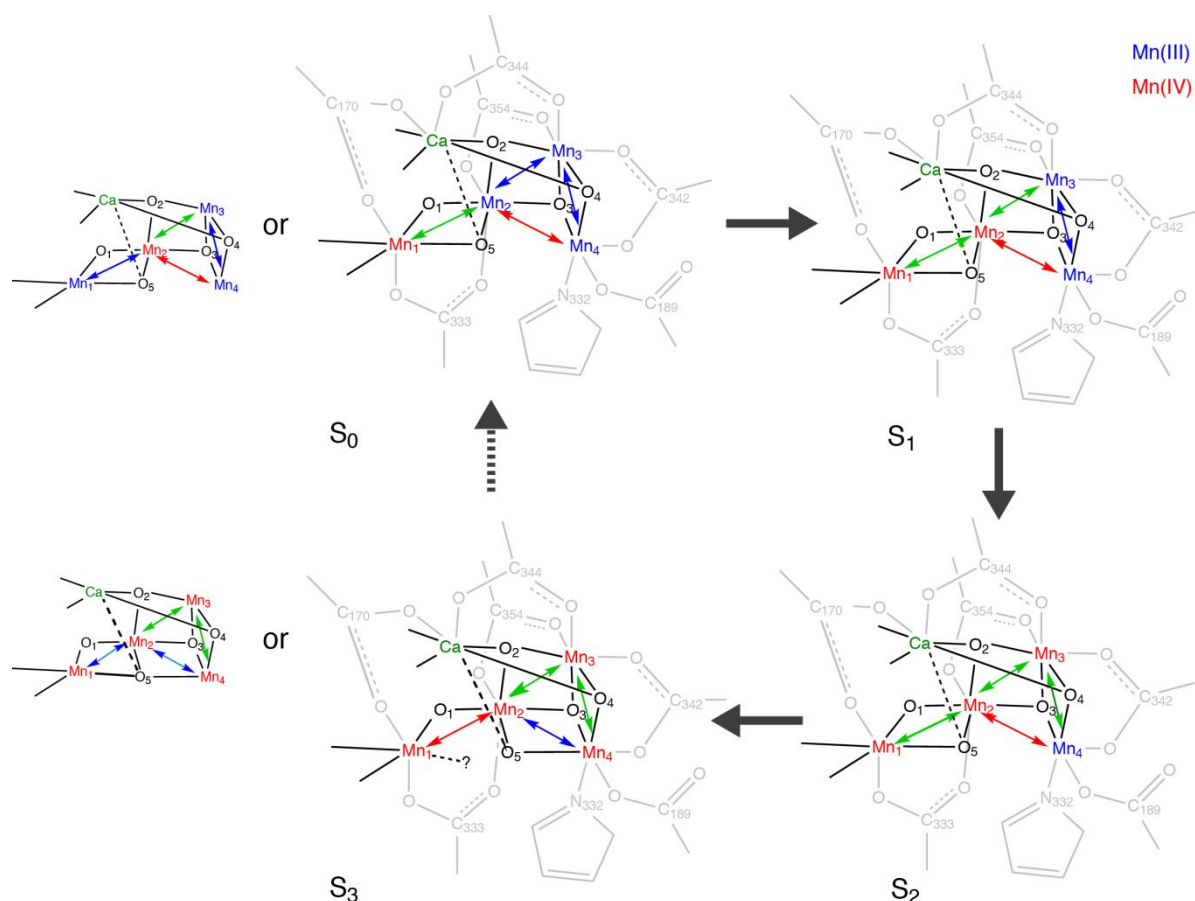


Figure 4.5 Possible structural changes of the Mn_4CaO_5 cluster during the S state transitions.

Possible structural changes of the Mn_4CaO_5 cluster during the S_1 to S_0 state transitions are depicted. For the S_0 and S_3 state two possible models are presented. The different oxidation states of the Mn atoms are color coded: Mn(III) in blue, Mn(IV) in red. Mn-Mn distances of 3.3 Å are shown as red arrows, 2.8 Å as blue arrows and 2.7 Å as green arrows. The dashed line between the Ca atom and O5 depicts the third possible Mn-Ca interaction at 3.4 Å. The surrounding ligand environment is shown in grey. The focus of this illustration is to accommodate the distance changes revealed by the EXAFS measurements. Possible changes in ligand environment (type of ligands and ligation modes) or possible protonation states (at oxo-bridging and terminal water molecules) are not included in the figure.

The S_0 to S_1 state transition experiences a shortening of Mn-ligand distances and one Mn-Mn distance from about 2.8 Å to around 2.7 Å. Supported by EPR/ENDOR studies, the formal oxidation state assignment of the four Mn atoms is $Mn_4(III_3,IV)$ in the S_0 state and $Mn_4(III_2,IV_2)$ in the S_1 state (234, 241). Mn-ligand distances are shortened upon Mn oxidation from Mn(III) to Mn(IV), but the Mn-Mn distances within Mn(III)/Mn(IV) and Mn(IV)/Mn(IV) multinuclear complexes were found to depend strongly on the direction of the Jahn-Teller axis (axis of elongation, see page 87 for explanation) (104). Therefore, the shortening of the Mn-ligand and Mn-Mn distances could be explained by the elimination of the Jahn-Teller effect at one Mn atom. In the S_0 state, a $Mn(III)_3Ca$ open cubane moiety is

assumed as this structural arrangement can account for the elongation of the Mn-ligand distances observed in the S_3 to S_0 state transition. The Mn atom that is oxidized during the S_0 to S_1 state transition could either be Mn2 or Mn1 (see two different models for the S_1 state in Fig. 4.5).

A shortening of one Mn-Mn interaction around 2.7 Å in the dark stable S_1 to S_2 state transition can be observed in our obtained EXAFS results. The resulting three short Mn-Mn interactions are assigned to the distances between Mn1-Mn2, Mn2-Mn3 and Mn3-Mn4 in the S_2 state model (Fig. 4.5). The formal oxidation state distribution for the Mn1 to Mn4 atoms in the S_2 state is believed to be $Mn_4(IV,IV,IV,III)$, according to ^{55}Mn ENDOR measurements (233, 242). This indicates the oxidation of one Mn(III) to Mn(IV) during the S_1 to S_2 state transition. Moreover, FTIR difference spectroscopy studies showed evidence that the Mn atom, which is ligated to the amino acid residue Ala344A, is oxidized in the S_1 to S_2 state transition (243). Therefore, the Mn oxidation happening during this transition was assigned to Mn3 (Fig. 4.5). This is in accordance with ENDOR studies (233, 235, 242), which suggested that Mn4 possesses the oxidation state Mn(III) in the S_2 state. In contrast to the S_0 to S_1 or S_1 to S_2 state transitions, elongations of the Mn-Mn distances are observed in the S_2 to S_3 state transition. This finding leads to the suggestion that fundamental changes of the geometry of the whole Mn_4CaO_5 cluster take place during the S_2 to S_3 state transition, rather than a simple one-oxidation state change of a Mn atom. The elongation of di- μ -oxo bridged Mn-Mn distances (di- μ -oxo Mn-Mn bridge is depicted in Fig. 2.3 (C)) from 2.72 Å to 2.84 Å and to 2.92 Å was shown to occur upon the stepwise protonation of both oxo bridges without a change of the Mn oxidation state (244). At the S_2 to S_3 state transition, this event is unlikely except protons from terminal water molecules are transferred to the neighboring Mn bridging oxygens. In the present study, this structural change is explained with the shift of oxygen O5 from the Mn1 side to Mn4 (Fig. 4.5). The possibility of O5 shuffling has recently been suggested by Isobe *et al.* in the S_2 to S_3 state transition using DFT calculations and by Pantazis *et al.* in EPR studies of the S_2 spin state changes (236, 239, 245). In the case, that oxygen O5 is moved toward the Mn_3Ca open cubane site, a Mn_3CaO_4 closed cubane is formed in the S_3 state. The repositioning of O5 could be accompanied by alternations of the Mn4 ligand symmetry, if Mn4 becomes six-coordinated. This would result in the Mn-Mn distance of 3.26 Å for Mn1-Mn2 (Fig 4.5). For the S_3 state, two possible structural configurations are shown in Figure 4.5 for the case that a Mn_3CaO_4 closed cubane-like moiety is formed: One model has a six-coordinated Mn1, and the other a five-coordinated Mn1 including O5 shuffling. In the latter model, a six coordination of Mn1 could also be maintained by a new ligand to Mn1 (either water or carboxylate from the amino acid residues Asp170A or Glu333A). The model with a five-coordinated Mn1 possesses a better fit quality and approximates the

experimental data slightly better (192). The Mn XANES pre-edge region is generally sensitive to the ligand symmetry, and the intensity increases slightly during the S_2 to S_3 state transition (see Fig. 4.2). This intensity growth might indicate that Mn1 changes from a six to a five-coordinated metal in the S_3 state. However, no conclusive answer can be given at the current state and a detailed pre-edge analysis combined with theoretical calculation is needed for further analysis.

In the S_3 to S_0 state transition, the Mn-Mn distances around 2.7 Å were found to become shortened. This is contrary to what would have been expected, because the Mn oxidation state of the Mn_4CaO_5 cluster changes during this transition from the most oxidized ($Mn_4(IV,IV,IV,IV)$ in S_3) to the most reduced form ($Mn_4(III,III,III,IV)$ in S_0). Still, the shortening of the Mn-Mn distances (~ 2.7 Å) could be explained, if the Mn_4CaO_5 cluster geometry returns from the closed cubane-like structure to the open cubane-like structure during S_3 to S_0 state transition (Fig. 4.5). Thus, the Mn_4CaO_5 cluster geometry in the S_0 state would be similar to the one in the S_1 and S_2 states.

As mentioned earlier, the information about changes of Mn-Ca interactions during the S state cycle is restricted in the present XAS study due to the interference with signals from Mn-Mn interactions that are present at the same distance (peak III region, Fig. 4.3 (b)). Therefore, it is necessary to look at the results obtained from Sr XAS studies on Ca/Sr-exchanged dPSIicc (Mn_4SrO_5 cluster) from *T. elongatus* (223) for the interpretation of our data. The two major peaks of the FT spectrum in (223) were assigned to Sr-O (peak I) and Sr-Mn (peak II) interactions. Substantial spectral changes of the EXAFS spectra were found to occur in the S_2 to S_3 state transition, where peak II (Sr-Mn interactions) splits into two. This is in accordance with our spectral observations (Fig. 4.3) and, hence, demonstrates that Ca/Sr plays an important role during the S_2 to S_3 state transition. This finding is consistent with the observations that in the absence of Ca the S state transition does not proceed beyond the S_2 state (246-252). Recent results from EPR and ENDOR spectroscopy on Ca-depleted spinach thylakoid membranes showed that the depletion of Ca from the Mn_4CaO_5 cluster does not disturb the overall structure of the Mn_4 moiety on the spin-state level in the S_1 and S_2 states (253). Also, it was reported in former studies, that Ca can be removed more easily in the S_3 state compared to the S_1 and the S_2 state (254). All these results together imply that the Mn-Ca binding modes are changed upon the S_2 to S_3 state transition, confirming the here observed spectral changes (Fig. 4.3).

Note, that more detailed structural changes that could evidence, for example, which Mn-Mn distances are shortened or elongated upon an S state transition, require orientational information which can be gained from oriented membrane EXAFS or single crystal EXAFS studies (see Sec. 4.5).

In addition to the discussed structural changes of the Mn_4CaO_5 cluster, distances to terminal ligands from carboxylates and histidine residues, as well as to water/hydroxo ligands most likely undergo changes during the S_1 state cycle. EXAFS studies only provide averaged distance information and, therefore, it is difficult to extract any detailed information on metal-ligand interactions from EXAFS spectra. However, it has been shown in site-directed mutant studies that some ligands play a critical role in the activity of the OEC (255, 256). For example, only the replacement of the amino acid residue His332A (terminal ligand to Mn4 in our proposed model, Fig 4.5; and to Mn1 in the 1.9 Å resolution crystal structure, Fig. 1.13) by a glutamate residue led to great variations in the according EXAFS and XANES spectra (255, 256). The results demonstrate the strong interaction of ligands with the Mn_4CaO_5 cluster and their importance in maintaining the active-site structure.

4.3 Effect of radiation damage to the Mn_4CaO_5 cluster in the S_1 state

As depicted in Section 1.3.4, the structure of dPSIicc in the dark stable S_1 state has been studied intensely by EXAFS methods and XRD crystallography. The recent XRD crystal structure at 1.9 Å resolution revealed the following distances within the Mn_4CaO_5 cluster: Mn-ligand distances in average at about 2.2 Å, three shorter Mn-Mn interactions around 2.8 - 2.9 Å and one long Mn-Mn interaction around 3.3 Å (25). The 3:1 ratio of short to long Mn-Mn interactions is in agreement with the various former EXAFS studies as well as with the present work (see previous section). However, the overall atomic distances disagree in the XRD and EXAFS experiments. The EXAFS studies showed shorter Mn-ligands (1.9 Å) and Mn-Mn interactions (2.7 - 2.8 Å). This discrepancy arises in some extend from the distance uncertainties in both methods (XRD ~ 0.19 Å at 1.9 Å resolution, and EXAFS ~ 0.02 Å), but also from the inherent X-ray damage to the Mn atoms during XRD crystallography (see Sec. 1.3.4).

In this study, the effect of radiation damage to the Mn_4CaO_5 cluster was evaluated in more detail. The XAS spectra of intact dPSIicc solution samples in the S_1 state is directly compared with 25% X-ray damaged dPSIicc solution samples (Fig. 4.6). For this purpose, dPSIicc solution samples were damaged, prior to XAS spectra recording, by exposing them to X-ray doses as used in XRD crystallography, which induce the reduction of Mn(III/IV) to Mn(II). Additionally, the XAS spectra of dPSIicc solution samples with 5 and 10% X-ray damage were measured (Fig. 4.6). It can be clearly seen that the XAS spectra of 5, 10 and 25% X-ray damaged dPSIicc solution samples differ from each other and from the non-damaged S_1 state sample.

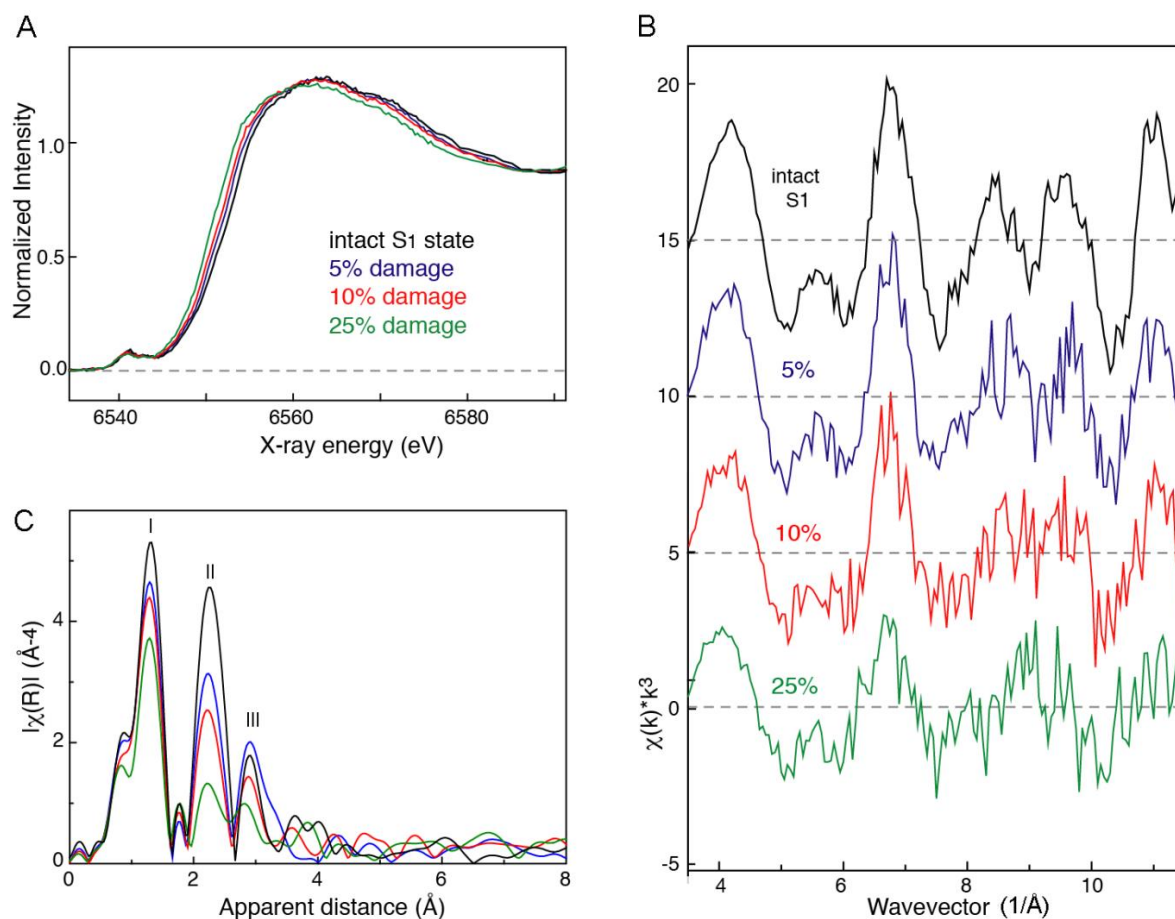


Figure 4.6 XAS spectra of dPSIIcc solution sample with 0, 5, 10 and 25% of reduced Mn.

The (A) XANES, (B) k^3 -weighted EXAFS and (C) FT amplitude spectra of dPSIIcc solution sample with 0, 5, 10 and 25% reduced Mn are shown in black, blue, red and green, respectively. The radiation damage was caused by exposing the samples to X-rays at 100 K previous to XAS data collection. The dose for the different damage levels was calculated based on (116).

A great discrepancy exists between the spectra of the intact S₁ state sample and the 25% X-ray damaged dPSIIcc solution sample. The Mn K-edge position shifts toward lower energies with increasing X-ray damage to the dPSIIcc samples, showing the reduction of the Mn atoms in the Mn₄CaO₅ cluster (Fig. 4.6 (A)). In the k^3 -weighted EXAFS spectra (Fig. 4.6 (B)) the amplitude intensities decrease and the oscillations are more damped with an increasing Mn reduction. The in the S₁ state pronounced oscillation between 6 and 8 \AA^{-1} clearly reduces upon increasing Mn damage. In the higher k-space (range between 8 - 11.5 \AA^{-1}), a dephasing particularly at 10 and 25% Mn reduction can be seen in comparison to the undamaged S₁ state. The FT peak intensities of the X-ray damaged dPSIIcc samples are much lower especially in the peak II and III region and also peak shifts toward shorter distances are visible (Fig. 4.6 (C)). The corresponding EXAFS curve fitting results (Table A.3) demonstrate that with increasing Mn reduction the number of shorter Mn-Mn interaction is diminished and the number of longer Mn-Mn interaction

increases. These observations indicate that the Mn_4CaO_5 cluster in the 1.9 Å resolution crystal structure of dPSIIcc does not represent the natural cluster structure but an altered or even disrupted structure instead (25).

The origin of the elongation of the atomic distances in the crystal structure of dPSIIcc from *T. vulcanus* has been discussed by several groups. The presence of pre- S_0 states such as S_{-1} , S_{-2} , and S_{-3} in the crystal structure were debated as one possibility (257, 258). Furthermore, it was considered as another possibility that the X-ray radiation reduces the dPSIIcc complexes in the crystals from the S_1 state to the S_0 state by cycling backwards through the S states (257). In this study, the 25% radiation-damaged dPSIIcc solution EXAFS FT spectrum is also compared with the spectrum of intact S_0 state dPSIIcc solution samples. Figure 4.7 shows, that the two samples are substantially different from each other, especially in the peak II and peak III region. This finding excludes the possibility that the Mn_4CaO_5 cluster is reduced from the S_1 to the S_0 state as a consequence of X-ray radiation. It also implies that the X-ray induced Mn reduction of the Mn_4CaO_5 cluster does not necessarily go through the catalytic pathway.

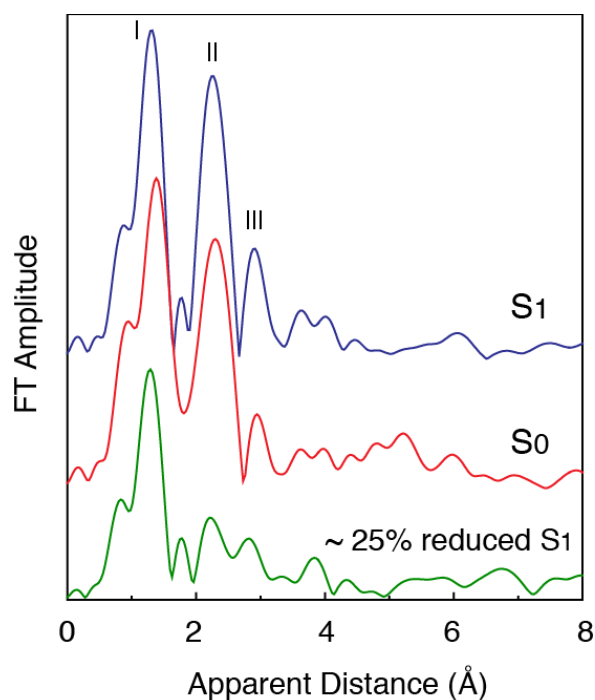


Figure 4.7 Comparison of the EXAFS FT spectra of dPSIIcc solution sample in the S_1 and S_0 state with 25% reduced S_1 state.

The EXAFS FT spectra of dPSIIcc solution sample in the S_1 (blue) and S_0 (red) state are compared with the S_1 state containing 25% reduced Mn atoms (green). The radiation damage was caused by exposing the samples to X-rays at 100 K previous to XAS data collection. The dose for the 25% damage was calculated based on (116).

4.4 X-ray absorption spectroscopy on mPSIIcc solution samples in the S_1 state

The use of mPSIIcc single crystals for polarized EXAFS measurements is of very high interest due to their spectroscopic advantageous crystal form (see Sec. 1.3.6). As the monomeric form of PSIIcc does not represent a precursor complex or a photodamaged product of dPSIIcc (pointed out in Sec. 1.3.6), it is expected that the XAS spectra of mPSIIcc and dPSIIcc in the dark stable S_1 state are essentially identical. To test their analogy, the Mn XAS spectra of mPSIIcc solution samples in the S_1 state were collected prior to EXAFS studies on single mPSIIcc crystals (see next section). The obtained data are compared with the XAS spectra of dPSIIcc S_1 state solution samples. Additionally, the mPSIIcc and dPSIIcc XAS spectra are compared with XAS measurements of spinach PSII thylakoid membrane fragments, to demonstrate possible differences between the organisms regarding the organization of the Mn_4CaO_5 cluster (192).

In the XANES region, mPSIIcc and dPSIIcc solution samples are identical (Fig. 4.8 (a), black and red lines), confirming that these two samples have the same electronic structure, and the monomer or dimer assembly does not affect the ligand environment around the OEC. The EXAFS FT spectra of dPSIIcc and mPSIIcc solution samples are also identical in the peak I, II and III regions (Fig. 4.8 (b), black and red lines). This comparison proves the mPSIIcc preparation to be suitable for XAS studies and for use in further XAS investigations (see next section).

On the other hand, the XANES spectrum of spinach PSII thylakoid membrane fragments is slightly different from that of the PSIIcc solution samples (Fig. 4.8 (a), top panel). The differences become more pronounced in the second derivative of the XANES spectrum (Fig. 4.8 (a), bottom panel). This result points toward little differences between the electronic structure of the Mn_4CaO_5 cluster of *T. elongatus* PSIIcc and spinach PSII. ^{55}Mn ENDOR measurements on spinach PSII-enriched membrane fragments and *T. elongatus* dPSIIcc in the S_2 state likewise led to the conclusion that the electronic structure of the Mn_4CaO_5 cluster is very similar but not identical between both species (235). The similarity of the Mn_4CaO_5 cluster structure in dPSIIcc, mPSIIcc and spinach PSII thylakoid membrane fragments is indicated by their almost identical EXAFS FT spectra (Fig. 4.8 (b)).

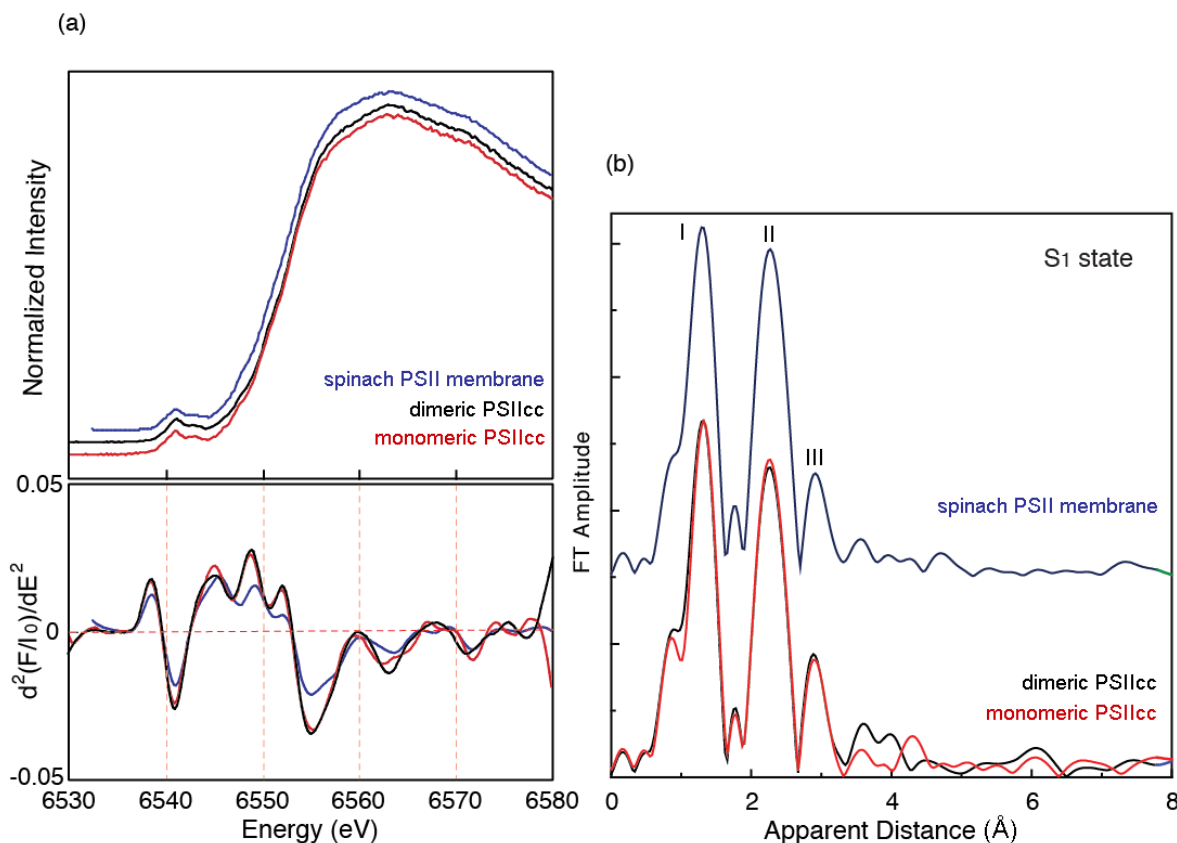


Figure 4.8 XAS spectra of mPSIIcc and dPSIIcc solution compared with spinach PSII thylakoid membrane fragments.

Comparisons of the S_1 state Mn XANES spectra (a) and the EXAFS FT spectra (b) of mPSIIcc (red line) and dPSIIcc (black line) solution samples, and spinach PSII thylakoid membrane fragments (blue line).

The alignment of the amino acid sequence of subunit D1 from *T. elongatus* (strain BP-1) and *Spinacia oleracea* (spinach) showed a sequence identity of 84.7% (calculated with UniProt). Within a radius of 20 Å around the OEC, nine amino acid residues are not fully conserved, but eight of them are conserved between groups with strongly similar properties (Fig. 4.9). This high conservation makes it unlikely that the slight differences between spinach and *T. elongatus* PSII Mn XAS spectra are due to the differences in subunit D1. However, the subunit composition of spinach PSII and *T. elongatus* PSIIcc is somewhat different. While PSIIcc from cyanobacteria possess the extrinsic subunits PsbO, PsbU and PsbV, spinach PSII has neither PsbU nor PsbV but PsbP and PsbQ instead (see Sec. 1.3.2). The exact localization of PsbP and PsbQ is not yet resolved, but various studies found these two subunits to be important for the stability and activity of the OEC (for review see (259) and references therein). PsbV and PsbU are known to bind in the vicinity of the OEC and to directly interact with the C-terminus of subunit D1 (Fig. 4.9). Thus, replacing PsbU and PsbV with PsbP and PsbQ might induce structural changes in

the environment of the OEC which could be the origin of the small variations that can be observed in the XAS spectra (Fig.4.8).

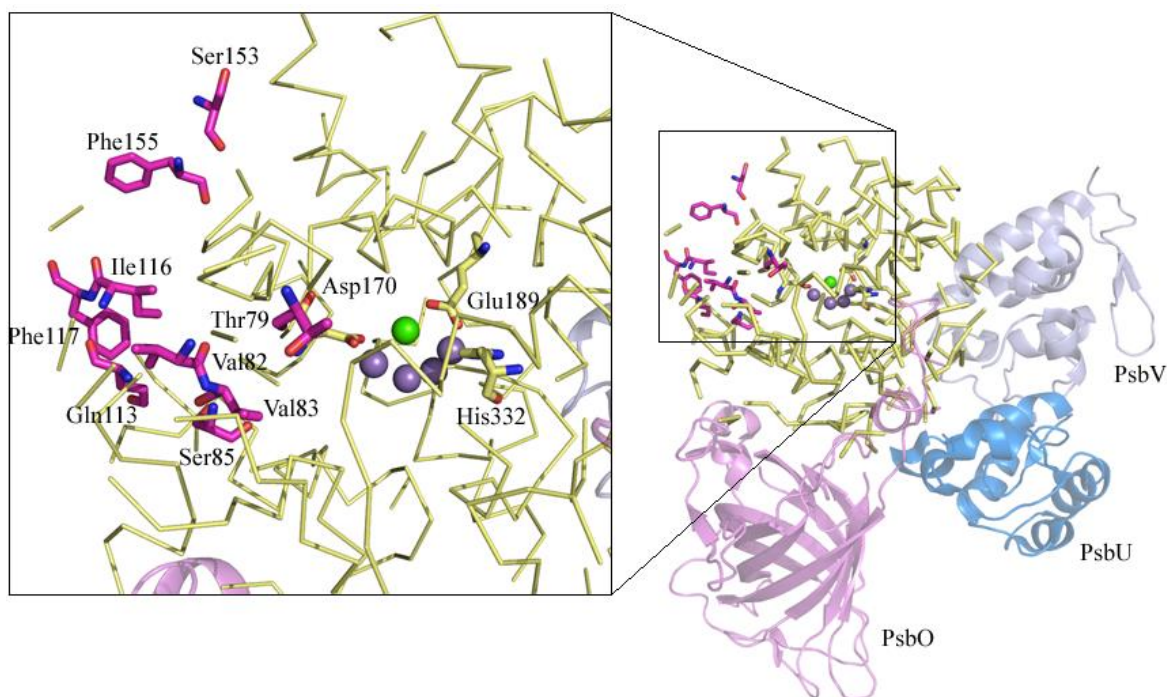


Figure 4.9 Amino acid residues within a radius of 20 Å around the Mn_4Ca cluster.

The amino acid residues within a radius of 20 Å around the Mn_4Ca cluster are depicted according to the structural model of dPSIIcc from *T. elongatus* at 2.9 Å resolution (22). The right panel shows in yellow (ribbon mode) the amino acid residues within a radius of 20 Å around the Mn_4Ca cluster (Mn: purple spheres, Ca: green sphere). Amino acids of subunit D1 different from spinach PSII are highlighted in pink and are labeled in the enlarged view on the left (distances are given in Table S1). For better orientation, the amino acid residues Asp170A, Glu189A and His332A are shown in stick mode. The extrinsic subunits PsbO (purple), PsbU (blue) and PsbV (light blue) are shown in cartoon mode. View is of one monomer looking onto the monomer-monomer interface along the membrane plane (tilted by 45° to the left), with the cytoplasm above and the lumen below.

4.5 X-ray absorption spectroscopy on single crystals of mPSIIcc

The advantage of single crystals over solution samples of a protein is the high order in all three dimensions. This feature, which is also absent in membrane layers, can be used to obtain orientation-dependent spectroscopic data, which in turn can yield information about the 3-dimensional orientation of the studied part of the protein (e.g. a specific cofactor).

Due to the dichroism of PSIIcc crystals (see introduction of Chapter 4), the absorption intensity in both, the XANES and EXAFS spectra, varies depending on the orientation of the crystal relative to the direction of the electric field vector of the polarized X-ray beam (227). The dichroism obtained from polarised EXAFS on single crystals of dPSIIcc was

mostly pronounced in the region of peak III which represents the long Mn-Mn (about 3.3 Å) and Mn-Ca (about 3.4 Å) interactions (227). This superposition of at least two vectors of nearly equal length makes its analysis difficult. Nevertheless, the obtained data gave many constraints to screen the large number of previously proposed models and, by incorporating X-ray crystallography data (21), led to the proposal of four possible structural models of the Mn_4Ca cluster (see Fig. 4.1) (102, 227). It was not possible to choose between the remaining three models, due to the ambiguity which is caused *inter alia* by the arrangement of the dPSIIcc in the unit cell (space group $\text{P}2_12_12_1$) and the non-crystallographic $\text{C}2$ symmetry inherent in the dimer.

As described in Section 1.3.6, the crystal form of mPSIIcc (space group $\text{C}222_1$), however, possesses two important features, which address the just described ambiguity (23): (i) the lack of the non-crystallographic $\text{C}2$ symmetry, which reduces the number of possible orientations of the manganese cluster within the unit cell and (ii) the orientation of the membrane normal perpendicular to the crystallographic b -axis, which allows a better discrimination between absorber-backscatter vectors oriented parallel and perpendicular to the membrane plane (see Fig. 1.21). Such a sterical arrangement is proposed for the Mn-Ca vector and the mono- μ -oxo-bridged Mn-Mn vector. Therefore, the analysis of a complete set of polarized EXAFS spectra along the three crystal axes of mPSIIcc will most likely extend the available structural information about the Mn_4CaO_5 cluster and in particular with regard to the Mn-Ca interaction. Another advantage over the former studies on dPSIIcc crystals is the now available Mn_4CaO_5 cluster geometry obtained from the 1.9 Å resolution crystal structure (25). The latter can be used to reduce the number of possible models. Initial experiments of polarized XAS on single crystals of mPSIIcc were already reported in (180) and were continued during this work.

The data of numerous measurements have to be averaged in order to generate a smooth XAS spectrum of which the oscillation of the EXAFS region can be extracted. Although a high number of mPSIIcc crystals have been measured, the data quality is still limited due to the low signal-to-noise level obtained from the single crystals. The signal-to-noise level depends on the amount of Mn atoms in the sample and, therefore, the overall crystal size matters in EXAFS measurements. The mPSIIcc crystal used for polarized EXAFS were in the range of $0.6 \times 0.4 \times 0.2$ mm and is slightly smaller than the size of dPSIIcc crystals (about $1.0 \times 0.3 \times 0.1$ mm) investigated with EXAFS.

However, despite the low signal-to-noise level a clear dichroism is visible in the Mn K-edge spectra along the crystal axes a , b and c of the mPSIIcc crystals and is shown in Figure 4.10. Higher absorption intensities are observable when the crystallographic b -axis of the monomer crystal is oriented parallel to the X-ray e -vector.

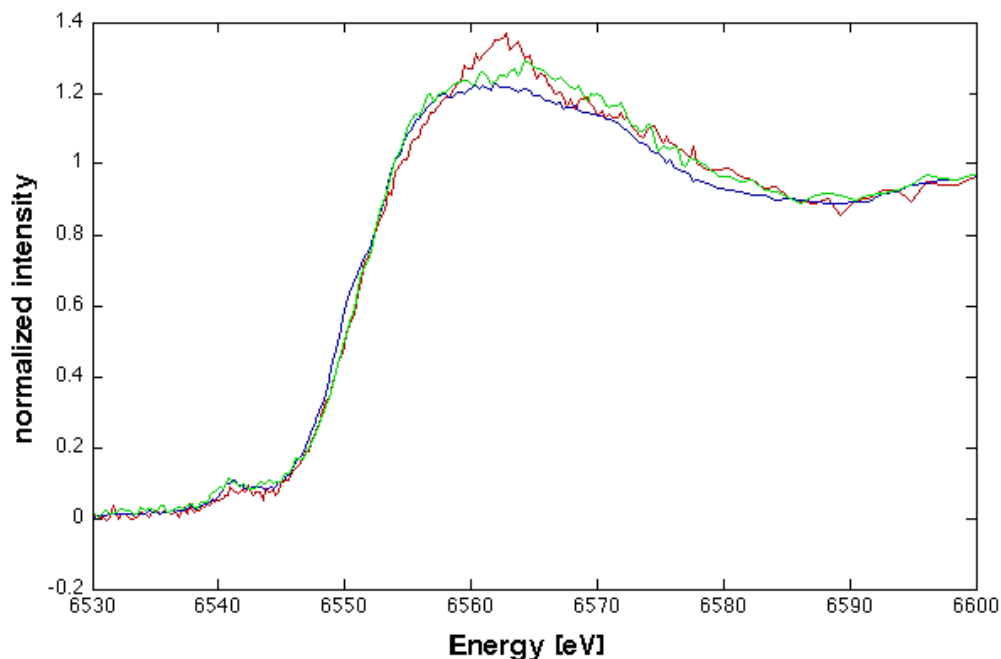


Figure 4.10 XAS on mPSIIcc single crystals.

Polarized Mn K-edge spectra of crystals from the mPSIIcc are shown in different orientations. The X-ray e-vector is parallel to the crystal axes *a*, *b* and *c* (see Fig. 1.21) and the spectra are depicted in red, blue and green, respectively.

Besides the limitation of the data quality due to the low signal-to-noise level, another difficulty occurred during the measurements. A large part of the measured XAS spectra of mPSIIcc single crystals showed a clearly shifted Mn K-edge position toward lower energies, indicating a reduction of the Mn atoms (Fig. 4.11). Compared to XAS spectra of single crystals of dPSIIcc, the K-edge of mPSIIcc single crystals shifts toward lower energies by about 1.2 eV denoting the presence of free Mn(II) atoms. This shift was neither observed in XAS spectra of mPSIIcc solution samples nor in XAS spectra of dPSIIcc solution samples (Fig. 4.8) and single crystals (Fig. 4.11). Therefore, the reduction of the Mn atoms to Mn(II) and their release from the OEC was assumed to be associated with the crystallization conditions of mPSIIcc, which differ significantly from the crystallization conditions of dPSIIcc. The crystallization of mPSIIcc requires the presence of about 19% PEG 400 and 0.2 M CaCl₂ in 0.1 M PIPES (pH 7.0), whereas dPSIIcc is crystallized using 6.4 – 8.2% PEG 2,000 and only 0.01 M CaCl₂ in 0.1 M PIPES (pH 7.0).

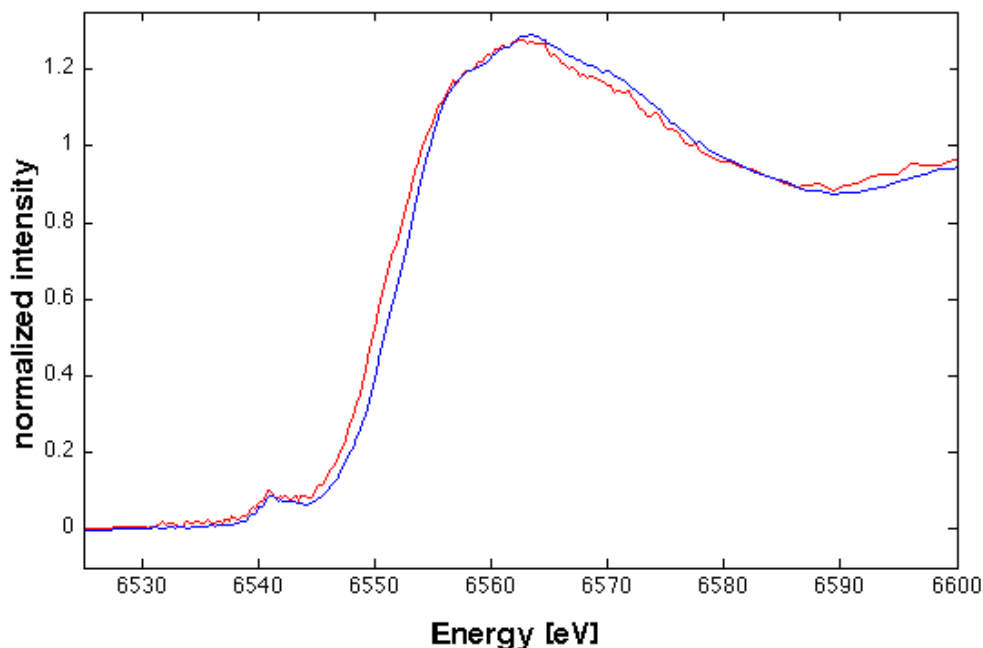


Figure 4.11 Comparison of XAS on mPSIIcc and dPSIIcc single crystals.

A comparison of the Mn K-edge spectra of crystals from the monomeric (in red) and dimeric (in blue) form of PSIIcc is shown. The Mn K-edge of mPSIIcc single crystals is shifted toward lower energies, by about 1.2 eV. Both spectra were obtained by the combination of the polarized spectra recorded along the *a*, *b*, and *c* crystal axes.

It was observed previously that re-dissolved crystals of mPSIIcc show a reduced oxygen evolving capacity in comparison to mPSIIcc solution prior to crystallization (180). It was also found, that mPSIIcc solution incubated overnight in buffer containing 0.2 M CaCl₂ showed a significant reduction of the initial activity. In contrast, the oxygen evolving activity of dPSIIcc was not found to be influenced at CaCl₂ concentration up to 0.35 M. Therefore, it was suggested that mPSIIcc possess a distinct sensitivity to increased amounts of CaCl₂. In former studies on spinach PSII membranes, it was reported that in the presence of high salt concentrations like 1 M CaCl₂, 1 M MgCl₂ or 1M NaCl the evolution of oxygen is inhibited and also extrinsic subunits are released from PSII (260, 261). Pauly *et al.* investigated the influence of several salts on the oxygen evolving activity of PSIIcc isolated from cyanobacterial *Synechococcus* sp. (262). It was found that less than 25 μM CaCl₂ (in the absences of other additional salts) results in an inhibition of oxygen evolution by more than 80%. However, increasing amounts of CaCl₂ activate the oxygen evolution until saturation is observed at about 4 mM CaCl₂. In accordance with the results of spinach PSII, the *Synechococcus* sp. PSII was found to have almost no oxygen evolving activity (only 4%) in the presence of about 1 M CaCl₂. These results demonstrated that a certain amount of CaCl₂ is supporting the activity of PSII. This can be explained by the increased protein solubility due to the salt binding to the protein surface.

At higher salt concentrations, however, unspecific binding to the protein occurs and may lead to the dissociation of subunits (263, 264).

In this study, the effect of 0.2 M CaCl_2 on mPSIIcc was additionally investigated by EPR measurements. The EPR spectra showed an increase of the Mn(II) signal when mPSIIcc samples were incubated (for 45 min) in a buffer containing 30% glycerol and 0.2 M CaCl_2 (Fig. 4.12). EPR is very sensitive to detect even low amounts of Mn(II) as the Mn(II)-hexaquo complex shows a characteristic six-line EPR spectrum centered around 3300 G (Fig. 4.12, gray line). In mPSIIcc samples treated only with 30% glycerol (Fig. 4.12, red line) or 30% glycerol and 20% PEG 400 (Fig. 4.12, black line) no indication of this signal is found. In contrast, in the mPSIIcc sample treated with 0.2 M CaCl_2 (Fig. 4.12, green line) five of the expected Mn(II) lines can be found (the sixth line is hidden underneath the Y_D signal at 3280 G). Together, these findings clearly indicate, that the presence of 0.2 M CaCl_2 in the crystallization buffer of mPSIIcc is responsible for the partial reduction and release of Mn(II) from the OEC.

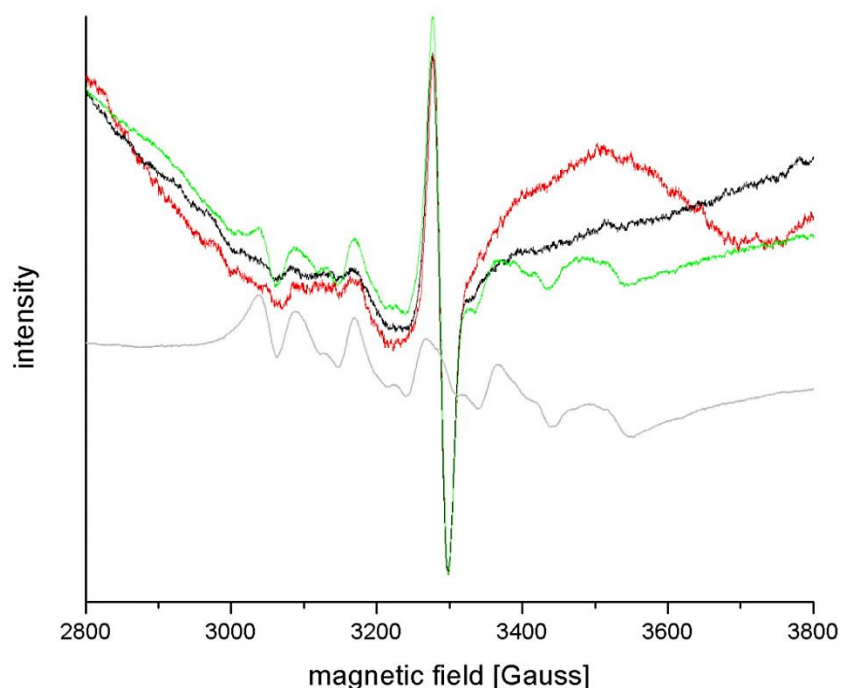


Figure 4.12 EPR measurements of mPSIIcc samples compared to the Mn(II)-hexaquo complex.

The EPR signal of mPSIIcc samples treated in different buffers (30% glycerol, red line; 30% glycerol and 20% PEG 400, black line; 30% glycerol and 0.2 M CaCl_2 , green line) were measured and compared to the signal of Mn(II)-hexaquo complex (grey line, scaled to match the signal height of the CaCl_2 treated sample). The Mn(II)-hexaquo complex shows a characteristic six-line EPR spectrum centered around 3300 G. The mPSIIcc sample treated with 0.2 M CaCl_2 (green line) shows five of the expected Mn(II) lines, whereas the sixth line is hidden underneath the Y_D signal at 3280 G.

However, according to (180) the amount of 0.2 M CaCl_2 is essential for the formation of mPSIIcc crystals with good quality. Lower CaCl_2 concentrations were reported to lead to the formation of crystals with high irregularities or even crystallite-aggregates. Due to the high amount of CaCl_2 , electrostatic interactions between the protein complexes most likely lead to the crystal formation of mPSIIcc. In contrast, crystals of dPSIIcc are probably formed due to hydrophobic interactions.

In order to perform XAS measurements on mPSIIcc single crystals without the occurrence of free Mn(II), it is necessary to find crystallization conditions for mPSIIcc with a reduced content of calcium, maintaining the natural oxidation states of the manganese ions. During this work, initial experiments addressing this issue were performed and are reported in the following.

4.6 Initial experiments toward new crystallization conditions for mPSIIcc

The first crystals of mPSIIcc were obtained under the compromise of using 0.2 M CaCl_2 which was likewise demonstrated to reduce the oxygen activity of mPSIIcc (23, 180). Another condition for getting mPSIIcc crystals was the division of the mPSIIcc eluting peak fraction (as obtained in the last chromatographic purification step) in a first and a second part named P1 and P2. These two fractions were reported to show significantly different crystallization behaviors. Only mPSIIcc samples from the P1 fraction yielded nicely shaped and well-ordered mPSIIcc crystals (180). The observed inhomogeneity of the mPSIIcc eluting peak fraction could not be explained as analytical methods did not reveal significant differences between the two peak fractions. This inhomogeneity could arise from the use of the strong anion-exchange matrix (HR-Sepharose Q) in the third and last chromatographic purification step of mPSIIcc as described in (180). Even though no indications were found for a disintegration of mPSIIcc due to the used matrix, a purification protocol with a weak anion-exchange matrix (similar to the purification of dPSIIcc) would be preferable to ensure the integrity of the protein and possibly yield one homogenous mPSIIcc fraction. Therefore, the variation of the mPSIIcc purification procedure was performed as first step toward improved crystallization conditions.

4.6.1 Purification

After the second purifications step, the mPSIIcc containing fraction is still contaminated with dPSIIcc, phycobilisome proteins and ATP synthase (23). The major challenge here is the separation of the ATP synthase. In the present approach, the weak anion-exchange matrix DEAE-Sepharose Fast Flow (GE Healthcare) was used, which combines the

properties of the chromatography materials ToyoPearl DEAE 650 S (used in the first two chromatographic purification steps) and HR-Sepharose Q. Phycobilisome proteins and PSIIcc can be observed spectroscopically by light absorption at a wavelength of 280 nm (by tryptophan residues). For the detection of the almost tryptophan-less ATP synthase (265), light with a wavelength of 205 nm has to be used, which is mainly absorbed by the protein backbone. With a MES buffer system at pH 6.0 no adequate separation of mPSIIcc and ATP synthase was achieved. However, lowering the pH to 5.5 allowed a clear separation of the components in a highly reproducible way (Fig. 4.13). The obtained peak fraction was characterized by oxygen evolution measurements, gel permeation chromatography, MALDI-TOF mass spectrometry and blue native PAGE.

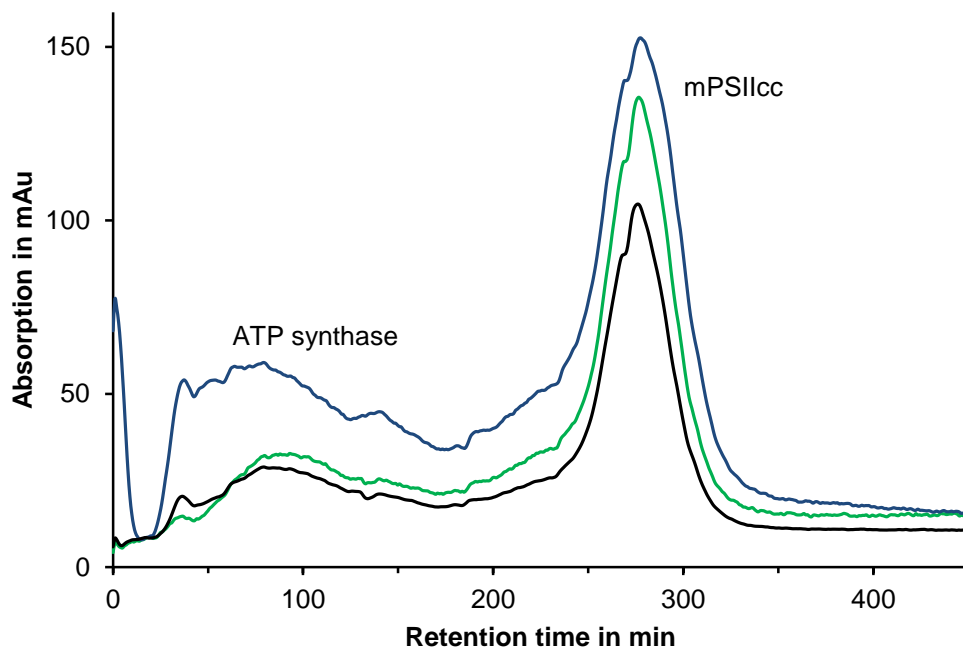


Figure 4.13 Separation chromatogram of mPSIIcc and ATP synthase at pH 5.5.

The third purification step was performed with a DEAE-Sepharose matrix. Protein detection was performed at 205 nm (blue), 280 nm (black) and 673 nm (green). At a wavelength of 673 nm chlorophyll pigments absorb, which are only present in PSIIcc. The first rather broad peak at 205 nm can therefore be assigned to the ATP synthase and the second sharp peak to mPSIIcc.

Furthermore, the fractions of the mPSIIcc peak were split in three different parts (A, B and C as indicated in Fig. 4.14) similar to the P1 and P2 fraction in (180) and analysed separately in terms of activity and subunit composition.

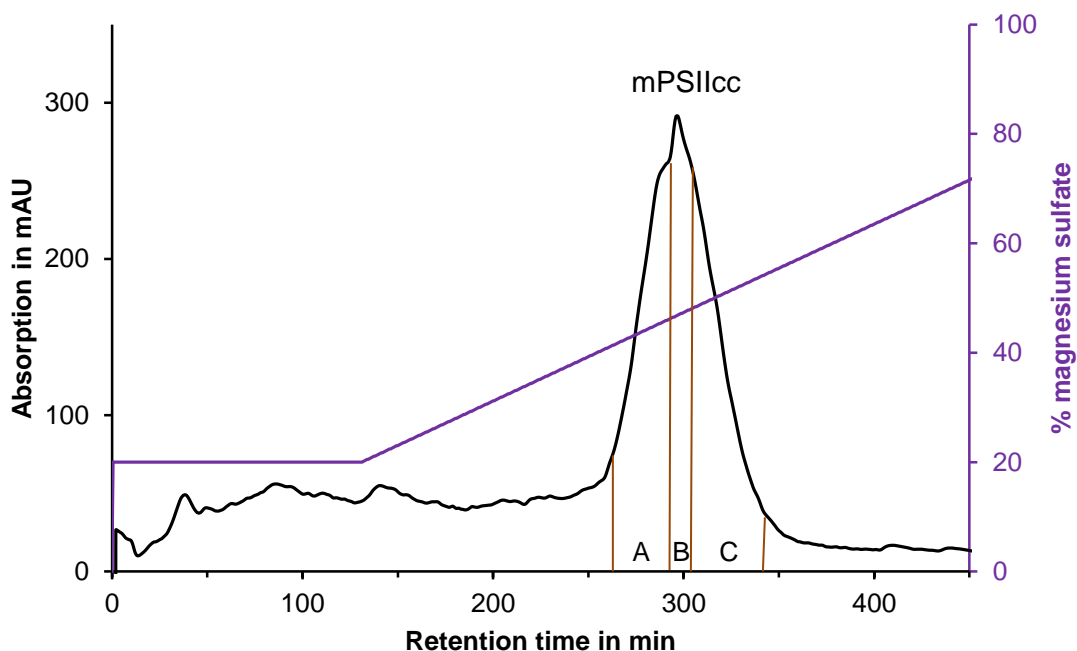


Figure 4.14 Purification of mPSIIcc at pH 5.5 on DEAE-Sephrose matrix.

To elute mPSIIcc a linear Mg_2SO_4 salt gradient was applied and is shown in purple. Absorption at 280 nm wavelength is depicted in black. The mPSIIcc peak fraction was divided in three parts A, B and C and was characterized separately.

4.6.2 Characterization

Oxygen evolution measurements

The oxygen evolution activity per single flash gives information about the purity and the integrity of the obtained fraction. Note, that the obtained number of Chl a per active center ($^{1/4} O_2 \times \text{flash}$)⁻¹ has to be corrected as several factors, like double hits (two photons absorbed by the same photochemical center) and misses (charge-separation but no S state transition (266)), are not accounted for in the measured Chl a number. Due to further instrumental errors during calibration and concentration determination, an error of about 15% is assumed for this method. The activity of mPSIIcc solution was measured before and after the third purification step. Before the third column, the oxygen evolution capacity of the mPSIIcc containing sample was in the range of ($^{1/4} \text{ mol } O_2 / (45 - 85 \text{ mol Chl}a \times \text{flash})$), similar to the values reported in (180). After the purification step with DEAE-Sephrose as column material and at pH 5.5, oxygen evolution capacity of mPSIIcc was found to be ($^{1/4} \text{ mol } O_2 / (45 - 56 \text{ mol Chl}a \times \text{flash})$). In accordance with (23), the capacity of oxygen evolution increased to ($^{1/4} \text{ mol } O_2 / (34 - 40 \text{ mol Chl}a \times \text{flash})$) when the buffer was changed to pH 7.0 (even after incubation for 24 h at pH 5.5). The activity of the three parts A, B and C were found to be in the same range.

Gel permeation chromatography

Gel permeation chromatography was applied to prove the oligomerization state of the obtained PSIIcc fraction. Samples of dPSIIcc and mPSIIcc (purified according to the protocol in (23)) were used as standards. The retention volume of standard dPSIIcc is 13.1 ml, whereas the one of standard mPSIIcc is 14.3 ml. The analysed peak fraction derived from the third purification step with DEAE-Sepharose as column material showed a retention volume of 14.2 ml and, therefore, can be assigned as monomeric form of PSIIcc. The chromatography runs are depicted in Figure 4.15.

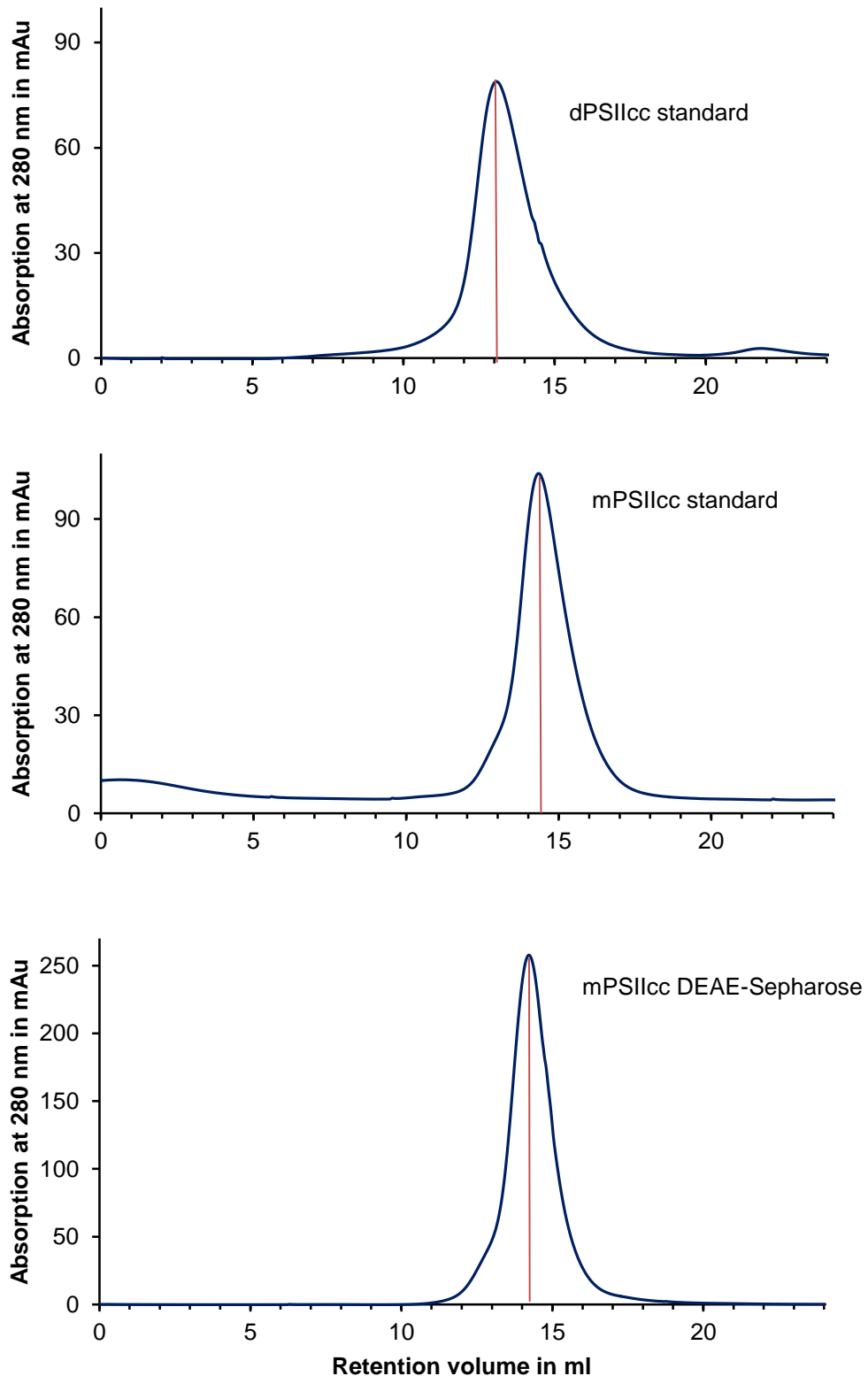


Figure 4.15 Gel permeation chromatography of mPSIIcc and dPSIIcc solutions.

The first two chromatograms are of dPSIIcc and mPSIIcc purified under standard conditions as described in (23, 86) with retention volumes of 13.1 and 14.3 ml, respectively. The mPSIIcc sample from the purification with DEAE-Sepharose matrix elutes in one single peak at 14.2 ml and can therefore be assigned to pure mPSIIcc. Absorption at 280 nm is depicted in dark blue and the red vertical lines indicate the peak positions.

Mass spectrometry

Matrix-assisted laser desorption/ionization time-of-flight mass spectrometry (MALDI-TOF MS) was used to investigate the protein composition and purity of mPSIIcc after the third purification step. The accuracy of the mass determination together with the available sequence data allows the confirmation of the presence of protein subunits in the sample, especially for the low molecular weight subunits. For larger proteins (> 30 kDa) only broad peaks are obtained, making the assignment of peaks to different PSIIcc subunits difficult. The contamination of the protein sample with ATP synthase can be detected, as the presence of subunit c of ATP synthase at 8235 Da can be monitored.

A dPSIIcc sample was used as standard and a comparison of the MALDI-TOF MS spectra of dPSIIcc and mPSIIcc samples, including the three parts A, B and C of the mPSIIcc peak, is shown in Figure 4.16. All samples show the same MALDI-TOF MS spectra and, thus, have an identical protein composition. The differences in the peak intensities are most likely caused by small variations of the crystallization grade of the sinalpinic acid matrix that influence the ionisation of the proteins. Masses for the subunits PsbE, PsbF, PsbH, PsbI, PsbJ, PsbK, PsbL, PsbM, PsbO, PsbT, PsbU, PsbV, PsbX, PsbY, ycf12 and PsbZ were detected in all samples. The masses of the larger subunits D1, D2, CP43 and CP47 could not be determined due to their unfavorable flight behaviour. A mass peak for subunit c of ATP synthase at 8235 Da was only detected in the sample of mPSIIcc containing all fractions and in mPSIIcc fraction A. This means that the first part of the mPSIIcc peak fraction is still contaminated with ATP synthase and the separation is not yet complete. The theoretical and experimental determined masses of the smaller subunits are summarized in Table 4. Note, MALDI-TOF-MS is only a qualitative analysis and the peak intensities cannot be related to the concentration of the subunits.

4. X-ray absorption spectroscopy on PSIIcc

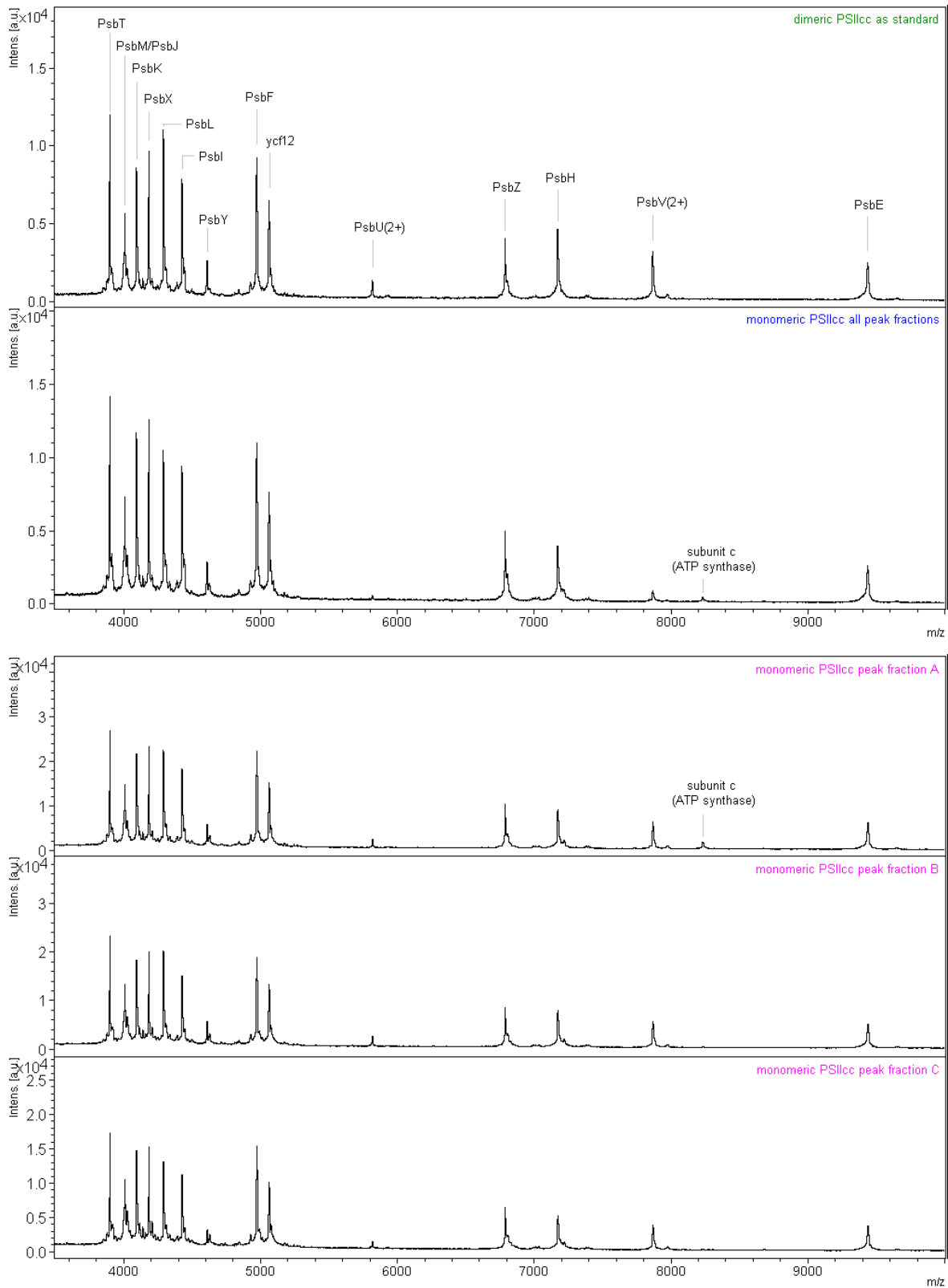


Figure 4.16 MALDI-TOF MS spectra of mPSIIcc and dPSIIcc.

MALDI-TOF MS spectra of dPSIIcc is shown for comparison in the first panel and mass peaks of the small subunits are labelled (double ionized masses at $1/2$ m/z are labelled (2+)). A mass peak for subunit c of ATP synthase at 8235 Da was detected in the sample of mPSIIcc containing all fractions and in mPSIIcc fraction A (as indicated) and is absent in mPSIIcc fractions B and C .

Table 4 Masses of mPSIIcc obtained by MALDI-MS.

Masses obtained by MALDI-MS in the linear mode from mPSIIcc samples. Calculated masses are given as average mass for $[M+H]^+$ from the sequence of the full length precursor protein.

Subunit	cyanobase gene number	calculated mass unprocessed form $[M+H]^+$ in Da	experimental determined mass in m/z
PsbT	tsr1531	3875.8	3897
PsbM	tsl2052	3980.7	4013
PsbJ	tsr1544	4105.9	4017
PsbK	tsl0176	5027.1	4097
PsbX	tsr2013	5233.4	4185
PsbL	tsr1543	4298.1	4294
PsbI	tsr1074	4406.3	4431
PsbY	tsl0836	4773.9	4610
PsbF	tsr1542	5066	4974
ycf12	tsr1242	5038.2	5063
PsbZ	tsr1967	6765.2	6790
PsbH	tsl1386	7355	7176
PsbE	tsr1541	9573.9	9439
PsbV	tll1285	15018	11642
PsvU	tll2409	18028	15746
PsbO	tll0444	29607.6	26828

Blue native PAGE

Blue native PAGE (BN-PAGE) was performed to analyse the different fractions of the mPSIIcc containing peak in terms of their purity. As a native PAGE is run under non-denaturing conditions, the protein complexes do not split in their subunits. Hence, the complexes can be detected as one band in the gel. The proteins PSIIcc (a trimer) and dPSIIcc were loaded onto the gel as size markers. Figure 4.17 shows a BN-PAGE of PSIIcc, dPSIIcc and the mPSIIcc before and after the third purification, including fractions A, B and C as well as P1 and P2 (see (180)) from the monomer containing peak. The mPSIIcc sample before the third column run (lane 2 in Fig. 4.17) shows a faint band at the same height of dPSIIcc. This band is also visible in one sample of peak fraction P2 (lane 4 in Fig. 4.17) as well as in peak fraction C (lane 8 in Fig. 4.17). This indicates a slight contamination of these mPSIIcc fractions with dPSIIcc and might explain the different crystallization behavior of peak fraction P2 as observed in (180).

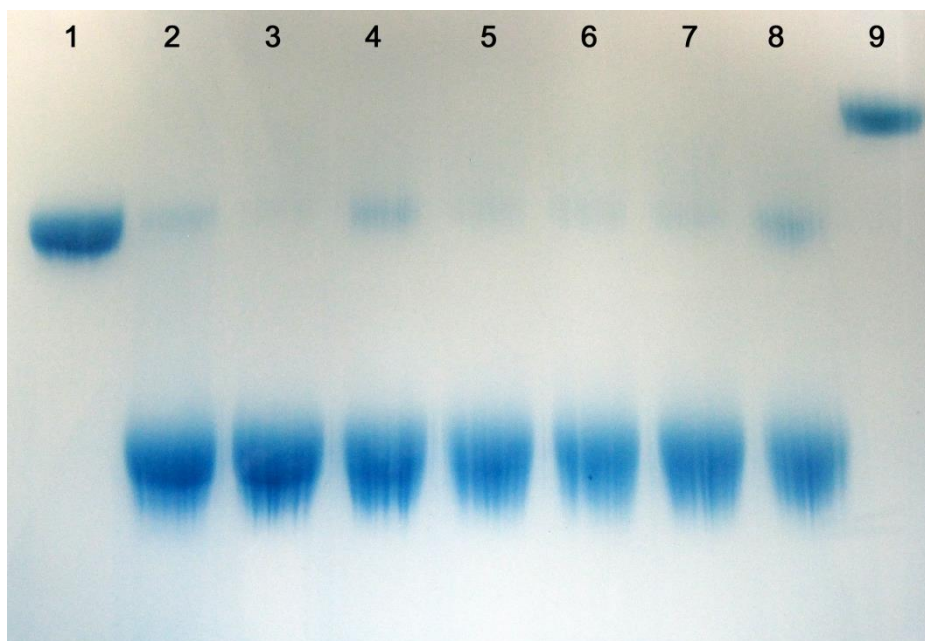


Figure 4.17 Blue native PAGE of PSIIcc, dPSIIcc and mPSIIcc samples.

Blue native PAGE of mPSIIcc peak fraction before and after the third purification step, with PSIIcc trimer and dPSIIcc as size markers. Lane 1: dPSIIcc; lane 2: mPSIIcc containing peak after the second purification step; lane 3: mPSIIcc peak fraction P1; lane 4 and 5: mPSIIcc peak fraction P2 (two different preparations); lane 6: mPSIIcc peak fraction A; lane 7: mPSIIcc peak fraction B; lane 8: mPSIIcc peak fraction C; lane 9: PSIIcc.

4.6.3 Crystallization screens

Based on the above described results of the peak fraction characterization, the mPSIIcc peak fraction B was used for initial crystallization screens. In this fraction no contaminations with proteins such as ATP synthase and dPSIIcc were detected with the applied methods. However, in the tested screens and with the used protein concentrations no crystals of mPSIIcc were obtained so far. Instead, phase separation was observed in many cases and also no changes occurred in various set-ups. The condition similar to the one used for the crystallization of mPSIIcc purified according to the protocol described in (180) did neither yield crystals. It has to be stated here, that the mPSIIcc middle peak fraction B might still contain very small and undetectable amounts of ATP synthase and/or dPSIIcc as an entire separation from the adjacent peak fractions A and C is not possible. These minor contaminations could prevent the formation of mPSIIcc crystals.

4.7 Summary

The structural changes which occur during the S state transitions of the Mn_4CaO_5 cluster in the OEC were investigated using XAS. For the first time *T. elongatus* dPSIIcc solution samples were studied and structural information about the Mn_4CaO_5 cluster, gained from

the recent 1.9 Å resolution XRD crystal structure of dPSIIcc (25), could be incorporated in the obtained spectroscopic data. Thus, the present work closes the gap between XRD studies on cyanobacterial dPSIIcc crystals and EXAFS studies on the catalytic cycle using spinach thylakoid membranes. Also, the discrepancies in the Mn-ligand and Mn-Mn distances in the S_1 state as obtained from XRD and EXAFS data were addressed. The recent XRD crystal structure model of the Mn_4CaO_5 cluster was found to contain about 25% of reduced Mn atoms due to the radiation damage (25). Even though this Mn(II) content is almost three quarters less than compared to former XRD crystal structures (19-22, 24), the present study found the damage to be still too high to approach the intact S_1 state structure of the Mn_4CaO_5 cluster. This was shown by comparing the XAS spectra of S_1 state dPSIIcc solution samples with 0, 5, 10 and 25% of reduced Mn. Additionally, it was demonstrated that the reduction of the Mn_4CaO_5 cluster during XRD does not go through the catalytic path, as also the XAS spectra of dPSIIcc solution samples in the S_0 state are clearly different from the spectra of the 25% damaged sample.

The EXAFS spectra presented in this study and the curve fitting results of the dPSIIcc S states show that the structure of the Mn_4CaO_5 cluster changes during the catalytic cycle. In particular, the short Mn-Mn interactions undergo distance changes in the range of 2.7 to 2.8 Å. In this work, a model for the structural changes is proposed in which the Mn_4CaO_5 cluster in the S_1 and S_2 states is assumed to have an open-cubane like structure. That is supported by theoretical calculations but stands in contrast to the 1.9 Å XRD crystal structure model (25). In the S_2 to S_3 state transition, substantial changes in the XAS spectra were observed and it is suggested that the geometry of the whole Mn_4CaO_5 cluster changes due to the shuffling of oxygen O5 from the Mn1 to the Mn4 side, leading to a closed-cubane like structure in the S_3 state. The relative position of the bridging oxygen O5 in the Mn_4CaO_5 cluster may play a critical role during the S state transition. However, elucidating the nature of the electronic structural changes in the S_2 to S_3 state transition may require complete understanding of the S_2 and S_3 states. Furthermore, combining the present data with results of former studies it is implied that the Mn-Ca binding modes are changed during the S_2 to S_3 state transition.

More detailed information on the shortening or elongation of Mn distances during the S state transitions can be gained from polarized EXAFS studies on single PSIIcc crystals. These studies provide more precise orientational information and especially polarized EXAFS studies on crystals of the monomeric form of PSIIcc are advantageous due to the orientation of the membrane normal vector (corresponding to the non-crystallographic $C2$ axis of dPSIIcc) perpendicular ($\sim 87^\circ$) to the crystallographic b -axis. In the present study, mPSIIcc solution samples were showed to be suitable for XAS measurements as the

obtained spectra of the S_1 state are similar to the ones of dPSIIcc. However, XAS measurements on single crystals of mPSIIcc revealed a relatively high amount of free Mn(II) which was detected by the K-edge shift in the XANES spectra by about 1.2 eV relative to the XANES spectra of dPSIIcc crystals. Using oxygen evolution measurements and EPR studies, the reason for the Mn reduction and release from the Mn_4CaO_5 cluster was found to be the high amount of $CaCl_2$ (0.2 M) necessary for the crystallization of mPSIIcc. In order to still perform EXAFS experiments with single crystals of mPSIIcc, different crystallization conditions are needed which avoid the reduction of Mn atoms. Therefore, initial experiments toward a different purification protocol that might lead to improved crystallization conditions are reported in this work. It was possible to perform the last purification step for mPSIIcc with a DEAE-Sepharose matrix at pH 5.5, yielding a mPSIIcc fraction being highly active in oxygen evolution and entire in its subunit composition. For crystallization screens however, only one part of the mPSIIcc peak could be used as still slight contaminations with ATP synthase and dPSIIcc were detected in the border peak fractions (fraction A and C). So far no crystals were obtained, but the here presented results are a first important step toward new crystallization conditions.

5. Outlook

In order to provide a further understanding of the effect of herbicide binding to the Q_B pocket it is necessary to also co-crystallize PSIIcc with a phenolic herbicide. These studies could provide the structural basis for a deeper understanding of the opposite influence that triazine and phenolic herbicides bound to the Q_B site exert on the redox potential of Q_A . Moreover, understanding the influence of herbicides on photoinhibition would also benefit from structural information on phenolic herbicide binding to PSIIcc. In the case that herbicide binding caused the detected chloride movement at the donor side of dPSIIcc, a structural model of PSIIcc with a bound phenolic herbicide could possibly give a further indication. Also, the elucidation of herbicide binding at a higher crystal structure resolution may reveal the involvement of water molecules in stabilizing herbicide binding at the Q_B pocket. One way to achieve higher crystal structure resolutions could be the introduction of the detergent HTG (in addition to β DM) into the preparation of *T. elongatus* PSIIcc, as used in (25). A combination with the dehydration protocol of the crystals prior to XRD experiments as reported in (25) might lead to a further improvement of the crystal structure resolution.

As also different native PSIIcc crystal structures assigned distinct numbers of chloride ions – an effect that is ascribed to the various amount of $CaCl_2$ used in the purification protocols – it is important to clarify the natural chloride amount in PSII. Future work should address this issue by controlled variations of the chloride content in the PSIIcc preparations and subsequent crystallographic analysis.

Radiation damage to redox-active metalloproteins even at cryogenic temperatures is the big limitation of XRD using synchrotron radiation (267). Therefore, a further improvement in the crystallographic data using classical XRD is a doubtful way to obtain more structural information about the Mn_4CaO_5 cluster.

One possible way to avoid radiation damage is the use of neutron crystallographic studies. This method is non-destructive for the Mn_4CaO_5 cluster or the PSIIcc protein matrix and additionally, it is much easier to locate water molecules or even hydrogen. The applicability of neutron crystallography, however, is still limited due to little suitable neutron sources.

Another way to avoid radiation damage is the very recently reported “probe before destroy” approach of XRD (123). In this approach, femtosecond X-ray laser pulses are used and diffraction data is collected before the onset of radiation damage. Besides avoiding radiation damage, this method also provides the advantage of data collection at room temperature, which represents the functional temperature of PSII in nature. The “probe before destroy” method can also be applied to several PSIIcc crystal variations

including PSIIcc/herbicide co-crystals. Note, that microcrystals are needed for the current set-up at LCLS.

Initial experiments toward the optimization of mPSIIcc crystallization were performed in the present work, but crystals were not yet obtained and further improvement is needed. Concerning the newly developed last purification step of mPSIIcc, further work should be investigated in the variation of buffer conditions (e.g. the pH, salt concentrations, buffer system) and the salt gradient applied in the chromatographic runs in order to achieve one highly pure mPSIIcc fraction. Concerning mPSIIcc crystallization, future work should include a broader bandwidth of crystallization screens, including variations of the protein concentration as well as the temperature. Once new crystallization conditions for mPSIIcc are established, XRD measurements should also be conducted to possibly improve the current crystal structure resolution of 3.6 Å. This could enlarge the knowledge about dimer formation of PSII and the role of lipids in that context. Similar to dPSIIcc, an improvement of the diffraction quality of mPSIIcc crystals may also be achieved with the introduction of the detergent HTG into the protein preparation, in combination with the crystal dehydration procedure prior to XRD measurements as applied in (25).

New directions for dynamic studies just opened with the groundbreaking approach of simultaneous XRD/XES on dPSIIcc microcrystals at room temperature reported by Kern *et al.* (111). The XFEL of LCLS was used to get undamaged diffraction data of dPSIIcc (in the S_1 and in S_2 states) and simultaneously XES data were collected to get information about the Mn oxidation states in the Mn_4CaO_5 cluster. The diffraction data were processed to a resolution of 5.7 Å (S_1 state) and 5.9 Å (S_2 state), but at this resolution no small structural changes between the S_1 and S_2 state can be resolved. The XES data do not have an optimal signal to noise level yet, but clearly demonstrated that the Mn_4CaO_5 cluster is not photo-reduced by the used optical illumination pump protocol or the X-ray pulse. The simultaneous XRD/XES method is just at the beginning, but gives many possibilities for future dynamic studies. It provides for example the possibility to investigate the interplay between the donor and acceptor side, as upon every S state transition a picture of the acceptor side is likewise obtained and changes can be investigated. Also, chloride movement could be tracked during the S state transitions and could elucidate its role.

In a long and stepwise progress, photosynthesis research gets more and more insight into the natural water oxidation and oxygen formation, a photochemical process that is performed by cyanobacteria, algae and plants every day as a matter of course.

Appendix

Table A.1 EXAFS fit table for the S_0 , S_1 and S_2 states.

The following parameter values were used: $k = 2.4 - 11.3$ (\AA^{-1}), $E_0 = 6561.30$ eV, $S_0^2 = 0.85$. The bold letters show the fixed parameters. The σ^2 values of shorter Mn-O and longer Mn-O/Mn-N interactions were linked, and assumed to be the same (shown in italic letters). In the same manner the σ^2 values of ~ 2.7 \AA Mn-Mn and ~ 2.8 \AA Mn-Mn interactions were linked. The numbers in parenthesis show the results when the N ratio of the shorter vs. longer Mn-Ca interactions is fixed to 0.75:0.25.

	S_0			S_1			S_2		
Path	R	N	σ^2	R	N	σ^2	R	N	σ^2
MnO	1.91	4.5 (4.4)	<i>0.009</i>	1.86	3.9	<i>0.005</i>	1.86	4.1	<i>0.006</i>
MnO/N	2.26	1.5 (1.6)	<i>0.009</i>	2.05	2.1	<i>0.005</i>	2.02	1.9	<i>0.006</i>
MnMn	2.68	0.5	<i>0.002</i>	2.71	1.0	<i>0.002</i>	2.74	1.5	0.002
MnMn	2.77	1.0	<i>0.002</i>	2.79	0.5	<i>0.002</i>			
MnMn	3.30	0.5	0.007	3.28 (3.27)	0.5	0.002 (0.003)	3.30	0.5	0.005
MnC*	3.05 (3.04)	1.5	0.005	2.99 (3.00)	1.5	0.005	2.99	1.5	0.005
MnCa	3.36	0.5 (0.75)	0.007	3.36	0.5 (0.75)	0.007	3.36	0.5 (0.75)	0.007
MnCa	3.99	0.5 (0.25)	0.015	3.99	0.5 (0.25)	0.008	3.99	0.5 (0.25)	0.008
MnO*	3.34	2.5	0.015	3.14	2.5	0.091 (0.085)	3.14	2.5	0.086
R factor (%)	3.5 (3.7) $\Delta E = -7.2$ (-6.8)			1.8 (2.0) $\Delta E = -9.8$ (-9.5)			2.8 (2.6) $\Delta E = -8.0$ (-8.3)		

* Mn-C interactions (Mn to C of carboxylates) and Mn-O interactions (Mn to O of carboxylates) were included in the fit, although their contribution is minor.

Table A.2 EXAFS fit table for the S₃ state.

For detailed description see Table A.1.

Path	S ₃ fitA			S ₃ fitB		
	R	N	σ^2	R	N	σ^2
MnO	1.84 (1.88)	3.5 (6.0)	0.005 (0.009)	1.85	3.8	0.004
MnO/N	1.97 (2.14)	2.5 (0.0)	0.005 (0.009)	1.99 (2.00)	2.2 (2.1)	0.004
MnMn	2.75	1.0	0.002	2.72 (2.76)	1.0	0.002 (0.003)
MnMn	2.79 (2.78)	0.5	0.002	2.82 (2.78)	1.0	0.002 (0.003)
MnMn	3.26	0.5	0.002			
MnC*	2.96	1.5	0.005	3.58 (2.96)	1.5	0.005
MnCa	3.37 (3.36)	0.5 (0.75)	0.007 (0.009)	3.34 (3.31)	0.5 (0.75)	0.002
MnCa	3.99	0.5 (0.25)	0.009 (0.015)	3.99	0.5 (0.25)	0.009
MnO*	3.06	2.5	0.015	3.08 (3.06)	2.5	0.015
R factor (%)	2.6 (2.7) $\Delta E = -8.8 (-9.6)$			4.5 (3.1) $\Delta E = -7.9 (-7.1)$		

* Mn-C interactions (Mn to C of carboxylates) and Mn-O interactions (Mn to O of carboxylates) were included in the fit, although their contribution is minor.

Table A.3 EXAFS fit table for 5%, 10% and 25% damaged dPSIlcc solution samples.

The following parameter values were used: $k = 2.4 - 11.4$ (\AA^{-1}), $S_0 = 0.85$.

5% damage				
Path	R	N	σ^2	R (%)
MnO18	1.85	3.4	0.007	4.2 $E_0 = -15.0$
MnO/N20	2.03	2.6	0.012	
MnMn27	2.73	1.1	0.005	
MnMn32	3.28	1.0	0.004	
MnCa34	3.61	0.75	0.010	
10% damage				
MnO18	1.86	3.2	0.007	4.6 $E_0 = -14.6$
MnO/N20	2.09	2.8	0.014	
MnMn27	2.73	0.6	0.003	
MnMn32	3.27	1.2	0.049	
MnCa34	3.61	0.75	0.010	
25% damage				
MnO18	1.88	3.0	0.008	3.7 $E_0 = -14.2$
MnO/N20	2.12	3.0	0.017	
MnMn27	2.75	0.2	0.003	
MnMn32	3.26	1.5	0.011	
MnCa34	3.61	0.75	0.030	

List of Figures and Tables

Figures

Figure 1.1 Chemical structures of light absorbing pigments in cyanobacteria.	3
Figure 1.2 Absorption spectra of photosynthetic pigments.	4
Figure 1.3 Structure of lipids in thylakoid membranes.	6
Figure 1.4 Schematic view of the thylakoid membrane with protein complexes involved in oxygenic photosynthesis.	7
Figure 1.5 Z-scheme of photosynthesis.	9
Figure 1.6 Schematic representation of components of PSIIcc in cyanobacteria.	12
Figure 1.7 Cofactor arrangements in dPSIIcc.	13
Figure 1.8 General architecture of dPSIIcc according to the structural model at 2.9 Å resolution.	15
Figure 1.9 Cluster of lipids forming a bilayer structure within dPSIIcc.	21
Figure 1.10 Kok-cycle of water oxidation.	23
Figure 1.11 Extended S state cycle.	24
Figure 1.12 Structure of the Mn ₄ CaO ₅ cluster.	25
Figure 1.13 Ligands of the Mn ₄ CaO ₅ cluster.	26
Figure 1.14 Possible trajectories of substrate and product channels leading to and away from the OEC as obtained by the cavity search algorithm method.	29
Figure 1.15 Possible trajectories of water molecules leading to and away from the Mn ₄ CaO ₅ cluster.	31
Figure 1.16 Two chloride binding sites in the vicinity of the Mn ₄ CaO ₅ cluster.	32
Figure 1.17 Structure of the acceptor side of dPSIIcc.	34
Figure 1.18 Positions of the head groups of the Q _A and Q _B cofactors.	35
Figure 1.19 Calculated channels for PQ/PQH ₂ exchange.	38
Figure 1.20 Simplified scheme for possible charge recombination pathways of P _{D1} ⁺⁺ Q _A ⁻	39
Figure 1.21 Orientation of the membrane normal vector in mPSIIcc crystals.	41
Figure 2.1 Schematic illustration of X-ray photon absorption.	52
Figure 2.2 Schematic illustration of K-edge and L-edge transitions for Mn(II).	53
Figure 2.3 XANES and EXAFS spectra of Mn XAS of dPSIIcc samples.	54
Figure 2.4 Schematic illustration of the outgoing and backscattered photoelectron wave.	56
Figure 3.1 Structural formulas of the triazine herbicides DCMU and terbutryn, and the phenolic herbicide ioxynil.	61
Figure 3.2 Terbutryn titration by flash-induced fluorescence measurements.	64
Figure 3.3 Plastoquinone bound to the Q _B site of native dPSIIcc.	67
Figure 3.4 Superposition of plastoquinone and terbutryn binding in dPSIIcc.	68
Figure 3.5 Terbutryn binding in the dPSIIcc/terbutryn crystal structure.	68

Figure 3.6 Terbutryn binding in the pbRC/terbutryn crystal structure.....	69
Figure 3.7 Plastoquinone binding in the crystal structure of native dPSIIcc at 1.9 Å resolution.	71
Figure 3.8 Superposition of bicarbonate in the native and terbutryn-bound dPSIIcc crystal structures.....	72
Figure 3.9 The Q_A -His214D-Fe-His215A- Q_B bridge in the native and terbutryn bound dPSIIcc crystal structures.....	73
Figure 3.10 Opposition of chloride binding sites in both native dPSIIcc crystal structures.	74
Figure 3.11 Positions of chloride ions in the crystal structure of the dPSIIcc/terbutryn complex at 3.2 Å resolution.....	75
Figure 3.12 Opposition of chloride binding sites in the native dPSIIcc (2.9 Å resolution) and in the dPSIIcc/terbutryn crystal structure.....	76
Figure 3.13 Opposition of chloride binding sites in the native dPSIIcc (1.9 Å resolution) and in the dPSIIcc/terbutryn crystal structure.....	77
Figure 3.14 Chloride positions found according to the dPSIIcc/terbutryn crystal structure relative to calculated channels leading from the Mn_4Ca cluster to the lumen.	79
Figure 4.1 Proposed models of the Mn_4Ca cluster in the S_1 state.	83
Figure 4.2 XANES spectra of dPSIIcc solution samples in the S_0 , S_1 , S_2 , and S_3 states.	86
Figure 4.3 EXAFS and FT spectra of dPSIIcc solutions in the S_0 , S_1 , S_2 and S_3 states....	88
Figure 4.4 FT from Mn EXAFS curve fitting result of dPSIIcc solution in S_0 to S_3 states...89	
Figure 4.5 Possible structural changes of the Mn_4CaO_5 cluster during the S state transitions.	92
Figure 4.6 XAS spectra of dPSIIcc solution sample with 0, 5, 10 and 25% of reduced Mn.	96
Figure 4.7 Comparison of the EXAFS FT spectra of dPSIIcc solution sample in the S_1 and S_0 state with 25% reduced S_1 state.	97
Figure 4.8 XAS spectra of mPSIIcc and dPSIIcc solution compared with spinach PSII thylakoid membrane fragments.....	99
Figure 4.9 Amino acid residues within a radius of 20 Å around the Mn_4Ca cluster.	100
Figure 4.10 XAS on mPSIIcc single crystals.	102
Figure 4.11 Comparison of XAS on mPSIIcc and dPSIIcc single crystals.	103
Figure 4.12 EPR measurements of mPSIIcc samples compared to the Mn(II)-hexaquo complex.	104
Figure 4.13 Separation chromatogram of mPSIIcc and ATP synthase at pH 5.5.....	106
Figure 4.14 Purification of mPSIIcc at pH 5.5 on DEAE-Sepharose matrix.	107
Figure 4.15 Gel permeation chromatography of mPSIIcc and dPSIIcc solutions.	109

Figure 4.16 MALDI-TOF MS spectra of mPSIIcc and dPSIIcc.....	111
Figure 4.17 Blue native PAGE of PSIcc, dPSIIcc and mPSIIcc samples.....	113

Tables

Table 1.1 Equations of oxygenic photosynthesis.....	8
Table 1.2 Comparison of lipid and detergent content (per monomer) in dPSIIcc crystal structures from <i>T. elongatus</i> at 2.9 Å resolution and <i>T. vulcanus</i> at 1.9 Å resolution.....	19
Table 1.3 Ligands of the manganese and calcium ions of the Mn_4CaO_5 cluster.....	27
Table 1.4 Overview the channel nomenclature.....	30
Table 1.5 Differences in the subunit and cofactor compositions (per monomer) between the structural models of dPSIIcc crystals at 2.9 Å and 1.9 Å resolution.....	43
Table 3 Data collection and refinement statistics.....	66
Table 4 Masses of mPSIIcc obtained by MALDI-MS.....	112
Table A.1 EXAFS fit table for the S_0 , S_1 and S_2 states.....	119
Table A.2 EXAFS fit table for the S_3 state.....	120
Table A.3 EXAFS fit table for 5%, 10% and 25% damaged dPSIIcc solution samples.....	121



Danksagung

Zu allererst möchte ich mich bei meiner Betreuerin Prof. Dr. Athina Zouni bedanken. Sie hat mir die Arbeit an dem spannenden und abwechslungsreichen Thema „Photosystem II“ ermöglicht und stand mir stets beratend, motivierend und unterstützend zur Seite. Auch danke ich ihr für die Möglichkeit, an internationalen Kooperationen und Konferenzen teilzunehmen. Ich danke der ganzen PSII-Arbeitsgruppe für die tolle Zeit und die angenehme Arbeitsatmosphäre: Meiner lieben Kollegin und Freundin Julia Hellmich danke ich für die schöne gemeinsame Zeit und all die unvergesslichen und lustigen Erlebnisse auf unseren Mess- und Konferenzreisen. Mit ihr hat selbst das stundenlange Arbeiten im Grünlicht Spaß gemacht. Dr. Matthias Broser danke ich für die umfangreichen Einweisungen und die Übergabe seines Monomer-Projektes. Auch bedanke ich mich bei ihm für seine Unterstützung, die gute Zusammenarbeit, die hilfreichen Gespräche und Ratschläge. Dr. Frank Müh danke ich für die vielen fruchtbaren Diskussionen und seine stets frohe Natur. Bei Selcan Ceylan möchte ich mich für die tolle und zuverlässige Hilfe im Labor bedanken. Dörte DiFiore gilt der größte Dank für all die präparative und technische Unterstützung. Bei meinem ehemaligen Kollegen Dr. Joachim Frank bedanke ich mich für die angenehme Zusammenarbeit.

Auch allen Kollegen aus dem ganzen Max-Volmer Institut danke ich für die stets nette und heitere Atmosphäre. Besonders danke ich Dr. Eberhard Schlodder für die Benutzung einiger seiner Geräte und Lars Paasche dafür, dass er bei technischen Problemen immer meine Rettung war. In Erinnerung an Prof. Dr. Gernot Renger bedanke ich mich für die zahlreichen Anregungen und Anekdoten aus der Photosynthese-Welt. Für die Finanzierung dieses Projektes im Rahmen des Exzellenzclusters UniCat (Teilprojekt B1) bin ich sehr dankbar.

Der Arbeitsgruppe von Vittal Yachandra in Berkeley (USA) danke ich für die stets so motivierende und produktive Zusammenarbeit. Auch wenn die Messzeiten noch so anstrengend und manchmal auch zum Verzweifeln waren, blieb die Stimmung immer positiv. Das Team hat mich durch seinen Enthusiasmus begeistert und ich denke mit Freude an die Zeiten in Berkeley zurück. Ein ganz besonderer Dank gilt Dr. Jan Kern. Neben seiner Offenheit, mich bei seiner Familie wohnen zu lassen und mir mit konstruktiven Korrekturen bezüglich dieser Arbeit zu helfen, wird er nie müde, Zusammenhänge zu erklären. Dr. Junko Yano danke ich ganz besonders für alle EXAFS „curve fittings“, die ausführliche Datenauswertung und die vielen hilfreichen Erklärungen.

Dem ehemaligen Kristallographie-Team von Prof. Dr. Wolfram Saenger (FU Berlin) danke ich für die nette Zusammenarbeit und umfangreiche Datenauswertung. Besonders

bedanke ich mich bei Dr. Azat Gabdulkhakov und Dr. Albert Guskov, für die Modellierung der dPSIIcc/Terbutryn-Komplex Struktur.

Prof. Dr. Holger Dau (FU Berlin) und Dr. Joachim Buchta danke ich für die produktive Zusammenarbeit bezüglich der Fluoreszenzmessungen. Ebenso bedanke ich mich bei Dr. Christoph Weise (FU Berlin) für die MALDI-TOF-MS Messungen. Sabine Kussin und Neslihan Tavraz aus der Arbeitsgruppe von Prof. Dr. Thomas Friedrich (TU Berlin) danke ich für ihre Assistenz und Hilfe bei der Durchführung der BN-PAGE Experimente.

Bei Prof. Dr. Holger Dobbek (HU Berlin) bedanke ich mich für das Zurverfügungstellen von diversen Beamzeiten und für seine Bereitschaft diese Arbeit zu begutachten. Dr. Martin Bommer danke ich für seine Assistenz und Hilfe am BESSY und bei der Benutzung des Kristallisationsroboters.

Ich möchte mich bei Prof. Dr. Thomas Friedrich (TU Berlin) für seine Bereitschaft diese Arbeit zu begutachten und bei Prof. Dr. Thorsten Ressler (TU Berlin) für seine Funktion als Prüfungs-Vorsitzender bedanken.

Ein ganz großes Dankeschön an meine Eltern Monika und Hansjörg, meinen Bruder Mario und meine Freundinnen Stephanie Duus und Maike Schäfer, die mich alle während der ganzen Zeit und besonders in der letzten Phase dieser Arbeit bedingungslos unterstützt haben. Dank ihrer vielen Babysitter-Dienste haben sie mir mehr Zeit zum Schreiben verschafft. Meinem Sohn Elian danke ich von ganzem Herzen dafür, dass er bei uns ist und für all die Freude, die er uns jeden Tag schenkt. Mein allergrößter Dank gilt meinem wundervollen Mann Cesar Ceballos für seine fortwährende Geduld, Unterstützung, Motivation und für die vielen zusätzlichen Stunden ungestörten Schreibens, die er mir ermöglicht hat.

References

1. Holleman, A. F., Wiberg, N. (2007) *Lehrbuch der Anorganischen Chemie*, Vol. 102, de Gruyter, Berlin.
2. Schmidt, R. F., Thews, G. (1995) *Physiologie des Menschen*, Springer, Berlin.
3. Kunsch, K., Kunsch, S. (2000) *Der Mensch in Zahlen*, Spektrum Akademischer Verlag, Heidelberg.
4. Laufmann, P. (2013) Tief-Durch-Atmen!, Bayerische Staatsforsten AöR, Regensburg, online at http://www.baysf.de/de/home/unternehmen_wald/aktuelles/detailansicht/article/94/tief-durch-atmen-1.html (17th of April 2013).
5. Ke, B. (2001) *Photosynthesis - Photobiochemistry and Photophysics*, Vol. 10, Kluwer Academic Publishers, Dordrecht, Netherlands.
6. Najafpour, M. M., Moghaddam, A. N., Allakhverdiev, S. I., and Govindjee. (2012) Biological water oxidation: Lessons from Nature, *Biochim. Biophys. Acta* 1817, 1110-1121.
7. Renger, G. (2008) Overview of Primary Processes of Photosynthesis, In *Primary Processes of Photosynthesis - Principles and Apparatus* (Renger, G., Ed.), pp 5-35, RSC Publishing, Cambridge.
8. Björn, L., Papageorgiou, G., Blankenship, R., and Govindjee. (2009) A viewpoint: Why chlorophyll a?, *Photosynth. Res.* 99, 85-98.
9. Mimuro, M., Kobayashi, M., Murakami, A., Tsuchiya, T., Miyashita, H. (2008) Oxygen-Evolving Cyanobacteria, In *Primary Processes of Photosynthesis: Principles and Apparatus* (Renger, G., Ed.), pp 261-299, RSC Publishing, Cambridge.
10. Pilon, L., Berberoğlu, H., and Kandilian, R. (2011) Radiation transfer in photobiological carbon dioxide fixation and fuel production by microalgae, *J. Quant. Spectrosc. Radiat. Transfer* 112, 2639-2660.
11. Buick, R. (2008) When did oxygenic photosynthesis evolve?, *Philos. Trans. R. Soc. Lond., B, Biol. Sci.* 363, 2731-2743.
12. Yamaoka, T., Satoh, K., Katoh, S. (1978) Photosynthetic activities of a thermophilic blue-green alga, *Plant Cell Physiol.* 19, 943-954.
13. Zouni, A. (2008) From Cell Growth to the 3.0 Å Resolution Crystal Structure of Cyanobacterial Photosystem II, In *Primary Processes of Photosynthesis: Principles and Apparatus* (Renger, G., Ed.), pp 193-236, RSC Publishing, Cambridge.
14. Kern, J., Zouni, A., Guskov, A., Krauß, N. (2009) Lipids in the Structure of Photosystem I, Photosystem II and the Cytochrome *b₆f* Complex, In *Lipids in Photosynthesis* (Wada, H., Murata N., Ed.), pp 203-242, Springer, Dordrecht.
15. Mizusawa, N., and Wada, H. (2012) The role of lipids in photosystem II, *Biochim. Biophys. Acta* 1817, 194-208.
16. Taiz, L., Zeiger, E. (2006) *Plant Physiology, Fourth Edition*, Sinauer Associates, Inc., Sunderland, Massachusetts.
17. Horton, H. R., Moran, L. A., Scrimgeour, K. G., Perry, M. D., Rawn, J. D. (2008) *Biochemie, 4. aktualisierte Auflage*, Pearson Studium, München.
18. Deisenhofer, J., Epp, O., Miki, K., Huber, R., and Michel, H. (1984) X-ray structure analysis of a membrane protein complex. Electron density map at 3 Å resolution and a model of the chromophores of the photosynthetic reaction center from *Rhodospseudomonas viridis*, *J. Mol. Biol.* 180, 385-398.
19. Zouni, A., Witt, H.-T., Kern, J., Fromme, P., Krauß, N., Saenger, W., and Orth, P. (2001) Crystal Structure of Photosystem II from *Synechococcus elongatus* at 3.8 Å Resolution, *Nature* 409, 739-743.
20. Ferreira, K. N., Iverson, T. M., Maghlaoui, K., Barber, J., and Iwata, S. (2004) Architecture of the photosynthetic oxygen-evolving center, *Science* 303, 1831-1838.

21. Loll, B., Kern, J., Saenger, W., Zouni, A., and Biesiadka, J. (2005) Towards complete cofactor arrangement in the 3.0 Å resolution structure of photosystem II, *Nature* 438, 1040-1044.
22. Guskov, A., Kern, J., Gabdulkhakov, A., Broser, M., Zouni, A., and Saenger, W. (2009) Cyanobacterial photosystem II at 2.9 Å resolution: role of quinones, lipids, channels and chloride, *Nat. Struct. Mol. Biol.* 16, 334 - 342.
23. Broser, M., Gabdulkhakov, A., Kern, J., Guskov, A., Müh, F., Saenger, W., and Zouni, A. (2010) Crystal structure of monomeric photosystem II from *Thermosynechococcus elongatus* at 3.6 Å resolution, *J. Biol. Chem.* 285, 26255-26262.
24. Kamiya, N., and Shen, J. R. (2003) Crystal structure of oxygen-evolving photosystem II from *Thermosynechococcus vulcanus* at 3.7 Å resolution, *Proc. Natl. Acad. Sci. U.S.A.* 100, 98-103.
25. Umena, Y., Kawakami, K., Shen, J. R., and Kamiya, N. (2011) Crystal structure of oxygen-evolving photosystem II at a resolution of 1.9 Å, *Nature* 473, 55-60.
26. Adachi, H., Umena, Y., Enami, I., Henmi, T., Kamiya, N., and Shen, J. R. (2009) Towards structural elucidation of eukaryotic photosystem II: Purification, crystallization and preliminary X-ray diffraction analysis of photosystem II from a red alga, *Biochim. Biophys. Acta* 1787, 121-128.
27. Piano, D., El Alaoui, S., Korza, H. J., Filipek, R., Sabala, I., Haniewicz, P., Buechel, C., De Sanctis, D., and Bochtler, M. (2010) Crystallization of the photosystem II core complex and its chlorophyll binding subunit CP43 from transplastomic plants of *Nicotiana tabacum*, *Photosynth. Res.* 106, 221-226.
28. Watanabe, M., Iwai, M., Narikawa, R., and Ikeuchi, M. (2009) Is the photosystem II complex a monomer or a dimer?, *Plant Cell Physiol.* 50, 1674-1680.
29. Takahashi, T., Inoue-Kashino, N., Ozawa, S., Takahashi, Y., Kashino, Y., and Satoh, K. (2009) Photosystem II complex in vivo is a monomer, *J. Biol. Chem.* 284, 15598-15606.
30. Nixon, P. J., Michoux, F., Yu, J., Boehm, M., and Komenda, J. (2010) Recent advances in understanding the assembly and repair of photosystem II, *Ann. Bot.* 106, 1-16.
31. Michel, H., and Deisenhofer, J. (1988) Relevance of the photosynthetic reaction center from purple bacteria to the structure of photosystem II, *Biochemistry* 27, 1-7.
32. Deisenhofer, J., and Michel, H. (1989) The photosynthetic reaction center from the purple bacterium *Rhodospseudomonas viridis*, *Science* 245, 1463-1473.
33. Feher, G., Allen, J. P., Okamura, M. Y., and Rees, D. C. (1989) Structure and function of bacterial photosynthetic reaction centres, *Nature* 339, 111-116.
34. Govindjee, Kern, J. F., Messinger, J., and Whitmarsh, J. (2010) Photosystem II, In *Encyclopedia of Life Sciences*, John Wiley & Sons, Ltd, Chichester.
35. Müh, F., Glöckner, C., Hellmich, J., and Zouni, A. (2012) Light-induced quinone reduction in photosystem II, *Biochim. Biophys. Acta* 1817, 44-65.
36. Renger, G., and Holzwarth, A. (2005) Primary Electron Transfer, In *Photosystem II: The Light-Driven Water: Plastoquinone Oxidoreductase* (Wydrzynski, T., and Satoh, K., Eds.), pp 139-175, Springer, Dordrecht.
37. Petrouleas, V., and Crofts, A. R. (2005) The iron-quinone acceptor complex, In *Photosystem II: The Light-Driven Water: Plastoquinone Oxidoreductase* (Wydrzynski, T. J., and Satoh, K., Eds.), pp 177-206, Springer, Dordrecht.
38. Lancaster, C. R. (2008) Structures of reaction centers in anoxygenic bacteria, In *Primary processes of photosynthesis: basic principles and apparatus* (Renger, G., Ed.), pp 5-56, RSC Publishing, Cambridge.
39. Parson, W. W. (2008) Functional pattern of reaction centers in anoxygenic photosynthetic bacteria, In *Primary processes of photosynthesis: basic principles and apparatus* (Renger, G., Ed.), pp 57-109, RSC Publishing, Cambridge.

40. Kato, Y., and Sakamoto, W. (2009) Protein quality control in chloroplasts: a current model of D1 protein degradation in the photosystem II repair cycle, *J. Biochem.* **146**, 463-469.
41. Aro, E. M., Virgin, I., and Andersson, B. (1993) Photoinhibition of Photosystem II. Inactivation, protein damage and turnover, *Biochim. Biophys. Acta* **1143**, 113-134.
42. Kós, P. B., Deák, Z., Cheregi, O., and Vass, I. (2008) Differential regulation of *psbA* and *psbD* gene expression, and the role of the different D1 protein copies in the cyanobacterium *Thermosynechococcus elongatus* BP-1, *Biochim. Biophys. Acta* **1777**, 74-83.
43. Sicora, C. I., Ho, F. M., Salminen, T., Styring, S., and Aro, E. M. (2009) Transcription of a "silent" cyanobacterial *psbA* gene is induced by microaerobic conditions, *Biochim. Biophys. Acta* **1787**, 105-112.
44. Loll, B., Broser, M., Kos, P. B., Kern, J., Biesiadka, J., Vass, I., Saenger, W., and Zouni, A. (2008) Modeling of variant copies of subunit D1 in the structure of photosystem II from *Thermosynechococcus elongatus*, *Biol. Chem.* **389**, 609-617.
45. Sugiura, M., Kato, Y., Takahashi, R., Suzuki, H., Watanabe, T., Noguchi, T., Rappaport, F., and Boussac, A. (2010) Energetics in photosystem II from *Thermosynechococcus elongatus* with a D1 protein encoded by either the *psbA1* or *psbA3* gene, *Biochim. Biophys. Acta* **1797**, 1491-1499.
46. Hughes, J. L., Cox, N., Rutherford, A. W., Krausz, E., Lai, T. L., Boussac, A., and Sugiura, M. (2010) D1 protein variants in Photosystem II from *Thermosynechococcus elongatus* studied by low temperature optical spectroscopy, *Biochim. Biophys. Acta* **1797**, 11-19.
47. Ogami, S., Boussac, A., and Sugiura, M. (2012) Deactivation processes in PsbA1-Photosystem II and PsbA3-Photosystem II under photoinhibitory conditions in the cyanobacterium *Thermosynechococcus elongatus*, *Biochim. Biophys. Acta* **1817**, 1322-1330.
48. Guskov, A., Gabdulkhakov, A., Broser, M., Glöckner, C., Hellmich, J., Kern, J., Frank, J., Müh, F., Saenger, W., and Zouni, A. (2010) Recent progress in the crystallographic studies of photosystem II., *ChemPhysChem* **11**, 1160-1171.
49. Müh, F., Renger, T., and Zouni, A. (2008) Crystal structure of cyanobacterial photosystem II at 3.0 Å resolution: a closer look at the antenna system and the small membrane-intrinsic subunits, *Plant Physiol. Biochem.* **46**, 238-264.
50. Koua, F. H., Umena, Y., Kawakami, K., and Shen, J. R. (2013) Structure of Sr-substituted photosystem II at 2.1 Å resolution and its implications in the mechanism of water oxidation, *Proc. Natl. Acad. Sci. U.S.A.* **110**, 3889-3894.
51. Regel, R. E., Ivleva, N. B., Zer, H., Meurer, J., Shestakov, S. V., Herrmann, R. G., Pakrasi, H. B., and Ohad, I. (2001) Deregulation of electron flow within photosystem II in the absence of the PsbJ protein, *J. Biol. Chem.* **276**, 41473-41478.
52. Komenda, J., Tichy, M., and Eichacker, L. A. (2005) The PsbH protein is associated with the inner antenna CP47 and facilitates D1 processing and incorporation into PSII in the cyanobacterium *Synechocystis* PCC 6803, *Plant Cell Physiol.* **46**, 1477-1483.
53. Bergantino, E., Brunetta, A., Touloupakis, E., Segalla, A., Szabo, I., and Giacometti, G. M. (2003) Role of the PSII-H subunit in photoprotection: novel aspects of D1 turnover in *Synechocystis* 6803, *J. Biol. Chem.* **278**, 41820-41829.
54. Komenda, J., Lupinkova, L., and Kopecky, J. (2002) Absence of the *psbH* gene product destabilizes photosystem II complex and bicarbonate binding on its acceptor side in *Synechocystis* PCC 6803, *Eur. J. Biochem.* **269**, 610-619.
55. Mayers, S. R., Dubbs, J. M., Vass, I., Hideg, E., Nagy, L., and Barber, J. (1993) Further characterization of the *psbH* locus of *Synechocystis* sp. PCC 6803: inactivation of *psbH* impairs Q_A to Q_B electron transport in photosystem 2, *Biochemistry* **32**, 1454-1465.
56. Iwai, M., Katoh, H., Katayama, M., and Ikeuchi, M. (2004) PSII-Tc protein plays an important role in dimerization of photosystem II, *Plant Cell Physiol.* **45**, 1809-1816.

57. Bentley, F. K., Luo, H., Dilbeck, P., Burnap, R. L., and Eaton-Rye, J. J. (2008) Effects of inactivating *psbM* and *psbT* on photodamage and assembly of photosystem II in *Synechocystis* sp. PCC 6803, *Biochemistry* **47**, 11637-11646.
58. Loll, B., Gerold, G., Slowik, D., Voelter, W., Jung, C., Saenger, W., and Irrgang, K. D. (2005) Thermostability and Ca²⁺ binding properties of wild type and heterologously expressed PsbO protein from cyanobacterial photosystem II, *Biochemistry* **44**, 4691-4698.
59. Murray, J. W., and Barber, J. (2006) Identification of a calcium-binding site in the PsbO protein of photosystem II, *Biochemistry* **45**, 4128-4130.
60. Kawakami, K., Umena, Y., Kamiya, N., and Shen, J.-R. (2011) Structure of the catalytic, inorganic core of oxygen-evolving photosystem II at 1.9 Å resolution, *J. Photochem. Photobiol. B* **104**, 9-18.
61. Williamson, A. K. (2008) Structural and functional aspects of the MSP (PsbO) and study of its differences in thermophilic versus mesophilic organisms, *Photosynth. Res.* **98**, 365-389.
62. Yi, X., McChargue, M., Laborde, S., Frankel, L. K., and Bricker, T. M. (2005) The manganese-stabilizing protein is required for photosystem II assembly/stability and photoautotrophy in higher plants, *J. Biol. Chem.* **280**, 16170-16174.
63. Enami, I., Okumura, A., Nagao, R., Suzuki, T., Iwai, M., and Shen, J. R. (2008) Structures and functions of the extrinsic proteins of photosystem II from different species, *Photosynth. Res.* **98**, 349-363.
64. Shen, J. R., Vermaas, W., and Inoue, Y. (1995) The role of cytochrome c-550 as studied through reverse genetics and mutant characterization in *Synechocystis* sp. PCC 6803, *J. Biol. Chem.* **270**, 6901-6907.
65. Kimura, A., Eaton-Rye, J. J., Morita, E. H., Nishiyama, Y., and Hayashi, H. (2002) Protection of the oxygen-evolving machinery by the extrinsic proteins of photosystem II is essential for development of cellular thermotolerance in *Synechocystis* sp. PCC 6803, *Plant Cell Physiol.* **43**, 932-938.
66. Veerman, J., Bentley, F. K., Eaton-Rye, J. J., Mullineaux, C. W., Vassiliev, S., and Bruce, D. (2005) The PsbU subunit of photosystem II stabilizes energy transfer and primary photochemistry in the phycobilisome-photosystem II assembly of *Synechocystis* sp. PCC 6803, *Biochemistry* **44**, 16939-16948.
67. Roose, J. L., Wegener, K. M., and Pakrasi, H. B. (2007) The extrinsic proteins of Photosystem II, *Photosynth. Res.* **92**, 369-387.
68. Scheer, H. (2008) Chlorophylls, In *Primary Processes of Photosynthesis - Principles and Apparatus* (Renger, G., Ed.), pp 101-149, RSC Publishing, Cambridge.
69. Raszewski, G., and Renger, T. (2008) Light harvesting in photosystem II core complexes is limited by the transfer to the trap: can the core complex turn into a photoprotective mode?, *J. Am. Chem. Soc.* **130**, 4431-4446.
70. Renger, T., and Schlodder, E. (2010) Primary photophysical processes in photosystem II: bridging the gap between crystal structure and optical spectra, *ChemPhysChem* **11**, 1141-1153.
71. Miloslavina, Y., Szczepaniak, M., Müller, M. G., Sander, J., Nowaczyk, M., Rögner, M., and Holzwarth, A. R. (2006) Charge separation kinetics in intact photosystem II core particles is trap-limited. A picosecond fluorescence study, *Biochemistry* **45**, 2436-2442.
72. Tumino, G., Casazza, A. P., Engelmann, E., Garlaschi, F. M., Zucchelli, G., and Jennings, R. C. (2008) Fluorescence lifetime spectrum of the plant photosystem II core complex: photochemistry does not induce specific reaction center quenching, *Biochemistry* **47**, 10449-10457.
73. Rappaport, F., and Diner, B. A. (2008) Primary photochemistry and energetics leading to the oxidation of the Mn₄Ca cluster and to the evolution of molecular oxygen in Photosystem II, *Coord. Chem. Rev.* **252**, 259-272.
74. Renger, G., and Renger, T. (2008) Photosystem II: The machinery of photosynthetic water splitting, *Photosynth. Res.* **98**, 53-80.

75. Cogdell, R. J., and Gardiner, A. T. (1993) Functions of carotenoids in photosynthesis, *Methods Enzymol.* 214, 185-193.
76. Frank, H. A., and Cogdell, R. J. (1996) Carotenoids in photosynthesis, *Photochem. Photobiol.* 63, 257-264.
77. Frank, H. A., and Brudvig, G. W. (2004) Redox functions of carotenoids in photosynthesis, *Biochemistry* 43, 8607-8615.
78. Telfer, A. (2005) Too much light? How beta-carotene protects the photosystem II reaction centre, *Photochem. Photobiol. Sci.* 4, 950-956.
79. Martínez-Junza, V., Szczepaniak, M., Braslavsky, S., Sander, J., Rögner, M., and Holzwarth, A. (2008) Triplet Photoprotection by Carotenoid in Intact Photosystem II Cores, In *Photosynthesis. Energy from the Sun* (Allen, J., Gantt, E., Golbeck, J., and Osmond, B., Eds.), pp 137-140, Springer, Dordrecht, Netherlands.
80. Trebst, A., and Depka, B. (1997) Role of carotene in the rapid turnover and assembly of photosystem II in *Chlamydomonas reinhardtii*, *FEBS Lett.* 400, 359-362.
81. Gast, P., Hemelrijk, P. W., VanGorkom, H. J., and Hoff, A. J. (1996) The association of different detergents with the photosynthetic reaction center protein of *Rhodobacter sphaeroides* R26 and the effects on its photochemistry, *Euro. J. Biochem.* 239, 805-809.
82. Müh, F., Rautter, J., and Lubitz, W. (1996) Effects of zwitterionic detergents on the primary donor of bacterial reaction centers, *Ber. Bunsenges. Phys. Chem.* 100, 1974-1977.
83. Müh, F., and Zouni, A. (2005) Extinction coefficients and critical solubilisation concentrations of photosystems I and II from *Thermosynechococcus elongatus*, *Biochim. Biophys. Acta* 1708, 219-228.
84. Müh, F., and Zouni, A. (2008) Micelle formation in the presence of photosystem I, *Biochim. Biophys. Acta* 1778, 2298-2307.
85. le Maire, M., Champeil, P., and Møller, J. V. (2000) Interaction of membrane proteins and lipids with solubilizing detergents, *Biochim. Biophys. Acta* 1508, 86-111.
86. Kern, J., Loll, B., Lüneberg, C., DiFiore, D., Biesiadka, J., Irrgang, K. D., and Zouni, A. (2005) Purification, characterisation and crystallisation of photosystem II from *Thermosynechococcus elongatus* cultivated in a new type of photobioreactor, *Biochim. Biophys. Acta* 1706, 147-157.
87. Sakurai, I., Shen, J. R., Leng, J., Ohashi, S., Kobayashi, M., and Wada, H. (2006) Lipids in oxygen-evolving photosystem II complexes of cyanobacteria and higher plants, *J. Biochem.* 140, 201-209.
88. Itoh, S., Kozuki, T., Nishida, K., Fukushima, Y., Yamakawa, H., Domonkos, I., Laczko-Dobos, H., Kis, M., Ughy, B., and Gombos, Z. (2012) Two functional sites of phosphatidylglycerol for regulation of reaction of plastoquinone Q_B in photosystem II, *Biochim. Biophys. Acta* 1817, 287-297.
89. Gombos, Z., Varkonyi, Z., Hagio, M., Iwaki, M., Kovacs, L., Masamoto, K., Itoh, S., and Wada, H. (2002) Phosphatidylglycerol requirement for the function of electron acceptor plastoquinone Q_B in the photosystem II reaction center, *Biochemistry* 41, 3796-3802.
90. Hasegawa, K., and Noguchi, T. (2012) Molecular interactions of the quinone electron acceptors Q_A, Q_B, and Q_C in photosystem II as studied by the fragment molecular orbital method, *Photosynth. Res.*
91. Sakurai, I., Hagio, M., Gombos, Z., Tyystjarvi, T., Paakkarinen, V., Aro, E. M., and Wada, H. (2003) Requirement of phosphatidylglycerol for maintenance of photosynthetic machinery, *Plant Physiol.* 133, 1376-1384.
92. Gabdulkhakov, A., Guskov, A., Broser, M., Kern, J., Müh, F., Saenger, W., and Zouni, A. (2009) Probing the Accessibility of the Mn₄Ca Cluster in Photosystem II: Channels Calculation, Noble Gas Derivatization, and Cocrystallization with DMSO, *Structure* 17, 1223-1234.

93. Marsh, D., Dzikovski, B. G., and Livshits, V. A. (2006) Oxygen profiles in membranes, *Biophys. J.* **90**, L49-51.
94. Murray, J. W., Maghlaoui, K., Kargul, J., Sugiura, M., and Barber, J. (2008) Analysis of xenon binding to photosystem II by X-ray crystallography, *Photosynth. Res.* **98**, 523-527.
95. Loll, B., Kern, J., Saenger, W., Zouni, A., and Biesiadka, J. (2007) Lipids in photosystem II: interactions with protein and cofactors, *Biochim. Biophys. Acta.* **1767**, 509-519.
96. Sozer, O., Kis, M., Gombos, Z., and Ughy, B. (2011) Proteins, glycerolipids and carotenoids in the functional photosystem II architecture, *Front. Biosci.* **16**, 619-643.
97. Joliot, P., Barbieri, G., and Chabaud, R. (1969) A New Model of the Photochemical Centers of System II, *Photochem. Photobiol.* **10**, 309-329.
98. Kok, B., Forbush, B., and McGloin, M. (1970) Cooperation of charges in photosynthetic oxygen evolution. I. A linear four step mechanism, *Photochem. Photobiol.* **11**, 457-475.
99. McEvoy, J. P., and Brudvig, G. W. (2006) Water-Splitting Chemistry of Photosystem II, *Chem. Rev.* **106**, 4455-4483.
100. Hillier, W., and Messinger, J. (2005) Mechanism of Photosynthetic Oxygen Production, In *Photosystem II* (Wydrzynski, T., Satoh, K., and Freeman, J., Eds.), pp 567-608, Springer Dordrecht, Netherlands.
101. Müh, F., and Zouni, A. (2011) Light-induced water oxidation in photosystem II, *Front. Biosci.* **16**, 3072-3132.
102. Grundmeier, A., and Dau, H. (2012) Structural models of the manganese complex of photosystem II and mechanistic implications, *Biochim. Biophys. Acta* **1817**, 88-105.
103. Dau, H., and Haumann, M. (2008) The manganese complex of photosystem II in its reaction cycle - Basic framework and possible realization at the atomic level, *Coord. Chem. Rev.* **252**, 273-295.
104. Mukhopadhyay, S., Mandal, S. K., Bhaduri, S., and Armstrong, W. H. (2004) Manganese clusters with relevance to photosystem II, *Chem. Rev.* **104**, 3981-4026.
105. Dau, H., and Haumann, M. (2007) Eight steps preceding O-O bond formation in oxygenic photosynthesis - A basic reaction cycle of the Photosystem II manganese complex, *Biochim. Biophys. Acta* **1767**, 472-483.
106. Messinger, J., and Renger, G. (2008) Photosynthetic water splitting, In *Primary Processes of Photosynthesis, Part 2 Principles and Apparatus* (Renger, G., Ed.), pp 291-351, RSC Publishing, Cambridge.
107. Brudvig, G. W. (2008) Water oxidation chemistry of photosystem II, *Philos. Trans. R Soc. Lond. B Biol. Sci.* **363**, 1211-1219.
108. Siegbahn, P. E. (2009) Structures and energetics for O₂ formation in photosystem II, *Acc. Chem. Res.* **42**, 1871-1880.
109. Renger, G. (2011) Light induced oxidative water splitting in photosynthesis: Energetics, kinetics and mechanism, *J. Photochem. Photobiol. B.* **104**, 35-43.
110. Siegbahn, P. E. (2008) A structure-consistent mechanism for dioxygen formation in photosystem II, *Chemistry* **14**, 8290-8302.
111. Kern, J., Alonso-Mori, R., Tran, R., Hattne, J., Gildea, R. J., Echols, N., Glöckner, C., Hellmich, J., Laksmono, H., Sierra, R. G., Lassalle-Kaiser, B., Koroidov, S., Lampe, A., Han, G., Gul, S., Di Fiore, D., Milathianaki, D., Fry, A. R., Miahnahri, A., Schafer, D. W., Messerschmidt, M., Seibert, M. M., Koglin, J. E., Sokaras, D., Weng, T. C., Sellberg, J., Latimer, M. J., Grosse-Kunstleve, R. W., Zwart, P. H., White, W. E., Glatzel, P., Adams, P. D., Bogan, M. J., Williams, G. J., Boutet, S., Messinger, J., Zouni, A., Sauter, N. K., Yachandra, V. K., Bergmann, U., and Yano, J. (2013) Simultaneous Femtosecond X-ray Spectroscopy and Diffraction of Photosystem II at Room Temperature, *Science*.

112. Saito, T., Yamanaka, S., Kanda, K., Isobe, H., Takano, Y., Shigeta, Y., Umena, Y., Kawakami, K., Shen, J. R., Kamiya, N., Okumura, M., Shoji, M., Yoshioka, Y., and Yamaguchi, K. (2012) Possible mechanisms of water splitting reaction based on proton and electron release pathways revealed for CaMn_4O_5 cluster of PSII refined to 1.9 Å X-ray resolution, *Int. J. Quant. Chem.* 112, 253-276.
113. Sproviero, E. M., McEvoy, J. P., Gascon, J. A., Brudvig, G. W., and Batista, V. S. (2008) Computational insights into the O_2 -evolving complex of photosystem II, *Photosyn. Res.* 97, 91-114.
114. Ravelli, R. B., and McSweeney, S. M. (2000) The 'fingerprint' that X-rays can leave on structures, *Structure* 8, 315-328.
115. O'Neill, P., Stevens, D. L., and Garman, E. F. (2002) Physical and chemical considerations of damage induced in protein crystals by synchrotron radiation: a radiation chemical perspective, *J. Synchrotron Radiat.* 9, 329-332.
116. Yano, J., Kern, J., Irrgang, K.-D., Latimer, M. J., Bergmann, U., Glatzel, P., Pushkar, Y., Biesiadka, J., Loll, B., Sauer, K., Messinger, J., Zouni, A., and Yachandra, V. K. (2005) X-ray Damage to the Mn_4Ca Complex in Photosystem II Crystals: A Case Study for Metallo-Protein X-ray Crystallography, *Proc. Natl. Acad. Sci. U.S.A* 102, 12047-12052.
117. Grabolle, M., Haumann, M., Muller, C., Liebisch, P., and Dau, H. (2006) Rapid loss of structural motifs in the manganese complex of oxygenic photosynthesis by x-ray irradiation at 10-300 K, *J. Biol. Chem.* 281, 4580-4588.
118. Chapman, H. N., Fromme, P., Barty, A., White, T. A., Kirian, R. A., Aquila, A., Hunter, M. S., Schulz, J., DePonte, D. P., Weierstall, U., Doak, R. B., Maia, F. R., Martin, A. V., Schlichting, I., Lomb, L., Coppola, N., Shoeman, R. L., Epp, S. W., Hartmann, R., Rolles, D., Rudenko, A., Foucar, L., Kimmel, N., Weidenspointner, G., Holl, P., Liang, M., Barthelmess, M., Caleman, C., Boutet, S., Bogan, M. J., Krzywinski, J., Bostedt, C., Bajt, S., Gumprecht, L., Rudek, B., Erk, B., Schmidt, C., Homke, A., Reich, C., Pietschner, D., Struder, L., Hauser, G., Gorke, H., Ullrich, J., Herrmann, S., Schaller, G., Schopper, F., Soltau, H., Kuhnel, K. U., Messerschmidt, M., Bozek, J. D., Hau-Riege, S. P., Frank, M., Hampton, C. Y., Sierra, R. G., Starodub, D., Williams, G. J., Hajdu, J., Timneanu, N., Seibert, M. M., Andreasson, J., Rocker, A., Jonsson, O., Svenda, M., Stern, S., Nass, K., Andritschke, R., Schroter, C. D., Krasniqi, F., Bott, M., Schmidt, K. E., Wang, X., Grotjohann, I., Holton, J. M., Barends, T. R., Neutze, R., Marchesini, S., Fromme, R., Schorb, S., Rupp, D., Adolph, M., Gorkhover, T., Andersson, I., Hirsemann, H., Potdevin, G., Graafsma, H., Nilsson, B., and Spence, J. C. (2011) Femtosecond X-ray protein nanocrystallography, *Nature* 470, 73-77.
119. Kirian, R. A., White, T. A., Holton, J. M., Chapman, H. N., Fromme, P., Barty, A., Lomb, L., Aquila, A., Maia, F. R., Martin, A. V., Fromme, R., Wang, X., Hunter, M. S., Schmidt, K. E., and Spence, J. C. (2011) Structure-factor analysis of femtosecond microdiffraction patterns from protein nanocrystals, *Acta Crystallogr. A* 67, 131-140.
120. Hunter, M. S., DePonte, D. P., Shapiro, D. A., Kirian, R. A., Wang, X., Starodub, D., Marchesini, S., Weierstall, U., Doak, R. B., Spence, J. C., and Fromme, P. (2011) X-ray diffraction from membrane protein nanocrystals, *Biophys. J.* 100, 198-206.
121. Barty, A., Caleman, C., Aquila, A., Timneanu, N., Lomb, L., White, T. A., Andreasson, J., Arnlund, D., Bajt, S., Barends, T. R. M., Barthelmess, M., Bogan, M. J., Bostedt, C., Bozek, J. D., Coffee, R., Coppola, N., Davidsson, J., DePonte, D. P., Doak, R. B., Ekeberg, T., Elser, V., Epp, S. W., Erk, B., Fleckenstein, H., Foucar, L., Fromme, P., Graafsma, H., Gumprecht, L., Hajdu, J., Hampton, C. Y., Hartmann, R., Hartmann, A., Hauser, G., Hirsemann, H., Holl, P., Hunter, M. S., Johansson, L., Kassemeyer, S., Kimmel, N., Kirian, R. A., Liang, M., Maia, F. R. N. C., Malmerberg, E., Marchesini, S., Martin, A. V., Nass, K., Neutze, R., Reich, C., Rolles, D., Rudek, B., Rudenko, A., Scott, H., Schlichting, I., Schulz, J., Seibert, M. M., Shoeman, R. L., Sierra, R. G., Soltau, H., Spence, J. C. H., Stellato, F., Stern,

- S., Struder, L., Ullrich, J., Wang, X., Weidenspointner, G., Weierstall, U., Wunderer, C. B., and Chapman, H. N. (2012) Self-terminating diffraction gates femtosecond X-ray nanocrystallography measurements, *Nat. Photon.* 6, 35-40.
122. Boutet, S., Lomb, L., Williams, G. J., Barends, T. R., Aquila, A., Doak, R. B., Weierstall, U., DePonte, D. P., Steinbrener, J., Shoeman, R. L., Messerschmidt, M., Barty, A., White, T. A., Kassemeyer, S., Kirian, R. A., Seibert, M. M., Montanez, P. A., Kenney, C., Herbst, R., Hart, P., Pines, J., Haller, G., Gruner, S. M., Philipp, H. T., Tate, M. W., Hromalik, M., Koerner, L. J., van Bakel, N., Morse, J., Ghonsalves, W., Arnlund, D., Bogan, M. J., Caleman, C., Fromme, R., Hampton, C. Y., Hunter, M. S., Johansson, L. C., Katona, G., Kupitz, C., Liang, M., Martin, A. V., Nass, K., Redecke, L., Stellato, F., Timneanu, N., Wang, D., Zatsepin, N. A., Schafer, D., DeFevers, J., Neutze, R., Fromme, P., Spence, J. C., Chapman, H. N., and Schlichting, I. (2012) High-resolution protein structure determination by serial femtosecond crystallography, *Science* 337, 362-364.
123. Kern, J., Alonso-Mori, R., Hellmich, J., Tran, R., Hattne, J., Laksmono, H., Glöckner, C., Echols, N., Sierra, R. G., Sellberg, J., Lassalle-Kaiser, B., Gildea, R. J., Glatzel, P., Grosse-Kunstleve, R. W., Latimer, M. J., McQueen, T. A., DiFiore, D., Fry, A. R., Messerschmidt, M., Miahnahri, A., Schafer, D. W., Seibert, M. M., Sokaras, D., Weng, T. C., Zwart, P. H., White, W. E., Adams, P. D., Bogan, M. J., Boutet, S., Williams, G. J., Messinger, J., Sauter, N. K., Zouni, A., Bergmann, U., Yano, J., and Yachandra, V. K. (2012) Room temperature femtosecond X-ray diffraction of photosystem II microcrystals, *Proc. Natl. Acad. Sci. U.S.A.* 109, 9721-9726.
124. Murray, J. W., and Barber, J. (2007) Structural characteristics of channels and pathways in photosystem II including the identification of an oxygen channel, *J. Struct. Biol.* 159, 228-237.
125. Ho, F. M., and Styring, S. (2008) Access channels and methanol binding site to the CaMn₄ cluster in Photosystem II based on solvent accessibility simulations, with implications for substrate water access, *Biochim. Biophys. Acta* 1777, 140-153.
126. Petrek, M., Otyepka, M., Banas, P., Kosinova, P., Koca, J., and Damborsky, J. (2006) CAVER: a new tool to explore routes from protein clefts, pockets and cavities, *BMC Bioinformatics* 7, 316.
127. Vassiliev, S., Comte, P., Mahboob, A., and Bruce, D. (2010) Tracking the flow of water through photosystem II using molecular dynamics and streamline tracing, *Biochemistry* 49, 1873-1881.
128. Vassiliev, S., Zaraiskaya, T., and Bruce, D. (2012) Exploring the energetics of water permeation in photosystem II by multiple steered molecular dynamics simulations, *Biochim. Biophys. Acta* 1817, 1671-1678.
129. Sandusky, P. O., and Yocum, C. F. (1984) The chloride requirement for photosynthetic oxygen evolution. Analysis of the effects of chloride and other anions on amine inhibition of the oxygen-evolving complex, *Biochim. Biophys. Acta* 766, 603-611.
130. Brudvig, G. W., Beck, W. F., and De Paula, J. C. (1989) Mechanism of photosynthetic water oxidation, *Annu. Rev. Biophys. Biophys. Chem.* 18, 25-46.
131. Popelkova, H., and Yocum, C. F. (2007) Current status of the role of Cl⁻ ion in the oxygen-evolving complex, *Photosynth. Res.* 93, 111-121.
132. Murray, J. W., Maghlaoui, K., Kargul, J., Ishida, N., Lai, T.-L., Rutherford, A. W., Sugiura, M., Bousac, A., and Barber, J. (2008) X-ray crystallography identifies two chloride binding sites in the oxygen evolving centre of Photosystem II, *Energy Environ. Sci.* 1, 161-166.
133. Kawakami, K., Umena, Y., Kamiya, N., and Shen, J. R. (2009) Location of chloride and its possible functions in oxygen-evolving photosystem II revealed by X-ray crystallography, *Proc. Natl. Acad. Sci. U.S.A.* 106, 8567-8572.
134. Bousac, A. (1995) Exchange of chloride by bromide in the manganese photosystem-II complex studied by cw- and pulsed-EPR, *Chem. Phys.* 194, 409-418.

135. van Vliet, P., and Rutherford, A. W. (1996) Properties of the chloride-depleted oxygen-evolving complex of photosystem II studied by electron paramagnetic resonance, *Biochemistry* 35, 1829-1839.
136. Olesen, K., and Andreasson, L. E. (2003) The function of the chloride ion in photosynthetic oxygen evolution, *Biochemistry* 42, 2025-2035.
137. Rivalta, I., Amin, M., Lubner, S., Vassiliev, S., Pokhrel, R., Umena, Y., Kawakami, K., Shen, J.-R., Kamiya, N., Bruce, D., Brudvig, G. W., Gunner, M. R., and Batista, V. S. (2011) Structural-Functional Role of Chloride in Photosystem II, *Biochemistry* 50, 6312-6315.
138. Pokhrel, R., McConnell, I. L., and Brudvig, G. W. (2011) Chloride regulation of enzyme turnover: application to the role of chloride in photosystem II, *Biochemistry* 50, 2725-2734.
139. Boussac, A., Ishida, N., Sugiura, M., and Rappaport, F. (2012) Probing the role of chloride in Photosystem II from *Thermosynechococcus elongatus* by exchanging chloride for iodide, *Biochim. Biophys. Acta* 1817, 802-810.
140. Rumberg, B., Schmidt-Mende, P., and Witt, H. T. (1964) Different Demonstrations of the Coupling of Two Light Reactions in Photosynthesis, *Nature* 201, 466-468.
141. Crofts, A. R., and Wraight, C. A. (1983) The electrochemical domain of photosynthesis, *Biochim. Biophys. Acta* 726, 149-185.
142. Minagawa, J., Narusaka, Y., Inoue, Y., and Satoh, K. (1999) Electron transfer between Q_A and Q_B in photosystem II is thermodynamically perturbed in phototolerant mutants of *Synechocystis* sp. PCC 6803, *Biochemistry* 38, 770-775.
143. Oettmeier, W. (1999) Herbicide resistance and supersensitivity in photosystem II, *Cell. Mol. Life Sci.* 55, 1255-1277.
144. Trebst, A. (2007) Inhibitors in the functional dissection of the photosynthetic electron transport system, *Photosyn. Res.* 92, 217-224.
145. Kern, J., and Guskov, A. (2011) Lipids in photosystem II: multifunctional cofactors, *J. Photochem. Photobiol. B* 104, 19-34.
146. Kruk, J., and Strzalka, K. (2001) Redox changes of cytochrome b_{559} in the presence of plastoquinones, *J. Biol. Chem.* 276, 86-91.
147. Kaminskaya, O., Shuvalov, V. A., and Renger, G. (2007) Evidence for a novel quinone-binding site in the photosystem II (PS II) complex that regulates the redox potential of cytochrome b_{559} , *Biochemistry* 46, 1091-1105.
148. Kaminskaya, O., Shuvalov, V. A., and Renger, G. (2007) Two reaction pathways for transformation of high potential cytochrome b_{559} of PS II into the intermediate potential form, *Biochim. Biophys. Acta* 1767, 550-558.
149. Kern, J., and Renger, G. (2007) Photosystem II: structure and mechanism of the water:plastoquinone oxidoreductase, *Photosyn. Res.* 94, 183-202.
150. Waters, M. L. (2002) Aromatic interactions in model systems, *Curr. Opin. Chem. Biol.* 6, 736-741.
151. Ishikita, H., and Knapp, E. W. (2005) Control of quinone redox potentials in photosystem II: Electron transfer and photoprotection, *J. Am. Chem. Soc.* 127, 14714-14720.
152. Ishikita, H., Hasegawa, K., and Noguchi, T. (2011) How does the Q_B site influence propagate to the Q_A site in photosystem II?, *Biochemistry* 50, 5436-5442.
153. de Wijn, R., and van Gorkom, H. J. (2001) Kinetics of electron transfer from Q_A to Q_B in photosystem II, *Biochemistry* 40, 11912-11922.
154. Graige, M. S., Paddock, M. L., Bruce, J. M., Feher, G., and Okamura, M. Y. (1996) Mechanism of Proton-Coupled Electron Transfer for Quinone (Q_B) Reduction in Reaction Centers of *Rb. Sphaeroides*, *J. Am. Chem. Soc.* 118, 9005-9016.
155. Graige, M., Paddock, M., Feher, G., and Okamura, M. (1998) The mechanism of proton-coupled electron transfer in mutant RCs from *Rb. sphaeroides*, *Biophys. J* 74, A135.
156. Graige, M. S., Paddock, M. L., Feher, G., and Okamura, M. Y. (1999) Observation of the Protonated Semiquinone Intermediate in Isolated Reaction Centers from

- Rhodobacter sphaeroides*: Implications for the Mechanism of Electron and Proton Transfer in Proteins, *Biochemistry* 38, 11465-11473.
157. Okamura, M. Y., Paddock, M. L., Graige, M. S., and Feher, G. (2000) Proton and electron transfer in bacterial reaction centers, *Biochim. Biophys. Acta* 1458, 148-163.
 158. Haumann, M., and Junge, W. (1994) The rates of proton uptake and electron transfer at the reducing side of photosystem II in thylakoids, *FEBS Lett.* 347, 45-50.
 159. Vass, I., Aro, E. (2008) Photoinhibition of photosynthetic electron transport, In *Primary Processes of Photosynthesis, Principles and Apparatus* (Renger, G., Ed.), pp 393-425, RSC Publishing, Cambridge.
 160. Šetlík, I., Allakhverdiev, S., Nedbal, L., Šetlíková, E., and Klimov, V. (1990) Three types of Photosystem II photoinactivation, *Photosyn. Res.* 23, 39-48.
 161. Vass, I., Styring, S., Hundal, T., Koivuniemi, A., Aro, E. M., and Andersson, B. (1992) Reversible and Irreversible Intermediates During Photoinhibition of Photosystem II: Stable Reduced Q_A Species Promote Chlorophyll Triplet Formation, *Proc. Natl. Acad. Sci. U.S.A.* 89, 1408-1412.
 162. Hideg, É., Spetea, C., and Vass, I. (1994) Singlet oxygen and free radical production during acceptor- and donor-side-induced photoinhibition: Studies with spin trapping EPR spectroscopy, *Biochim. Biophys. Acta* 1186, 143-152.
 163. Hideg, É., Spetea, C., and Vass, I. (1994) Singlet oxygen production in thylakoid membranes during photoinhibition as detected by EPR spectroscopy, *Photosyn. Res.* 39, 191-199.
 164. Keren, N., Berg, A., van Kan, P. J. M., Levanon, H., and Ohad, I. (1997) Mechanism of photosystem II photoinactivation and D1 protein degradation at low light: The role of back electron flow, *Proc. Natl. Acad. Sci. U.S.A.* 94, 1579-1584.
 165. Gross, C. (2008) Entstehung von Singulett-Sauerstoff und Superoxid am Photosystem II, PhD thesis, University of Freiburg, Freiburg.
 166. Krieger, A., Rutherford, A. W., and Johnson, G. N. (1995) On the Determination of Redox Midpoint Potential of the Primary Quinone Electron-Acceptor, Q_A , in Photosystem II, *Biochim. Biophys. Acta* 1229, 193-201.
 167. Krieger-Liszky, A., and Rutherford, A. W. (1998) Influence of herbicide binding on the redox potential of the quinone acceptor in photosystem II: relevance to photodamage and phytotoxicity, *Biochemistry* 37, 17339-17344.
 168. Fufezan, C., Gross, C. M., Sjodin, M., Rutherford, A. W., Krieger-Liszky, A., and Kirilovsky, D. (2007) Influence of the redox potential of the primary quinone electron acceptor on photoinhibition in photosystem II, *J. Biol. Chem.* 282, 12492-12502.
 169. Johnson, G. N., Rutherford, A. W., and Krieger, A. (1995) A Change in the Midpoint Potential of the Quinone Q_A in Photosystem II Associated With Photoactivation of Oxygen Evolution, *Biochim. Biophys. Acta* 1229, 202-207.
 170. Krieger, A., and Rutherford, A. W. (1997) Comparison of chloride-depleted and calcium-depleted PSII: The midpoint potential of Q_A and susceptibility to photodamage, *Biochim. Biophys. Acta* 1319, 91-98.
 171. Komenda, J., Reisinger, V., Muller, B. C., Dobakova, M., Granvogl, B., and Eichacker, L. A. (2004) Accumulation of the D2 protein is a key regulatory step for assembly of the photosystem II reaction center complex in *Synechocystis* PCC 6803, *J. Biol. Chem.* 279, 48620-48629.
 172. Nowaczyk, M. M., Hebel, R., Schlodder, E., Meyer, H. E., Warscheid, B., and Rogner, M. (2006) Psb27, a cyanobacterial lipoprotein, is involved in the repair cycle of photosystem II, *Plant Cell* 18, 3121-3131.
 173. Roose, J. L., and Pakrasi, H. B. (2008) The Psb27 protein facilitates manganese cluster assembly in photosystem II, *J. Biol. Chem.* 283, 4044-4050.
 174. Clint, J. H. (1975) Micellization of mixed nonionic surface active agents, *J. Chem. Soc., Chem. Commun.* 71, 1327-1334.

175. Seddon, A. M., Curnow, P., and Booth, P. J. (2004) Membrane proteins, lipids and detergents: not just a soap opera, *Biochim. Biophys. Acta* 1666, 105-117.
176. Michel, H., Epp, O., and Deisenhofer, J. (1986) Pigment-protein interactions in the photosynthetic reaction centre from *Rhodospseudomonas viridis*, *EMBO J* 5, 2445-2451.
177. Lancaster, C. R., Bibikova, M. V., Sabatino, P., Oesterhelt, D., and Michel, H. (2000) Structural basis of the drastically increased initial electron transfer rate in the reaction center from a *Rhodospseudomonas viridis* mutant described at 2.00 Å resolution, *J. Biol. Chem.* 275, 39364-39368.
178. Sobolev, V., and Edelman, M. (1995) Modeling the Q_B binding site of the photosystem-II reaction center using notions of complementarity and contact-surface between atoms, *Proteins* 21, 214-225.
179. Messinger, J., Robblee, J. H., Bergmann, U., Fernandez, C., Glatzel, P., Visser, H., Cinco, R. M., McFarlane, K. L., Bellacchio, E., Pizarro, S. A., Cramer, S. P., Sauer, K., Klein, M. P., and Yachandra, V. K. (2001) Absence of Mn-centered oxidation in the S₂ to S₃ Transition: Implications for the mechanism of photosynthetic water oxidation, *J. Am. Chem. Soc.* 123, 7804-7820.
180. Broser, M. (2010) Purification, crystallization and structural analysis of the monomeric Photosystem II core complex from *Thermosynechococcus elongatus*, PhD thesis, Technical University of Berlin, Berlin.
181. Clark, L. C. J. (1956) Monitor and Control of Blood and Tissue Oxygen Tensions, *ASAIO J.* 2, 41-48.
182. Schägger, H. (2006) Tricine-SDS-PAGE, *Nat. Protoc.* 1, 16-22.
183. Krivanek, R., Kern, J., Zouni, A., Dau, H., and Haumann, M. (2007) Spare quinones in the Q_B cavity of crystallized photosystem II from *Thermosynechococcus elongatus*, *Biochim. Biophys. Acta* 1767, 520-527.
184. Grabolle, M., and Dau, H. (2005) Energetics of primary and secondary electron transfer in photosystem II membrane particles of spinach revisited on basis of recombinant-fluorescence measurements, *Biochim. Biophys. Acta* 1708, 209-218.
185. Buchta, J., Grabolle, M., and Dau, H. (2007) Photosynthetic dioxygen formation studied by time-resolved delayed fluorescence measurements -method, rationale, and results on the activation energy of dioxygen formation, *Biochim. Biophys. Acta* 1767, 565-574.
186. Kabsch, W. (1993) Automatic processing of rotation diffraction data from crystals of initially unknown symmetry and cell constants, *J. Appl. Cryst.* 26, 795-800.
187. McCoy, A. J., Grosse-Kunstleve, R. W., Adams, P. D., Winn, M. D., Storoni, L. C., and Read, R. J. (2007) Phaser crystallographic software, *J. Appl. Cryst.* 40, 658-674.
188. Emsley, P., and Cowtan, K. (2004) Coot: model-building tools for molecular graphics, *Acta Crystallogr. D Biol. Crystallogr.* 60, 2126-2132.
189. Brünger, A. T., Adams, P. D., Clore, G. M., DeLano, W. L., Gros, P., Grosse-Kunstleve, R. W., Jiang, J. S., Kuszewski, J., Nilges, M., Pannu, N. S., Read, R. J., Rice, L. M., Simonson, T., and Warren, G. L. (1998) Crystallography & NMR system: A new software suite for macromolecular structure determination, *Acta Crystallogr. D Biol. Crystallogr.* 54 905-921.
190. Yano, J., and Yachandra, V. K. (2009) X-ray absorption spectroscopy, *Photosynth. Res.* 102, 241-254.
191. Koningsberger, D. C., Prins, R., (Ed.) (1988) *X-ray absorption: principles, application, techniques of EXAFS, SEXAFS and XANES*, Wiley, New York.
192. Glöckner, C., Kern, J., Broser, M., Zouni, A., Yachandra, V., Yano, J. (2013) Structural Changes of the Oxygen Evolving Complex in Photosystem II during the Catalytic Cycle., *J. Biol. Chem.* DOI:10.1074/jbc.M113.476622.
193. Oettmeier, W. (1992) Herbicides of photosystem II, In *Topics in photosynthesis Vol. 11: the photosystems: structure, function and molecular biology* (Barber, J., Ed.), pp 349-408, Elsevier Science Publishers B. V., Amsterdam.

194. Trebst, A. (1987) The three-dimensional structure of the herbicide binding niche on the reaction center polypeptides of photosystem II, *Z. Naturforsch. C* 42, 742-750.
195. Hirschberg, J., and McIntosh, L. (1983) Molecular Basis of Herbicide Resistance in *Amaranthus hybridus*, *Science* 222, 1346-1349.
196. Ajlani, G., Kirilovsky, D., Picaud, M., and Astier, C. (1989) Molecular analysis of *psbA* mutations responsible for various herbicide resistance phenotypes in *Synechocystis* 6714, *Plant Mol. Biol.* 13, 469-479.
197. Zimmermann, K., Heck, M., Frank, J., Kern, J., Vass, I., and Zouni, A. (2006) Herbicide binding and thermal stability of photosystem II isolated from *Thermosynechococcus elongatus*, *Biochim. Biophys. Acta* 1757, 106-114.
198. Rutherford, A. W., and Krieger-Liszkay, A. (2001) Herbicide-induced oxidative stress in photosystem II, *Trends Biochem. Sci.* 26, 648-653.
199. Takano, A., Takahashi, R., Suzuki, H., and Noguchi, T. (2008) Herbicide effect on the hydrogen-bonding interaction of the primary quinone electron acceptor Q_A in photosystem II as studied by Fourier transform infrared spectroscopy, *Photosynth. Res.* 98, 159-167.
200. Krieger-Liszkay, A., Fufezan, C., and Trebst, A. (2008) Singlet oxygen production in photosystem II and related protection mechanism, *Photosynth. Res.* 98, 551-564.
201. Lancaster, C. R., and Michel, H. (1999) Refined crystal structures of reaction centres from *Rhodospseudomonas viridis* in complexes with the herbicide atrazine and two chiral atrazine derivatives also lead to a new model of the bound carotenoid, *J. Mol. Biol.* 286, 883-898.
202. Gleiter, H., Haag, E., Inoue, Y., and Renger, G. (1993) Functional characterisation of a purified homogeneous Photosystem II core complex with high oxygen evolution capacity from spinach, *Photosynth. Res.* 35, 41-53.
203. Reifler, M. J., Szalai, V. A., Peterson, C. N., and Brudvig, G. W. (2001) Effects of tail-like substituents on the binding of competitive inhibitors to the Q_B site of photosystem II, *J. Mol. Recognit.* 14, 157-165.
204. Katona, G., Snijder, A., Gourdon, P., Andreasson, U., Hansson, O., Andreasson, L. E., and Neutze, R. (2005) Conformational regulation of charge recombination reactions in a photosynthetic bacterial reaction center, *Nat. Struct. Mol. Biol.* 12, 630-631.
205. Egner, U., Hoyer, G. A., and Saenger, W. (1993) Modeling and energy minimization studies on the herbicide binding protein (D1) in photosystem II of plants, *Biochim. Biophys. Acta* 1142, 106-114.
206. Takahashi, R., Boussac, A., Sugiura, M., and Noguchi, T. (2009) Structural coupling of a tyrosine side chain with the non-heme iron center in photosystem II as revealed by light-induced Fourier transform infrared difference spectroscopy, *Biochemistry* 48, 8994-9001.
207. Shevela, D., Eaton-Rye, J. J., Shen, J. R., and Govindjee. (2012) Photosystem II and the unique role of bicarbonate: a historical perspective, *Biochim. Biophys. Acta* 1817, 1134-1151.
208. Takahashi, R., Hasegawa, K., Takano, A., and Noguchi, T. (2010) Structures and binding sites of phenolic herbicides in the Q_B pocket of photosystem II, *Biochemistry* 49, 5445-5454.
209. Renger, G. (2007) Oxidative photosynthetic water splitting: energetics, kinetics and mechanism, *Photosynth. Res.* 91, 186-186.
210. Lindberg, K., and Andréasson, L.-E. (1996) A One-Site, Two-State Model for the Binding of Anions in Photosystem II, *Biochemistry* 35, 14259-14267.
211. Barber, J., Ferreira, K., Maghlaoui, K., and Iwata, S. (2004) Structural model of the oxygen-evolving centre of photosystem II with mechanistic implications, *Phys. Chem. Chem. Phys.* 6, 4737-4742.
212. Ishikita, H., Saenger, W., Loll, B., Biesiadka, J., and Knapp, E. W. (2006) Energetics of a possible proton exit pathway for water oxidation in photosystem II, *Biochemistry* 45, 2063-2071.

213. Sproviero, E. M., Gascon, J. A., McEvoy, J. P., Brudvig, G. W., and Batista, V. S. (2007) Quantum mechanics/molecular mechanics structural models of the oxygen-evolving complex of photosystem II, *Curr. Op. Struct. Biol.* **17**, 173-180.
214. Tietjen, K. G., Kluth, J. F., Andree, R., Haug, M., Linding, M., Müller, K. H., Wroblowsky, H. J., and Trebst, A. (1990) The herbicide binding niche of photosystem II - a model, *Pestic. Sci.* **31**, 65-72.
215. Egner, U., Hoyer, G. A., and Saenger, W. (1992) The binding of triazine herbicides to the photosynthetic reaction center of *Rhodospseudomonas viridis*. Energy minimization studies, *Eur. J. Biochem.* **206**, 685-690.
216. Razeghifard, M. R., and Pace, R. J. (1999) EPR Kinetic Studies of Oxygen Release in Thylakoids in PSII Membranes: A Kinetic Intermediate in the S_3 to S_0 Transition, *Biochemistry* **38**, 1252-1257.
217. Clausen, J., and Junge, W. (2005) Search for intermediates of photosynthetic water oxidation, *Photosynth. Res.* **84**, 339-345.
218. Shevela, D., Beckmann, K., Clausen, J., Junge, W., and Messinger, J. (2011) Membrane-inlet mass spectrometry reveals a high driving force for oxygen production by photosystem II, *Proc. Natl. Acad. Sci. U.S.A.* **108**, 3602-3607.
219. Haumann, M., Müller, C., Liebisch, P., Iuzzolino, L., Dittmer, J., Grabolle, M., Neisius, T., Meyer-Klaucke, W., and Dau, H. (2005) Structural and oxidation state changes of the photosystem II manganese complex in four transitions of the water oxidation cycle ($S_0 \rightarrow S_1$, $S_1 \rightarrow S_2$, $S_2 \rightarrow S_3$, and $S_{3,4} \rightarrow S_0$) characterized by X-ray absorption spectroscopy at 20 K and room temperature, *Biochemistry* **44**, 1894-1908.
220. Cinco, R. M., Holman, K. L. M., Robblee, J. H., Yano, J., Pizarro, S. A., Bellacchio, E., Sauer, K., and Yachandra, V. K. (2002) Calcium EXAFS establishes the Mn-Ca cluster in the oxygen-evolving complex of photosystem II, *Biochemistry* **41**, 12928-12933.
221. Latimer, M. J., DeRose, V. J., Mukerji, I., Yachandra, V. K., Sauer, K., and Klein, M. P. (1995) Evidence for the Proximity of Calcium to the Manganese Cluster of Photosystem II: Determination by X-Ray Absorption Spectroscopy, *Biochemistry* **34**, 10898-10909.
222. Cinco, R. M., Robblee, J. H., Rompel, A., Fernandez, C., Yachandra, V. K., Sauer, K., and Klein, M. P. (1998) Strontium EXAFS Reveals the Proximity of Calcium to the Manganese Cluster of Oxygen-Evolving Photosystem II, *J. Phys. Chem. B* **102**, 8248-8256.
223. Pushkar, Y. L., Yano, J., Sauer, K., Boussac, A., and Yachandra, V. K. (2008) Structural changes in the Mn_4Ca cluster and the mechanism of photosynthetic water splitting, *Proc. Natl. Acad. Sci. U.S.A.* **105**, 1879-1884.
224. Haumann, M., Barra, M., Loja, P., Löscher, S., Krivanek, R., Grundmeier, A., Andreasson, L. E., and Dau, H. (2006) Bromide does not bind to the Mn_4Ca complex in its S_1 state in Cl^- -depleted and Br^- -reconstituted oxygen-evolving photosystem II: Evidence from X-ray absorption spectroscopy at the Br K-edge, *Biochemistry* **45**, 13101-13107.
225. Yachandra, V. K., Sauer, K., and Klein, M. P. (1996) Manganese Cluster in Photosynthesis: Where Plants Oxidize Water to Dioxygen, *Chem. Rev.* **96**, 2927-2950.
226. Sauer, K., and Yachandra, V. K. (2004) The water-oxidation complex in photosynthesis, *Biochim. Biophys. Acta* **1655**, 140-148.
227. Yano, J., Kern, J., Sauer, K., Latimer, M., Pushkar, Y., Biesiadka, J., Loll, B., Saenger, W., Messinger, J., Zouni, A., and Yachandra, V. K. (2006) Where Water is Oxidized to Dioxygen: Structure of the Photosynthetic Mn_4Ca Cluster, *Science* **314**, 821-825.
228. Cinco, R. M., Robblee, J. H., Messinger, J., Fernandez, C., Holman, K. L. M., Sauer, K., and Yachandra, V. K. (2004) Orientation of calcium in the Mn_4Ca cluster of the oxygen-evolving complex determined using polarized strontium EXAFS of photosystem II membranes, *Biochemistry* **43**, 13271-13282.

229. Visser, H., Anxolabéhère-Mallart, E., Bergman, U., Glatzel, P., Robblee, J. H., Cramer, S. P., Girerd, J.-J., Sauer, K., Klein, M. P., and Yachandra, V. K. (2001) Mn K-edge XANES and K β XES Studies of Two Mn-oxo Binuclear Complexes. Investigation of Three Different Oxidation States Relevant to the Oxygen-Evolving Complex of Photosystem II., *J. Am. Chem. Soc.* **123**, 7031-7039.
230. Liang, W., Roelofs, T. A., Cinco, R. M., Rompel, A., Latimer, M. J., Yu, W. O., Sauer, K., Klein, M. P., and Yachandra, V. K. (2000) Structural change of the Mn cluster during the S₂→S₃ state transition of the Oxygen-Evolving Complex of Photosystem II. Does it reflect the onset of water/substrate oxidation? Determination by Mn X-ray absorption spectroscopy, *J. Am. Chem. Soc.* **122**, 3399-3412.
231. Yano, J., Pushkar, Y., Glatzel, P., Lewis, A., Sauer, K., Messinger, J., Bergmann, U., and Yachandra, V. K. (2005) High-resolution Mn EXAFS of the Oxygen-evolving Complex in Photosystem II: Structural Implications for the Mn₄Ca Cluster, *J. Am. Chem. Soc.* **127**, 14974-14975.
232. Robblee, J. H., Messinger, J., Cinco, R. M., McFarlane, K. L., Fernandez, C., Pizarro, S. A., Sauer, K., and Yachandra, V. K. (2002) The Mn Cluster in the S₀ State of the Oxygen-Evolving Complex of Photosystem II Studied by EXAFS Spectroscopy: Are There Three Di- μ -oxo-bridged Mn₂ Moieties in the Tetranuclear Mn Complex?, *J. Am. Chem. Soc.* **124**, 7459-7471.
233. Cox, N., Rapatskiy, L., Su, J. H., Pantazis, D. A., Sugiura, M., Kulik, L., Dorlet, P., Rutherford, A. W., Neese, F., Boussac, A., Lubitz, W., and Messinger, J. (2011) Effect of Ca²⁺Sr²⁺ substitution on the electronic structure of the oxygen-evolving complex of photosystem II: A combined multifrequency EPR, ⁵⁵Mn-ENDOR, and DFT study of the S₂ state, *J. Am. Chem. Soc.* **133**, 3635-3648.
234. Kulik, L. V., Epel, B., Lubitz, W., and Messinger, J. (2007) Electronic Structure of the Mn₄O_xCa Cluster in the S₀ and S₂ states of the Oxygen-Evolving Complex of Photosystem II based on Pulse ⁵⁵Mn-ENDOR and EPR Spectroscopy *J. Am. Chem. Soc.* **129**, 13421–13435.
235. Su, J. H., Cox, N., Ames, W., Pantazis, D. A., Rapatskiy, L., Lohmiller, T., Kulik, L. V., Dorlet, P., Rutherford, A. W., Neese, F., Boussac, A., Lubitz, W., and Messinger, J. (2011) The electronic structures of the S₂ states of the oxygen-evolving complexes of photosystem II in plants and cyanobacteria in the presence and absence of methanol, *Biochim. Biophys. Acta* **1807**, 829-840.
236. Pantazis, D. A., Ames, W., Cox, N., Lubitz, W., and Neese, F. (2012) Two interconvertible structures that explain the spectroscopic properties of the oxygen-evolving complex of photosystem II in the S₂ state, *Angew. Chem. Int. Ed. Engl.* **51**, 9935-9940.
237. Siegbahn, P. E. (2011) The effect of backbone constraints: the case of water oxidation by the oxygen-evolving complex in PSII, *ChemPhysChem* **12**, 3274-3280.
238. Siegbahn, P. E. (2011) Recent theoretical studies of water oxidation in photosystem II, *J. Photochem. Photobiol. B* **104**, 94-99.
239. Cox, N., Pantazis, D. A., Neese, F., and Lubitz, W. (2013) Biological Water Oxidation, *Accounts Chem. Res.*
240. Ames, W., Pantazis, D. A., Krewald, V., Cox, N., Messinger, J., Lubitz, W., and Neese, F. (2011) Theoretical evaluation of structural models of the S₂ state in the oxygen evolving complex of Photosystem II: protonation states and magnetic interactions, *J. Am. Chem. Soc.* **133**, 19743-19757.
241. Kulik, L. V., Epel, B., Lubitz, W., and Messinger, J. (2005) Mn-55 pulse ENDOR at 34 GHz of the S₀ and S₂ states of the oxygen-evolving complex in photosystem II, *J. Am. Chem. Soc.* **127**, 2392-2393.
242. Teutloff, C., Pudollek, S., Kessen, S., Broser, M., Zouni, A., and Bittl, R. (2009) Electronic structure of the tyrosine D radical and the water-splitting complex from pulsed ENDOR spectroscopy on photosystem II single crystals, *Phys. Chem. Chem. Phys.* **11**, 6715-6726.

243. Chu, H. A., Hillier, W., and Debus, R. J. (2004) Evidence that the C-terminus of the D1 polypeptide of photosystem II is ligated to the manganese ion that undergoes oxidation during the S₁ to S₂ transition: An isotope-edited FTIR study, *Biochemistry* 43, 3152-3166.
244. Baldwin, M. J., Stemmler, T. L., Riggs-Gelasco, P. J., Kirk, M. L., Penner-Hahn, J. E., and Pecoraro, V. L. (1994) Structural and Magnetic Effects of Successive Protonations of Oxo Bridges in High-Valent Manganese Dimers, *J. Am. Chem. Soc.* 116, 11349-11356.
245. Isobe, H., Shoji, M., Yamanaka, S., Umena, Y., Kawakami, K., Kamiya, N., Shen, J. R., and Yamaguchi, K. (2012) Theoretical illumination of water-inserted structures of the CaMn₄O₅ cluster in the S₂ and S₃ states of oxygen-evolving complex of photosystem II: full geometry optimizations by B3LYP hybrid density functional, *Dalton Trans.* 41, 13727-13740.
246. Boussac, A., Zimmermann, J.-L., and Rutherford, A. W. (1989) EPR signals from modified charge accumulation states of the oxygen evolving enzyme in Ca²⁺-deficient photosystem II, *Biochemistry* 28, 8984-8989.
247. Boussac, A., Zimmermann, J. L., Rutherford, A. W., and Lavergne, J. (1990) Histidine Oxidation In The Oxygen-Evolving Photosystem-II Enzyme, *Nature* 347, 303-306.
248. Sivaraja, M., Tso, J., and Dismukes, G. C. (1989) A calcium-specific site influences the structure and activity of the manganese cluster responsible for photosynthetic water oxidation, *Biochemistry* 28, 9459-9464.
249. Hallahan, B. J., Nugent, J. H. A., Warden, J. T., and Evans, M. C. W. (1992) Investigation of the origin of the S₃ EPR signal from the oxygen-evolving complex of photosystem II: the role of tyrosine Z, *Biochemistry* 31, 4562-4573.
250. Gilchrist, M. L., Jr., Ball, J. A., Randall, D. W., and Britt, R. D. (1995) Proximity of the manganese cluster of Photosystem II to the redox-active tyrosine Y_Z, *Proc. Natl. Acad. Sci. U.S.A.* 92, 9545-9549.
251. Tang, X. S., Randall, D. W., Force, D. A., Diner, B. A., and Britt, R. D. (1996) Manganese-tyrosine interaction in the photosystem II oxygen- evolving complex, *J. Am. Chem. Soc.* 118, 7638-7639.
252. Mino, H., Kawamori, A., Matsukawa, T., and Ono, T.-A. (1998) Light-Induced High-Spin Signals from the Oxygen Evolving Center in Ca²⁺-Depleted Photosystem II Studied by Dual Mode Electron Paramagnetic Resonance Spectroscopy, *Biochemistry* 37, 2794-2799.
253. Lohmiller, T., Cox, N., Su, J. H., Messinger, J., and Lubitz, W. (2012) The basic properties of the electronic structure of the oxygen-evolving complex of photosystem II are not perturbed by Ca²⁺ removal, *J. Biol. Chem.* 287, 24721-24733.
254. Miqyass, M., van Gorkom, H. J., and Yocum, C. F. (2007) The PSII calcium site revisited, *Photosyn. Res.* 92, 275-287.
255. Debus, R. J. (2008) Protein Ligation of the Photosynthetic Oxygen-Evolving Center, *Coord. Chem. Rev.* 252, 244-258.
256. Yano, J., Walker, L. M., Strickler, M. A., Service, R. J., Yachandra, V. K., and Debus, R. J. (2011) Altered Structure of the Mn₄Ca Cluster in the Oxygen-evolving Complex of Photosystem II by a Histidine Ligand Mutation, *J. Biol. Chem.* 286, 9257-9267.
257. Luber, S., Rivalta, I., Umena, Y., Kawakami, K., Shen, J. R., Kamiya, N., Brudvig, G. W., and Batista, V. S. (2011) S₁-state model of the O₂-evolving complex of photosystem II, *Biochemistry* 50, 6308-6311.
258. Galstyan, A., Robertazzi, A., and Knapp, E. W. (2012) Oxygen-evolving Mn cluster in photosystem II: the protonation pattern and oxidation state in the high-resolution crystal structure, *J. Am. Chem. Soc.* 134, 7442-7449.
259. Ifuku, K., Ido, K., and Sato, F. (2011) Molecular functions of PsbP and PsbQ proteins in the photosystem II supercomplex, *J. Photochem. Photobiol. B* 104, 158-164.

260. Ono, T.-A., and Inoue, Y. (1983) Mn-preserving extraction of 33-, 24- and 16-kDa Proteins from O₂-evolving PS II particles by divalent salt-washing, *FEBS Lett.* **164**, 255-260.
261. Åkerlund, H.-E., Jansson, C., and Andersson, B. (1982) Reconstitution of photosynthetic water splitting in inside-out thylakoid vesicles and identification of a participating polypeptide, *Biochim. Biophys. Acta* **681**, 1-10.
262. Pauly, S., Schlodder, E., and Witt, H. T. (1992) The influence of salts on charge separation (P680⁴Q_A) and water oxidation of photosystem II complexes from thermophilic cyanobacteria. Active and inactive conformational states of photosystem II, *Biochim. Biophys. Acta* **1099**, 203-210.
263. Von Hippel, P. H., and Schleich, T. (1969) In *Structure and Stability of Biological Macromolecules* (Timasheff, S. N., and Fasman, G. D., Eds.), pp 417-574, Marcel Dekker, New York.
264. Timasheff, S. N., and Arakawa, T. (1989) In *Protein Structure - A Practical Approach* (Creighton, T., Ed.), pp 331-345, IRL Press, Oxford.
265. Nakamura, Y., Kaneko, T., Sato, S., Ikeuchi, M., Katoh, H., Sasamoto, S., Watanabe, A., Iriguchi, M., Kawashima, K., Kimura, T., Kishida, Y., Kiyokawa, C., Kohara, M., Matsumoto, M., Matsuno, A., Nakazaki, N., Shimpo, S., Sugimoto, M., Takeuchi, C., Yamada, M., and Tabata, S. (2002) Complete genome structure of the thermophilic cyanobacterium *Thermosynechococcus elongatus* BP-1, *DNA Res.* **9**, 123-130.
266. Renger, G., and Hanssum, B. (2009) Oxygen detection in biological systems, *Photosynth. Res.* **102**, 487-498.
267. Corbett, M. C., Latimer, M. J., Poulos, T. L., Sevrioukova, I. F., Hodgson, K. O., and Hedman, B. (2007) Photoreduction of the active site of the metalloprotein putidaredoxin by synchrotron radiation, *Acta Crystallogr. D Biol. Crystallogr.* **63**, 951-960.